Towards an Efficient Gas Exchange Monitoring with Electrical Impedance Tomography

Optimization and validation of methods to investigate and understand pulmonary blood flow with indicator dilution

Zur Erlangung des akademischen Grades eines

DOKTOR-INGENIEURS

von der KIT-Fakultät für

Elektrotechnik und Informationstechnik

des Karlsruher Instituts für Technologie (KIT)

genehmigte

DISSERTATION

von

Michael Kircher, M.Sc.

geb. in Bietigheim-Bissingen

Tag der mündlichen Prüfung:	09. Juli 2020
Referent:	Prof. Dr. rer. nat. Olaf Dössel
Korreferent:	Prof. Dr. med. Inéz Frerichs

Abstract

In many patients suffering from severely impaired gas exchange in the lungs, regional pulmonary ventilation and perfusion are not aligned. Especially, if patients are suffering from the acute respiratory distress syndrome, very heterogeneous distributions of ventilation and perfusion are observed, and patients need to be artificially ventilated and monitored in an intensive care unit, in order to ensure sufficient gas exchange. In severely injured lungs, it is very challenging to find an optimal trade off between recruiting collapsed regions by applying high pressures and volumes, while protecting the lung from further damage caused by the externally applied pressure. In order to ensure lung protective ventilation and to optimize and to support clinical decision making, a growing need for bedside monitoring of regional lung ventilation, as well as regional perfusion, has been reported.

Electrical Impedance Tomography (EIT) is a non-invasive, radiation-free and portable system, which has raised interest especially among physicians treating critically ill patients in intensive care units. It provides high temporal sampling and a functional spatial resolution, which allows to visualize and monitor dynamic (patho-) physiological processes. Medical EIT research has mainly focused on estimating spatial ventilation distributions, and commercially available systems have proven that EIT is a valuable extension for clinical decision making during mechanical ventilation. Estimating pulmonary perfusion with EIT nevertheless has not been established yet and might represent the missing link to enable the analysis of pulmonary gas exchange at bedside. Though some publications have shown the principle feasibility of indicator-enhanced EIT to estimate spatial distributions of pulmonary blood flow, the methods need to be optimized and validated against gold-standards of pulmonary perfusion monitoring. Additionally, further research is needed to understand the underlying physiological information of EIT perfusion estimations.

The aim of this thesis is to contribute to the question, whether EIT can be applied clinically to provide spatial information of pulmonary blood flow alongside regional ventilation to potentially assess pulmonary gas exchange at the bedside. Spatial distributions of perfusion were estimated by injecting a conductive saline indicator bolus, to trace the passage of the indicator during its progression through the vascular system of the lungs. Different dynamic EIT reconstruction methods as well as perfusion parameter estimations were developed and compared, to be able to robustly assess pulmonary blood flow. The estimated regional EIT perfusion distributions were validated against gold-standard lung perfusion measurement techniques. A first validation has been conducted using data of an experimental animal study, where multidetector Computed Tomography was used as comparative lung perfusion

measure. On top, a comprehensive preclinical animal study has been conducted to investigate pulmonary perfusion with indicator-enhanced EIT and Positron Emission Tomography during multiple different experimental states. Besides a thorough method comparison, we aimed to investigate the clinical applicability of the indicator-enhanced EIT perfusion measurement by analyzing the minimal indicator concentration, which allows robust perfusion estimations and presents no harm to the patient.
Besides the experimental validation studies, two *in-silico* investigations were conducted to firstly evaluate the sensitivity of EIT to the passage of a conductive indicator through the lungs in front of severely heterogeneous pulmonary backgrounds. Secondly, the physiological contributors to the reconstructed EIT perfusion image were studied to find basic limitations of the method.
To conclude, pulmonary perfusion estimation based on indicator-enhanced EIT shows great potential to be applied in clinical practice, since we were able to validate it against two established perfusion measurement techniques and provided valuable information about the physiological contributors to the estimated EIT perfusion distributions.

Zusammenfassung

In vielen Fällen sind bei Patienten, die unter stark gestörtem Gasaustausch der Lunge leiden, die regionale Lungenventilation und die Perfusion nicht aufeinander abgestimmt. Besonders bei Patienten mit akutem Lungenversagen sind sehr heterogene räumliche Verteilungen von Belüftung und Perfusion der Lunge zu beobachten. Diese Patienten müssen auf der Intensivstation künstlich beatmet und überwacht werden, um einen ausreichenden Gasaustausch sicherzustellen. Bei schweren Lungenverletzungen ist es schwierig, durch die Anwendung hoher Beatmungsdrücke und -volumina eine optimale Balance zwischen dem Rekrutieren kollabierter Regionen zu finden, und gleichzeitig die Lunge vor weiterem Schaden durch die von außen angelegten Drücke zu schützen. Das Interesse für eine bettseitige Messung und Darstellung der regionalen Belüftungs- und Perfusionsverteilung für den Einsatz auf der Intensivstation ist in den letzten Jahren stark gestiegen, um eine lungenprotektive Beatmung zu ermöglichen und klinische Diagnosen zu vereinfachen.
Die Elektrische-Impedanztomographie (EIT) ist ein nicht-invasives, strahlungsfreies und sehr mobil einsetzbares System. Es bietet eine hohe zeitliche Abtastung und eine funktionelle räumliche Auflösung, die es ermöglicht, dynamische (patho-) physiologische Prozesse zu visualisieren und zu überwachen. Die medizinische Forschung an EIT hat sich dabei hauptsächlich auf die Schätzung der räumlichen Belüftung konzentriert. Kommerziell erhältliche Systeme haben gezeigt, dass die EIT eine wertvolle Entscheidungshilfe während der mechanischen Beatmung darstellt. Allerdings ist die Abschätzung der pulmonalen Perfusion mit EIT noch nicht etabliert. Dies könnte das fehlende Glied sein, um die Analyse des pulmonalen Gasaustauschs am Krankenbett zu ermöglichen. Obwohl einige Publikationen die prinzipielle Machbarkeit der indikatorgestützten EIT zur Schätzung der räumlichen Verteilung des pulmonalen Blutflusses gezeigt haben, müssen diese Methoden optimiert und durch Vergleich mit dem Goldstandard des Lungenperfusions-Monitorings validiert werden. Darüber hinaus ist weitere Forschung notwendig, um zu verstehen welche physiologischen Informationen der EIT-Perfusionsschätzung zugrunde liegen.
Mit der vorliegenden Arbeit soll die Frage beantwortet werden, ob bei der klinischen Anwendung von EIT neben der regionalen Belüftung auch räumliche Informationen des pulmonalen Blutflusses geschätzt werden können, um damit potenziell den pulmonalen Gasaustausch am Krankenbett beurteilen zu können. Die räumliche Verteilung der Perfusion wurde durch Bolusinjektion einer leitfähigen Kochsalzlösung als Indikator geschätzt, um die Verteilung des Indikators während seines Durchgangs durch das Gefäßsystem der Lunge zu verfolgen. Verschiedene dynamische EIT-Rekonstruktionsmethoden und Perfusionsparameter-

Schätzmethoden wurden entwickelt und verglichen, um den pulmonalen Blutfluss robust beurteilen zu können. Die geschätzten regionalen EIT-Perfusionsverteilungen wurden gegen Goldstandard Messverfahren der Lungenperfusion validiert. Eine erste Validierung wurde anhand von Daten einer tierexperimentellen Studie durchgeführt, bei der die Multidetektor-Computertomographie als vergleichende Lungenperfusionsmessung verwendet wurde. Darüber hinaus wurde im Rahmen dieser Arbeit eine umfassende präklinische Tierstudie durchgeführt, um die Lungenperfusion mit indikatorverstärkter EIT und Positronen-Emissions-Tomographie während mehrerer verschiedener experimenteller Zustände zu untersuchen. Neben einem gründlichen Methodenvergleich sollte die klinische Anwendbarkeit der indikatorgestützten EIT-Perfusionsmessung untersucht werden, indem wir vor allem die minimale Indikatorkonzentration analysierten, die eine robuste Perfusionsschätzung erlaubte und den geringsten Einfluss für den Patienten darstellt.
Neben den experimentellen Validierungsstudien wurden zwei *in-silico*-Untersuchungen durchgeführt, um erstens die Sensitivität von EIT gegenüber des Durchgangs eines leitfähigen Indikators durch die Lunge vor stark heterogenem pulmonalen Hintergrund zu bewerten. Zweitens untersuchten wir die physiologischen Einflüsse, die zu den rekonstruierten EIT-Perfusionsbildern beitragen, um die Limitationen der Methode besser zu verstehen.
Die Analysen zeigten, dass die Schätzung der Lungenperfusion auf der Basis der indikatorverstärkten EIT ein großes Potenzial für die Anwendung in der klinischen Praxis aufweist, da wir sie mit zwei Goldstandard-Perfusionsmesstechniken validieren konnten. Zudem konnten wertvolle Schlüsse über die physiologischen Einflüsse auf die geschätzten EIT-Perfusionsverteilungen gezogen werden.

Acknowledgments

This thesis marks the endpoint of my scientific work at the Institute of Biomedical Engineering (IBT) of the Karlsruhe Institute of Technology (KIT) during the last years. Science is always team work and many people have contributed to the finalization of this work. I would like to sincerely thank them for their support.
My sincere gratitude goes to Prof. Dr. rer. nat. Olaf Dössel for giving me the opportunity to be part of his research group, for his valuable support, for his scientific enthusiasm and for always having my back. I would also like to thank Prof. Dr. med. Inéz Frerichs very much for her valuable advice and feedback, for providing data for my research, as well as for refereeing this thesis.
I would also like to thank my project partners at Drägerwerk AG. & Co. KGaA. Above all, I am especially grateful to Birgit Stender, who has contributed strongly to my research and has provided valuable feedback, guidance and unlimited support. She has not only planned the cooperation project between the IBT and Dräger, but has been also mainly responsible for the design and concept of the experimental study in Dresden. On top, I have benefited strongly from her comprehensive proofreading of this thesis and other publications. Additionally, I would like to thank Christian Bozsak for many very productive and interesting discussions, and for his support during the different studies we have conducted together.
I also want to say thank you to Prof. Dr. med. habil. Marcelo Gama de Abreu and his Pulmonary Engineering group, especially Thomas Bluth and Anja Braune, for the productive cooperation during the experimental study and the subsequent analysis.
A big thank you also goes to Gunnar Elke for providing valuable data for my research, for his valuable feedback and our very productive cooperation.
To all my colleagues at the IBT, I would like to express a heartfelt thank you for the great time I had at the institute. I want to thank Axel Loewe and Gunnar Seemann for creating a team atmosphere among the assistants. I would like to thank Manfred Schroll for his countless hours of fixing our problems, Irene Günter for her very valuable organizational assistance and all other technical or organizational staff for your individual contributions. A very special thank you goes to many of my former and current PhD companions: Gustavo Lenis for introducing me to biomedical engineering; Stefan Pollnow and Christian Ritter for their scientific input and for always letting me win; Ady Naber for being the best office mate ever; Yannick Lutz for your countless and very welcome distractions; Nicolas Pilia for your enthusiasm and team work; Steffen Schuler for being a legend; Mark Nothstein for always pushing my self esteem and confidence and to Eki, Laura and Danila for many very nice

conversations and sportive distractions.
I want to thank all my students, who have contributed to the work described in this thesis. In particular, I want to mention Areg Noshadi, Felix Schuderer, Ibrahim Tabet, Xenia Augustin and especially María Hernández Mesa, who has helped me a lot during the last challenging time of my research.
A special thank you goes to all my friends, who have distracted, motivated and inspired me throughout my time at the university.
Most importantly, I want to say thank you to my family: To my parents who have always supported me unconditionally, who have motivated and grounded me and who have always been there for me. Both of you are my idols in so many ways. To my sister, who has been an inspiration and support in all challenging times and for always believing in me and having my back. And finally, from the bottom of my heart, to Nina: I cannot imagine, how I could have finished my thesis without you. You have always picked me up, motivated me and believed in me no matter what. My accomplishments are also your achievements. Thank you for absolutely everything.

Contents

Abbreviations and symbols

Abbreviations

acCT	Computed Tomography based attenuation correction
AIF	arterial input function
ALI	acute lung injury
AR	amplitude response
ARDS	acute respiratory distress syndrome
AUC	area under the curve
BF	blood flow
BGA	blood gas analysis
BV	blood volume
CEM	complete electrode model
CO	cardiac output
CRIC	circulation related conductivity change
CT	Computed Tomography
CVT	central volume theorem
EBCT	Electron Beam Computed Tomography
ECG	electrocardiogram
EIT	Electrical Impedance Tomography
FEM	finite element method
FF	filling factor
FRC	functional residual capacity
GCV	generalized cross validation
GREIT	Graz consensus reconstruction algorithm for EIT
HPV	hypoxic pulmonary vasoconstriction
HU	Hounsfield unit (CT tissue density)
ICU	intensive care unit
IIR	infinite impulse response
IQR	interquartile range
LA	left cardiac atrium
LNTD	linearized and normalized time difference
LoA	limits of agreement
LV	left cardiac ventricle

MAA	macroaggregated human serum albumin
MDCT	multidetector Computed Tomography
MIP	maximum intensity projection
MRI	magnetic resonance imaging
MTT	mean transit time
NaCl	sodium chloride
NF	noise figure
PA	pulmonary artery
PAC	pulmonary artery catheter
PAP	pulmonary artery pressure
PBF	pulmonary blood flow
PBV	pulmonary blood volume
PCA	principle component analysis
PCB	pulmonary capillary bed
PCR	point cloud registration
PCV	pressure controlled ventilation
PE	position error
PET	Positron Emission Tomography
pH	pH value
PSD	power spectral density
PSF	point spread function
PTT	pulmonary transit time
PV	pulmonary vein
RA	right cardiac atrium
RES	reconstruction resolution
RMSE	root mean square error
RNG	ringing
ROI	region of interest
RRV	residual respiratory volume
RV	right cardiac ventricle
SD	shape deformation
SNR	signal-to-noise ratio
SOS	second order structure
SPECT	Single Photon Emission Computed Tomography
STD	standard deviation
SV	stroke volume
SVD	singular value decomposition
TF	transfer function
TLC	total lung capacity
tSVD	truncated singular value decomposition
TTP	time to peak
US	ultrasound

VALI	ventilator associated lung injury
VC	vital capacity
VCV	volume controlled ventilation
VIF	ventricular input function
VILI	ventilator induced lung injury
$\dot{V}/\dot{Q}$	ventilation-perfusion ratio

Clinical parameters

C_{rs}	static respiratory compliance
ΔP	driving pressure
F_IO_2	fraction of inspired oxygen
HR	heart rate
I:E	inspiration:expiration time ratio
MAP	mean arterial pressure
MPAP	mean pulmonary arterial pressure
MV	minute volume
$paCO_2$	partial pressure of arterial carbon dioxide
paO_2	partial pressure of arterial oxygen
iPEEP	intrinsic positive end-expiratory pressure
PEEP	positive end-expiratory pressure
$p_{et}CO_2$	partial pressure of end-tidal carbon dioxide
PIP	peak inspiratory pressure
P_{peak}	(maximal) peak pressure
P_{plat}	end-inspiratory plateau pressure
PVR	pulmonary vascular resistance
RR	respiratory rate
R_{rs}	static respiratory resistance
SpO_2	peripheral capillary oxygen saturation
SvO_2	mixed venous oxygen saturation
V_T	tidal volume

Symbols

g	amplitude of gamma variate
$\mathbf{A}$	system matrix of pulmonary transit function estimation
α	shape parameter of gamma variate
$\mathbf{B}$	binary matrix to separately analyze spatio-temporal contributors to EIT reconstructions (see chapter 8)
β	shape parameter of gamma variate
c	condition of a matrix
χ	Eigenvalue
D	spatial measurement domain
∂D	boundary of spatial measurement domain
$\Delta\sigma_k(n)$ $\Delta\boldsymbol{\sigma}(n)$ $\Delta\boldsymbol{\Sigma}$	conductivity change due to saline indicator dilution
$\Delta v_m(n)$ $\Delta\mathbf{v}(n)$ $\Delta\mathbf{V}$	measured voltage changes at EIT electrodes due to saline indicator dilution
$\not{\mathbf{D}}$	diagonal matrix
$d_k(n)$ $\mathbf{d}(n)$ $\mathbf{D}$	slow drift (recirculation) due to indicator diffusion
$\mathbf{e}$	measurement noise or measurement/estimation error
$\mathbf{E}$	electrical field strength
ε	dielectric permittivity
η	mesh quality index
f	frequency
f_{3dB}	cutoff frequency of a digital filter
f_{95}	frequency below which 95 % of spectral power is located
f_I	frequency of the stimulation current of an EIT measurement
f_{Resp}	respiratory frequency or respiratory rate (RR)
f_s	frame rate of an EIT measurement
$\gamma_k(n)$ $\boldsymbol{\gamma}(n)$ $\boldsymbol{\Gamma}$	gamma variate (model for indicator dilution signal) / estimated first-pass indicator dilution signal
$h_k(n)$ $\mathbf{h}(n)$ $\mathbf{H}$	pulmonary (system) impulse response
$\mathbf{I}$	unit matrix
i	complex unit or iteration index (e.g. for simulated spheres in chapter 7)
$\mathbf{j}$	(vector field of) current density
$\mathbf{J}$	Jacobian or sensitivity matrix of the EIT forward problem
$k \in [1\ K]$	spatial sampling (two spatial domains exist in chapter 8: simulated 3D space with K elements and reconstructed 2D space with H elements)
κ	weighting factor for integral model of superimposed slow drift
$\mathbf{L}$	Laplacian regularization matrix for an EIT reconstruction
$\boldsymbol{\Lambda}$	GREIT mapping matrix to train the reconstruction matrix $\boldsymbol{\Theta}_G$
λ	regularization (weighting) factor / hyperparameter of an EIT reconstruction

$\mathbf{L}_T$	tissue label matrix
$m \in [1\ M]$	number of voltage measurements per measurement frame
μ	magnetic permittivity
$n \in [1\ N]$	temporal sampling points
$n_A\ t_A$	arrival time (sample) of an indicator to a specific spatial compartment
$n_A^\circ\ t_A^\circ$	arrival time (sample) of a global γ-interval
$n_E\ t_E$	leaving/end time (sample) of an indicator from a specific spatial compartment
$n_E^\circ\ t_E^\circ$	leaving/end time (sample) of a global γ-interval
n_E	number of EIT electrodes
$n_{max}\ t_{max}$	maximum time (sample) of an indicator dilution curve
$\mathbf{n}$	normal vector
$n_{S+}\ t_{S+}$	time (sample) of maximal positive slope of an indicator dilution curve
$n_{S-}\ t_{S-}$	time (sample) of maximal negative slope of an indicator dilution curve
$\mathbf{O}$	right Eigenvector matrix of a SVD
ω	angular frequency
$\mathbf{P}$	weighting matrix for the solution norm of an EIT reconstruction
$\mathbf{p}$	spatial coordinates
$p_{E,m}\ \mathbf{p}_E$	coordinates of EIT electrodes
ϕ	(scalar field of the) electrical potential
$q\ Q$	blood volume
$\dot{\mathbf{q}}\ \dot{\mathbf{Q}}$	blood flow
r	*Pearson* correlation coefficient or radius of conductive spheres
$\mathbf{R}$	spatial regularization matrix of an EIT reconstruction
$rC\ \mathbf{rC}$	relative contribution of simulated 3D compartment to 2D EIT reconstruction (see chapter 8)
$\boldsymbol{\rho}_{CT}$	tissue density (as measured by CT)
$\Delta\boldsymbol{\rho}$	spatial intensity/ tissue density change caused by indicator dilution
$\boldsymbol{\rho}_{max}$	temporal maximum intensity projection of 4D CT measurement
R_{max}	maximum of correlation function
$\mathbf{S}$	spatial forward sensitivity distribution
$\sigma_k(n)\ \boldsymbol{\sigma}(n)\ \boldsymbol{\Sigma}$	conductivity
$\boldsymbol{\sigma}_0$	arbitrary and spatially homogeneous background conductivity distribution
$\boldsymbol{\sigma}_B$	(static) background conductivity distribution for an EIT measurement
$\bar{t}_k\ \bar{\mathbf{t}}$	mean transit time
$\mathbf{t}$	synthetic targets to train a GREIT reconstruction matrix
τ	tortuosity
$\boldsymbol{\Theta}$	linear EIT reconstruction matrix
t	time
$\mathbf{U}$	left Eigenvector matrix of a SVD
$v_m(n)\ \mathbf{v}(n)\ \mathbf{V}$	measured voltage at EIT electrodes

V	volume (of gas/air)
$v_{0,m}$ $\mathbf{v}_0$	measured voltage at EIT electrodes corresponding to homogeneous conductivity distribution $\boldsymbol{\sigma}_0$
$v_{B,m}$ $\mathbf{v}_B$	measured voltage at EIT electrodes corresponding to background conductivity distribution $\boldsymbol{\sigma}_B$
$\dot{V}$	flow of gas/air
$\mathbf{W}$	weighting matrix for the residual norm of an EIT reconstruction
w_{PET}	cranial-caudal/vertical weighting of 3D PET perfusion onto 2D plane (for comparison to EIT perfusion in chapter 12)
z_E	EIT electrode plane (cranial-caudal/vertical coordinate)

Indices and operators

$(\ldots)_k$	in/of spatial element k
$(\ldots)_m$	corresponding to EIT measurement m
$(\ldots)_{CT}$	estimated/measured by CT
$(\ldots)_{EIT}$	estimated/measured by EIT
$(\ldots)_{PET}$	estimated/measured by PET
$\lvert\ldots\rvert$	absolute
$\lVert\ldots\rVert_2$	Euclidean norm
$\lVert\ldots\rVert_{fro}$	Frobenius norm
$\tilde{(\ldots)}$	desired
$\hat{(\ldots)}$	estimated
$\bar{(\ldots)}$	mean/average
$\mathscr{F}\{\ldots\}$	Fourier transform

PART I

INTRODUCTION AND FUNDAMENTALS

Chapter 1

Introduction

1.1 Motivation

The supply of oxygen to and removal of carbon dioxide from the cells of the human body are of vital importance. The cardio-respiratory system comprising the heart and lungs plays the central role in this gas exchange process. The heart pumps deoxygenated and carbon dioxide rich blood from the cells to the lungs, where carbon dioxide is expired and the blood is enriched with oxygen. The oxygenated blood can subsequently be supplied to the cells of the body. If gas exchange is impaired, the blood is insufficiently oxygenated (hypoxemia) and carbon dioxide is insufficiently eliminated (hypercapnia). Patients suffer from shortness of breath and in severe cases need to be artificially ventilated and constantly monitored in an intensive care unit (ICU).

A severe type of respiratory failure is the acute respiratory distress syndrome (ARDS), which is characterized by a fast widespread inflammation of the lungs. Larger regions of the lungs collapse due to diffuse injury to cells in the gas exchange barrier between the blood vessels and the air sacks (alveoli) [1]. Approximately 200 000 patients suffer from ARDS in the United states per year and approximately over 3 million patients world wide, which is about 10% of all ICU admissions [2]. Currently, as the world experiences a global pandemic caused by the Covid-19 virus, these numbers might be even substantially higher. As stated in first studies about the virus, in severe forms of the Covid-19 infection, ARDS developed within approximately 8-9 days after the onset of the illness [3, 4]. The lethality of ARDS is around 40 % [2, 5] and patients who survive often suffer from a decreased quality of life due to exercise limitation caused by residual pulmonary function abnormalities [6]. The cause of death is in most cases not the acute lung injury, but an inflammation induced multiple organ failure [7].

Patients suffering from ARDS are mechanically ventilated to recruit collapsed alveolar regions and enable sufficient gas exchange. Typical invasive clinical artificial ventilation in ICUs is achieved by applying positive pressure through endotracheal tubes. While controlled

mechanical ventilation is essential for ARDS patients, high pressures and volumes can be harmful to the lungs and ventilation parameters have to be chosen carefully. The concept of *lung protective ventilation* is generally recommended to avoid or at least minimize ventilator associated lung injury (VALI) [8, 9]. The guideline in [9] suggests to limit the tidal volume (V_T) and the end-inspiratory plateau pressure (P_{plat}) of the mechanical ventilation. At the same time it is recommended to recruit the lung with high static positive end-expiratory pressures (sPEEPs) for a short period of time and to subsequently reduce it to a minimal but sufficiently high level to prevent lung regions from collapse during expiration. The cyclic collapse of alveoli during a respiratory cycle has proven to be exceptionally harmful due to mechanical stress. Finding an optimal PEEP has yet turned out to be a nontrivial task. Besides its influence on the distribution of ventilation within the lung, the spatial distribution of perfusion[1] is strongly influenced by the PEEP applied. Small capillaries around the alveoli are compressed by increased positive pressures, thus sufficient alveolar recruitment is useless if simultaneously perfusion is restricted to the recruited lung region. Both pulmonary ventilation and perfusion have to be considered for the choice of ventilation parameters. For clinical practice, it might therefore be beneficial if the ventilation-perfusion ratio ($\dot{V}/\dot{Q}$) could be monitored at bedside during mechanical ventilation.

Electrical Impedance Tomography (EIT) is a non-invasive method to estimate changes in electrical conductivity distributions within a body by injecting a small alternating current at electrodes attached to the body surface and measuring the resulting electrical potentials. EIT has a high temporal resolution (frame rate of an EIT measurement f_s up to 50 Hz), is cost-efficient and can be easily applied at bedside. Nevertheless, the spatial resolution is relatively low (about 10% of the circumference [10] for a placement of 16 electrodes in a 2D plane around the thorax), but provides sufficient resolution to gain regional information of conductivity changes within the lung. EIT reconstructions are mostly calculated with respect to a reference conductivity distribution, since an absolute reconstruction is very ill-posed. For this reason conductivity changes are mainly measured in clinical application. Since inspired air has a relatively low electrical conductivity compared to other biological tissue, EIT is able to track regional changes in aeration if the electrodes are attached around the thorax of a patient. The estimation of ventilation distributions with EIT has been already validated against other gold standard clinically established imaging methods [11–17]. At the same time, blood is conducting electrical current very well due to its high ionic concentration. The estimation of regional pulmonary perfusion with EIT has been investigated since decades but is still a matter of research. During a cardiac cycle, pulsatile conductivity changes (generally known as circulation related conductivity change (CRIC)) can be observed in perfused regions, which are thought to originate mainly from regional blood volume changes, alignment of red

[1] Perfusion describes the supply of tissue by a certain volume of blood within a measurable amount of time. It is generally measured in ml/min/g. Yet, in medical practice, perfusion is often used interchangeably with the term blood flow and is defined as blood volume per time. Throughout this thesis, we will consider the medical definition of perfusion. Due to its low resolution, EIT will not be able to estimate tissue density or mass, thus we will only be able to reconstruct blood flow in units of volume per time.

blood cells during acceleration and movement of larger blood vessels [18]. CRIC amplitudes are nevertheless relatively small and are not fully understood. Though it has been shown to be very promising to non-invasively estimate cardiac output (CO), its application to estimate regional pulmonary perfusion has underperformed compared to an indicator-enhanced EIT approach [19, 20]. For the latter approach, a hypertonic, conductive saline bolus is injected central-venously and followed during its passage through the lungs. From the progression of the indicator through the lungs, transfer parameters can be estimated based on the indicator dilution theory [21]. The method has not been established for clinical practice, since many computational and physiological aspects have yet to be optimized and understood.

This thesis contributes to the efficient and robust estimation of regional indicator-enhanced EIT blood flow in order to allow EIT to become a regional $\dot{V}/\dot{Q}$ monitor to support, optimize and potentially automatize mechanical ventilation in the future. The detailed objectives are formulated in the next section.

1.2 Objectives of the thesis

The main focus of this thesis is to optimize indicator-enhanced EIT perfusion estimation for robust and reliable practical clinical application. Herefore, two simulation studies have been performed to identify the main contributors of the the pulmonary circulation to EIT perfusion images and to understand the forward and inverse sensitivity of indicator dilution in front of substantially inhomogeneous conductivity backgrounds. To provide the physician with reliable and robust estimations of pulmonary blood flow based on indicator-enhanced EIT measurements, different EIT reconstruction and indicator transfer estimation algorithms were developed and optimized. The estimated EIT perfusion distributions were compared against established pulmonary perfusion measurements in two preclinical studies. Finally, the optimized algorithms were applied in first clinical measurements, which will be described in the outlook of this study.

In detail, this thesis aims to achieve the following research objectives:

1) Understand the forward and inverse sensitivity of indicator dilution in front of substantially inhomogeneous conductivity backgrounds by means of EIT bio-impedance simulation.

2) Understand the contributions of different spatio-temporal compartments of the pulmonary circulation to the indicator-enhanced EIT blood flow distribution image (e.g. cardiac chambers, large pulmonary arteries, capillaries, pulmonary veins) by means of bio-impedance simulation.

3) Identify the minimal saline indicator concentration necessary:

- to achieve similar spatial forward and inverse sensitivities independent of the conductivity background (to ensure the comparability of pulmonary blood flow estimations during therapy such as recruitment maneuvers);

- to achieve a sufficient signal-to-noise ratio (SNR) to estimate pulmonary blood flow based on preclinical measurements.

4) Develop and optimize algorithms to calculate indicator-enhanced EIT blood flow distributions, which:
- reconstruct the spatio-temporal indicator signals,
- robustly separate the first pass indicator signal from recirculation, and
- estimate vascular transfer parameters from the indicator conductivity. curves

5) Compare the indicator-enhanced EIT blood flow estimations during respiratory hold phases to reference perfusion imaging:
- comparison against multidetector CT perfusion in models of sublobar ARDS;
- comparison against Positron Emission Tomography (PET) perfusion in different ventilation and perfusion experiments.

6) Develop algorithms to enable indicator dilution during ongoing mechanical ventilation.
7) Analyze temporal parameters of pulmonary indicator passage.

1.3 Organization of the thesis

Part I presents the motivation, the necessary medical and technical fundamentals and the state of the art in order to put the research described in this thesis into its context.

- **Chapter 2** gives an overview about the cardiorespiratory anatomy and physiology. The influence of regional ventilation and perfusion on the overall gas exchange is described and the acute respiratory distress syndrome (ARDS) is introduced. Additionally, the modes and parameters as well as the clinical challenges of controlled mechanical ventilation are introduced.
- **Chapter 3** contains the basics of EIT. The measurement concept, the mathematical forward problem of EIT as well as the reconstruction of electrical conductivity tomograms are introduced. The state of the art and research of indicator-enhanced EIT measurements to reconstruct regional pulmonary blood flow distributions as well as global hemodynamic parameters are provided.
- **Chapter 4** introduces the fundamental principle of the indicator dilution theory and its application to blood flow measurements.

Part II describes the preclinical studies conducted and analyzed during the research for this thesis.

- **Chapter 5** presents the experimental concept and protocol of the preclinical study in pigs conducted and analyzed in close cooperation with the partners of the Drägerwerk AG & Co. KGaA and the Pulmonary Engineering Group of the Department of

Anesthesiology and Intensive Care Medicine, University Hospital Carl Gustav Carus and Technical University Dresden.

- **Chapter 6** introduces the preclinical porcine study data provided by the Department of Anaesthesiology and Intensive Care Medicine, University Medical Centre Schleswig-Holstein in Kiel, Germany, which was evaluated during the research for this thesis.

Part III presents the simulation studies investigating the sensitivity of indicator-enhanced EIT in the context of pulmonary blood flow.

- **Chapter 7** contains the simulation study investigating the sensitivity of indicator-enhanced EIT in front of the inhomogeneous distribution of background conductivity in injured and inhomogeneously ventilated lungs. The chapter introduces and describes the investigations of forward as well as inverse or reconstruction sensitivity.
- **Chapter 8** describes a dynamic indicator simulation study which evaluates the sources of spatial EIT blood flow estimates.

Part IV describes the developed and implemented methods necessary to reconstruct spatial pulmonary blood flow estimations from EIT voltage measurements.

- **Chapter 9** describes different EIT inversion approaches to reconstruct the spatial distribution of indicator dilution curves.
- **Chapter 10** presents the necessary signal processing to extract the first-pass indicator dilution signal and estimate the blood flow parameters.

Part V contains the evaluation and comparison of the spatial EIT blood flow reconstructions to established reference pulmonary perfusion tomography.

- **Chapter 11** describes the preclinical analysis of the Iowa study and the comparison of spatial blood flow EIT estimates to indicator-dilution with multidetector Computed Tomography (MDCT). The additional study related methods and the results are described and finally discussed.
- **Chapter 12** presents the comprehensive analysis of the conducted preclinical study in Dresden. The EIT blood flow estimations are compared with PET perfusion.

Part VI summarizes the described research and the main important contribution of this thesis and presents and outlook on possible next steps

- **Chapter 13** contains the final conclusions of this work.
- **Chapter 14** presents possible next steps to continue the research.

During my research work at the IBT, I published three journal papers as first author and one as a co-author (currently under review). In total, seven peer-reviewed conference articles and nine conference abstracts were published as either first author or co-author. Furthermore, I supervised ten student theses, which have partly contributed to the methods and results

of this thesis (see list of publications and supervised theses at the end of the thesis). Both, publications and student theses are referenced in the corresponding sections of this thesis.

Chapter 2

Medical fundamentals

2.1 Cardiorespiratory anatomy and physiology

A brief introduction into the cardiorespiratory anatomy, physiology and pathophysiology is presented in this chapter. The chapter is meant to give an overview of the necessary medical fundamentals for the understanding of the research described in this thesis.

2.1.1 Cardiorespiratory anatomy and physiology

Within the research for this thesis, a preclinical study in Dresden has been planned, conducted and evaluated, and a second preclinical study has been analyzed. In both studies domestic pigs have been investigated. For this reason, the pulmonary anatomy and physiology is mainly described for domestic pigs, and differences to the human anatomy and physiology are pointed out.
Regarding their lobar structure, the lungs of the pigs are very similar to human lungs. The left lung consists of a cranial and caudal lobe, which are both ventilated by one main airway. The cranial lobe is sometimes also described to be divided into a cranial and middle lobe [22]. The right lung of pigs comprises four lung lobes (cranial, middle, caudal and accessory/intermediate lobe), a difference compared to human lungs, which only have three lobes [23]. Overall, the right porcine lung is about 25 % larger than the left lung [22], which is similar to human lungs. A graphical depiction of a porcine lung is given in Figure 2.1.

Airways, airflow and ventilation Air is inspired into the lung through the trachea, which divides into the main left and right bronchi, supplying both lungs. The bronchi subdivide into smaller bronchioles to provide airflow to the individual lung lobes [24], and branch again into a series of many smaller conducting airways. According to the idealization of Weibel [25], the conducting airways can be described by 16 generations of branchings until the level of terminal bronchioles. The conducting airways have a smooth surface and do not

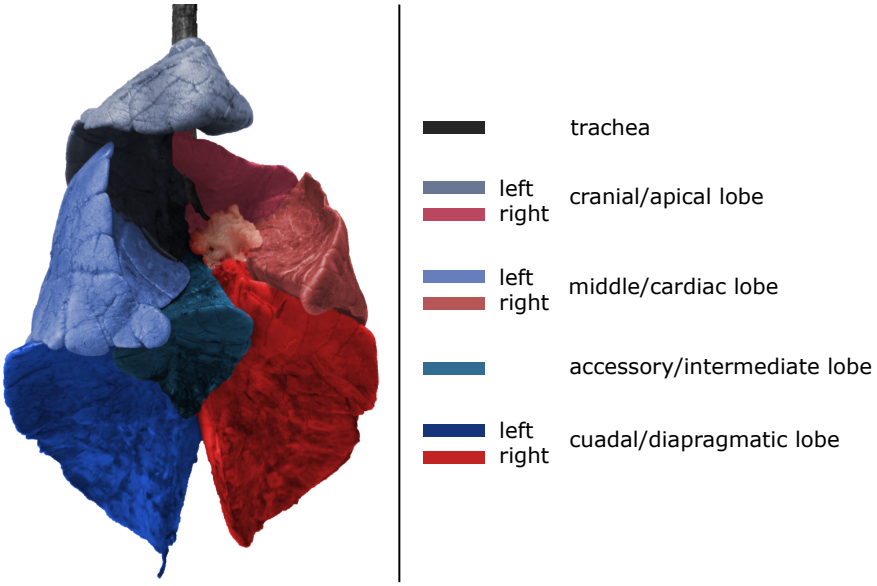

Figure 2.1: Pulmonary anatomy of a domestic pig. The image shows a porcine lung recorded after an experiment of the preclinical study in Dresden (see chapter 5). In literature different names for the lung lobes can be found. The lobe names are taken from [22, 23].

contain the small air sacks or alveoli responsible for the main amount of gas exchange and therefore do not directly participate in gas exchange. With further penetration of the airways into the lungs, the airways become narrower and contain alveoli. The zone of these smaller branches are referred to as the respiratory zone. Within the respiratory zones, the airways branch seven more times [26]. The total human volume of the conducting airways is about 150 ml and is often called the *anatomic dead space*[1], while the respiratory zones have an overall volume of about 2.5-3 l at expiration. [26]

The term ventilation describes the transport of gas between the atmosphere and the alveoli during inspiration and expiration. The airflow into and out of the lungs is mainly controlled by the contraction and relaxation of the diaphragm, and the action of the intercostal muscles. During inspiration, the diaphragm contracts and therefore descents, while the intercostal muscles lift the rib cage to the sides and to the front. The volume of the lungs increases and air is pulled into the lungs from the outside by negative pressure, to fill the increased intra-pulmonary space. Through the larger airways until the respiratory zone, the inhaled air flows downstream by bulk flow. Afterwards, due to the large cross-sectional area within the airways and the small forward velocity of the inspired air, the main mechanism of the gas movement is diffusion. Overall, a very small pressure gradient along the airways (between the atmosphere and the alveoli) of approximately 1 mbar is sufficient to enable a flow rate of 1 l/s. Nevertheless, due to the surface tension of the liquid around the millions of alveoli, strong forces that tend to collapse the alveoli, develop. To increase stability, cells around the alveoli secrete a substance called *surfactant*, which reduces the surface tension. During

[1] *Dead space*: regions of the lungs which are ventilated but do not receive blood flow [26].

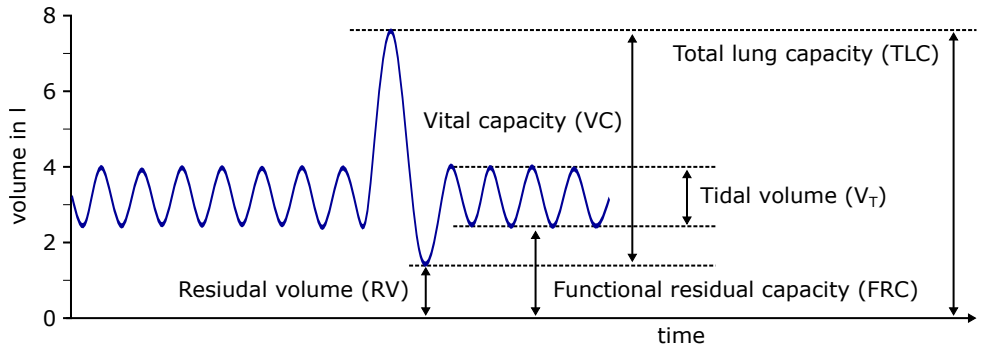

Figure 2.2: Graphical description of the different important lung volumes of an adult human. The idea for the graphic was taken from [26, 27].

expiration, the diaphragm passively relaxes and the elastic lungs return to their resting volume, while the inspired air is forced out of the lungs. [26]

The static volumes of the lung are summarized in Figure 2.2. The tidal volume (V_T) describes the volume of air inspired and expired during normal breathing. The vital capacity (VC) describes the air volume expired between a maximal inspiration and maximal expiration. Both of these volumes are typically measured by spirometry. After a maximal expiration, some air volume still remains within the lungs, which is called residual respiratory volume (RRV). The functional residual capacity (FRC) is defined as the amount of air remaining in the lung after normal expiration. The overall volume at maximal inspiration, which is the sum of the RRV and the VC, is called the total lung capacity (TLC). The residual volumes and the TLC can not be measured with spirometry. They are typically measured with gas dilution techniques. [26, 28]

Blood flow through the pulmonary circuit The vena cava inferior and superior transport deoxygenated blood from the systemic circulation into the right cardiac atrium. During the diastole, the blood enters the right ventricle, and leaves the heart during systole through the pulmonary artery. The full cardiac output (CO) is injected into the main pulmonary artery dividing into the right and left pulmonary artery. Initially within the conducting zone, the pulmonary arteries are accompanied by the bronchi. The arteries branch into a dense network of small capillaries surrounding the alveoli. This network of small capillaries of cross sections, just large enough for red blood cells to pass, form an almost continuous sheet of blood within the alveolar walls [25, 29, 30]. This arrangement provides an enormous surface for potential blood to alveolar gas exchange, only separated by a very thin blood-gas barrier. Although the thin separation between blood capillaries and alveoli is very efficient for gas exchange, the capillaries can easily be damaged or constricted especially by large inspired lung volumes (important to keep in mind during mechanical ventilation as explained in section 2.2.3). The red blood cells traverse the capillary network in approximately 0.75 s (in adult humans). During this time, the equilibrium between alveolar and capillary partial pressures of blood gases is reached. The sheet of blood carrying capillaries around the

alveoli reunite in smaller pulmonary veins. The united larger pulmonary veins also follow the bronchi and end in the left cardiac atrium. [26]
In comparison to the systemic circulation, the blood pressures within the pulmonary circulation are lower (approximately 1-3 mbar in the pulmonary artery [28]). The pressure gradient between inflow and outflow of blood is approximately 10 mbar [28, 31]. Thus, the flow is mainly dependent on passive effects such as hydrostatics and perivascular pressures. Larger arteries and veins, which do not belong to the alveolar caplliaries, are exposed to the intrapleural pressure, which is smaller than the atmospheric pressure. During inspiration, these vessels are pulled open by the elastic lung parenchym surrounding them. The pressure around alveolar capillaries is the alveolar pressure, which is similar to atmospheric pressure. If the alveolar pressure rises, the capillaries are compressed. [31]
In comparison to the vascular resistance of the systemic circulation, the pulmonary vascular resistance (PVR), defined by the transpulmonary pressure gradient divided by the overall blood flow, is also substantially smaller. The PVR is the main control of the flow and its distribution and is mainly influenced by passive effects. On the one hand, if the blood flow increases and the blood pressures rise, the PVR decreases either by a distension of the blood vessels or by recruitment of previously unperfused blood vessels. On the other hand, an increase of lung volume pulls the extra-alveolar larger vessels open and decreases PVR at high lung volumes. At lower volumes, the muscles in the vessel walls decrease the caliber of the larger vessels and the PVR is decreased. For the very small alveolar capillaries, high lung volumes compress the thin walled vessels and PVR is increased. A minimal PVR can be observed roughly at normal ventilation, where capillaries are not compressed and larger vessels are sufficiently pulled open. Besides the passive control of PVR, the muscles in the extra-alveolar vessels can influence blood flow actively. The main active effect is described in the next paragraph. [26, 28]

Hypoxic pulmonary vasoconstriction While the ventilation in the pulmonary bronchi can be altered by sympathetic or parasympathetic innervation, no such control mechanism exists for the PVR. Besides the described passive influences on the PVR, a decrease of partial pressure of oxygen (O_2) in alveoli within a region of the lung, leads to a constriction of its supplying blood vessels. This process is called *hypoxic pulmonary vasoconstriction* or *Euler-Liljestrand mechanism* and was first described in 1946 [32]. Smaller arteries with diameters of around $200-400\,\mu$m are responsible for this effect. The tension of smooth muscle cells within the vascular walls are directly affected by hypoxia resulting in blockade of a potassium channel within the muscle cell membranes leading to a depolarization [33, 34]. The mechanism is a purely regional effect, and it is certain that the central nervous system is not involved in the process, since the effect was also observed in excised isolated lungs. The effect allows to redistribute the regional pulmonary blood flow to areas with sufficient ventilation in pathological conditions such as collapsed lung regions. [26, 28]

Alveolar gas exchange O_2 and carbon dioxide (CO_2) are exchanged through the alveolar walls by diffusion. The lung anatomy is ideal for this process, since the millions of alveoli

with the network of capillaries around them define an enormous surface participating in gas exchange (about 50-100 m^2) and the thickness of the alveolar wall is as thin as 0.3 μm. Due to its higher solubility and a similar molecular weight, CO_2 diffuses 20 times faster than O_2. In addition, the difference in partial pressures of alveolar and vascular O_2 and carbondioxide determine the transfer rate. In a healthy and rested subject, the vascular partial pressure of a volume of blood meets the alveolar partial pressure after a third of its way through the capillary. By exercise, alveolar hypoxia or a thickened blood-gas barrier, the diffusion process can be impaired and the volume of blood leaving the capillary might not be sufficiently oxygenated. [26]

2.1.2 Spatial distribution of ventilation and blood flow

The distribution of ventilation $\dot{V}$ and blood flow $\dot{Q}$ throughout the lung is inhomogeneous and dependent on the posture. The spatial distribution of pulmonary blood flow is mainly determined by gravity [35]. Gravity dependent regions[2] of the lungs are perfused stronger than independent areas. For most of our measurements, the analyses have been carried out in supine position. In this posture, a strong gradient between ventral and dorsal regions of the lungs exist, with large blood flows in dorsal regions. For an upright position of humans, the gradient is even stronger. The gravity dependent imbalance of pulmonary blood flow can be explained by differences of hydrostatic pressures. In upper regions, the arterial and venous pressures are small and might even sometimes fall below alveolar (atmospheric) pressure. In this case, the alveolar vessels are compressed and no or only a small blood flow is possible. In medial regions, the arterial pressure increases, but the venous pressure does not change substantially. Thus, blood flow in these regions is mainly driven by the pressure difference between alveolar and arterial pressure. Towards the lowest regions, the arterial and venous pressure substantially increase because of the hydrostatic pressure from the down- or upstream blood above. Blood flow in lower regions is mainly determined by the pressure difference between arterial and venous pressures. In these lower regions, more alveolar capillaries might also be recruited due to the increased hydrostatic pressure. The gravitation is most likely not the only determinant of pulmonary perfusion distribution. Glenny et al. have reported, that the perfusion pattern might be predominantly defined genetically [36]. They also state, that a perfusion redistribution after posture change leads to a shifting of lung parenchyma. This shifting might confound the interpretation, that gravity is the main determined.[26, 28]
For the alveolar ventilation, similar distributions occur within the lungs. In supine position, the ventilation tends to be higher in dorsal/posterior regions and lower in ventral/anterior regions. In upright posture, ventilation to basal regions of the lungs exceed the ventilation to apical regions. Gravity is also the main influence for the ventilation gradients. The weight of the lower regions (e.g. dorsal regions in supine position) pulls on the upper regions, therefore decreasing the intrapleural pressure. The alveolar walls are distended and become stiffer,

[2]The lowest pulmonary region in relation to gravity is referred to as (gravity) dependent region.

which results in a decreased ventilation. The ventilation gradient (present especially in supine position) is nevertheless substantially smaller than for the pulmonary blood flow. In addition, the regional supply of blood vessels and airways is variable. For an overall optimal gas exchange, the ratio of ventilation and blood flow should be in the vicinity of $\dot{V}/\dot{Q} = 1$ [36]. Due to the above described difference in ventilation and blood flow distribution, $\dot{V}/\dot{Q}$ is heterogeneously distributed across the lungs even for a normal and healthy state. [28]

In medical practices, extremes of the ratio of ventilation and blood flow $\dot{V}/\dot{Q}$ are defined as:

- **Shunt**:
  regions of normal/high blood flow but no ventilation $\rightarrow \quad \mathbf{\dot{V}/\dot{Q} = 0}$
- **Hypoventilation**:
  regions of normal/high blood flow but small ventilation $\rightarrow \quad \mathbf{\dot{V}/\dot{Q} \ll 1}$
- **Hyperventilation**:
  regions of small blood flow but high ventilation $\rightarrow \quad \mathbf{\dot{V}/\dot{Q} \gg 1}$
- **Alveolar or physiological dead space**:
  regions of almost no blood flow and normal or high ventilation $\rightarrow \quad \mathbf{\dot{V}/\dot{Q} \rightarrow \infty}$

These imbalances can occur regionally and always impair the gas exchange and lead to hypoxemia[3]. The effect of a $\dot{V}/\dot{Q}$ imbalance on the concentration of O_2 in the blood is larger than in CO_2 elimination. This is mainly due to the different shapes of disassociation curves of O_2 and CO_2. The disassociation curve of O_2 is very nonlinear while the one for CO_2 is almost linear. Yet, hypoxemia can be reduced by hypoxic pulmonary vasoconstriction improving the overall gas exchange by e.g. directing blood away from dead space or hypoventilated regions. [26, 28]

2.1.3 Acute respiratory distress syndrome

Acute lung injury (ALI) is mainly characterized by diffuse alveolar damage associated with pulmonary infiltrates. The patients develop respiratory distress, which often leads to respiratory failure. The most severe form of ALI is known as acute respiratory distress syndrome (ARDS). The abbreviation ARDS was first used in 1967 [37], describing severely threatening reactions of the lung to inflammation processes not necessarily restricted to the lungs. The mortality rate of patients suffering from ARDS is still very significant. In reviews from 2005 [38] and 2009 [39], clinical studies addressing the mortality rate of ARDS patients were summarized and mortality rates of around 30-40 % were found. To overcome different definitions of the pathology and optimizing and standardizing treatment of the syndrome, a definition has been established during a European-American ARDS conference in 1994 [40]. In 2011, this definition was refined [41]. The respiratory symptoms are classified as

[3] Hypoxemia: an unhealty low concentration of O_2 in the blood

ARDS if [42]:

- bilateral pulmonary infiltrates are observed in x-ray images (not caused by cardiogenic pulmonary edema)
- hypoxemia occurs, as defined by the ratio of partial pressure of arterial oxygen (paO_2) and fraction of inspired oxygen (F_IO_2):
  - **mild** $200\,\text{mmHg} < paO_2/F_IO_2 < 300\,\text{mmHg}$
  - **moderate** $100\,\text{mmHg} < paO_2/F_IO_2 < 200\,\text{mmHg}$
  - **severe** $paO_2/F_IO_2 < 100\,\text{mmHg}$
- lung edema are observed (no cardiac origin)

ARDS patients in an early stage show an increased permeability through the capillary-alveolar barrier. Two main effects were observed due to the increased permeability. Firstly, fluid is able to enter the alveoli, which leads to a formation of pulmonary edemas. Secondly, the epithelial lining cells within the alveolar walls are damaged and decrease or fully cease the production of surfactant. The compliance of the alveoli therefore decreases, and the alveoli collapse. The overall gas exchange is therefore strongly impaired, and tidal volume is distributed to ventilated alveoli, which overdistend and might be damaged. [42, 43]
The properties and the distribution of pulmonary blood flow are also affected by ARDS. The PVR substantially increases due to multiple causes. By hypoxic pulmonary vasoconstriction, blood flow is redirect to properly ventilated regions and away from collapsed areas, which increases PVR since some arterial branches are closed or at least compressed by muscles in the arterial walls. In addition, there is strong evidence that lung injury leads to blood coagulation in ARDS, causing local thrombosis which again increases PVR. Finally, it has been shown that in late and very severe ARDS, the capillary bed is more and more destructed. [44]

In all patients suffering from ARDS, artificial or mechanical ventilation is needed. The choice of ventilator settings has to be made very careful in order to improve gas exchange. Otherwise the artificial ventilation might additionally harm the patient. Mechanical ventilation and injuries resulting from a bad choice of respiratory parameters (ventilator associated lung injury (VALI)), as well as concepts for lung protective mechanical ventilation, especially for ARDS patients, are introduced in the next section.

2.2 Mechanical ventilation

Mechanical or artificial ventilation describes the support or complete replacement of the natural ventilation by an extracorporeal ventilatory machine. The ventilator acts as an additional muscle to drive the airflow in and out of the lungs. For ARDS patients mechanical ventilation is necessary at some point to recruit collapsed alveoli, improve gas exchange and prevent hypoxemia. Nevertheless, high pressures can lead to overdistension in ventilated alveoli and compress alveolar capillary. Lung protective ventilation is therefore aimed for to prevent VALI. Typical modes of mechanical ventilation are introduced in the first section, followed by a short description of lung injuries associated with mechanical ventilation for ARDS patients. Finally, the concept of lung protective ventilation is described and the benefit of an estimation of regional pulmonary blood flow.

2.2.1 Modes of mechanical ventilation

Mechanical ventilation in clinical scenarios is mainly conducted applying a positive pressure at the airway opening. During an acute phase of ARDS, the patient is usually sedated and does not have the possibility to trigger and perform spontaneous respiration. The ventilation is typically performed invasively, thus the patient is intubated and a positive pressure is

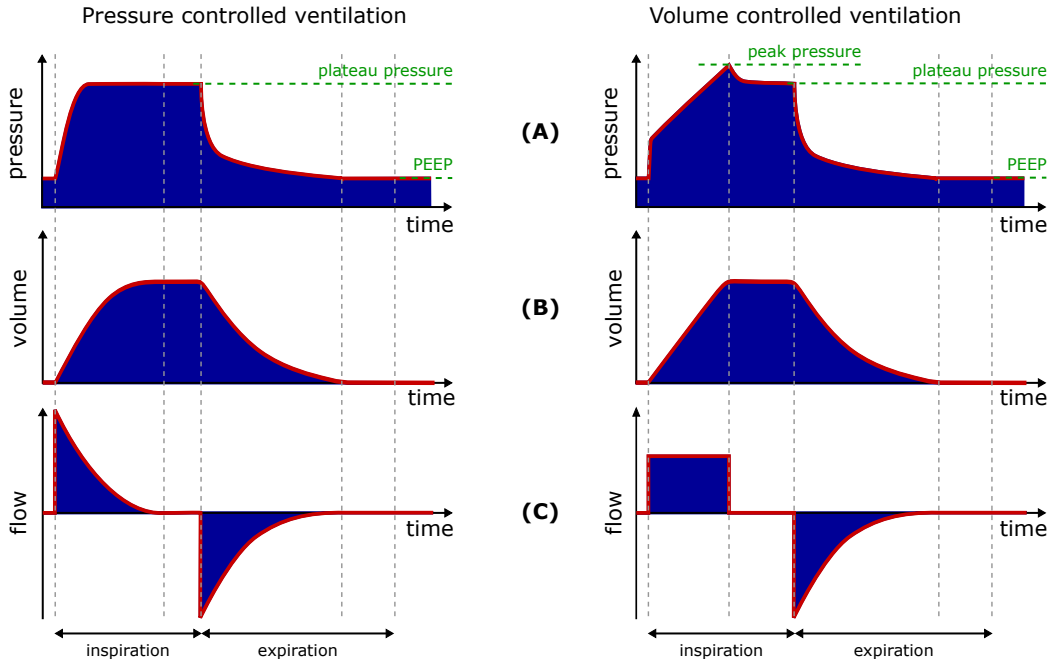

Figure 2.3: Airway pressure (A), volume (B) and air flow (C) time curves for pressure and volume controlled ventilation modes. The idea for the depiction was taken from [45, 46].

applied on the trachea. Typically, two different modes of ventilation are considered, which only differ in the variable which is controlled.

Volume controlled ventilation For the volume controlled ventilation (VCV) mode, the tidal volume V_T and the respiratory rate (RR) are set by the physician. The VCV guarantees the predefined volume. Yet, the maximal and the plateau pressure after inspiration are only indirectly defined by the current mechanical respiratory properties. If the lung is very stiff and has a small static respiratory compliance (C_{rs}), the plateau pressure rises and might cause overdistension of ventilated alveoli. If additionally, the static respiratory resistance (R_{rs}) is high (due to e.g. atelectatic (collapsed) regions), the (maximal) peak pressure (P_{peak}) increases as well. High pulmonary pressures might additionally have a negative influence on pulmonary blood flow, since PVR is increased and the right heart afterload is increased. The pressure, volume and flow time curves are depicted in the right column of Figure 2.3.

Pressure controlled ventilation In comparison to the VCV, the pressure controlled ventilation (PCV) guarantees predefined pressures. The physician defines the driving pressure (ΔP) and the RR. Peak pressures are therefore reduced, though the lung volume is not directly controlled, and again depends on the current mechanical properties of the lungs. The flow during inspiration is not constant but decreases exponentially (compare left column of Figure 2.3). The plateau pressure in PCV mode is reached earlier compared to the VCV mode. This increases the possibility for ARDS patients, that collapsed regions are recruited. If more alveoli are recruited, the volume is distributed within a larger alveolar space and the chance of overdistention of healthy alveoli is reduced [47].
For both modes, some timing parameters can be set additionally. The inspiration:expiration time ratio (I:E) as well as a pause time may be defined. The F_IO_2 has to be chosen as well. For a long term ventilation, the choice should not exceed approximately 60 % because the free radicals of pure O_2 can be toxic [47, 48]. Nevertheless, increasing the F_IO_2 might also help to improve the blood oxygenation and reduce hypoxemia, though if larger shunted regions are responsible for the low O_2 saturation, increasing the F_IO_2 does not have any influence.

Positive end-expiratory pressure In ARDS patients, recruiting collapsed lung regions is one major goal of the mechanical ventilation. By applying tidal volumes or driving pressures with VCV and PCV, collapsed alveoli can be recruited. Nevertheless, the possibility for the alveoli to collapse again after expiration is high. For this reason, a static positive end-expiratory pressure (PEEP) is applied to prevent the alveoli from collapse during the expiratory pause and from cyclic re-opening and -closing, which additionally stresses the alveolar tissue. On the offside, a high PEEP also increases the PVR and can therefore decrease the CO. Additionally another potentially harming effect has to be taken into account when applying PEEP values. Different regions within regionally injured lungs have different mechanical properties and therefore substantially different alveolar inspiratory and expiratory time constants. If the respiratory rate is high (typical for ARDS patients), the

expiratory time might not be sufficient to remove the full inspired volume (air trapping). Hereby, the PEEP is increased by an intrinsic positive end-expiratory pressure (iPEEP) caused by the remaining residual volume within the alveoli.
While a broad agreement of the benefit of a PEEP exists, the choice of an optimal PEEP is still controversially discussed [48]. Many factors have to be considered to define an optimal PEEP. Besides analyzing the amount of collapse and overdistension, the regional analysis of the influence on pulmonary blood flow should be taken into account as well, to be able to assess regional $\dot{V}/\dot{Q}$ ratios.

2.2.2 Ventilator associated lung injury

Since its introduction, mechanical ventilation has improved clinical outcome for severe pulmonary diseases significantly. Yet, it is well known, that mechanical ventilation can have negative effects, which need to be limited. Ventilator associated lung injury (VALI) describes injuries or the worsening of patient health, which is associated with mechanical ventilation. The definite source for the negative effect is often not known. If it is known and a clear proof for mechanical ventilation being the cause is given, the term ventilator induced lung injury (VILI) is used interchangeably [42, 49]. VALI/VILI is not limited to patients with ARDS, but can occur in originally healthy lungs as well. It was found that, in 24 % of clinically ventilated patients, VALI develops within the first 5 days of artificial ventilation, with a higher probability in ARDS patients [50].
The main mechanisms of VALI are damages caused by overdistension due to too high volumes (volutrauma), or high pressures (barotrauma). In some cases, high pressures lead to a rupture of alveoli and to pneumothoraces. In these cases, air accumulates within the pleural cavity. The third main component is associated with a cyclic recruitment and collapse of certain alveolar regions, which increases stress within the lungs. This injury is called atelectotrauma. [51]
The choice of ventilation parameters has to be made very carefully. The tidal volume, the peak pressure, the RR and the PEEP should be considered as most important ones and are controlling mechanical power [52]. Gattinoni et al. have described, that in order to minimize VALI, mechanical power should be decreased to reduce harmful strain, as well as lung homogeneity should be increased [52].

2.2.3 Lung protective ventilation

To prevent or at least minimize VALI, the parameters of controlled mechanical ventilation need to be chosen carefully to protect the lung, while still sufficiently optimizing the gas exchange in severely ill patients. The ventilation mode (VCV or PCV) seems to play a minor role. In a review paper from 2015, Rittayamani summarized many studies comparing VCV and PCV ventilation modes regarding harmfulness and clinical outcome for ARDS patients [53], and no clear difference between both ventilation modes could be found. Independent of the mode of ventilation, it is very important to choose the ventilation parameters such as PEEP, driving pressure ΔP, V_T and F_IO_2 carefully, to reduce the possibility for VALI. The fundamental goals of a lung protective ventilation strategy are [8]:

- limitation of V_T to avoid volutrauma
- limitation of end-inspiratory plateau (P_{plat}) (and peak pressure (P_{peak})) to avoid barotrauma
- choice of adequate PEEP to keep the lung open to avoid alveolar collapse and atelectotrauma
- limitation of F_IO_2 to prevent inflammation and toxicity

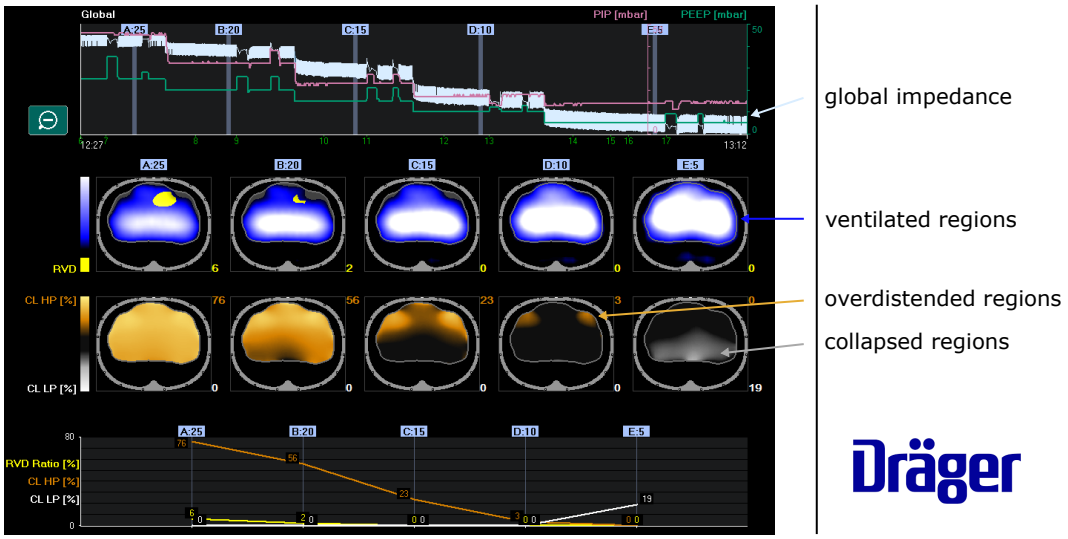

Figure 2.4: Method to choose optimal PEEP using a decremental PEEP trial and the approach described in [54]. The presented and analyzed data shows a decremental PEEP trial performed in a supine domestic pig performed during the preclinical study in Dresden (see section 5). The analysis was created with the *PulmoVista*^{TM}*500* of Drägerwerk AG & Co. KGaA. The optimal PEEP was chosen to PEEP $= 10$ mbar (forth image column from the left), since it was the optimal trade-off between a minimum of collapsed and overdistended regions.

The V_T and end-inspiratory plateau pressure (P_{plat}) are directly interrelated. Generally, the ARDS network (ARDSNet)[4] suggests to set the tidal volume to $V_T = 6\,ml/kg$ and limit the end-inspiratory plateau pressure to $P_{plat} = 30\,mbar$. The respiratory rate is adapted in order to achieve a certain minute volume goal. [8]
Besides limiting the volume and pressure applied to the lung and its alveoli, it is important to recruit the lung and keep it open to minimize the amount of collapsed regions. The concept of keeping the lung open is generally known as *open lung concept*, and was described by Lachmann [55] based on theoretical considerations in [56]. The idea is to recruit collapsed lung regions as complete as possible, by applying high PEEPs and lowering the PEEP afterwards to a minimal pressure that is sufficient to keep the lung permanently open. While the idea is intuitive, finding the optimal PEEP, which is sufficient to keep the lung open while not overdistending alveolis, is not a trivial problem and is still a matter of research and ongoing discussion.
The spatial information of EIT reconstructions of the lung ventilation have been proposed as a valuable additional contribution to find an optimal PEEP. In [54], two measures estimating regional collapse and overdistension have been proposed which are calculated from the local impedance change caused by ventilation. The idea is to find an optimal PEEP where the amount of collapsed and overdistended regions is minimal. Herefore, a decremental PEEP titration is performed as depicted in Figure 2.4. The approach has been implemented in the *Diagnostics* view of the *PulmoVista*^{TM}*500* of Drägerwerk AG & Co. KGaA.

Although the spatial information about collapsed and overdistended regions might prove to be clinically helpful, the knowledge of the spatial distribution of perfusion within the lung might help to find abnormalities in regional $\dot{V}/\dot{Q}$ ratios. Similar to the idea of minimizing collapse and overdistension, reducing $\dot{V}/\dot{Q}$ inhomogeneity as a function of the PEEP, might represent a strategy to find an optimal PEEP not only targeting respiratory mechanics but gas exchange. The simple depiction of the idea can be acknowledged in Figure 2.5.

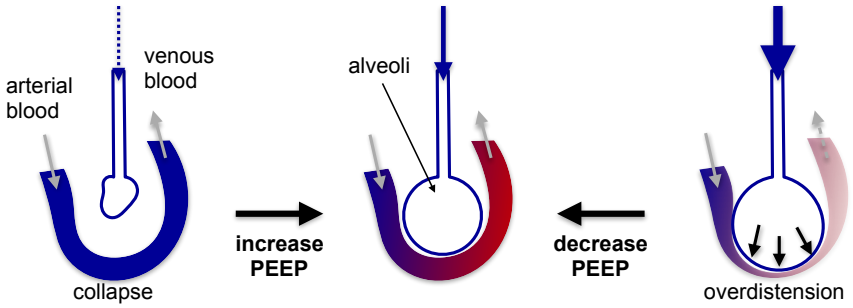

Figure 2.5: Visualization of PEEP optimization based on analyzing ventilation and perfusion. To recruit atelectatic regions of the lungs, a static pressure is applied to reopen collapsed alveoli and enable gas exchange in these regions. Yet, the PEEP needs to be chosen carefully to prevent overdistention, which again increases PVR and reduces the blood flow into the region.

[4]Research network to study ARDS (http://www.ardsnet.org/)

Chapter 3

Electrical Impedance Tomography for pulmonary hemodynamic monitoring

Electrical impedance tomography (EIT) is a clinically available functional imaging modality, which allows bedside monitoring of spatial changes in electrical tissue conductivity. Its current main clinical application is the visualization of conductivity changes in the human thorax, while other applications such as the observation of gastro-intestinal emptying [57] or the bladder volume [58], analyzing brain function such as cortical neural activity [59], locating internal haemorrhage [60, 61] or detecting breast cancer [62] are also investigated. The concept of EIT has first been introduced by Henderson and Webster in 1978 [63] and was initially applied for medical purposes during the 1980's by Barber and Brown [64]. Since the 1990's there has been an increasing research interest in this functional imaging technology. The technology has received even more recognition due to the release of two commercially available clinically certified systems in 2011 and 2013. In 2011, Drägerwerk & Co. KGaA released the *PulmoVista® 500* followed by the *Swisstom BB*^{2} of Swisstom AG in 2013. In this thesis, EIT will be applied to measure pulmonary blood flow and general cardio-respiratory hemodynamic monitoring. The following chapter will provide the necessary fundamentals to understand the technical principles of cardio-pulmonary EIT monitoring. A thorough overview of the state of the art of this application of EIT will be presented in the last section of this chapter.

3.1 Technical principles of EIT

3.1.1 EIT measurements

The principle of medical EIT bases on the fact, that the human body consists of many different biological tissues with distinguishable electrical properties such as electrical con-

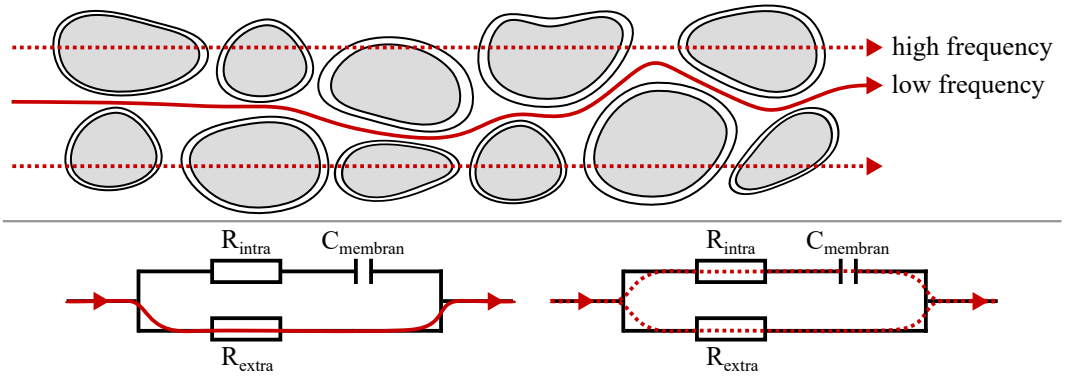

Figure 3.1: Microscopical illustration of the current paths through a cell compound and the resulting equivalent circuit as introduced by [65]. The current paths at low and high frequency are depicted. At low frequencies, the cell membranes with their capacitive behavior can not be penetrated by the current. The current flows through the extracellular space which is modeled by the resistor R_{extra} in the equivalent circuit. At high frequencies, the current is able to flow through the cells as well. The intra-cellular space is modeled as resistor R_{intra} and the membrane as capcitor $C_{membrane}$. The illustration is created based on the idea from [66–68].

ductivity σ and dielectric permittivity ε. These tissue properties often change with (patho-) physiological function and vary significantly with frequency. The flow of electrical currents is mainly determined by the movement of ions within the body. At low frequencies, the extra-cellular fluid is mainly responsible for the current propagation and can be described by an electrical resistor. With increasing current frequency, the capacitive cell membranes allow current to penetrate the intra-cellular space. Overall, biological tissue can be described by an equivalent circuit with resistors for the intra- and extra-cellular space and a capacitance for the cell membrane. This model was introduced by Cole and Cole [65] and is depicted in Figure 3.1.

To measure the tissue properties, a small current is injected through two surface electrodes into the body, and other electrodes placed around the thorax measure the resulting potential field. A suitable stimulation current frequency has to be chosen, which is a compromise between multiple considerations: The electrode-skin contact impedance decreases with increasing frequency and reduces the errors due to impedance imbalances on the measuring electrodes [68, 69]. With higher frequencies the maximally permitted injected current amplitude considered harmless increases, which results in higher signal-to-noise ratios (sSNRs) [70]. Nevertheless, at high frequencies the design of analog circuits becomes substantially more complex and capacitive effects of parasitic capacitances increase [69]. For these opposing reasons, EIT injection frequencies are typically chosen between $f_I = 10 - 1000\,\mathrm{kHz}$ [71]. Throughout the research for this thesis, only time-difference EIT has been performed with single frequency injections. Measurements have been analyzed from two distinct systems. Their technical properties are summarized in Table 3.1.

Both devices, deployed for measurements during the research for this thesis, use $n_E = 16$ electrodes placed around the thorax in a 2D plane and use an adjacent stimulation as well as measurement protocol (see Figure 3.2). A current is injected into the body D through

	n_E	f_I (kHz)	f_s (Hz)	EIT protocol	
				stimulation	measurement
Care Fusion *Goe MF II*	16	5-500	25	adjacent	adjacent
Dräger *PulmoVista® 500*	16	80-130	50	adjacent	adjacent

Table 3.1: Property overview of the systems used for clinical and preclinical measurements.

two neighboring electrodes and the resulting potential differences are measured at all other neighboring electrode pairs on the surface ∂D. This type of impedance measurement is called *4-electrode measurement*, since the potential differences are measured at electrodes which do not carry a current simultaneously [72]. Due to the electrode-skin impedance a substantial voltage drop occurs at the stimulation electrodes, which influences the voltage measurement at the stimulating electrodes [69, 72]. The voltage measurement at all other electrodes is done with a very high input impedance, so that the electrode-skin impedance can be neglected. The current injection is successively repeated at all possible electrode pairs until a complete measurement cycle is completed. One measurement cycle will be called measurement frame throughout this thesis and allows the reconstruction of a single axial image of the internal tissue conductivity distribution. Although a 2D image is reconstructed, the flow of the injected current is not restricted to the 2D plane at electrode height. Thus, the cross-sectional image represents a projection of a 3D sensitive region around the electrode level onto a 2D-plane at electrode height. The frame rate f_s defines the measurement or image repetition rate. Thus, physiological processes with frequencies $f <= \frac{f_s}{2}$ can be monitored as defined by the *Nyquist-Shannon sampling theorem* [73]. For both devices a

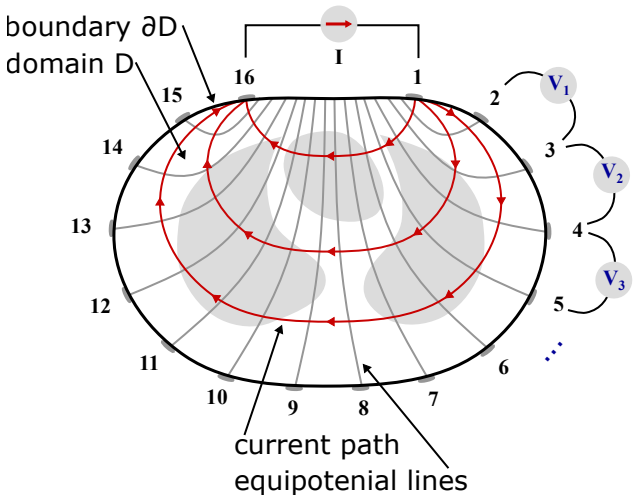

Figure 3.2: Illustration of the EIT measurement and stimulation pattern as it is used for example in the Dräger *PulmoVista® 500*. n_E electrodes are attached to the surface ∂D of the domain D and a current is injected through the electrode pair (16,1). The resulting potential differences are measured at all remaining electrodes. To complete a full measurement frame, the current injection is sequentially rotated around the body, injecting currents through the pairs (1,2);...;(15,16). The resulting equipotential lines and current paths are additionally displayed.

single measurement frame consists of $M = n_E(n_E - 3) = 208$ measurements with $\frac{M}{2} = 104$ being linear independent respecting *Green's reciprocity theorem* [74].
The positioning of the electrodes and the type of stimulation and measurement pattern have a substantial influence on the spatial distribution of measurement sensitivity within the body [75]. For the Care Fusion *Goe MF II* device (which was used during the Iowa study), the electrodes are placed equidistantly around the thorax with the first electrode on the sternum and the 9^{th} electrode close to the spine. Due to the low conductivity of bone tissue and the concave body surface at these positions, the electrodes are rearranged for the *PulmoVista® 500* as depicted in Figure 3.2. The adjacent stimulation and measurement pattern is more sensitive to conductivity changes closer to the boundary compared to changes in the center of the body [75, 76]. This is a disadvantage compared to the more homogeneous distribution of sensitivity for stimulation and measuring patterns between electrodes at opposite positions of the thorax. Nevertheless, the complexity of the hardware significantly increases for these types of patterns and the adjacent patterns are still a well working and clinically validated compromise [69]. For a mathematical description of the measurement sensitivity be referred to section 3.1.2.

3.1.2 Forward problem of EIT

The forward problem of EIT describes the mathematical function of calculating a resulting potential ϕ of a known distribution of (complex) conductivities $\underline{\sigma}$[1] within a domain and a known current injection at the surface of this domain. EIT's governing equation for the forward problem can be derived from Maxwell's equations [69, 77]. We herefore assume that a sinusoidal current with a frequency $f_I < 1\,\text{MHz}$ is injected into the domain $D \in \mathbb{R}^3$ at distinct positions on the domain boundary ∂D and we can neglect indirect currents induced by magnetic fields for this frequency range (magnetic permeability μ and the angular frequency of the current ω are relatively small) [69]. The current injection causes an electric field $\mathbf{E}(\mathbf{p})$ at positions $\mathbf{p} \in D$, which is linked to the the current density $\mathbf{j}(\mathbf{p})$ by the complex conductivity or admittivity $\underline{\sigma}(\mathbf{p}) = \sigma(\mathbf{p}) + i\omega\varepsilon(\mathbf{p})$:

$$\mathbf{J}(\mathbf{p}) = \big(\sigma(\mathbf{p}) + i\omega\varepsilon(\mathbf{p})\big) \cdot \mathbf{E}(\mathbf{p}) \tag{3.1}$$

Additionally, we do not expect any internal current sources in the stimulation frequency range within D, thus the divergence of $\mathbf{j}(\mathbf{p})$ is zero:

$$\nabla\mathbf{j}(\mathbf{p}) = 0 \tag{3.2}$$

With the aforementioned negligible magnetic field, the temporal derivative of the magnetic field vanishes and the electric field can be expressed by the spatial gradient of the scalar potential $\phi(\mathbf{p})$:

$$\mathbf{E}(\mathbf{p}) = -\nabla\phi(\mathbf{p}) \tag{3.3}$$

[1] Throughout this thesis only isotropic tissue conductivity is considered. In case of anisotropic conductivity, σ describe a tensor of $[3 \times 3]$

Combining equations (3.1), (3.2) and (3.3), we finally arrive at the generalized Laplace equation:

$$\nabla \cdot \left[(\sigma(\mathbf{p})) + i\omega\varepsilon(\mathbf{p}) \cdot \nabla\phi(\mathbf{p}) \right] = 0 \tag{3.4}$$

With EIT we try to recover the internal spatial distribution of the complex conductivity or admittivity $\underline{\sigma}(\mathbf{p})$ for a current stimulation by measuring potential differences at the surface ∂D of D. The complex component of the admittivity in the range of stimulation frequencies is often neglected due to its relatively small impact [71] and the Laplace equation can then be reduced to its real valued version:

$$\nabla \cdot \left[\sigma(\mathbf{p}) \cdot \nabla\phi(\mathbf{p}) \right] = 0 \tag{3.5}$$

The Laplace equations in (3.4) and (3.5) can be interpreted as continuum versions of Kirchhoff's law [69].

Since the current injection at electrode positions $\mathbf{p}_E \in \partial D$ on the boundary is known, we have to solve the boundary value problem described by equation (3.5) and the Neumann boundary condition defining the current density $\mathbf{j}(\mathbf{p})$ on the boundary $\mathbf{p} \in \partial D$:

$$\mathbf{j}(\mathbf{p}) = \begin{cases} \sigma(\mathbf{p}) \frac{\partial\phi(\mathbf{p})}{\partial \mathbf{n}} & \mathbf{p} \in \mathbf{p}_E \\ 0 & \mathbf{p} \notin \mathbf{p}_E \end{cases} \tag{3.6}$$

The vector $\mathbf{n}$ describes the normal vector on ∂D. This boundary condition refers to point EIT electrodes, which were generally used throughout this thesis, except during the simulation study in chapter 8. If full electrode models are considered, a more complex boundary problem needs to be solved [78–80].

The forward problem is generally solved numerically, since an analytic solution only exists for very simple geometries [81]. The typical approach to solve the Forward Problem of EIT is the finite element method (FEM) [69, 81]. The two- or three-dimensional domain D is discretized into K elements, typically triangular or tetrahedral. Within each element a constant conductivity is assumed, thus a vector $\boldsymbol{\sigma} \in \mathbb{R}^{Kx1}$ represents the discrete spatial distribution of conductivity. With the forward problem, we mathematically calculate the voltage measurements v_m between a pair of adjacent surface electrodes for a known spatial distribution of tissue conductivities $\boldsymbol{\sigma}$ and a known current injection I at another pair of electrodes. We can therefore define a discrete Forward Operator $\mathscr{F} : \boldsymbol{\sigma} \in \mathbb{R}^{Kx1} \rightarrow \mathbf{v} \in \mathbb{R}^{Mx1}$, therefore:

$$\mathbf{v} = \mathscr{F}(\boldsymbol{\sigma}, I) \tag{3.7}$$

For medical applications, EIT is mostly used to detect changes in conductivity due to dynamic physiological processes with respect to a static background conductivity $\boldsymbol{\sigma}_B \in \mathbb{R}^{Kx1}$. This special form of EIT is called *time-difference* EIT and has been used for all EIT measurements in this study. By considering only conductivity changes in terms of the reconstruction, the sensitivity of the nonlinear forward problem in equation (3.7) to modeling errors of the

boundary and to errors in electrode position can be substantially reduced [47, 82]. We herefore expand the nonlinear forward operator in equation 3.7) into a Taylor series:

$$\mathbf{v} = \mathscr{F}(\boldsymbol{\sigma}) \approx \mathscr{F}(\boldsymbol{\sigma}_B) + \frac{\partial \mathscr{F}(\boldsymbol{\sigma})}{\partial \boldsymbol{\sigma}}\Big|_{\boldsymbol{\sigma}=\boldsymbol{\sigma}_B} (\boldsymbol{\sigma} - \boldsymbol{\sigma}_B) + \dots \tag{3.8}$$

If we assume only small changes in conductivity $\Delta\boldsymbol{\sigma} \in \left\{\mathbb{R}^{Kx1} | \Delta\boldsymbol{\sigma} = \boldsymbol{\sigma} - \boldsymbol{\sigma}_B\right\}$, we can neglect higher order components of the Taylor series and approximate the forward problem with linearly, calculating the measured voltage changes $\Delta\mathbf{v} \in \mathbb{R}^{Mx1}$ as [83]:

$$\Delta\mathbf{v} \approx \frac{\partial \mathscr{F}(\boldsymbol{\sigma})}{\partial \boldsymbol{\sigma}}\Big|_{\boldsymbol{\sigma}=\boldsymbol{\sigma}_B} \Delta\boldsymbol{\sigma} = \mathbf{J} \cdot \Delta\boldsymbol{\sigma} \tag{3.9}$$

The voltage change $\Delta\mathbf{v} = \mathbf{v} - \mathbf{v}_B$ is the change with respect to a background voltage $\mathbf{v}_B \in \mathbb{R}^{Mx1}$ which corresponds to the background conductivity $\boldsymbol{\sigma}_B$. The linear approximation and first order component of the Taylor series of the forward operator is expressed by the Jacobian matrix $\mathbf{J} \in \mathbb{R}^{MxK}$. It projects the conductivity change in each spatial element k onto to the m^{th} voltage measurement at a specific current injection.
One common method to calculate a good estimate of the Jacobian $\mathbf{J}$ is the *perturbation technique* [84]. A small conductivity perturbation $\Delta\sigma_k$ is applied to a single element k and the resulting measurement voltage changes $\Delta\mathbf{v}$ are calculated with the FEM. We can therefore calculate each element of $\mathbf{J}$ by

$$J_{mk} = \frac{\Delta v_m}{\Delta\sigma_k} \tag{3.10}$$

A more sophisticated method to calculate the Jacobian directly from the derivatives of the FEM system matrix was introduced in [85]. This approach is more efficient computationally and increases the accuracy for large FEM element sizes.

The linear approximation of the forward problem with the Jacobian $\mathbf{J}$ enables a fast calculation of the measured voltage changes by simple matrix multiplication. This is beneficial especially for the inverse problem, which is described in the following section. Nevertheless, the Jacobian depends on the choice of $\boldsymbol{\sigma}_B$. In clinical reconstruction, the assumption, that the background conductivity is homogeneous, has often been considered and resulted in sufficiently good reconstructions.

3.1.3 Inverse problem of EIT

The goal of EIT is to recover the spatial distribution of conductivity or conductivity changes within a volume by measuring voltages at the surface of this volume. We therefore try to recover the source from its effect, which is the classical description of an *inverse problem*. Thus, for time-difference EIT, we want to recover the inverse of the forward problem relationship in equation (3.9):

$$\Delta\boldsymbol{\sigma} = \mathbf{J}^{-1} \cdot \Delta\mathbf{v} \tag{3.11}$$

For the reconstruction of the conductivity changes within the body, it is crucial to have a good estimate of the forward model $\mathbf{J}$. Nevertheless, the calculation of the Jacobian is also

very sensitive to modeling errors close to the boundary and to electrode position errors [82]. Especially for clinical application, it has therefore been useful to reconstruct normalized voltage changes based on a normalized Jacobian. The systematic errors are therefore canceled out [47] and the influence of the modeling errors are substantially reduced. The normalized reconstruction is described by:

$$\begin{aligned} \Delta\boldsymbol{\sigma}_n &= \mathbf{J}_n^{-1} \cdot \Delta\mathbf{v}_n \\ \text{with } \Delta\mathbf{v}_n &= \frac{\mathbf{v} - \mathbf{v}_B}{\mathbf{v}_B} \\ \Delta\boldsymbol{\sigma}_n &= \frac{\boldsymbol{\sigma} - \boldsymbol{\sigma}_B}{\boldsymbol{\sigma}_B} \\ \mathbf{J}_n &= diag(\bar{\mathbf{j}})^{-1} \cdot \mathbf{J} \end{aligned} \tag{3.12}$$

For the normalization of the Jacobian, the overall or global sensitivity of each measurement m is calculated:

$$\bar{j}_m = \sum_{k=1}^{K} J_{mk} \tag{3.13}$$

Throughout the whole thesis, the normalized reconstruction has been applied. For a simpler notation, the index $()_n$ indicating the normalization will be waived in the following.

To recover $\Delta\boldsymbol{\sigma}$, the Jacobian needs to be inverted. Unfortunately, $\mathbf{J}$ is generally not a square matrix and therefore not invertible. For this reason, the internal conductivity changes are approximated by minimizing the euclidean norm of an error function:

$$\Delta\hat{\boldsymbol{\sigma}} = \underset{\Delta\boldsymbol{\sigma}}{\operatorname{argmin}} \|\Delta\mathbf{v} - \mathbf{J} \cdot \Delta\boldsymbol{\sigma}\|_2^2 \tag{3.14}$$

The minimization can be performed explicitly using the generalized least squares method and the *Moore-Penrose-Pseudoinverse* Θ to get an approximation of the internal conductivity changes $\Delta\hat{\boldsymbol{\sigma}} \in \mathbb{R}^{Kx1}$ [86]:

$$\Delta\hat{\boldsymbol{\sigma}} = \left(\mathbf{J}^\top\mathbf{J}\right)^{-1}\mathbf{J}^\top \cdot \Delta\mathbf{v} = \Theta \cdot \Delta\mathbf{v} \tag{3.15}$$

The matrices $\mathbf{J}$ and $\mathbf{J}^\top\mathbf{J}$ are *ill-conditioned*[2]. Thus, the inverse problem of EIT violates at least one of the criteria of *well-conditioned* problems as defined by Hadamard [87, 88]:

Definition: Well-conditioned problem
A physical problem described by a mathematical system or model $\mathbf{A} : \mathbf{x} \rightarrow \mathbf{y}$ is well-conditioned if:

- **(existence)** for all measured data $\mathbf{y}$, a solution $\mathbf{x}$ exists
- **(uniqueness)** for all measured data $\mathbf{y}$, the solution $\mathbf{x}$ is unique

[2]The terms *ill-/well-conditioned* are used, since the described inverse problem is a discrete problem. The more commonly used description *ill-/well-posed* refers to continuous problems.

- **(stability)** the solution $\mathbf{x}$ depends continuously on the measured data $\mathbf{y}$ (small perturbations in $\mathbf{y}$ cause small changes in $\mathbf{x}$, therefore the inverse $\mathbf{x} = \mathbf{A}^{-1} \cdot \mathbf{y}$ is continuous)

The third criterion is the most crucial one for the inverse problem of EIT [69]. It can not be assumed that a spatial distribution of $\Delta\boldsymbol{\sigma}$ can be stably recovered from a boundary voltage measurement $\Delta\mathbf{v}$. To enforce the solvability of the inverse problem, additional constraints need to be imposed. Often some *a-priori* information about the solution is known, e.g. spatial smoothness or a realistic interval of possible solution values. Techniques, augmenting additional *a-priori* constraints to the solution, are called *regularization* techniques. Typical approaches to regularize inverse problems are the *Tikhonov regularization* or the *truncated singular value decomposition (tSVD)*. Both approaches will be introduced briefly in the following.

Tikhonov regularization

To generalize the description of a regularized inverse problem, the following simple ill-conditioned model[3] is introduced:

$$\begin{aligned} \mathbf{y} &= \mathbf{A} \cdot \mathbf{x} + \mathbf{e} \\ \text{with } \mathbf{y} &\in \mathbb{R}^{Mx1} \text{ , } \mathbf{e} \in \mathbb{R}^{Mx1} \\ \text{and } \mathbf{x} &\in \mathbb{R}^{Kx1} \text{ , } \mathbf{A} \in \mathbb{R}^{MxK} \end{aligned} \tag{3.16}$$

We arrive at the EIT reconstruction problem if we replace:

$$\begin{aligned} \mathbf{y} &:= \Delta\boldsymbol{\sigma} \\ \mathbf{A} &:= \mathbf{J} \\ \mathbf{x} &:= \Delta\mathbf{v} \end{aligned} \tag{3.17}$$

If we want to recover the sources $\mathbf{x}$ from the measurement $\mathbf{y}$ with the superimposed measurement noise $\mathbf{e}$, the system matrix $\mathbf{A}$ needs to be inverted. Since $\mathbf{A}$ is a non-invertible and ill-conditioned matrix, the inverse is approximated by minimizing the following functional including *a-priori* information [88]:

$$\hat{\mathbf{x}} = \underset{\mathbf{x}}{\operatorname{argmin}} \left(\|\mathbf{y} - \mathbf{A}\mathbf{x}\|_2^2 + \lambda \, \|\mathbf{R}\mathbf{x}\|_2^2 \right) \tag{3.18}$$

The second norm $\|\mathbf{R}\mathbf{x}\|_2^2$ of the functional introduces the imposed constraints on the approximation of the solution $\hat{\mathbf{x}}$ with a regularization matrix $\mathbf{R} \in \mathbb{R}^{KxK}$. The regularization parameter $\lambda \in \{\mathbb{R} \,|\, \lambda > 0\}$ controls the amount or order of regularization. To minimize the functional in equation (3.18) the *Moore-Penrose-Pseudoinverse* is calculated:

$$\hat{\mathbf{x}} = \left(\mathbf{A}^\top \mathbf{A} + \lambda \cdot \mathbf{R}^\top \mathbf{R} \right)^{-1} \mathbf{A}^\top \cdot \mathbf{y} \tag{3.19}$$

[3] The symbols $\mathbf{A}$, $\mathbf{x}$ and $\mathbf{y}$, describing the exemplary model, are introduced for simplicity and are only used within the current chapter and can not be found in the main symbol list.

The type of imposed constraint is defined by the regularization matrix $\mathbf{R}$. For the classical Tikhonov approach, the regularization matrix is chosen to be a unit matrix $\mathbf{R} = \mathbf{I}$. The estimates $\hat{\mathbf{x}}$ are forced to have the smallest possible amplitudes. Throughout this thesis, different regularization matrices are used and will be introduced in chapters 9 and 10.
The choice of the regularization parameter λ has a crucial impact on the quality of inversion. If λ is chosen too small, the solution $\hat{\mathbf{x}}$ tends to the general least squares minimization without any regularization, yet if it is too large, the influence of the regularization dominates and the actual inversion is neglected. A rough interval for suitable λ can be estimated by calculating the condition c of the matrix $\mathbf{A}^\top\mathbf{A} + \lambda \cdot \mathbf{R}^\top\mathbf{R}$ [47, 69]:

$$c\left(\mathbf{A}^\top\mathbf{A} + \lambda \cdot \mathbf{R}^\top\mathbf{R}\right) = \frac{\chi_1 + \lambda}{\chi_K + \lambda} \tag{3.20}$$

$\chi_1, \chi_2, ..., \chi_K \in \mathbb{R}$ describe the Eigenvalues of the matrix $\mathbf{A}^\top\mathbf{A}$. Without a regularization ($\lambda = 0$) the condition of the matrix to be inverted is defined by its Eigenvalues. For the inverse problem of EIT, $\chi_1 \gg \chi_K$ leads to a strongly ill-conditioned matrix. With $\lambda \gg \chi_K$ the condition can be improved [47]. In Figure 3.3, the Eigenvalues and the condition of the matrix without and with a Tikhonov regularization are depicted.

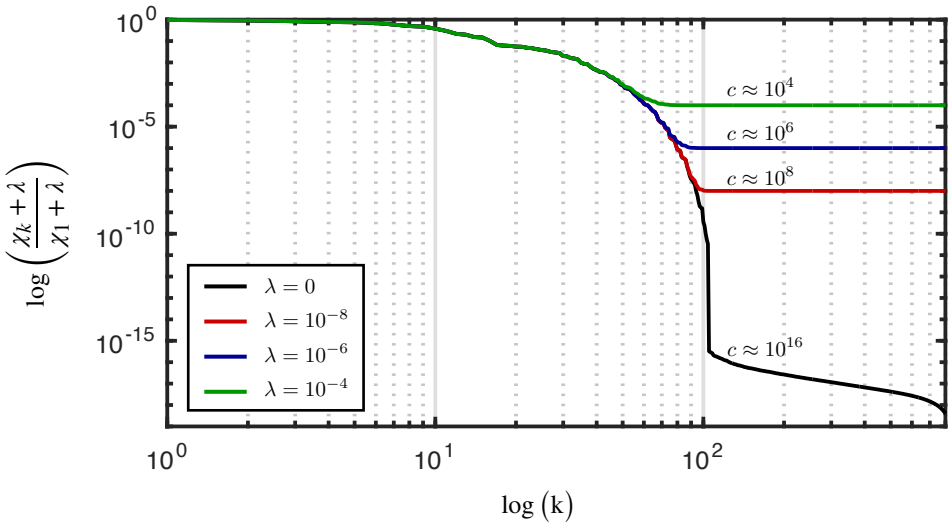

Figure 3.3: Graphic visualization for the Eigenvalues of the matrix $\mathbf{A}^\top\mathbf{A} + \lambda \cdot \mathbf{R}^\top\mathbf{R}$ for different values of λ. $\mathbf{R} = \mathbf{I}$ was chosen. The ratio between the smallest and the largest Eigenvalue, which determines the condition of the matrix, improves for increasing λ.

Multiple systematic approaches to optimize λ have been proposed in literature. The most well-known approaches are the *L-curve method*, the *generalized cross validation (GCV)* [89–91] and explicitly for EIT the optimization of the noise figure [92, 93].
In this thesis the L-curve is used if not stated otherwise. The underlying idea is to systematically find an optimal trade-off between minimizing the regularization or solution norm $\|\mathbf{R}\mathbf{x}(\lambda)\|_2^2$ and the residual norm $\|\mathbf{y} - \mathbf{A}\mathbf{x}(\lambda)\|_2^2$. If the logarithm of the solution norm is

plotted over the logarithm of the residual norm, we expect an L-shaped curve. The value of λ corresponding to the corner of the L-shaped curve therefore represents the optimal choice for the regularization parameter. An implementation of the approach in [90] has been used.

Equation 3.18 can be further extended considering weighted norms [84, 94]:

$$\hat{\mathbf{x}} = \underset{\mathbf{x}}{\operatorname{argmin}} \left(\|\mathbf{y} - \mathbf{A}\mathbf{x}\|_{\mathbf{W}}^2 + \lambda \, \|\mathbf{R}\mathbf{x}\|_{\mathbf{P}}^2 \right) \tag{3.21}$$

The matrices $\mathbf{W}, \mathbf{P} \in \mathbb{R}^{KxK}$ allow to weight the regularization and system matrix. $\mathbf{W}$ can be interpreted as the inverse of the measurement noise $\mathbf{e}$. If we assume uncorrelated noise between the measurement channels, $\mathbf{W}$ is chosen to be a diagonal matrix. It allows to weight the system matrix with its covariance. For the inverse problem of EIT, this means, if all measurements at the surface electrodes can be considered as having the same quality (similar electrode-skin impedances, gains,...), $\mathbf{W} = \mathbf{I}$ is chosen. Similarly, the matrix $\mathbf{P}^{-1}$ can be interpreted as covariance matrix of the expected image [95], though $\mathbf{P}$ can be chosen to impose any *a-priori* information and can also be integrated in $\mathbf{R}$. The final reconstruction can be conducted with the following *Moore-Penrose-Pseudoinverse*:

$$\hat{\mathbf{x}} = \left(\mathbf{A}^\top \mathbf{W} \mathbf{A} + \lambda \cdot \mathbf{R}^\top \mathbf{P} \mathbf{R} \right)^{-1} \mathbf{A}^\top \mathbf{W} \cdot \mathbf{y} \tag{3.22}$$

Truncated singular value decomposition (tSVD)

Another approach to regularize inverse problems is the truncated singular value decomposition (tSVD). To briefly introduce the method, the simple system described in equation (3.16) will be considered. The following introduction is a summary mostly from [96].
In order to find a regularized inverse of the ill-conditioned matrix $\mathbf{A}$, the matrix is approximated as in:

$$\mathbf{A} = \mathbf{U} \not{\mathbf{D}} \mathbf{O}^\top \tag{3.23}$$

The decomposition consists of the matrix $\mathbf{U} \in \mathbb{R}^{KxK}$ which contains the orthonormal Eigenvectors of $\mathbf{A}^\top \mathbf{A}$, the matrix $\mathbf{O} \in \mathbb{R}^{KxK}$ consisting of the orthonormal Eigenvectors of $\mathbf{A}\mathbf{A}^\top$ and a diagonal matrix $\not{\mathbf{D}} \in \mathbb{R}^{KxK}$. The diagonal elements of $\not{\mathbf{D}}$ are the square roots of the Eigenvalues $\chi_1, \chi_2, ..., \chi_K$ and are called *singular values*. Throughout this thesis, the *singular value decomposition* as implemented in *MATLAB R2019a* was used. As described for the Tikhonov regularization, the condition of a matrix is defined by the ratio between its largest and smallest Eigenvalue. Thus, the idea behind the tSVD is to remove the smallest k_r singular values and to approximate the matrix $\mathbf{A}$ by:

$$\mathbf{A} \approx \mathbf{A_r} = \mathbf{U}_r \not{\mathbf{D}} \mathbf{O}_r^\top \tag{3.24}$$

The matrices are therefore reduced in size. The matrices $\mathbf{U}_r, \mathbf{O}_r \in \mathbb{R}^{KxK-k_r}$ contain only the first $K - k_r$ Eigenvectors corresponding to the first Eigenvalues $\chi_1, ..., \chi_{K-k_r}$. To calculate an estimate of the solution $\hat{\mathbf{x}}$, the *Moore-Penrose-Pseudoinverse* is defined:

$$\hat{\mathbf{x}} = \left(\mathbf{A}_r^\top \mathbf{A}_r \right)^{-1} \mathbf{A}_r^\top \cdot \mathbf{y} \tag{3.25}$$

The number of neglected Eigenvalues k_r can be optimized with the methods described for the Tikhonov optimization.
By removing the smallest Eigenvalues, the condition of the matrix can be considerably improved. Since small Eigenvalues most likely correspond to high frequencies in the solution, the tSVD method can be considered as a sharp low-pass filter [90]. The Tikhonov regularization is a more smooth lowpass and more adaptive, since the type of imposed regularization can be chosen with more degrees of freedom by the matrix $\mathbf{R}$.

Graz consensus reconstruction algorithm for EIT (GREIT)

Following first discussions at the International Conference of Bioimpedance (ICEBI) in 2007, a unified 2D-EIT reconstruction algorithm has been developed and published in [93]. With the goal to define a standard linear 2D-EIT reconstruction algorithm, the general opinion of many experts has been consulted, in order to define a general consensus on the properties of a robust and high-performance reconstruction algorithm.
Firstly, multiple standardized figures of merit were defined in [93], which allow to analyze the performance of the reconstruction. These figures of merit have been applied during the sensitivity study in chapter 7 and will be introduced in detail in section 7.2. The defined reconstruction performance parameters comprise a measure of the amplitude response, which describes the ratio between the reconstructed amplitude and the target amplitude, a measure of the position error between reconstruction and the simulated target and other measures describing shape deformation, reconstructed resolution and ringing.
All above described linear reconstruction approaches derive a linear reconstruction matrix based on the implicit inversion of the Jacobian stabilized by some sort of regularization $\mathbf{R}$. The idea behind the GREIT reconstruction algorithm is to explicitly or directly define a reconstruction matrix $\mathbf{\Theta}_G \in \mathbb{R}^{K\times M}$ based on a training set of $i = [1,...,I]$ simulated conductivity target pertubations $\mathbf{t}^i \in \mathbb{R}^{K\times 1}$ and their corresponding forward calculated M normalized difference voltages $\Delta\mathbf{v}^i \in \mathbb{R}^{M\times 1}$. In order to compute an optimized reconstruction matrix $\mathbf{\Theta}_G$, desired reconstructed EIT images $\Delta\tilde{\boldsymbol{\sigma}}^i \in \mathbb{R}^{K\times 1}$ were defined. The desired images were calculated by $\Delta\tilde{\boldsymbol{\sigma}}^i = \mathbf{\Lambda}\mathbf{t}^i$ with a desired image mapping matrix $\mathbf{\Lambda} \in \mathbb{R}^{K\times 1}$, which can be interpreted as the desired point spread function of the EIT reconstruction. Utilizing $\mathbf{\Lambda}$ the reconstruction properties can be explicitly defined. To train $\mathbf{\Theta}_G$, the functional defined by the desired images of all targets $\Delta\tilde{\mathbf{\Sigma}} \in \mathbb{R}^{K\times I}$ is minimized and the simulated difference voltages corresponding to all simulated targets $\Delta\mathbf{V} \in \mathbb{R}^{K\times I}$ [93, 97]

$$e(\mathbf{\Theta}_G) = \|\Delta\tilde{\mathbf{\Sigma}} - \mathbf{\Theta}_G \cdot \Delta\mathbf{V}\|^2 \tag{3.26}$$

For the targets, a spatial distribution $\mathbf{t} \sim \mathcal{N}(0, \mathbf{C}_t)$ with a covariance C_t is considered. To additionally minimize the noise amplification of the reconstruction algorithm, J measurements of voltage differences $\Delta\mathbf{V}^n \in \mathbb{R}^{K\times J}$ solely caused by measurement noise were also considered. Measurement noise was modeled by Gaussian white noise with the covariance C_n: $\Delta\mathbf{V}^n \sim \mathcal{N}(0, \mathbf{C}_n)$. The target and noise measurements were simply concatenated (indicated by $[...|...]$) and the extended functional was minimized:

$$e(\mathbf{\Theta}_G) = \|[\Delta\tilde{\mathbf{\Sigma}}|\mathbf{0}] - \mathbf{\Theta}_G \cdot [\Delta\mathbf{V}|\Delta\mathbf{V}^n]\|^2 \tag{3.27}$$

Minimizing this functional with respect to $\mathbf{\Theta}_G$ results in:

$$\mathbf{\Theta}_G = \mathbf{\Lambda}\mathbf{C}_t^{-1}\Delta\mathbf{V}^\top \left(\Delta\mathbf{V}\Delta\mathbf{V}^\top + \Delta\mathbf{V}^n\Delta\mathbf{V}^{n\top}\right)^{-1} \tag{3.28}$$

For small targets, $\Delta\mathbf{V} \approx \mathbf{J}$ can be assumed, with $\mathbf{J}$ representing the Jacobian of the forward problem. The final reconstruction matrix strongly resembles the Tikhonov reconstruction matrix optimized by $\mathbf{\Lambda}$:

$$\mathbf{\Theta}_G = \mathbf{\Lambda}\mathbf{C}_t^{-1}\mathbf{J}^\top \left(\mathbf{J}\mathbf{C}_t\mathbf{J}^\top + \lambda\mathbf{C}_n\right)^{-1} \tag{3.29}$$

λ again controls the noise suppression and is generally optimized by optimizing the noise figure (NF) as introduced in [93]:

$$\mathrm{NF} = \frac{E\left\{mean|\Delta\tilde{\mathbf{\Sigma}}|\right\}/E\left\{std|\Delta\tilde{\mathbf{\Sigma}}^n|\right\}}{E\left\{mean|\Delta\mathbf{V}|\right\}/E\left\{std|\Delta\mathbf{V}^n|\right\}} \tag{3.30}$$

Thus, the reconstructed image SNR is compared to the voltage data SNR. A value of λ creating a $\mathrm{NF} = 0.5$ is recommended to be chosen [93].

3.2 State of the Art - pulmonary hemodynamic monitoring

The described EIT reconstruction algorithms have been applied in numerous studies and published research to identify regional distributions of ventilation. Although the idea of analyzing regional pulmonary blood flow related conductivity changes is nearly as old as EIT itself, there have been substantially less publications. The two main topics of cardio-pulmonary hemodynamic research focused on the estimation of stroke volume (SV) and cardiac output (CO) estimation, as well as the reconstruction of pulmonary perfusion. The following description of previous work will focus on regional pulmonary perfusion estimation.

Two different concepts of estimating regional pulmonary perfusion with EIT have been investigated in previous publications. Firstly, a continuous and fully noninvasive estimation has been investigated, which analyzes the circulation related conductivity change (CRIC) within the heart and the lungs. For the second approach, a hypertonic saline indicator was injected central venously and tracked during its passage through the pulmonary circulation. Both approaches have been applied in clinical studies and have also been compared to each other.

Pulmonary perfusion estimation based on CRIC To analyze the CRIC signal, it has to be separated from the substantially larger ventilation related conductivity or impedance changes. The simplest method to separate ventilation and blood circulation related signals is frequency domain filtering [20, 98]. If an electrocardiogram (ECG) is simultaneously recorded, ECG-gated ensemble averaging has been applied [19, 20, 98, 99] or even adaptive, more complex filters based on principle component analysis (PCA) have been proposed [100–102]. In many preclinical and clinical studies, the need to separate CRIC from ventilation related signal components has been circumvented by performing the EIT measurements during respiratory hold phases [103].
Already in 1989, the CRIC has been investigated by Eyuboglu et al. [99]. They already investigated CRIC in humans and separated it from ventilation-related signal components by ensemble averaging. They already hypothesized, that the origin of the pulsatile cardiac signal might be local blood volume changes of distensible blood vessels, flow characteristics and movement of the heart. In [104], a correlation between a decrease of CRIC amplitude and the loss of alveolar capillaries could be identified [98]. Smit et al. published similar findings [105]. They suggested that CRIC amplitudes are mainly determined by the size of the microvascular bed and rather little by SV. Intensive care physicians are especially interested in perfusion of the microvascular bed, since this is the perfusion participating in gas exchange. Yet, the origin of CRICs seem to be manifold and might be caused by multiple simultaneously occurring effects [18]. Borges et al. showed that indicator based perfusion estimation outperforms the CRIC approach in a small preclinical porcine study [19], while

Stowe et al. recently suggested that pulsatility based perfusion imaging could achieve similar results as the indicator dilution technique [20].
The CRIC most definitely contains information about pulmonary perfusion in the vascular bed, yet it seems to be superimposed by other effects. CRIC measurements can be acquired continuously at bedside, which is a clear advantage compared to indicator based approaches.

Indicator based perfusion estimation Initially, the use of contrast agents for the application of perfusion measurements with EIT was suggested by Brown et al. [106]. Since then, multiple experimental analyses using the method have been conducted while there is still need for comprehensive (clinical) validation studies [107]. The most important publications regarding the indicator dilution method will be summarized in the following:

- In 2002, Frerichs et al. performed a first preclinical feasibility study. Indicator-enhanced EIT perfusion was compared against Electron Beam Computed Tomography (EBCT) scans. The study was performed with three piglets and three different experimental states were investigated: uni-lateral injection of EBCT and EIT indicators through the distal port of a PAC to the left lung; proximal injection of indicators with the left pulmonary artery blocked with a balloon at the tip of a PAC; proximal injection of the indicator without obstruction of the pulmonary arteries. For EIT measurements, a hypertonic saline indicator was used with a concentration of 5.85 %. While the animals were quite small (20 kg), which simplifies the mathematical inversion, and the study group was relatively small (n=3), the study could prove the principle feasibility of indicator-enhanced EIT perfusion measurements.

- In 2012, a slightly larger preclinical study with n=6 piglets was conducted by Borges et al. [19]. EIT indicator perfusion was compared to Single Photon Emission Computed Tomography (SPECT) perfusion during seven different conditions: bi-lateral controlled ventilation, uni-lateral ventilation, uni-lateral ventilation with the attenuation of HPV by nitroprussid infusion, bi-lateral lung injury induced by lung lavage with and without the attenuation of HPV and bi-lateral ventilation after recruitment. EIT perfusion could follow SPECT perfusion nicely with limits of agreement of around 10 %. The saline indicator concentration was nevertheless very high (20 %). The usage of this concentration is arguably not applicable for clinical measurements due to its high osmolarity and its potential influence on cardiac electrophysiology [108]. The piglets were also relatively small compared to humans. The study introduced robust methods to estimate pulmonary blood flow parameters after the removal of recirculation using gamma variate fits. Additionally, CRIC was compared to SPECT and indicator EIT with clinically insufficient validation results, expecially regarding trending.

- In two PhD theses from 2011 [47] and 2015 [102], algorithms for indicator based blood flow were analyzed and further developed. Nevertheless, both theses lacked

gold standard validation and only show principle plausibility. Pikkemaat also compared different EIT reconstruction algorithms to computed regional dynamic indicator signals from voltage measurements, yet could not find a distinct optimal algorithm outperforming the others.

- In 2018, Hentze et al. published another preclinical study comparing indicator perfusion based on EIT against SPECT [109]. The study comprised four animals and measurements were conducted at two different PEEP levels (5 mbar and 15 mbar). A saline indicator with a concentration of 10 % was used. EIT perfusion distributions showed strong similarity with SPECT perfusion. The dorsal-ventral profiles of EIT perfusion correlated with SPECT (r=0.94). Additionally, EIT ventilation was also compared to SPECT and also showed very good accordance. The main contribution of the paper was a novel method of calculating regional blood flow estimates based on multi-compartment transfer functions. The method does not rely on pixelwise estimation but represents rather a system approach. The lack of regional information regarding transit times might be considered as a disadvantage. Additionally, the method should be evaluated with respect to robustness in a larger study.

Besides this major contributions, which either contributed algorithmically or validated indicator perfusion against a gold standard perfusion imaging method, there have been additional preclinical studies without the comparison against another perfusion measurement technique [110, 111]. In [20], indicator perfusion was compared against CRIC in lambs. During breath hold, CRIC performed equally well compared to indicator perfusion. A recent review [112] describes regional indicator perfusion measurements based on EIT as promising to be able to calculate ventilation-perfusion ratio ($\dot{V}/\dot{Q}$) distributions. Nevertheless, more validation studies are still essential.

Chapter 4

Indicator dilution theory

The theory of indicator dilution and previous applications of the indicator dilution in the context of pulmonary hemodynamics shall be introduced in this chapter to give a fundamental overview of the principle of this technique for the application to indicator-enhanced EIT.

4.1 Theoretical fundamentals

The measurement of blood flow using the indicator dilution method dates back to first measurements in Stuttgart published in 1829 [113]. In 1954, over 100 years later, a fundamentally important paper was published by Meier and Zierler [21], who proved and established the central volume theorem (CVT). Since then the method has been developed further and applied for different clinical measurements.
A fluid bolus $c_{in}(t)$ is injected into a system roughly instantaneously. With the indicator dilution theory, the blood flow (BF) $\dot{Q}_B$, the blood volume (BV) Q_B and the mean transit time (MTT) $\bar{t}_B$ can be estimated by measuring the output of the system $c_{out}(t)$ [21, 114]. The parameters are connected to each other by the CVT:

$$\dot{Q}_B = \frac{Q_B}{\bar{t}_B} \tag{4.1}$$

In order to estimate these blood circulation related parameters in a complex network of different sizes and number of parallel vessels, a transfer function from the input to the output needs to be estimated. Since this transfer function is dependent on the vascular network and its properties, it is not possible to identify such a system transfer function analytically and therefore needs to be estimated. For this estimation, multiple assumptions are typically made [21]:

- The blood flow $\dot{Q}_B(t) = \dot{Q}_B$ through the system as well as the volume $Q_B(t) = Q_B$ of the system are constant.
- No volume of fluid is stored within the system and recirculation does not occur.
- The indicator can be described by particles and the flow of the indicator particles is representative of the total fluid.

We define an indicator *transport function* $h(t)$, which can be regarded as the impulse response of the system [21, 109, 115]:

$$c_{out}(t) = c_{in}(t) * h(t) = \int_0^t c_{in}(\tau) \cdot h(t-\tau) d\tau \tag{4.2}$$

The transport function $h(t)$ can also be interpreted as probability density function of transversal times [116]. If we can find a good estimate of $h(t)$, the MTT is defined by the first moment of this density function:

$$\bar{t}_B = \frac{\int t h(t) dt}{\int h(t) dt} \tag{4.3}$$

To introduce the shape of a typical transport function $h(t)$, we consider a system, which consists of K serial compartments (tube model) [109, 116–118]. A graphical description of such a model is given in Figure 4.1. Each compartment has a volume of $Q_{B,K} = \frac{Q_B}{K}$, therefore the overall volume of all serial compartments is Q_B. The blood flow $\dot{Q}_B$ through the compartments is assumed to be constant. An indicator with the concentration $c_{in}(t)$ is injected into the first compartment of the tube and the concentration exiting the K^{th} compartment $c_{out}(t)$ is measured. To derive the transport function of the multi-compartment system, the approach by Hentze et al. [109] is summarized.
For a single ideally mixing compartment and the assumptions above, we can define the following differential equation [109, 117]

$$\frac{dc_{out}(t)}{dt} = \frac{K \cdot \dot{Q}_B}{Q_B} \cdot (c_{in}(t) - c_{out}(t)) \tag{4.4}$$

With the Laplace transform, the transfer function $H(s)$ in the Laplace domain is calculated:

$$sC_{out}(s) = \frac{K \cdot \dot{Q}_B}{V_B} (C_{in}(s) - C_{out}(s)) \tag{4.5}$$

$$H(s) = \frac{C_{out}(s)}{C_{in}(s)} = \frac{K \cdot \dot{Q}_B}{Q_B} \frac{1}{\frac{K \cdot \dot{Q}_B}{Q_B} + s} \tag{4.6}$$

With the inverse Laplace transform, the transport function $h(t)$ of a single ideally mixing compartment results:

$$H(s) = \frac{K \cdot Q_B}{V_B} \frac{1}{\frac{K \cdot Q_B}{V_B} + s} \bullet\!\!-\!\!\circ\, h(t) = \frac{K \cdot Q_B}{V_B} e^{-\frac{K \cdot Q_B}{V_B} t} \tag{4.7}$$

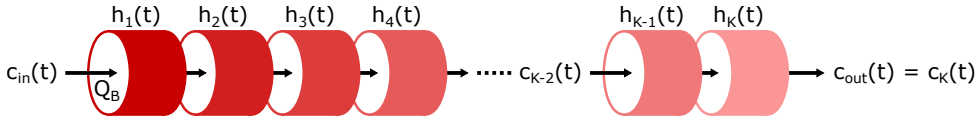

Figure 4.1: Graphical description of tube model with K compartments of equal volume Q_B/K. The compartments are ideally mixing compartments. The indicator $c_{in}(t)$ is injected in the first compartment and measured at the outflow of the K^{th} compartment. The impulse responses of the k^{th} element is described by $h_k(t)$. The illustration is motivated by the descriptions in [109, 116].

The full tube system consists of K equal serially connected ideally mixing compartments. The individual transfer functions of each compartment are multiplicatively connected in Laplace domain and the overall transfer is described by:

$$H(s) = \prod_{i=1}^{K} \frac{K \cdot \dot{Q}_B}{Q_B} \frac{1}{\frac{K \cdot \dot{Q}_B}{Q_B} + s} = \left(\frac{K \cdot \dot{Q}_B}{Q_B} \right)^K \frac{1}{\left(\frac{K \cdot \dot{Q}_B}{Q_B} + s \right)^K} \tag{4.8}$$

With the inverse Laplace transform, we finally arrive at the overall transport function:

$$h(t) = \mathscr{L}^{-1} \{H(s)\} = \left(\frac{K \cdot \dot{Q}_B}{Q_B} \right)^K \frac{t^{K-1}}{(K-1)!} e^{-\frac{K \cdot \dot{Q}_B}{Q_B} t} \quad \forall t > 0 \tag{4.9}$$

The shape of the transfer function $h(t)$ resembles for a large number of compartments $K \to \infty$ a gamma variate $\gamma(t)$ with the parameters g, α, β and $t_A \in \mathbb{R}$ [118–120]:

$$\gamma(t) = g \cdot (t - t_A)^{\alpha} \cdot e^{-\beta (t - t_A)} \tag{4.10}$$

If we compare the transport function $h(t)$ with the gamma variate $\gamma(t)$, the gamma variate describes the transport function, if we choose the parameters of the gamma variate to:

$$\begin{aligned} \alpha &= K - 1 \\ \beta &= \frac{K \cdot \dot{Q}_B}{Q_B} \\ g &= \beta^K \frac{1}{\alpha!} \end{aligned} \tag{4.11}$$

If the indicator is injected instantaneously $c_{in}(t) = \delta(t)$ and transferred through the system with a gamma variate $h(t) = \gamma(t)$, the concentration at the output $c_{out}(t)$ also resembles a gamma variate. Thus, the gamma-variate is an appropriate model of the concentration outflows and the transport function.

PART II

EXPERIMENTAL DATA

Chapter 5

Preclinical animal study Dresden

The study has been approved by the *Institutional Animal Care and Welfare Committee* and the Government of the State Saxony, Germany (DD24-5131/354/64).
The study was planned and conducted under the lead of the cooperation partner at Drägerwerk AG & CO. KGaA, Birgit Stender and Christian Bozsak, and together with the *Pulmonary Engineering Group* lead by Prof. Dr. med. Marcelo Gama de Abreu of the Anesthesiology Department of Prof. Dr. med. Thea Koch. The experiments were performed at the Department of Radiation Therapy and Oncology (University Hospital *Carl Gustav Carus* in Dresden) of Prof. Dr. med. Jörg Kotzerke between December 2016 and June 2017.

We initially published the study and the main analyses in [121]. Besides this main journal publication, the study was part of multiple conference publications [122–128]. The measurements of the study have also been the fundamental database for multiple Bachelor and Master theses of students under my supervision[129–134].

5.1 Study design and objective

Until the end of June 2017, 15 farm raised pigs (52.9 kg $\pm$ 4.9 kg) were included in this study. For animal 8, 10 and 11 the experimental protocol (see section 5.4) could not be fully completed due to premature deaths of the animals. Compared to other studies, fully grown pigs were included in the study with similar thorax circumferences as humans.

Initially, the following main objectives have been defined:
The **primary goal** of the study was to compare relative pulmonary blood flow distributions based on indicator-enhanced EIT measurements to a established lung perfusion imaging in different conditions of regional pulmonary ventilation and perfusion. PET perfusion imaging with ^{68}Gallium (^{68}Ga)-labeled microspheres was chosen as the reference method. The comparison was carried out in clinically relevant regions of interest (ROIs) with multiple similarity measures. The conductive saline EIT indicator (NaCl) was used in four different

concentrations (2 %, 3 %, 5 % and 10 %) and applied during respiratory hold phases to be able to neglect the influence of the ventilation on the EIT measurement.
To increase the potential for clinical application, as a **secondary objective** we investigated, whether the indicator-enhanced EIT measurement could be performed during regular mechanical ventilation with comparable similarity to the established reference measurement.

5.2 EIT measurements

The EIT measurements (*PulmoVista® 500*, Drägerwerk & Co. KGaA, Lübeck, Germany) were conducted continuously throughout the experiment. An elastic fabric electrode belt (prototype, Drägerwerk & Co. KGaA, Lübeck, Germany) with 16 electrodes was attached to the thorax of the animal. The commercially available electrode belt was not used, since it produces large CT artifacts. For each animal, the electrode belt was attached to the mid-chest region, such that the attached electrodes comprised the caudal part of the heart near the apex during end-inspiration and end-expiration. Correct positioning also guaranteed, that the diaphragm of the lungs did not reach into the electrode plane. The correct positioning of the electrode belt was verified by CT measurements in inspiratory and expiratory hold phases and can be acknowledged in Figure 5.1. The EIT measurements were conducted with

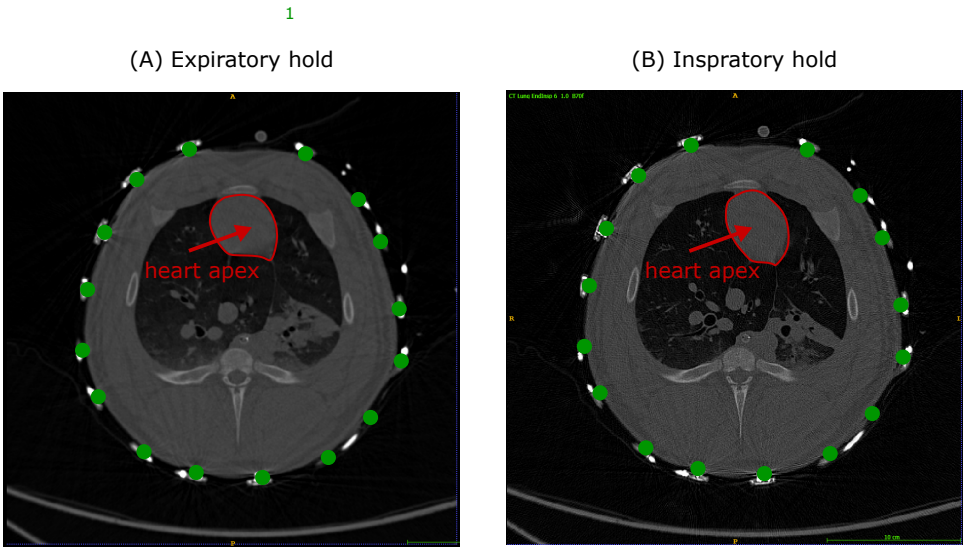

Figure 5.1: CT images during expiratory and inspiratory hold phases to verify EIT electrode positioning. The electrode belt (Drägerwerk AG & Co. KGaA) was attached beneath the front legs of the pig in supine position. With the CT images, the position around the apex of the heart during inspiration and expiration was verified in the beginning of the experiment.

the highest possible injection current frequency $f_I = 130\,\text{kHz}$, if no significant noise was present around this frequency. The frame rate of the EIT measurements was set to $f_s = 50\,\text{Hz}$. The electrode-skin contact resistance was initially checked with the tools provided by the

PulmoVista® 500 and generally improved during the experiment.
The continuous stream of EIT measurements was synchronized to the monitoring parameters using wave form data from the ventilator (flow and volume curve), since the ventilator was attached to the *PulmoVista® 500* via the *MEDIBUS* serial bus protocol (Drägerwerk AG & Co. KGaA, Lübeck, Germany) and to a recording Laptop.

5.3 PET/CT imaging

As described in sections 1.1 and 2.1, physicians at the ICU would benefit from knowledge about the potential pathological spatial distribution of alveolar blood flow or perfusion within the lungs especially in combination with regional lung aeration. To assess the regional quality of gas exchange in the lung parenchym, the perfusion in the vascular bed is crucial for the clinician while the pulmonary blood flow in larger vessels is less important. Only PET and Single Photon Emission Computed Tomography (SPECT) measurements are established and validated to provide this information currently [135].
The experimental measurement setup including the PET/CT scanner (*Biograph™* 16 Hi-Rez PET/CT, Siemens, Knoxville, TN, USA) is shown in Figure 5.2. The EIT device cannot be seen in the image.

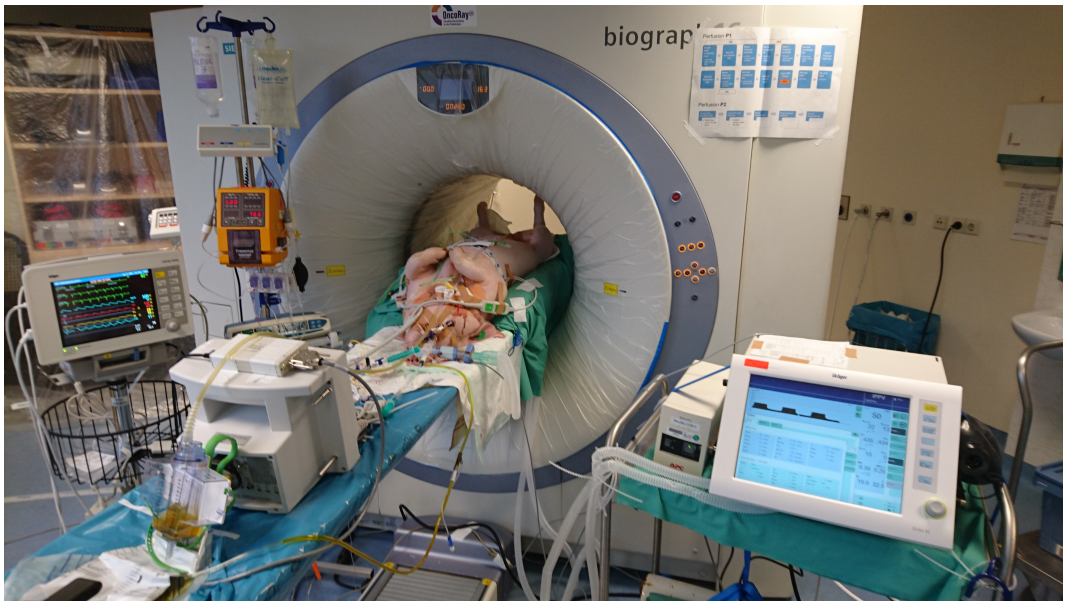

Figure 5.2: PET/CT scanner and setup during the preclinical study in Dresden

PET is a nuclear imaging method mainly for medical applications. To measure pulmonary perfusion using this approach, a nuclear tracer is injected through the proximal port of a

Swan-Ganz catheter. During the study in Dresden, ^{68}Gallium was used. The radiotracer decays and emits positrons, which when colliding with electrons, emit two gamma photons (annihilation photons). These photons travel in exactly opposite direction and are detected by rings of crystals around the object. By detecting coincident events, a 3D volume of tracer concentrations can be reconstructed. The injected tracer is distributed within the lung volume

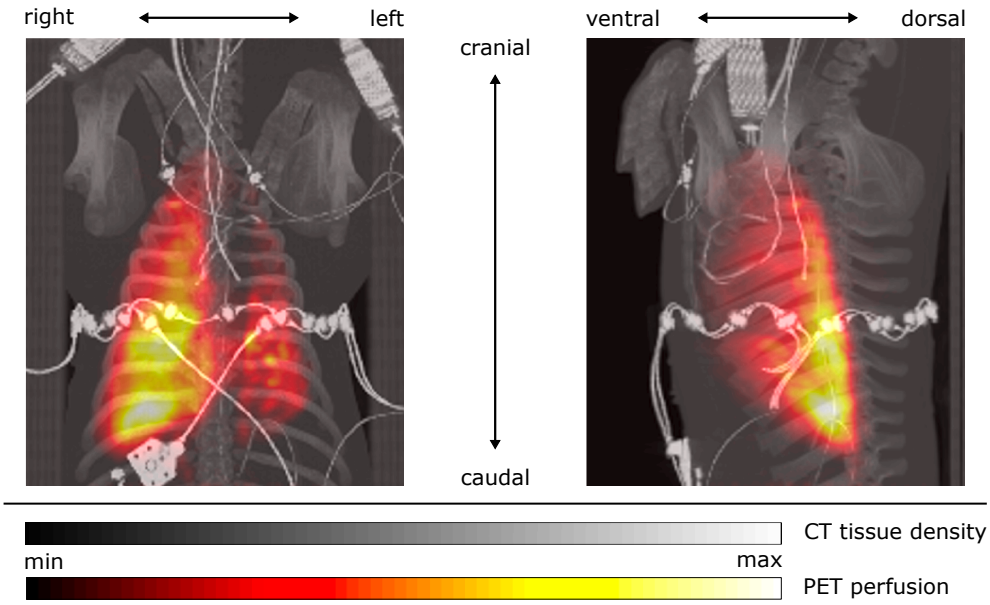

Figure 5.3: Qualitative overview of the PET/CT measurements. The CT images are superimposed by a MIP of the reconstructed relative PET perfusion. The left image depicts a frontal/top view of the porcine thorax. The right image shows the sagittal view.

during its first pass through the lung. An exemplary PET perfusion measurement during the single sided ventilation experiment is depicted in Figure 5.3. These PET tracer concentration maps are reflecting perfusion [135]. The ^{68}Gallium was bound to macroaggregated human serum albumin (MAA) microspheres. These microspheres have to be large enough to be taken up by the first capillary bed they encounter. As a result, more than 90% of the tracer was therefore extracted by the capillary bed of the lungs within the first passage of blood. Comparing indicator-enhanced EIT to PET perfusion allowed to investigate the amount of information about capillary perfusion, comprised in indicator-enhanced EIT measurements. Nevertheless, indicator based blood flow measurements are expected to include the blood flow in larger arteries, which do not participate in gas exchange.

5.4 Experimental protocol

Animal preparation The animal was premedicated using midazolam (1 mg/kg, midazolam, Ratiopharm, Ulm, Germany) and ketamine (ketamine, 10 mg/kg, Ratiopharm, Ulm, Germany) intramusculary. Afterwards, the animals were anesthetized intravenously (ketamine, 10-15 mg/kg/h; midazolam, 0.7-1.2 mg/kg/h) and additionally paralyzed (atracurium, 3 mg/kg/h, Ratiopharm, Ulm, Germany) . The animal was mechanically ventilated in volume controlled mode (*Evita® XL*, Drägerwerk AG & Co. KGaA, Lübeck, Germany) using the following settings: tidal volume (V_T) of 8 ml/kg, fraction of inspired oxygen (F_IO_2) of 0.5 and inspiration:expiration time ratio (I:E) = 1:1. A central venous and arterial port were surgically prepared to measure arterial and venous pressures and to acquire blood samples throughout the experiment. Blood gas analyses (BGAs) were acquired multiple times throughout the experiment (*ABL80™ FLEX Basic*, SV 3.12, Radiometer, Copenhagen, Denmark). Additionally, a pulmonary artery catheter (PAC) (*CCOmbo*, Edwards Lifesciences, Irvine, CA, USA) was used to measure the pulmonary artery pressure (PAP), the mixed venous oxygen saturation (SvO_2), the intermittent stroke volume (SV)/cardiac output (CO) and a continuous CO estimate [136].
The animal was positioned in supine position on the CT bed and continuously monitored (*Infinity® Delta*, Drägerwerk AG & Co. KGaA, Lübeck, Germany). No repositioning was necessary throughout the time course of all experiments.

For each animal, an extensive experimental protocol was conducted with multiple experimental steps being performed. For each step, a series of perfusion measurements by means of EIT and PET/CT were performed. These sets of measurements can be divided into two main groups:

P1: Experiments with PET/CT measurements
At first an arterial and central venous blood gas analysis (BGA) was conducted, followed by

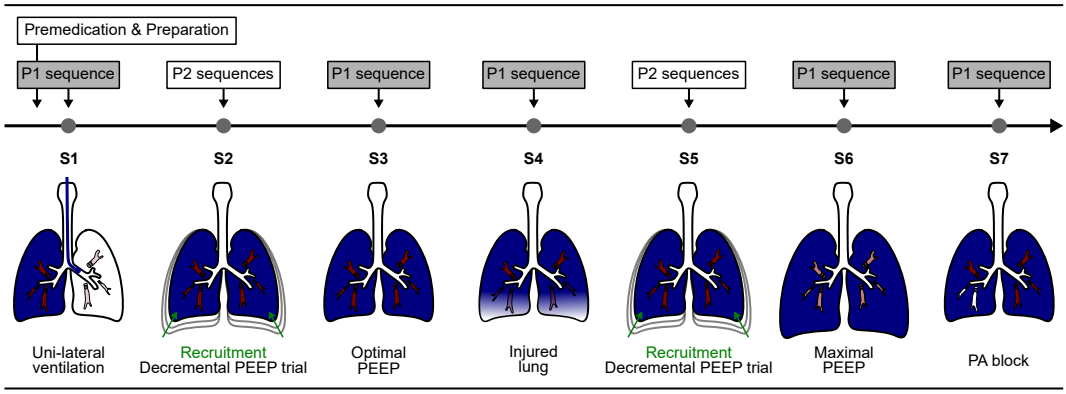

Figure 5.4: Schematic overview of the experimental protocol steps.

an intermittent CO measurement (thermodilution, mean of three injections).
Afterwards, the EIT perfusion measurements were performed. The EIT bolus perfusion measurements were generally conducted during a breath hold phase at mean airway pressure to remove the EIT component resulting from the aeration of the lungs. Electrically conductive saline boli with four different NaCl concentrations (2%, 3%, 5% and 10%) and a volume of 10 ml were injected through the proximal port of the PAC. In between, a respiratory hold phase without a saline bolus injection was conducted to analyze the potential of EIT pulsatility to monitor pulmonary perfusion based on the cardio-synchronous EIT signal component. Additionally, the injection of a 10 ml bolus with a 5% concentrated saline solution was performed during normal mechanical ventilation in order to evaluate the performance of the estimation of regional perfusion without the need for a respiratory hold.
After the EIT measurements had been performed, the PET/CT measurement was conducted. A residual scan had to be run after the first PET/CT scan in order to account for the remaining radioactive tracer from previous tracer injections. Right before the injection of the PET tracer, intermittent CO was measured a second time, to account for a possible change of the animal's hemodynamic state. A schematic description of the P1 sequence is shown in Figure 5.5.

P2: Experiments without PET/CT measurements

The second measurement sequence was a shorter modification of the sequence described above, not including a measurement of perfusion with the reference modality PET. Only a 5% NaCl bolus was injected during a respiratory hold phase for the EIT perfusion measurement. The PET/CT measurement was neglected, since the number of possible reference measurements was limited by the necessary exponential dose increase of the nuclear tracer

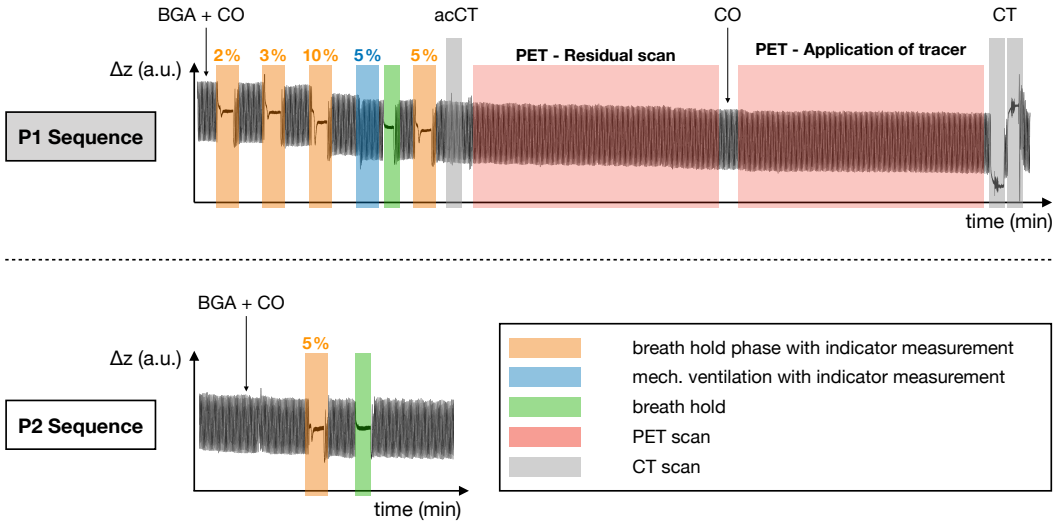

Figure 5.5: Schematic overview of the measurement sequences. The global impedance curve Δz is depicted with the relevant measurement sequences highlighted. BGA: blood gas analysis; CO: cardiac output; acCT: CT for attenuation correction of PET perfusion measurement.

for multiple sequential PET measurements.

Overall, seven different experimental protocol steps, containing P1 and/or P2 sequences, have been conducted and are visualized in Figure 5.4. The steps are additionally described in the following:

(S1) - Uni-lateral ventilation
The main left bronchus was blocked by a bifurcated endobronchial blocker (EZ-BlockerTM; Teleflex Medical Europe Ltd., Athlone, Ireland) inserted through an endotracheal tube. Since airflow to the left lung was prevented, the alveoli within the left lung collapsed. The complete left lung represented therefore an alveolar dead space and did not contribute to gas exchange. The pulmonary hemodynamics were only affected indirectly during this experimental step. Due to hypoxic pulmonary vasoconstriction (see section 2.1.1), the PVR in the left lung substantially increased and the blood flow was redirected to ventilated regions in the right lung, which improved gas exchange efficiency to some extent.

(S2) - First decremental PEEP trial
To recruit the left lung, which collapsed due to previous uni-lateral ventilation, the PEEP was step-wise increased to PEEP= 25 mbar (if the overall health of the pig allowed such a high PEEP) to recruit the collapsed regions of the lungs. To find an optimal PEEP to protectively ventilate the lung, a decremental PEEP trial was conducted to follow the approach described in section 2.2.3 and first published in [54]. The PEEP was decreased in steps of 5 mbar from 25 mbar to 5 mbar. In each of the PEEP levels, a P2 measurement sequence was performed. Afterwards, an optimal PEEP was chosen based on the Costa approach implemented in the *Diagnostic view* [137, p.28] of the *PulmoVista® 500* as described in section 2.2.3. The optimal trade-off between a minimum of collapse and a minimum of overdistension was generally found between PEEP= 8-12 mbar. The decremental PEEP trial is depicted in Figure 5.6.

(S3) - Bi-lateral ventilation at an optimal PEEP
Both lungs were ventilated with the previously defined optimal PEEP (always around 8-12 mbar). This lung state was regarded as reference for all other experimental steps. The previously collapsed left lung could be completely recruited for all animals.

(S4) - Atelectatic/injured lung
Bi-lateral lung injury was induced in the animal by repetitive lung lavage resulting in alveolar surfactant depletion. The surfactant washout lead to a collapse of the alveoli, since it reduces surface tension and therefore prevents the alveoli from collapsing (see section 2.1.1). The injury induced by repeated lung lavage was established as an experimental model of ARDS [138, 139] . Mainly the alveoli in the gravity dependent lungs collapsed. It was expected that pulmonary perfusion would shift towards aerated, more ventral regions of the lungs due to vasoconstriction.

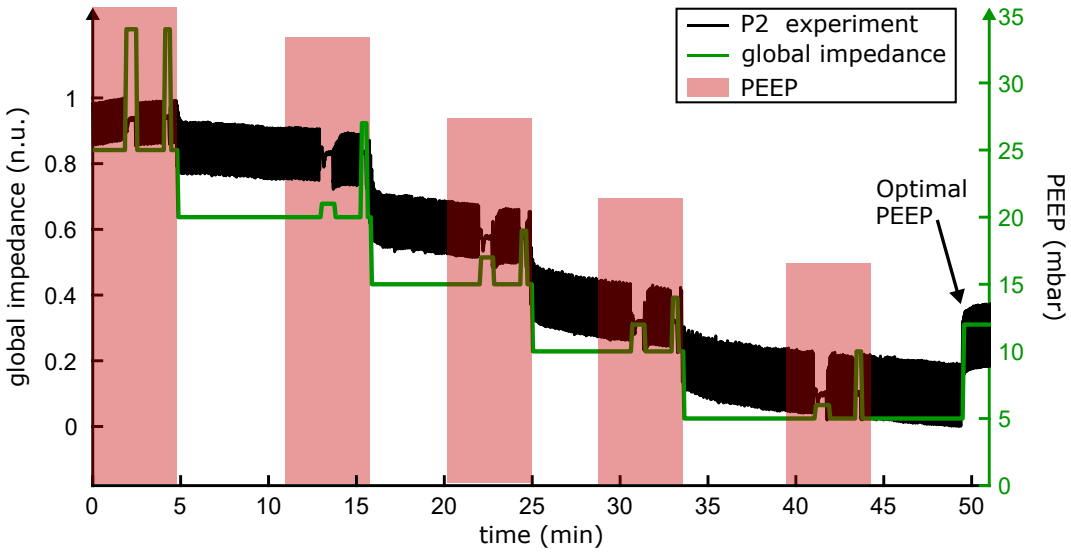

Figure 5.6: Graph of a decremental PEEP trial. The normalized global reconstructed impedance change (▬) is depicted together with the PEEP (▬).

The lung lavage was repeated 3-4 times and the remaining saline was removed from the lungs afterwards. To have stable experimental conditions, the recordings were started after achieving a hemodynamically stationary state. The pig was ventilated with no additional static pressure (PEEP = 0 mbar) to prevent recruiting of alveoli during the experiment.
Based on the monitoring parameters in Table 5.1, a decrease in gas exchange capability can be observed. The partial pressure of arterial oxygen (paO_2) in arterial blood decreased from the healthy reference (S3) state to the injured state (S4) from 29.2 kPa to 11.5 kPa and the partial pressure of arterial carbon dioxide ($paCO_2$) increased by 1.3 kPa. The CO increased by approximately 2 l/min, most likely to overcome the increasing PVR and to optimize gas exchange. Yet, another cause for the increased CO could also be the PEEP decrease from 5 mbar to 0 mbar, which decreases the afterload of the right heart.

(S5) - Second decremental PEEP trial
Similar to experiment (S2), the PEEP was stepwise increased to 25 mbar followed by a decremental PEEP trial to recruit the injured lung. During the decremental PEEP trial, PEEP was decreased in steps of 5 mbar from 25 mbar to 5 mbar. In each of the PEEP levels, a P2 measurement sequence was performed to analyze the change in pulmonary blood flow with PEEP.

(S6) - Bi-lateral ventilation at maximal PEEP
After the decremental PEEP trial in (S5), the PEEP was set to a maximal tolerable PEEP level (commonly 25 mbar), which was defined based on the hemodynamic condition of the animal. Both lungs were ventilated.
Because of the high pressure in the lungs, the PVR increased substantially and resulted in a

decrease of the CO.

(S7) - Uni-lateral block of the pulmonary artery
One stem (by chance either left or right) of the pulmonary artery was blocked using the balloon at the tip of the pulmonary artery catheter. Ideally, either the left or right main PA stem was blocked. In most cases only the lower lobe of one lung was blocked completely, while the upper lobe was still perfused. During this state, a strong $\dot{V}/\dot{Q}$ mismatch was created in the shunted lung. The blood flowing through the pulmonary circuit could only participate in gas exchange in the perfused lung, while ventilation was present in both lungs.

An overview of the ventilator settings, the monitored ventilatory parameters and the hemodynamic parameters during the different experimental steps of the protocol is provided in Table 5.1. The parameters are only depicted for P1 sequences.

Parameter	**Step 1** Uni-lateral vent.	**Step 3** Optimal PEEP	**Step 4** Injury	**Step 6** Max. PEEP	**Step 7** PA block
Respiratory parameters					
V_T (ml/kg)	5.4 ± 0.2	8.6 ± 0.2	9.0 ± 0.2	8.5 ± 1.0	8.8 ± 0.2
RR (1/min)	27.0 ± 2.0	15.0 ± 2.0	15.0 ± 3.0	15.0 ± 3.0	13.0 ± 1.0
MV (l/min)	8.3 ± 1.1	7.3 ± 1.3	7.7 ± 1.5	7.3 ± 1.8	6.8 ± 0.7
PEEP (mbar)	5.0 ± 0.0	10.6 ± 1.2	0.0 ± 0.0	23.8 ± 2.1	4.5 ± 1.5
P_{peak} (mbar)	20.6 ± 2.3	20.7 ± 1.9	27.5 ± 5.5	41.6 ± 4.5	24.0 ± 3.9
ΔP (mbar)	10.3 ± 6.6	9.2 ± 1.4	24.0 ± 3.5	16.7 ± 3.0	17.4 ± 3.5
F_IO_2 (%)	100 ± 20	50 ± 10	100 ± 0	50 ± 0	100 ± 0
C_{rs} (ml/mbar)	31.3 ± 15.1	58.0 ± 7.9	21.0 ± 3.7	30.0 ± 6.6	29.0 ± 7.5
R_{rs} (mbar s/l)	18.8 ± 7.2	10.2 ± 3.1	11.2 ± 2.0	9.9 ± 1.5	10.5 ± 2.4
Gas exchange parameters					
paO_2 (kPa)	36.0 ± 13.1	29.2 ± 4.4	11.5 ± 6.7	75.7 ± 19.2	27.2 ± 17.3
$paCO_2$ (kPa)	7.7 ± 0.8	7.5 ± 0.8	8.8 ± 1.5	8.0 ± 1.2	9.3 ± 1.6
pH	7.36 ± 0.03	7.37 ± 0.03	7.28 ± 0.05	7.33 ± 0.04	7.26 ± 0.07
Hemodynamic parameters					
MAP (mmHg)	82 ± 10	79 ± 7	82 ± 9	62 ± 8	75 ± 7
MPAP (mmHg)	22 ± 2	20 ± 2	28 ± 4	28 ± 3	75 ± 7
HR (bpm)	96 ± 12	101 ± 18	120 ± 21	120 ± 27	125 ± 23
CO (l/min)	5.50 ± 0.72	5.66 ± 0.87	7.89 ± 1.20	3.73 ± 0.70	7.15 ± 1.45

Table 5.1: Overview of the most important respiratory, hemodynamic and gas exchange monitoring parameters. The values are depicted as mean $\pm$ SD for all experimental steps containing P1 measurement sequences.

Chapter 6

Preclinical animal study Iowa

A preclinical study was conducted at the experimental research center of the Advanced Pulmonary Physiomic Imaging Laboratory (APPIL) of the Department of Radiology, University of Iowa Carver College of Medicine, IA, USA. The study was approved prior to the start of the experiments by the Animal Care and Use Comittee of the University of Iowa (Permit Number: 0902022). The study was planned and conducted under the lead of Priv.-Doz. Dr. med. Gunnar Elke and Prof. Dr. med. Inéz Frerichs of the Department of Anesthesiology and Intensive Care Medicine, University Medical Centre Schleswig-Holstein in Kiel, Germany. Within the study, EIT ventilation distributions were compared to Xenon multidetector Computed Tomography (MDCT) imaging and indicator-enhanced EIT blood flow estimations were compared to indicator-enhanced MDCT blood flow estimates. The ventilation study was published in [140]. The comparative blood flow measurements described and evaluated in this thesis were generously made available by Priv.-Doz. Dr. med. Gunnar Elke and Prof. Dr. med. Inéz Frerichs. This chapter provides a short overview of the experimental protocol.

We published extensive analyses of the blood flow data from this study in [141, 142]. Our lung segmentation algorithm published in [143, 144] was also developed and tested based on the MDCT measurements of this study.

6.1 Experimental protocol

To compare images of indicator-enhanced EIT based blood flow to indicator MDCT images, the preclinical study comprised eight farm-raised pigs of both sex with a mean body weight of 33.6 kg $\pm$ 2.2 kg (mean $\pm$ standard deviation (STD)). Thus, the pigs were considerably smaller compared to the Dresden study (see chapter 5) and had smaller thorax circumferences.

Animal preparation An overview of relevant aspects will be presented in the following. A detailed description of the animal preparation can be found in [140]. Invasive mechanical VCV was initiated with a F_IO_2= 1.0, after anesthesia was established. A pigtail catheter was

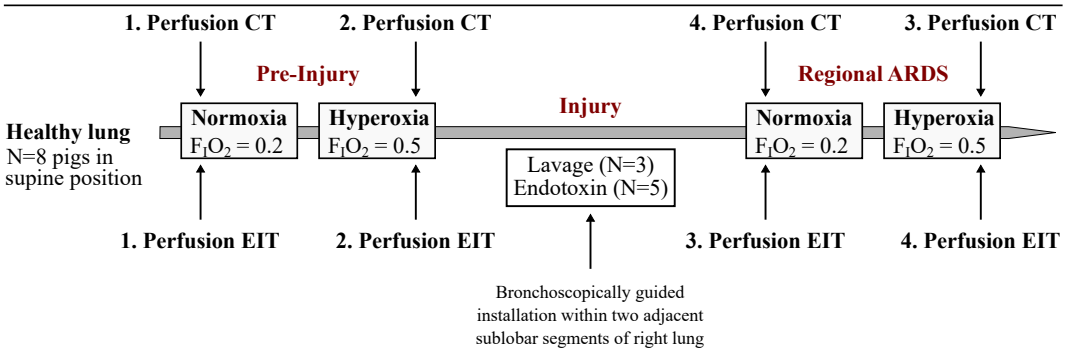

Figure 6.1: Schematic overview of the experimental protocol of the study performed in Iowa. The illustration was adapted from our publication [142] with permission.

placed into the right cardiac ventricle (RV), aside from an arterial and venous catheter. A pulmonary artery catheter (PAC) was advanced into the main pulmonary artery. Next, the animals were moved to the MDCT scanner. The animal was continuously ventilated in VCV mode RR = 20 min^{-1}, I:E = 1:2 and V_T, which maintained a partial pressure of end-tidal carbon dioxide ($p_{et}CO_2$) of 35–45 mmHg. During the experiment, the PEEP was fixed to 5 mbar. The animals were additionally paralyzed to suppress spontaneous breathing.

Experiments The animal remained in supine position and no repositioning was necessary throughout the experiment. Four different experimental steps were conducted and were considered for the analysis in this thesis (see Figure 6.1):

(E1) - Healthy-Normoxia
MDCT-perfusion and indicator enhanced EIT perfusion was measured after the start of the experiment as baseline reference state. The animal was ventilated with a normal fraction of inspired oxygen $F_IO_2 = 0.21$. As in all other experimental steps, respiratory and hemodynamic monitoring parameters were recorded including a CO measurement based on repeated thermodilution through the PAC. Arterial blood gases were also acquired.

(E2) - Healthy-Hyperoxia
F_IO_2 was increased to 1.0. MDCT and EIT perfusion measurements were performed to analyze whether the perfusion distribution changes due to an increase in inspired oxygen. It has been reported, that hyperoxia induces vasodilation and alters regional ventilation-perfusion relationships [145].

(E3) - Injury-Normoxia
Two different models of lung injury were considered. Regional saline lavage induced lung injury (n=3 pigs) was performed. Lung lavage (60 ml at 38 °) was repeated for five times.

Via a bronchoscope (Olympus, Center Valley, PA, USA), lung injury was established in two adjacent sub-lobar segments of the right lung, which were previously identified by MDCT measurements. In all other animals (n=5), lung injury was induced in the same lung region by bronchoscopic instillation of Endotoxin (2.5–5 mg Escherichia coli O55:H35 lipopolysaccharide: LPS; Sigma L4005, Sigma Chemical Co., St. Louis, MO, USA).
After a waiting period to assure a steady condition, EIT and MDCT perfusion imaging was conducted with at a normal $F_IO_2 = 0.21$.

(E4) - Injury-Hyperoxia
F_IO_2 was increased again to 1.0 and MDCT and EIT perfusion measurements were conducted.

6.2 EIT and reference imaging data acquisition

EIT perfusion measurements EIT measurements were performed with the *Goe-MF II* system (CareFusion, Höchberg, Germany). Herefore, 16 electrodes (*Blue Sensor BR-50-K*, Ambu, Ølstykke, Denmark) were attached to the thorax in a transversal plane close to the apex of the pig. The system was operated with adjacent stimulation measurement protocol with an effective current amplitude of 5 mA.The frame rate of image acquisition was set to $f_s = \frac{1}{t_s} = 25\,\text{Hz}$ and measurements were conducted during the time interval of $T = 60\,\text{s}$. To estimate the regional distribution of pulmonary blood flow, a conductive hypertonic indicator (NaCl 10%, 0.75 ml/kg) was injected central venously during continuous inspiratory breath hold phases.

MDCT perfusion measurements MDCT perfusion was recorded correspondingly in the same transverse region as the EIT measurement (*SOMATOM Sensation 64*, Siemens AG, Forchheim, Germany). The animals were not moved between EIT and MDCT measurements. Electrocardiographically gated dynamic MDCT images (80 kV, 150 mAs, 0.75 mm section thickness, 0.5-mm increments, 0.28-second rotation time, 25 time points, 4.2 mSv) was acquired in a region of 4 cm around the level of EIT electrodes in cranio-caudal direction. Iodinated contrast agent (0.5 mL/kg over 2 seconds; Isovue, 370 mg of iodine per milliliter, Bracco Diagnostics, Princeton NJ) was injected into the right ventricle during continuous breath holds.

PART III

EIT SENSITIVITY TO INDICATOR-ENHANCED MEASUREMENTS

Chapter 7

Spatial sensitivity of EIT to saline indicators in front of inhomogeneous pulmonary backgrounds

We published a preliminary pilot study based on a human geometry (recorded during the research for a Master thesis of a student under my supervision [146]) in [76] prior to this analysis. The algorithm to segment the injured lungs for the presented evaluation, including the collapsed regions was published in [143, 144]. The EIT simulation approach has been partly developed with the help of students during their research for Bachelor and Master theses [132, 147, 148].

7.1 Motivation

In order to clinically assess and monitor pulmonary blood flow during therapeutic interventions or (patho-) physiological conditions with EIT, it is important to understand and consider which spatial three dimensional region of the thorax is sensitive to the EIT measurement and how homogeneous the sensitivity is distributed. Normalized time-difference EIT measures tissue conductivity changes within the thorax relative to a static background during the measurement. For mechanically ventilated patients, the pulmonary conductivity background is in many cases very inhomogeneous due to either collapsed or well ventilated regions. If the perfusion of a collapsed region and of a ventilated region is equal, an indicator-enhanced EIT perfusion measurement might still estimate different blood flows, due to the non-identical contrast of the indicator to the background. Additionally, if the background of the same region is changing during therapy, such as during a lung recruitment maneuver (e.g. decremental PEEP trial) or before and after any other intervention, the spatial sensitivity to a pulmonary blood flow measurement with EIT should still not vary substantially in order to

be clinically useful. Otherwise, physiological changes in perfusion, which the physician is interested in, would be superimposed by measurement differences originating from the local changes of sensitivity.

From previous publications, it is known, that the sensitivity region for an EIT measurement with electrodes attached in a two-dimensional transverse plane around the surface is bell- or lens-shaped in the three-dimensional space [75, 112, 149–151]. These analyses have been conducted for healthy lungs, but studies including severely heterogeneous pulmonary backgrounds have not yet been performed. Additionally, it has at present not been determined, which indicator contrast is necessary to limit the influence of a background heterogeneity on regional perfusion estimation. For this reason, spatial EIT sensitivity profiles in front of three different pulmonary conductivity backgrounds at different concentrations of a saline indicator have been investigated. The similarity of the spatial profiles was quantitatively assessed and compared between experimental states and concentrations. Additionally, we evaluated the sensitivity variation within the electrode plane. Ideally, the sensitivity is constant within the EIT electrode plane for all states.

Objectives

The presented simulation study addresses the forward and inverse sensitivity of a saline indicator-enhanced EIT measurement to estimate distributions of pulmonary blood flow in front of realistic lung backgrounds. The aims of this chapter refer to the first and third main objective as stated in the introductory chapter 1.2. The following guiding theses shall be investigated in the following chapter:

- The sensitive region around the electrode level is bell shaped but influenced by the contrast of the indicator to the background.
- Sensitivity profiles of indicator measurements in front of realistic heterogeneous conductivity backgrounds become more similar with increasing indicator concentration.
- Forward sensitivity and amplitude response (inverse sensitivity) becomes more homogeneous/constant with increasing indicator concentration within the EIT electrode plane.

The inverse sensitivity has been investigated for three different EIT reconstruction approaches.

7.2 Methods

To investigate the sensitivity distribution of indicator-enhanced EIT measurements as well as the inverse sensitivity or amplitude response (AR) of the image reconstruction in front of different realistic backgrounds, a simulation study has been performed. The simulation setup and the calculation of different sensitivity and reconstruction quality measures are introduced in the following.

7.2.1 Simulation setup

For each *P1 experiment* of the preclinical porcine study in Dresden (see chapter 5) a CT scan during an end-inspiratory ventilation hold phase was recorded. The scans at the end of the *uni-lateral ventilation (S1)*, the *bi-lateral ventilation at optimal PEEP (S3)* and *atelectatic/injured lung (S4)* experiments were used to create bio-impedance simulation models. The background conductivity of the lungs was severely inhomogeneous during (S1) and (S4) due to a complete collapse of the left lung in (S1) and severe atelectasis in gravity dependent, therefore dorsal regions of the lungs in (S4). Experiment (S3) was included to include a healthy reference state with an approximately homogeneous distribution of air within the lungs (see histogram in Figure 7.2, lower graph).

Segmentation and tissue label map creation CT imaging scans (*Biograph*^{TM} 16 Hi-Rez PET/CT, Siemens, Knoxville, TN, USA) were reconstructed with a resolution of $0.7 \times 0.7\,\mathrm{mm}^2$ and a slice thickness of 1 mm. Overall, 395 image layers with image matrices of 512×512 voxel were reconstructed. The torso, the bones, the electrodes and the larger airways were semi-automatically segmented from the CT data using *ITKsnap* [152]. The heart was manually segmented for each state, since no automatic segmentation approach could separate the heart from the similar contrast of thoracic muscular tissue. The lungs were presegmented with *ITKsnap* and semi-automatically adapted and optimized in *MATLAB R2019a* using a developed approach, which was published in [143, 144]. The segmented volumes were smoothed using morphological operators in *MATLAB R2019a* and combined, resulting in a material label map matrix of the same size as the CT image volume ($512 \times 512 \times 395$). The label map cross-sections at the height of the electrodes for each experiment are depicted in Figure 7.1.

Mesh generation From the final label maps, the torso surface was extracted and triangulated in *MATLAB R2019a* and exported to *MeshLab* [153, 154]. In *MeshLab* the torso surface mesh was further smoothed using the *Taubin Smooth* algorithm [155] and the normals to

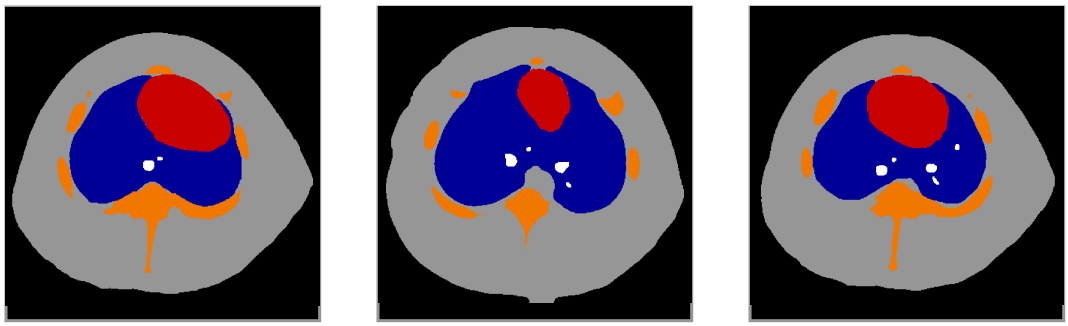

(S1) Uni-lateral ventilation **(S3) Optimal PEEP** **(S4) Injury/Atelectasis**

Figure 7.1: Cross section of the tissue label map for the simulated experiments. The different tissues are depicted with different colors: torso/muscle tissue, lungs, bones, heart and airways

the triangular mesh elements were equally reoriented to point outwards. Finally, each torso surface mesh was homogeneously remeshed with *Instant Meshes* [156] to achieve suitable resolutions and numerically stable equally large surface mesh triangles. Finally, the volume within the torso was meshed with tetrahedral elements with *gmesh* [157]. Characteristic properties of the meshes are summarized in Table 7.1. The mesh quality η represents the ratio of the shortest to the longest edge length of a tetrahedron.

Simulation	Number of elements	Edge length (mm)	Mesh quality η
(S1) Uni-lateral ventilation	877753	6.59 ± 0.58	0.66 ± 0.07
(S2) Optimal PEEP	929315	6.52 ± 0.57	0.66 ± 0.07
(S3) Injury/Atelectasis	867273	6.67 ± 0.58	0.66 ± 0.07

Table 7.1: Overview of the important mesh properties. The mesh quality η represents the ratio of the shortest to the longest edge length of a tetrahedron. The values are depicted as mean $\pm$ SD.

Conductivity and electrode mapping In the next step, the segmented tissue materials and the electrical conductivites had to be assigned to the tetrahedral elements. Thus, the tissue labels of the voxel based labels (depicted in Figure 7.1) were mapped to the tetrahedral mesh. For each tetrahedral mesh element, the mode of all tissue labels belonging to voxels fully enclosed by the tetrahedron was assigned as tissue label to the element.
A corresponding electrical conductivity was assigned to each mesh element according to its tissue label. An overview of important tissue conductivities is given in Table 7.2. The tissue conductivities vary with frequency of the electrical stimulation [158]. Within the range of the possible current stimulation frequencies $f_I = 80 - 130\,\text{kHz}$ of the *PulmoVista® 500*, the tissue conductivities vary only slightly (see Table 7.2). The stimulation frequency for all simulations was set to $f_I = 130\,\text{kHz}$ and the tissue conductivities were set accordingly. The decision for the injected current frequency was made to be consistent to the measurements described in chapter 5.
For all simulations, heart tissue was set to the conductivity of blood, bone tissue to the

Tissue	$\mathbf{f_I = 80\,kHz}$	$\mathbf{f_I = 100\,kHz}$	$\mathbf{f_I = 130\,kHz}$
Blood	$7.02 \cdot 10^{-1}$	$7.03 \cdot 10^{-1}$	$7.05 \cdot 10^{-1}$
Myocardium	$2.09 \cdot 10^{-1}$	$2.15 \cdot 10^{-1}$	$2.23 \cdot 10^{-1}$
Muscle	$3.58 \cdot 10^{-1}$	$3.62 \cdot 10^{-1}$	$3.68 \cdot 10^{-1}$
Lung (inflated)	$1.06 \cdot 10^{-1}$	$1.07 \cdot 10^{-1}$	$1.09 \cdot 10^{-1}$
Lung (deflated)	$2.68 \cdot 10^{-1}$	$2.72 \cdot 10^{-1}$	$2.76 \cdot 10^{-1}$
Fat	$4.34 \cdot 10^{-2}$	$4.34 \cdot 10^{-2}$	$4.35 \cdot 10^{-2}$
Skin	$3.69 \cdot 10^{-4}$	$4.51 \cdot 10^{-4}$	$6.00 \cdot 10^{-4}$
Vertebrae	$2.07 \cdot 10^{-2}$	$2.08 \cdot 10^{-2}$	$2.09 \cdot 10^{-2}$

Table 7.2: Overview of tissue conductivities (S m^{-1}) at different EIT current stimulation frequencies [158, 159]

conductivity of vertebrae and muscular conductivity was assigned to the soft tissue of the torso. The major airways, which are air filled and therefore hardly conductive, were assigned a relatively small conductivity of $\sigma_{air} = 10^{-5}\,\mathrm{Sm}^{-1}$. To account for the influence of the spatially inhomogeneous pulmonary parenchyma, conductivities corresponding to the local alveolar air filling were assigned to the mesh elements with the method described in the next paragraph.
For the simulations, point electrodes were used. To assign the electrodes to surface nodes, the coordinate centers of all $n_E = 16$ segmented electrodes were calculated and the surface mesh nodes with the smallest Euclidean distances were determined.

Conductivities of the lung parenchyma In order to simulate the inhomogeneous conductivity distribution of the lung parenchyma, the following section describes the method to relate parenchyma tissue density as measured with CT to electrical conductivities.
The electrical conductivity of lung parenchyma depends on the local amount of air within a tissue volume. The model introduced by Nopp et al. was used [160–162] to relate conductivity to the amount of air within a lung volume. The lung parenchyma consists of about $8 \cdot 10^5$ alveoli filled with air and a network of many blood vessels and airways [161]. According to Nopp et al., the main proportion of lung tissue is blood. About 85 % of lung tissue consists of blood filled vessels, 12% are made up by epi- and endothelial cells and 3% by intercellular fluid. The effective conductivity of completely collapsed alveolar tissue with no air within the alveoli is therefore defined by:

$$\sigma_{alv} = 0.85 \cdot \sigma_{blood} + 0.12 \cdot \sigma_{epi,endo} + 0.03 \cdot \sigma_{fluid} \tag{7.1}$$

In [160–162] the alveolar conductivity was calculated to be $\sigma_{alv} = 0.7284\,\mathrm{Sm}^{-1}$ at a frequency of 100 kHz (with assumed conductivities: $\sigma_{blood} = 0.655\,\mathrm{Sm}^{-1}$, $\sigma_{epi,endo} = 1.0\,\mathrm{Sm}^{-1}$ and $\sigma_{fluid} = 2.0\,\mathrm{Sm}^{-1}$. For the presented simulations at a stimulation frequency of 130 kHz, a similar conductivity was assumed. A conductivity $\sigma_{alv} = 0.7284\,\mathrm{kHz}$ was chosen for completely collapsed regions.
The amount of air within a volume V of the lung parenchyma can be described by the filling factor (FF) introduced by Nopp [160]:

$$\mathrm{FF} = \frac{V_{air}}{V_{tissue}} \tag{7.2}$$

The FF represents the ratio between the volume of air V_{air} and the volume of tissue V_{tissue} within a lung volume V. The relationship between the FF and the effective electrical lung tissue resistivity has been shown to be linear [160, 163–165]. The relationship for the lung tissue conductivity $\sigma_{lung}(\mathrm{FF})$ was described by [162]:

$$\sigma_{lung}(\mathrm{FF}) = \sigma_{alv} \cdot \frac{1}{\tau \cdot (\mathrm{FF} + 1)} \tag{7.3}$$

The tortuosity τ describes the squared ratio between the mean length of a current path through a porous volume of lung parenchyma and the length of the volume [166]. It changes

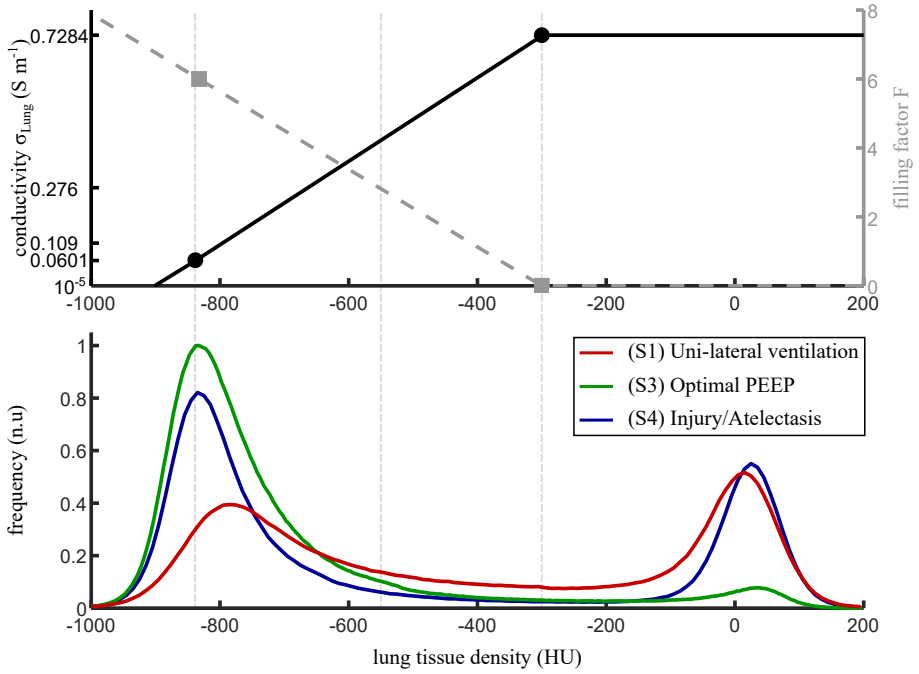

Figure 7.2: Method of relate tissue densities (HU) from CT measurements to electrical conductivities (S m^{-1}). The histograms in the lower plot depict the frequency of different tissue densities within the lung for the three different simulated experimental scenarios. The upper graph depicts the implemented corresponding air filling factor F and the effective electrical lung tissue conductivity σ_{Lung}.

with stress and therefore especially with the applied ventilatory pressures during mechanical ventilation. For the analysis in the following the tortuosity is assumed to be equal for all experimental states as previously assumed in [165].

In the final step, the tissue density measured by CT during an inspiratory hold phase has to be related to the FF. For this reason, the tissue densities within the lungs for all three experimental states were analyzed (depicted in the lower plot of Figure 7.2). Typical tissue densities of healthy ventilated lung parenchyma can be found between -910 HU to -500 HU [167]. Atelectatic and therefore collapsed regions of the lung typically have tissue density values within the interval $[-300\,\text{HU}, 200\,\text{HU}]$. In the calculated histograms in Figure 7.2, the tissue densities are well within these typical intervals. For the healthy reference state at optimal PEEP (S3), the number of voxels with atelectatic tissue densities were small and increased for the uni-lateral ventilation (S1) and the atelectatic lung (S4) experiment. For the healthy reference state (S3) we assumed that the mode tissue density ($\approx -850\,\text{HU}$) corresponds to voxels which have typical FFs at total lung capacity (TLC) or end-inspiration. A FF of 6 has been reported as typical at end-inspiration [165]. For fully collapsed or atelectatic lungs we assumed FF$= 0$.

With a mean tortuosity $\tau = 1.71$ [165], the electrical tissue conductivities can be calculated as depicted in the upper graph of Figure 7.2. The resulting lung parenchym tissue conductivities are depicted in Figure 7.3.

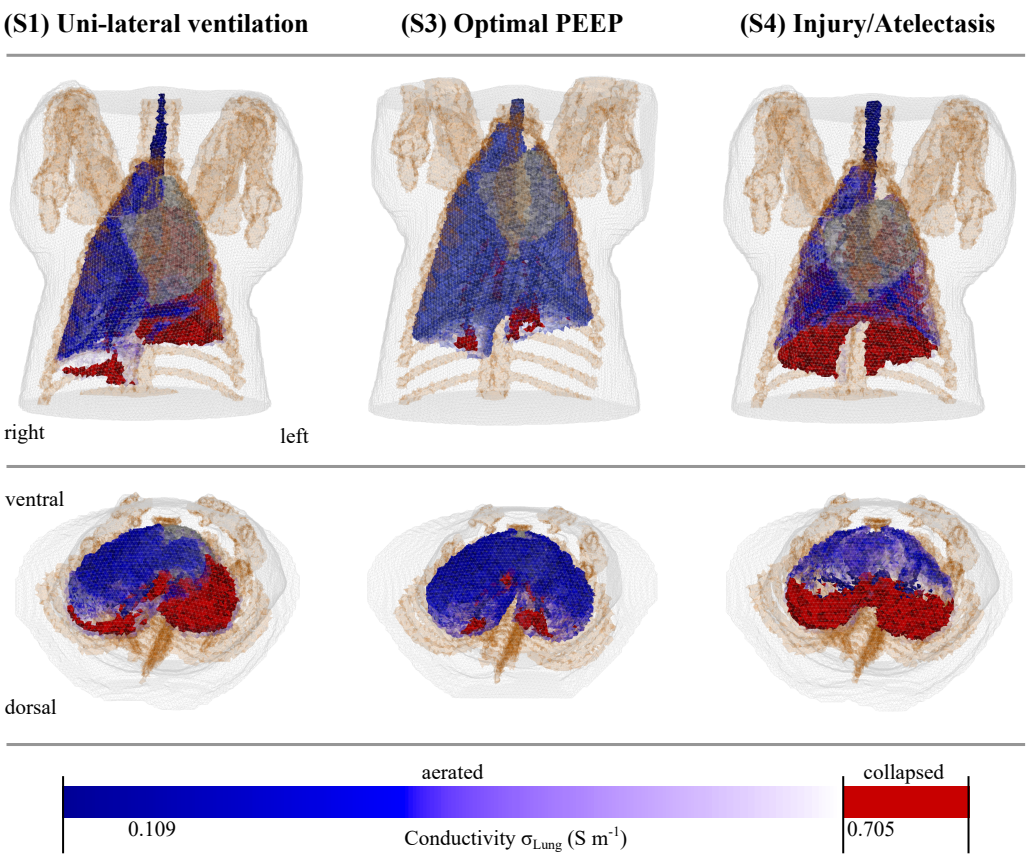

Figure 7.3: Volume meshes as used for the simulations with conductivity values assigned

Simulation scenarios The goal of the simulation study was to investigate the influence of the inhomogeneous electrical lung background on the forward and backward sensitivity of EIT measurements to injected saline indicators. A main contribution of this thesis is the determination of the lowest possible concentration required for tracking spatial distributions of pulmonary blood flow within the lung. Besides the experimental analysis in chapter 12, this chapter investigates to which extent the influence of a heterogeneous lung background conductivity distribution decreases with increasing saline contrast. For this reason, spheres

Type of inhomogeneity	Blood	0.9% NaCl	2% NaCl	3% NaCl	5% NaCl	10% NaCl
Conductivity (Sm^{-1})	0.705	1.44	3.02	4.35	7.01	12.6

Table 7.3: Overview of the defined conductive sphere inhomogeneities with their corresponding electrical conductivities.

of a conductive saline indicator were sequentially integrated at evenly distributed positions within the lung. During the study in Dresden (see chapter 5) a 10 ml bolus of the indicator solution was injected central-venously. The volume of the simulated spheres was defined

accordingly to be comparable with a corresponding radius $r = 13.4\,\text{mm}$. The electrical conductivity of the sodium chloride aqueous solution is dependent on the indicator concentration. The chosen concentrations in mass percent are listed together with their conductivities taken from the CRC Handbook [168] in Table 7.3.
Overall 18 different simulations were carried out resulting from six different types of spherical inhomogeneities and three different experimental lung states with their corresponding lung conductivity backgrounds. For each of those 18 simulations, $i = 1, ..., k_S$ spheres were evenly distributed within the lungs at the positions $\mathbf{p}_i \in \mathbb{R}^{1x3}$. The sequentially introduced spheres spatially overlapped by 50 %, to increase the number of simulated spheres.

7.2.2 Analysis of forward sensitivity

The forward sensitivity is a measure to describe the amount of voltage change at the measuring electrodes resulting from a conductivity change within a certain region of a certain volume. A spherical region of the volume $V_i \in \mathbb{R}$ was inserted at a position $\mathbf{p}_i$ and increased the background conductivity by $\Delta\sigma_i \in \mathbb{R}$ resulting in a voltage change at the electrodes of $\Delta\mathbf{v}_i = [\Delta v_{1i}, ..., \Delta v_{mi}, ..., \Delta v_{Mi}]^\top$. The forward sensitivity of the EIT measurement to a conductivity change of the i$^{\text{th}}$ spherical region was evaluated as:

$$S_i = \frac{1}{V_i} \cdot \sqrt{\frac{\sum_{m=1}^{M} (\Delta v_{mi})^2}{(\Delta\sigma_i)^2}} \tag{7.4}$$

Comparing the sensitivity calculation with the definition of the linearized forward operator or Jacobian $\mathbf{J}$ in chapter 3.1.2, the similarity is apparent. If we would investigate the sensitivity to FEM-element pertubations, the forward sensitivity in an element k is defined by $S_k = \frac{1}{V_k}\|\mathbf{J}_k\|$ with $\mathbf{J}_k$ being the k$^{\text{th}}$ column of the Jacobian $\mathbf{J}$ [75]. With this approach, we could nicely investigate different stimulation and measurement patterns of EIT. Yet, in this study we are investigating the sensitivity of EIT to spheres with a volume of 10 ml and with an increase of conductivity to the indicator conductivity relative to the background. Thus, the approach was adapted.
The forward sensitivity is dependent on the stimulation and measurement pattern of an EIT measurement and on the positioning of the electrodes. For an adjacent stimulation, the sensitivity is larger towards the surface of the body [75]. If a physician wants to track changes during a treatment with the same measurement setup, the spatial sensitivity should not change, otherwise the measured conductivity changes would not only represent an underlying physiological function, but also the altered sensitivity. The influence of the conductivity background on the spatial forward sensitivity was therefore investigated.

7.2.3 Analysis of inverse sensitivity

If two regions with equal forward sensitivity are exposed to the same distortion $\Delta\sigma$, the same voltage change results at the surface electrodes. This nevertheless does not mean, that the reconstruction algorithm will project these equal voltage changes to equal reconstructed conductivity changes $\Delta\hat{\sigma}$ [75]. For this reason, the inverse sensitivity should be investigated additionally.
The inverse sensitivity is strongly influenced by the type of reconstruction algorithm. The performance of three different normalized difference reconstruction algorithms were compared. As first and second method, two different variants of a standard one-step Gauss-Newton algorithm differing in Tikhonov regularization approaches (see section 3.1.3) were used. The first applied regularization was the standard Tikhonov regularization of 0^{th} order, penalizing large reconstructed values. Thus, the regularization matrix $\mathbf{R}$ of equation (3.22) was chosen to the identity matrix $\mathbf{R} = \mathbf{I}$. The reconstructed normalized conductivity change $\Delta\hat{\boldsymbol{\sigma}}_i$ resulting from a simulated sphere i at position $\mathbf{p}_i$ and of a volume V_i was reconstructed by:

$$\Delta\hat{\boldsymbol{\sigma}}_i = \left(\mathbf{J}^\top\mathbf{J} + \lambda\mathbf{I}\right)^{-1}\mathbf{J}^\top\Delta\mathbf{v}_i \tag{7.5}$$

For the second approach, a Laplacian matrix $\mathbf{R} = \mathbf{L}$ (2^{nd}-order Tikhonov) was chosen as regularization imposing spatial smoothness on the solution:

$$\Delta\hat{\boldsymbol{\sigma}}_i = \left(\mathbf{J}^\top\mathbf{J} + \lambda\mathbf{L}^\top\mathbf{L}\right)^{-1}\mathbf{J}^\top\Delta\mathbf{v}_i \tag{7.6}$$

The Jacobian $\mathbf{J}$ and the Laplacian $\mathbf{L}$ were calculated with EIDORS [169]. For both approaches the Jacobian was calculated assuming a homogeneous background, since in clinical scenarios the background conductivity is usually not known, because CT or MRT images can not assumed to be available in a reproducible manner. The regularization parameter λ was optimized for each experiment finding the maximal curvature of the L-curve [89, 90] for all spheres $i \in \left\{[1,k_S]|p_{i3} \in [-2\cdot r_{Sphere}, 2\cdot r_{Sphere}]\cdot z_E\right\}$ located within a small vertical zone around the electrode level z_E. The mean over all optimal λ of each individual sphere with the electrode plane was chosen for the reconstruction of all spherical inhomogeneities.
The Graz consensus reconstruction algorithm for EIT (GREIT) was chosen as third reconstruction algorithm. The algorithm was introduced in section 3.1.3. The noise figure was chosen to 0.5 as recommended in [93].
The 2D mesh for all reconstruction algorithms is depicted in the left image of Figure 7.4. After reconstruction, the triangular meshes were mapped onto a pixel grid of size [128×128] with a pixel edge length of 2 mm. The mapping was performed to minimize a potential influence of mesh differences between states. For simplicity, the spatial pixel index will also be called k, thus after mapping, $\Delta\hat{\boldsymbol{\sigma}}_i$ is a vector of $k = [1, K = 128^2]$ pixel, describing the pixel image with the reconstruction of the i^{th} simulated sphere .

As previously mentioned in section 3.1.3, Adler et al. [93] proposed *figures of merit* to analyze EIT reconstruction quality for small targets with diameters below the resolution of an

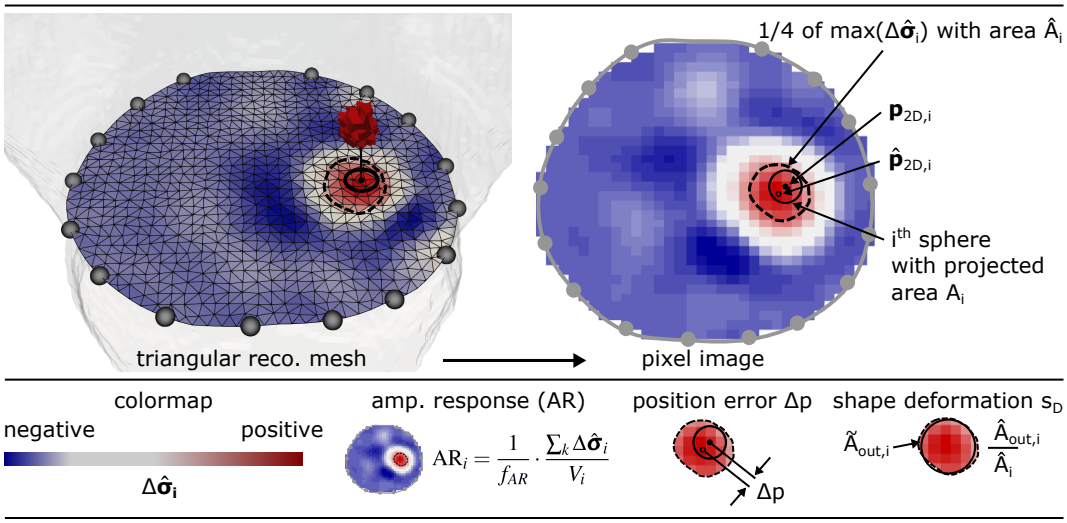

Figure 7.4: Overview of the method to analyze inverse sensitivity. The triangular reconstruction mesh (left image) was mapped onto a pixel mesh with a pixel edge length of 2 mm (right image). From the reconstructed image, a subset mask $\Delta\boldsymbol{\sigma}_{1/4,i}$ was computed. Based on this subset, the 2D position error Δp and the shape deformation was calculated besides other measures. The idea for the graphical description of the figures of merit was taken from [93].

16 electrode EIT system. These figures of merit were also used to optimize the reconstruction matrix of the GREIT algorithm. The evaluation parameters have been further developed in [75]. To investigate the influence of the realistic experimental lung backgrounds on the EIT reconstruction, these standardized parameters were used, though in some cases adapted slightly, and are introduced in the following.

At first, a subset of the reconstructed image $\Delta\boldsymbol{\sigma}_i$ was defined:

$$\Delta\hat{\boldsymbol{\sigma}}_{1/4,i} = \begin{cases} \Delta\hat{\sigma}_{k,i} & \text{if } \Delta\hat{\sigma}_{k,i} \geq \frac{1}{4} \cdot \max\limits_{k} \Delta\hat{\sigma}_{k,i} \\ 0 & \text{otherwise} \end{cases} \tag{7.7}$$

The subset $\Delta\hat{\boldsymbol{\sigma}}_{1/4,i}$ contained all elements with amplitudes exceeding $\frac{1}{4}$ of the maximal reconstructed amplitude and was otherwise zero. The area $\hat{A}_i$ of the set of amplitudes exceeding the threshold and the amplitude weighted centroid $\hat{\boldsymbol{p}}_{2D,i}$ of this subset was calculated, as it was done in [75]. The figures of merit were calculated as follows:

Amplitude response - inverse sensitivity The amplitude response (AR) was used as inverse sensitivity measure and was defined by:

$$\mathrm{AR}_i = \frac{1}{f_{AR}} \cdot \frac{\sum_k \Delta\hat{\sigma}_{ki}}{V_i} \tag{7.8}$$

The sum of all amplitudes in the reconstructed image defines the amplitude response of the reconstruction algorithm. The amplitudes were normalized to the volume of the simulated

sphere V_i to account for potential differences in simulated sphere volumes due to discretization. The amplitude response was normalized by a factor f_{AR} such that a sphere at the center of the torso within the electrode layer had an amplitude response of $\mathrm{AR}_i = 1$.

Position error The position error Δp described the absolute distance between the amplitude weighted centroid of the reconstructed image subset $\hat{\boldsymbol{p}}_{2D,i}$ and the position of the simulated sphere. Since only a 2D image was reconstructed, the center of the projection of the sphere parallel to the vertical axis onto the electrode plane was calculated. Thus, only the first two coordinates of $\boldsymbol{p}_{2D,i} = [p_{1,i}, p_{2,i}]^\top$ were considered. The position error was defined by:

$$\Delta p_i = \sqrt{\left(\hat{\boldsymbol{p}}_{2D,i} - \boldsymbol{p}_{2D,i}\right)^\top \cdot \left(\hat{\boldsymbol{p}}_{2D,i} - \boldsymbol{p}_{2D,i}\right)} \tag{7.9}$$

Shape deformation Since spheres were simulated, we expected circular reconstructions in the resulting image. Nevertheless, the shape of the torso boundary, the current paths through the thorax (which might be altered by changing background conductivity distributions) and by the position of the simulated sphere might lead to altered reconstruction shapes. The shape deformation measure $s_{D,i}$ therefore describes the similarity of the reconstructed image subset $\Delta\hat{\boldsymbol{\sigma}}_{1/4,i}$ to a circle C of area $\hat{A}_i$ with its center at $\hat{\boldsymbol{p}}_{2D,i}$. A very intuitive measure was introduced in [93], which was also used for the analysis in this thesis. The measure calculates the area $\hat{A}_{out,i}$ of the reconstructed subset outside of C and relates it to the overall area $\hat{A}_i$:

$$s_{D,i} = \frac{\hat{A}_{out,i}}{\hat{A}_i} \tag{7.10}$$

If the shape of the reconstructed subset is circular, $s_{D,i} = 0$ was expected. The measure is graphically described in Figure 7.4.

Point spread function - reconstruction resolution The point spread function (PSF) is a well known measure from image processing. It defines the (impulse) response of an imaging system to a point source. The parameter describes the reconstruction resolution. The PSF was defined by the relationship of the area of the reconstructed subset $\hat{A}_i$ compared to the overall area of the torso mesh A_{mesh}.

$$\mathrm{PSF}_i = \frac{\hat{A}_i}{A_{mesh}} \tag{7.11}$$

Ringing Ringing artifacts describe periodic oscillations around sharp spatial transients or edges due to the low-pass filter effects of the reconstruction. Around the reconstructed circular object, negative amplitudes appear if ringing is present. Ideally, these negative artifacts vanish if an optimal reconstruction is chosen. The ringing (RNG) measure was defined by:

$$\mathrm{RNG}_i = \frac{\sum\limits_{k \notin C \cap \Delta\hat{\sigma}_{ki} < 0} \Delta\hat{\sigma}_{ki}}{\sum\limits_{k \in C} \Delta\hat{\sigma}_{ki}} \tag{7.12}$$

Without ringing present, the measure will result in $\mathrm{RNG}_i = 0$.

7.3 Results

7.3.1 Analysis of forward sensitivity

The results of the forward sensitivity analysis are split in three sections. At first, the spatial sensitivity distributions are investigated qualitatively and the profiles of spatial sensitivity (right-left, dorsal-ventral and caudal-cranial) are compared between experiments and between indicator concentrations. Secondly, the similarity of spatial sensitivity profiles are quantitatively assessed and compared for different indicator concentrations. Similarity of spatial sensitivity is essential to allow clinical comparison of different lung states with different conductive backgrounds (e.g. collapsed and recruited lung). Lastly, the variation of forward sensitivity across conductive spheres within the electrode plane was evaluated. Ideally, the sensitivity remains constant within the electrode plane. Yet, for adjacent stimulation, we expect sensitivity to be higher close to the boundary and lower towards the center of the torso. Still we expect the sensitivity to be more homogeneously distributed within the electrode plane for higher indicator concentrations, since the influence of the background conductivity decreases.

Qualitative analysis For a qualitative assessment of the spatial forward sensitivity distribution in front of realistic pulmonary conductivity backgrounds, images of the distributions are depicted in Figures 7.5, 7.6 and 7.7. The Figures depict sagittal, frontal and transversal cross-sectional images of the sensitivity distribution to conductive spheres of blood (top row) and to conductive spheres of a saline indicator with a concentration of 5 % NaCl (middle row). The sensitivities were normalized to their spatial maximum and are presented in log-scale. The indicator concentration of 5 % NaCl was chosen as a representative concentration. The results of the quantitative comparison of sensitivities for all concentrations are described in the next section. The inhomogeneous background conductivity of the individual experimental states are shown alongside (bottom row) in order to be able to interpret the influence of the background on the EIT forward sensitivity.

Figure 7.5 depicts the distribution of forward sensitivity together with the respective background conductivity for a uni-lateral ventilation of the right lung (S1). The animal was ventilated with a PEEP $= 5$ mbar. Only the right lung was ventilated during this experiment, since airflow to the left lung was prevented using a bifurcated endobronchial blocker. As a result, all alveoli within the left lung collapsed, which corresponds to an FF $= 0$. The electrical tissue conductivity was thus reflected by the collapsed parenchyma tissue with a conductivity of $\sigma_{alv} \approx \sigma_{blood}$. Forward sensitivity $\mathbf{S}$ to spheres of blood was substantially lower within the left collapsed lung (top row). Sensitivity between left and right lung differed by a factor of approximately 100. Due to the collapsed left lung, the ventilated accessory/intermediate lobe of the right lung (see section 2.1) was pushed to the region of the left lung, which can be acknowledged in the images of the top row by the increased sensitivity in dorsal regions

within and around the electrode plane. The maximal sensitivity for spheres of blood (top row) as well as for spheres of a 5 % NaCl indicator (middle row) was observed at the dorsal tip of the right middle lobe, which was the closest point within the lung to the surface electrodes. The images in the middle row show the spatial forward sensitivity to spheres filled with a saline indicator with a concentration of 5 % NaCl. A decrease of forward sensitivity towards the center of the torso and with increasing distance to the electrode plane was observed. Between left and right lung, a similar sensitivity profile could be observed.

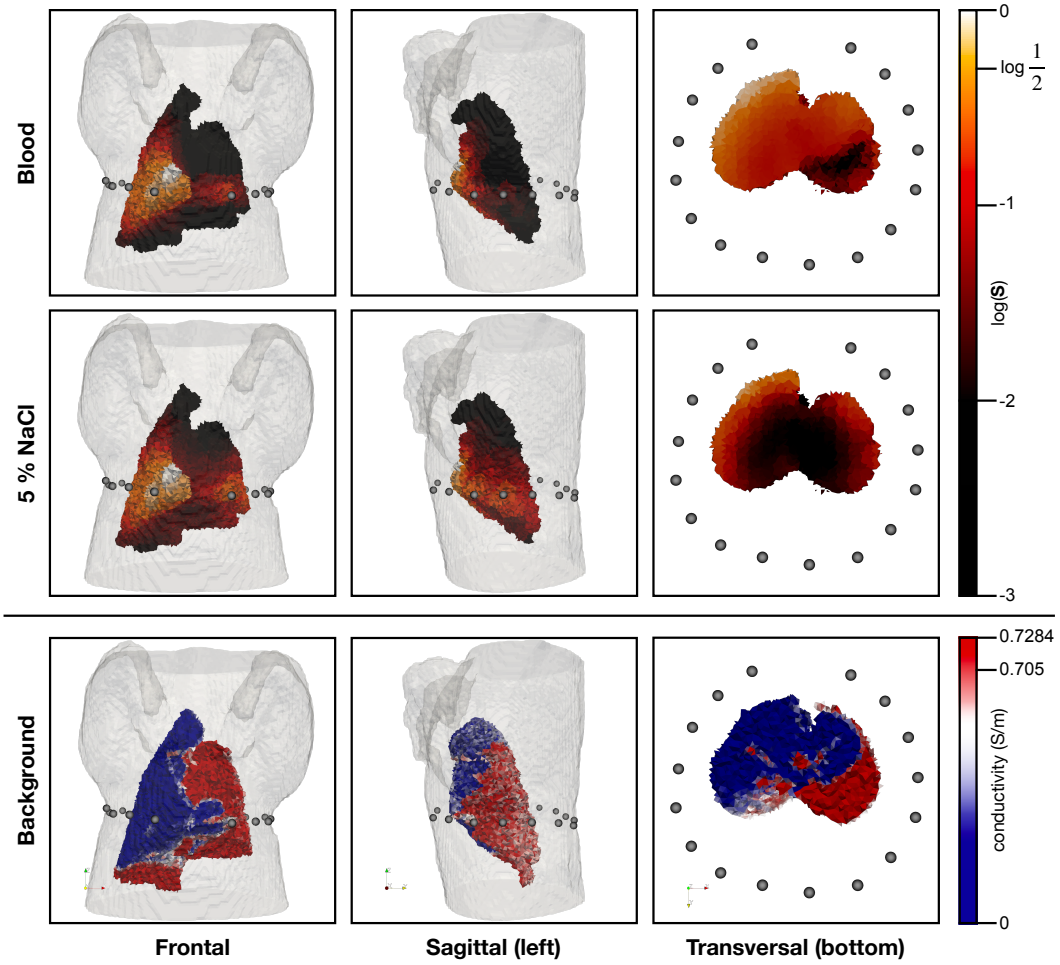

Figure 7.5: Logarithmic and normalized forward sensitivity **S** for experiment: **one lung ventilation (S1)**. The top row depicts the normalized sensitivity to spheres of 10 ml volume and the conductivity of blood in log-scale. The middle row the normalized sensitivity to spheres with the conductivity of 5 % NaCl in log-scale. The sensitivities are normalized to the largest spatial sensitivity. In the bottom row, the background conductivity is shown. The spatial distributions of sensitivity and background conductivity are depicted from three perspectives.

Figure 7.6 presents the spatial distribution of forward sensitivity as calculated for a bilateral ventilation at an optimal PEEP = 11 mbar (S3). The optimal PEEP was defined using a decremental PEEP trial and the approach described in [54] to minimize collapse and overdistension. The background conductivity within the lungs was homogeneous due to the homogeneous ventilation of both lungs. The larger arteries can be seen in the transversal image of the bottom row. Since the lung was homogeneously ventilated, no visible difference between the spatial sensitivity distribution to spheres of blood (top row) and to spheres filled with an 5 % NaCl indicator (bottom row) was found. The maximal sensitivity was again found at the dorsal tip of the right middle lobe close to the electrodes. The sensitivity decreased towards the center of the torso and for an increasing distance to the electrode belt for both types of spheres (blood and indicator).

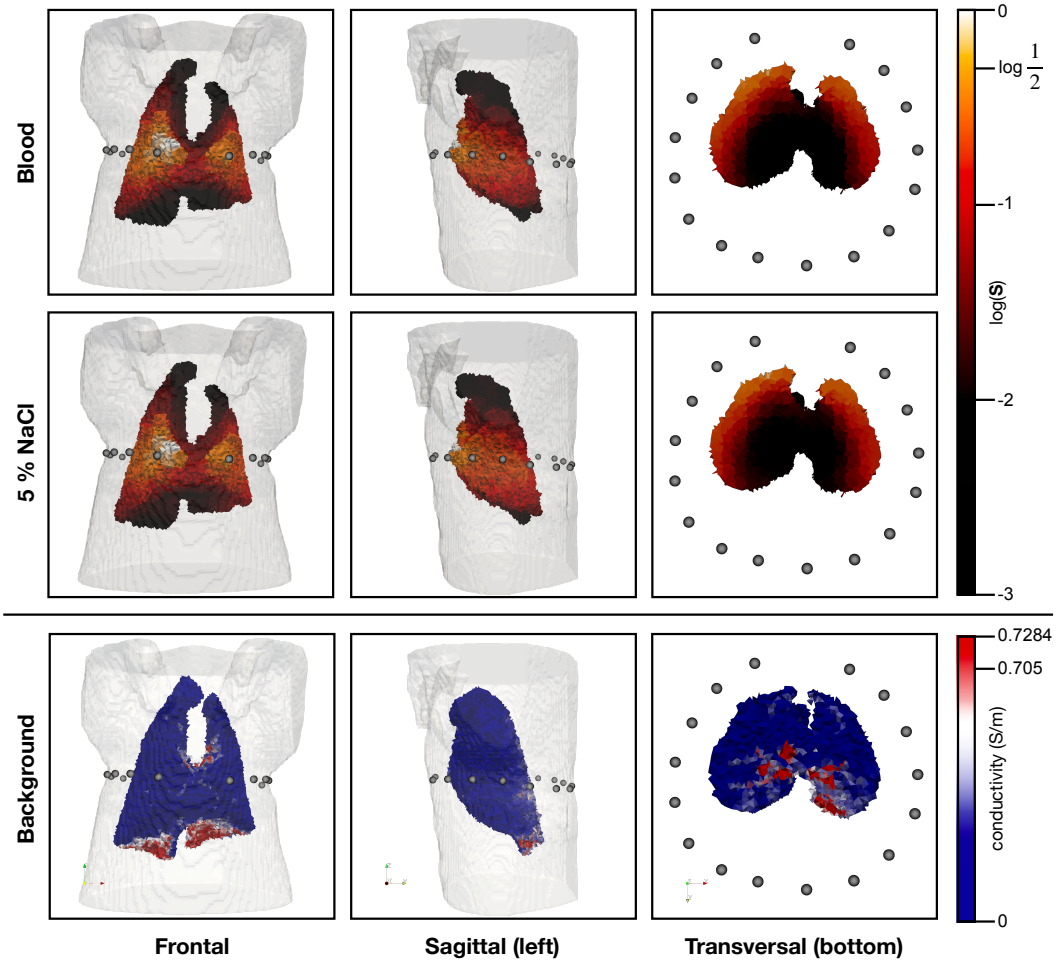

Figure 7.6: Logarithmic and normalized forward sensitivity $\mathbf{S}$ for experiment: **bilateral ventilation at optimal PEEP (S3)**. The top row depicts the normalized sensitivity to spheres of 10 ml volume and the conductivity of blood in log-scale. The middle row the normalized sensitivity to spheres with the conductivity of 5 % NaCl in log-scale. The sensitivities are normalized to the largest spatial sensitivity. In the bottom row, the background conductivity is shown. The spatial distributions of sensitivity and background conductivity are depicted from three perspectives.

In Figure 7.7, exemplary spatial forward sensitivity distributions for the third analyzed experimental state are shown. An experimental model of regional lung injury was induced by repeated lung lavage of both lungs. Alveolar surfactant was hereby washed out and regional alveolar collapse was observed in gravity dependent (dorsal) regions of the lungs. To keep the lung injury stable throughout the measurements and prevent the collapsed lung regions from recruitment, the animal was ventilated at a PEEP $= 0$ mbar. The dorsal collapse of alveoli leads to an increase of electrical tissue conductivity, which can be acknowledged in the images of the bottom row. The sensitivity to spheres of blood (top row) was again found to be substantially lower in regions of collapse due to the increase of alveolar conductivity to approximately the same as blood conductivity. The maximal sensitivity was found in the tips of the left and right middle/cranial lobes close to the electrodes.

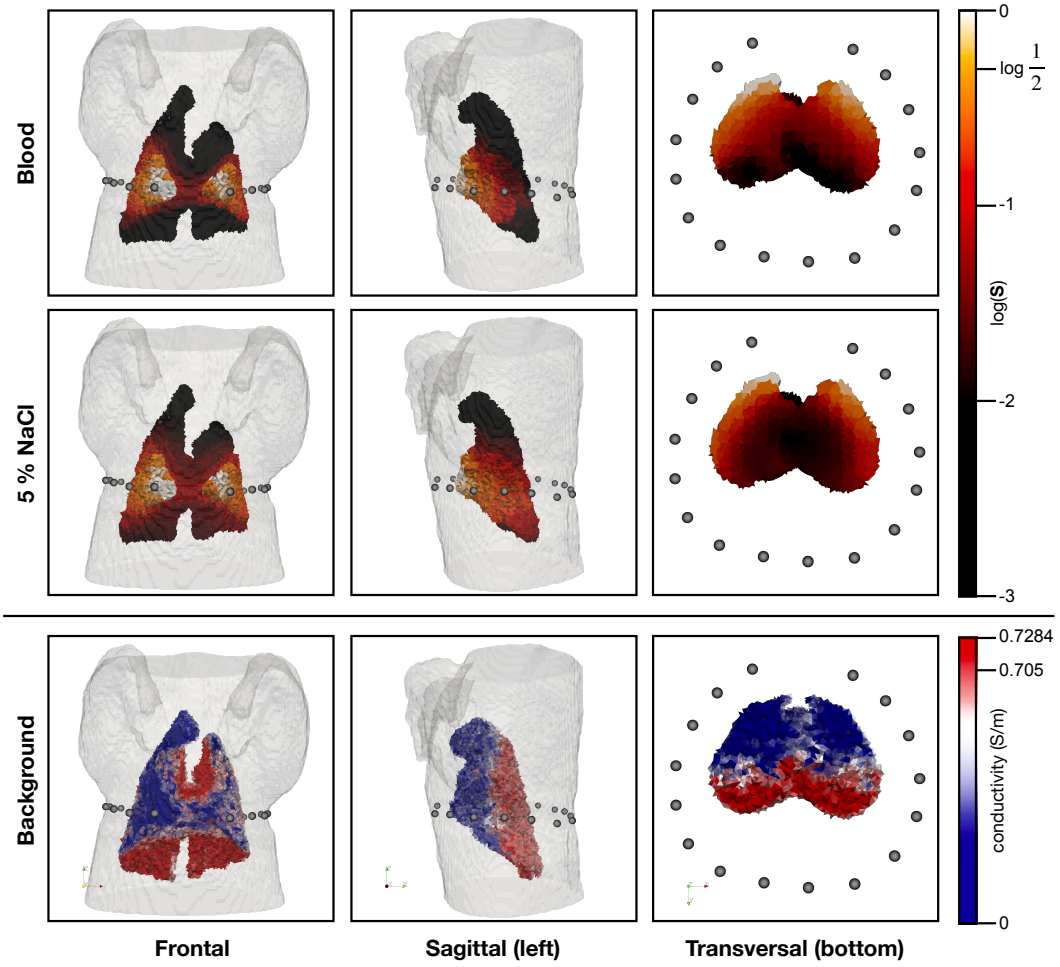

Figure 7.7: Logarithmic and normalized forward sensitivity $\mathbf{S}$ for experiment: **injury/atelectases (S4)**. The top row depicts the normalized sensitivity to spheres of 10 ml volume and the conductivity of blood in log-scale. The middle row the normalized sensitivity to spheres with the conductivity of 5 % NaCl in log-scale. The sensitivities are normalized to the largest spatial sensitivity. In the bottom row, the background conductivity is shown. The spatial distributions of sensitivity and background conductivity are depicted from three perspectives.

The sensitivity to spheres with a 5 % NaCl indicator showed again the typical decrease of sensitivity towards the center of the torso and with increasing distance to the electrode belt.

Figure 7.8 presents computed forward sensitivity profiles of the spatial forward sensitivity distributions for each experimental state. To compute the profiles, all simulated spheres were sorted according to their position $\mathbf{p}_i$. For the right-left profile, the spheres were sorted according to their first coordinate $p_{1,i}$, for the dorsal-ventral profile according to their second coordinate $p_{2,i}$ and for the caudal-cranial profile according to $p_{3,i}$. The sorted spheres were

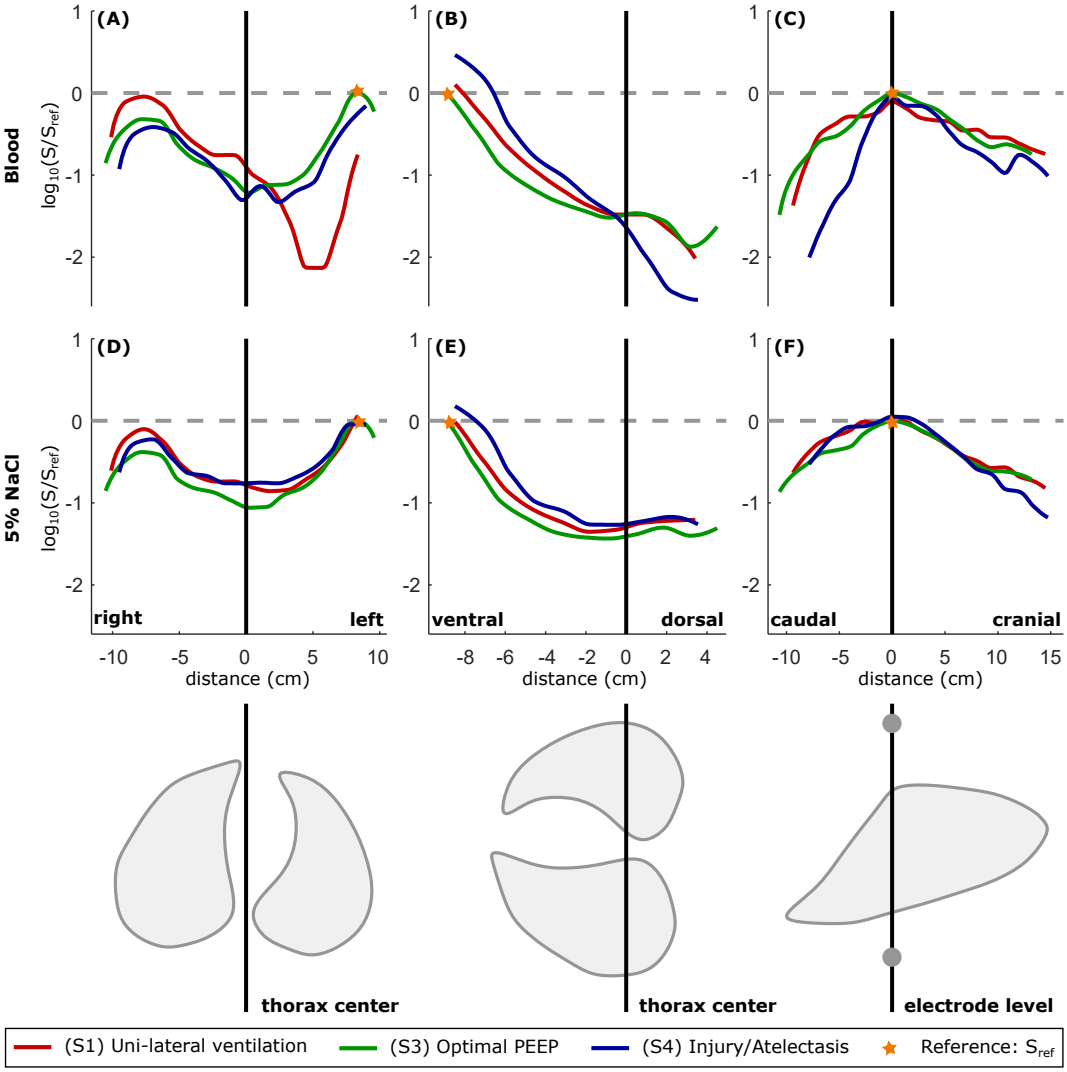

Figure 7.8: Visualization of the spatial forward sensitivity profiles for all experimental states (S1), (S3) and (S4). The right-left profile (A) and (D), the dorsal-ventral profile (B) and (E) and the caudal-cranial (C) and (F) are depicted. The profiles of forward sensitivity to spheres of blood (top row) and to spheres with a 5 % NaCl indicator (middle row) are depicted. The bottom row visualizes the direction of the calculated profiles with respect to the lungs. The sensitivity profiles are normalized to the maximum of the healthy reference state (S3) for each profile direction individually.

assigned to equidistant spatial intervals. Within each interval, the median of the sensitivity of all assigned spheres was calculated. The median sensitivity profiles were finally interpolated and centered around the torso center within the cross sectional plane of the EIT electrodes. In the top row of Figure 7.8, the spatial sensitivity profiles resulting from the integration of spheres with blood are depicted. In graph (A), the sensitivity across the right and left lung is depicted. The profiles of the healthy reference state (S3) and of the lung injury model (S4) were found to have a similar shape. In the torso center, the sensitivity was decreased, while within the lungs the sensitivity was maximal. For the unilateral ventilation (S1), the sensitivity was decreased by a factor of 100 within the left collapsed lung. The sensitivity profile differed strongly from the other profiles, which would strongly impair a comparison of spatial perfusion between these states during a clinical assessment. If an indicator of 5 % NaCl was used, as depicted in image (D), the right-left profiles of all states were found to be very similar.

In graph (B), the dorsal-ventral profiles of the forward sensitivity to blood are depicted. Forward sensitivity was decreased in dorsal and therefore collapsed regions of the lungs during lung injury (S4) compared to the other states. Again, with an indicator of 5 % NaCl solution, as shown in graph (E), the dorsal-ventral sensitivity profiles strongly aligned. The dorsal-ventral profiles uniformly showed a higher sensitivity in ventral regions than in dorsal regions.

For the caudal-cranial profile in graphs (C) and (F), a similar result was found. In collapsed dorsal regions the sensitivity to blood was strongly impaired during lung injury (S4), while the profiles became very similar with an indicator of 5 % NaCl. In graphs (C) and (F), the graphs show a bell shaped sensitivity profile in log-scale. The decrease of sensitivity with distance from the electrode plane was nevertheless not found to be similar in caudal and cranial direction. The sensitivity decreased faster in cranial direction than in caudal direction.

Quantitative assessment of spatial sensitivity similarity After the qualitative comparison of the spatial distribution of sensitivity to blood and to a 5 % NaCl indicator bolus, the similarity of spatial sensitivity distributions was quantified. With this analysis, the hypothesis, that spatial sensitivity distributions increase in similarity with increasing indicator concentrations, was investigated. The experimental state: bilateral ventilation at an optimal PEEP (S3) was considered as reference. The maximum of the correlation function R_{max} between reference state and unilateral ventilation (S1) and injury/atelectases (S4) for each spatial sensitivity profile (as depicted in Figure 7.8) was computed to assess similarity between the profiles. The maximum of the correlation function instead of Pearson's correlation coefficient was used to compare the profiles. This was necessary, since the profiles could be slightly shifted due to the different levels of PEEP during the individual experimental states. The graphs in Figure 7.9 depict the maximal correlation of the different amounts of indicator concentration (blood represents an indicator of 0 % NaCl).

The graphs in the left plot show an increase of the maximum of the correlation function with increasing indicator concentration especially for the similarity between (S1) and (S3) (red curve). In absence of an indicator was used (spheres of blood), the right-left profiles of state (S1) and (S3) are hardly similar ($R_{max} = 0.67$), since the sensitivity within the left lung is substantially decreased. For an indicator concentration of 2 %, the correlation value already increased to $R_{max} = 0.89$. The maximal similarity value for an indicator concentration of 10 % was found to be $R_{max} = 0.95$. Since lung lavages were performed in both lungs, the left-right profile was not expected to be substantially different from the one of the reference state. The similarity is constantly high for all indicator concentrations above 3 %.

For dorsal-ventral sensitivity profiles (center plot), the similarity was constantly high across indicator concentrations and only varied slightly for both comparisons. The correlation between (S4) and (S3) (blue curve) even decreased slightly with increasing indicator concen-

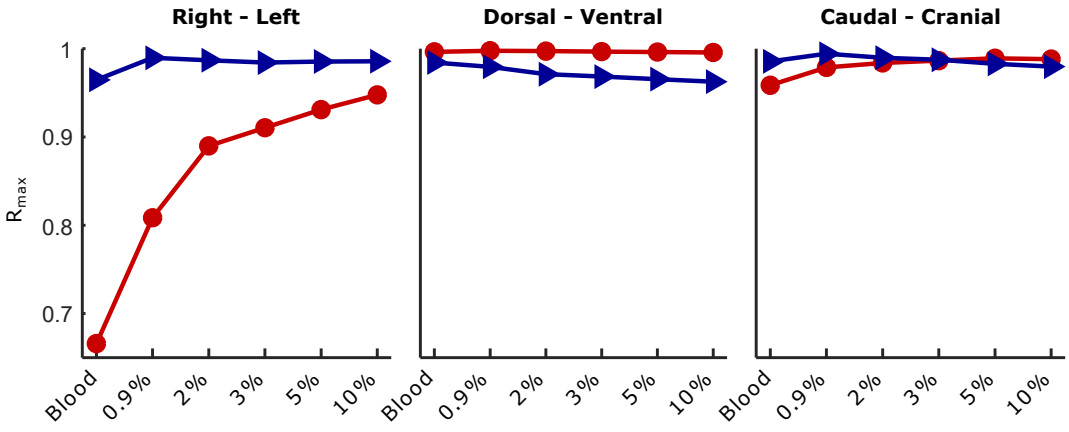

Figure 7.9: Similarity of forward sensitivity profiles for different indicator concentrations by correlation analysis. The maximum of the correlation function R_{max} between the profile of the reference state (S3) and the unilateral ventilation (S1) or the injury/atelectases state (S4) is depicted. The left shows the correlation analysis for the right-left profile, the middle plot the analysis for the dorsal-ventral profile and the right plot the similarity for the caudal-cranial profile.

tration (from $R_{max} = 0.98$ to $R_{max} = 0.96$).
The caudal-cranial profiles were also found to be very similar across all indicator concentrations as assessed by the maximum of the correlation function. The similarity between the profiles of (S4) and (S3) increased slightly with increasing indicator concentration from $R_{max} = 0.96$ to $R_{max} = 0.98$.

Variation of forward sensitivity within the EIT electrode plane With an adjacent stimulation and the arrangement of EIT electrodes in one single transversal plane, a completely homogeneous forward sensitivity across the whole lung cannot be expected. With increasing distance to the electrode plane, the sensitivity will decrease, since the current density provoked by an injected stimulation current is low in larger distance from the electrode plane. The current will always flow along the shortest path with the lowest resistance between electrodes. Even within the electrode plane, the sensitivity cannot be assumed to be homogeneous. Nevertheless, the variation of forward sensitivity within the electrode plane is hypothesized to decrease in a small region around the electrode plane, if the influence of the inhomogeneous background conductivity decreases. For this purpose, the median and interquartile range (IQR) was assessed within the electrode plane. The median and IQR was calculated over all spheres $i \in \left\{[1,k_S]|p_{3,i} \in [-2 \cdot r_{Sphere}, 2 \cdot r_{Sphere}] \cdot z_E\right\}$. The vertical (cranial-caudal) level of the electrode plane is described by z_E. Figure 7.10 depicts the median alongside with the IQR. The median and IQR were normalized to the median sensitivity within the electrode plane for the simulation of blood spheres. The median forward sensitivity decreased with increasing indicator concentration by up to 87 %.

Since median sensitivity decreased, the absolute IQR will also decrease independent of the background conductivity. To account for this effect and enable fair comparison between different indicator concentrations, the IQR of each indicator concentration was normalized to its respective median value. Normalized IQR (nIQR) decreased with increasing indicator concentrations as listed in Table 7.4. nIQR decreased strongly with increasing indicator

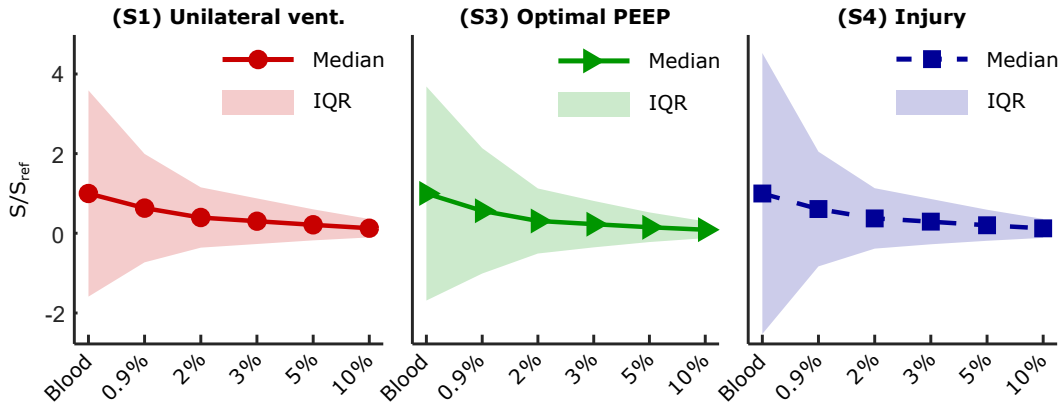

Figure 7.10: Median and IQR of the forward sensitivity within a small region around the electrode plane. The sensitivities are depicted for each experimental state separately.

Type of inhomogeneity	Blood	0.9% NaCl	2% NaCl	3% NaCl	5% NaCl	10% NaCl
nIQR (n.u.) for (S1)	2.59	2.15	1.91	1.88	1.82	1.82
nIQR (n.u.) for (S2)	2.67	2.79	2.64	2.54	2.45	2.35
nIQR (n.u.) for (S3)	3.52	2.36	2.03	1.94	1.93	1.92

Table 7.4: Normalized IQR (nIQR) of the forward sensitivity within a small region around the electrode plane. nIQR was normalized to its respective median value.

concentration for the unilateral ventilation state (S1) and the injury model state (S4). Yet, the sensitivity variation remains twice as large as the median sensitivity due to the inhomogenous distribution of sensitivity caused by the adjacent stimulation protocol.

7.3.2 Analysis of inverse sensitivity

In this subsection, the results of the inverse sensitivity analyses are again divided into three parts. At first, the sensitivities are assessed qualitatively and compared between different indicator concentrations and different reconstruction algorithms. Afterwards, spatial inverse sensitivity (amplitude response) profiles are compared for different indicator concentrations and for the different reconstruction algorithms. Finally, the figures of merit will be compared for all reconstruction algorithms and indicator concentrations.

Qualitative analysis of spatial inverse sensitivity To assess the spatial distributions of amplitude response to the spheres of different conductivity, profiles in three different dimension have been computed, in accordance to the procedure of forward sensitivity analysis. The profiles of inverse sensitivity are depicted in Figure 7.11. In graph (A), the right lung profiles of amplitude response to spheres of blood during all simulated experimental states can be observed. The amplitude response within the left lung during the unilateral ventilation (S1) was found to be more than one decade smaller compared to the other states. This sensitivity difference was not present any more, if the conductivity of the spheres was increased to the conductivity of a 5 % NaCl bolus (graph (D)). The profiles became much more similar between different experimental states.
The amplitude response to spheres of blood was also greatly decreased in caudal regions of the lung in the lung injury mode (S4) (graph (C)). The spatial sensitivity imbalance was minimized substantially, when the sphere conductivity was increased to the respective conductivity of a 5 % NaCl indicator.

Quantitative assessment of spatial inverse sensitivity similarity The regional similarity of amplitude response AR between the reference state (S3) and unilateral ventilation (S1), as well as between (S2) and lung injury (S4) was again assessed by the maximum of the correlation function R_{max} between the spatial profiles, as it was similarly done for the forward sensitivity. In Figure 7.12 the correlation values are depicted for all three spatial profiles and reconstruction algorithms.

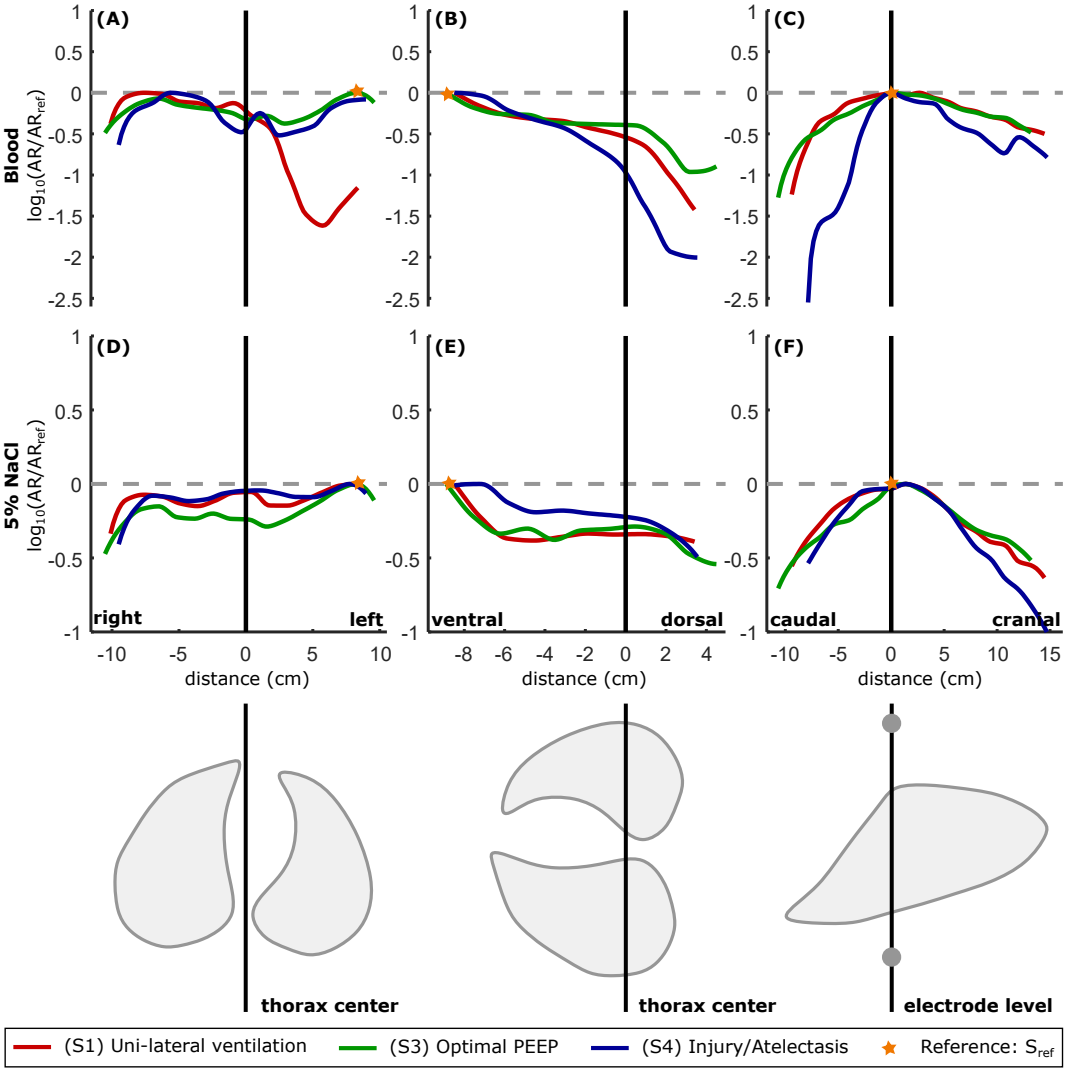

Figure 7.11: Visualization of the spatial inverse sensitivity (amplitude response) profiles for all experimental states (S1), (S3) and (S4). The right-left profile (A) and (D), the dorsal-ventral profile (B) and (E) and the caudal-cranial (C) and (F) are depicted. The profiles of inverse sensitivity to spheres of blood (top row) and to spheres with a 5 % NaCl indicator (middle row) are depicted. The bottom row visualizes the direction of the calculated profiles with respect to the lungs. The sensitivity profiles are normalized to the maximum of the healthy reference state (S3) for each profile direction individually. The depicted amplitude response profiles correspond to a reconstruction with a laplace regularization.

The correlation of the right-left profile between (S1) and (S3) (left graph, top row) increases substantially for all reconstruction algorithms with increasing sphere conductivity. From spheres of blood to spheres with a 2 % indicator the maximum of the correlation function increases from values as low as 0.82 (Laplace reconstruction for blood spheres) to 0.98 (for all reconstruction algorithms for 2 % NaCl). Beyond this level, increasing the indicator concentration did not further increase the similarity substantially.

The similarity between lung injury model (S4) and the healthy reference state (S3) greatly

increases for dorsal-ventral (bottom-center graph) and caudal-cranial profiles (bottom-right graph). For all reconstruction algorithms the increase in similarity is very comparable.

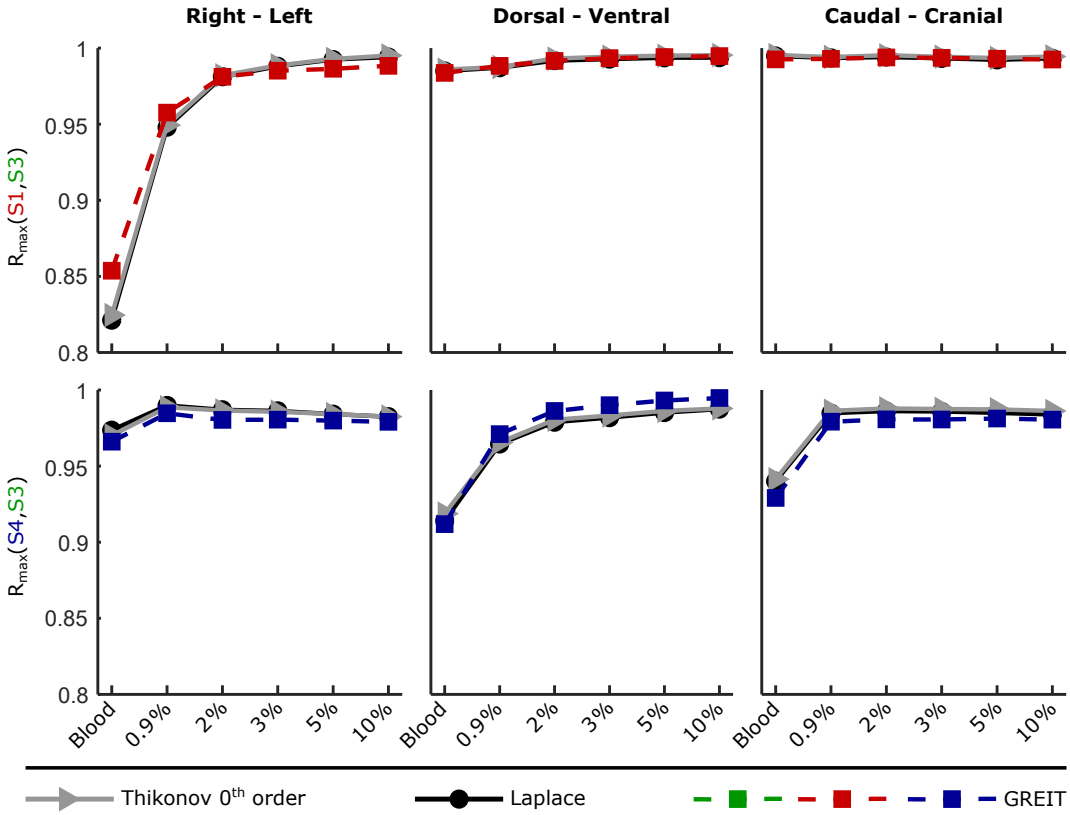

Figure 7.12: Assessment of amplitude response **AR** (inverse sensitivity) similarity by correlation of spatial profiles. The left column depicts the similarity of right-left profiles of amplitude response for all reconstruction algorithms, the center the similarity of dorsal-ventral profiles and the right column the similarity of caudal-cranial profiles. The upper row of graphs show the comparison of the reference state with the unilateral ventilation state (S1) and the lower row depicts the comparison to the lung injury model (S3).

Analysis of reconstruction parameters within the electrode plane In [93], desired behaviors for the reconstruction figures of merit were defined. Above all, constant amplitude responses, position errors and shape deformations would be desirable across the imaging plane. Since the decrease of amplitude response and the increase of shape deformation and position error with increasing distance from the electrode plane are determined by the 2D transversal placement of the electrodes and can not be influenced by the reconstruction algorithm, the analysis of the figures of merit were conducted within a small region around the electrode plane. All spheres $i \in \left\{[1,k_S]|p_{3,i} \in [-2 \cdot r_{Sphere}, 2 \cdot r_{Sphere}] \cdot z_E\right\}$. z_E were included in the analysis.

At first, the median of all figures or merit was calculated to compare the reconstruction quality among reconstruction methods and indicator concentrations. The median of the amplitude response $\bar{\text{AR}}$ was calculated and is depicted in the top row of Figure 7.13. The amplitude response decreases with increasing indicator concentration. The amplitude response is very similar for reconstruction algorithms with a slightly smaller amplitude response for the GREIT reconstruction. The amplitude response to spheres of blood for the lung injury model (S4) showed a very large value ($\bar{\text{AR}} \approx 7$ for all reconstruction approaches and is not shown in the top-right graph. The large value can be explained by the very large amplitude response to spheres at the tip of the middle lobe of both lungs and the very small amplitude responses in collapsed regions. The amplitude response values were normalized such that the most central sphere had an $\text{AR} = 1$ (as explained in section 7.2). The reference sphere was located within the collapsed region, thus scaling increased the AR values of ventral spheres even more.
The median position error $\Delta\bar{p}$ was not substantially affected by the indicator concentration (second row of Figure 7.13). The position error was generally smaller for the GREIT reconstruction by approximately 2 mm. The position error was largest for the Laplace regularization.
The median of the PSF was generally larger for the GREIT reconstruction, but also not dependent on the indicator concentration. The median of the shape deformation was found to be smaller for GREIT reconstruction and did not depend on the indicator concentration. Ringing was significantly decreased for the GREIT reconstruction with no dependency on the sphere conductivity.

Besides the median of the figures of merit, the variation of these reconstruction quality parameters was assessed. The IQRs of all parameters across all sphere within the small region around the electrode plane were calculated. The IQRs were normalized to their respective median to allow comparison between different concentrations, reconstruction approaches and experimental states.
Figure 7.14 depicts the normalized IQRs as a function of indicator concentration and for all different reconstruction algorithms. The top row depicts the IQR for the amplitude response AR_{iqr}. With increasing indicator concentration, the variation of the amplitude response within the area around the electrode plane decreased for all reconstruction algorithms. Thus,

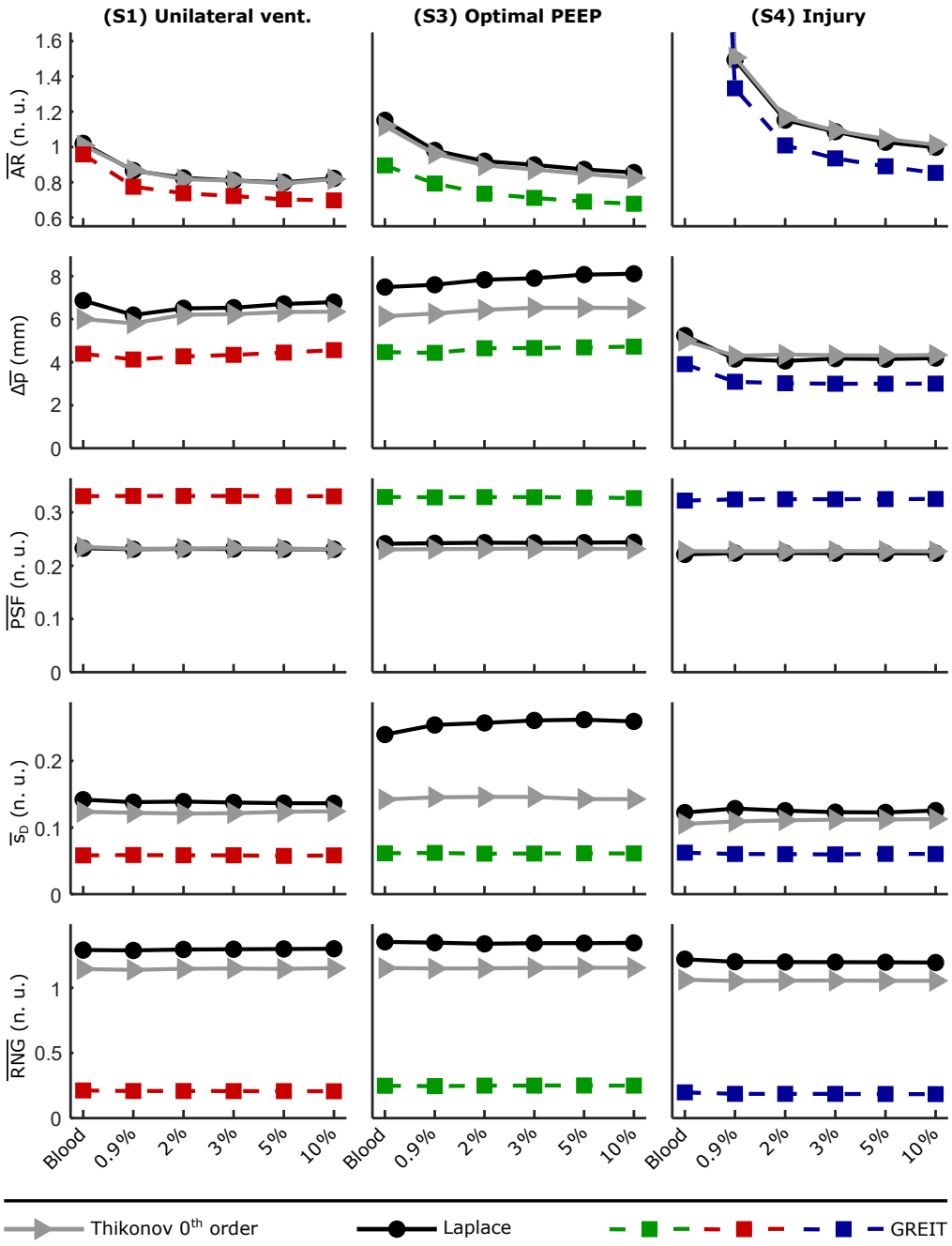

Figure 7.13: Median values of the figures of merit to assess reconstruction quality within a region around the electrode plane. The top row shows the median of the amplitude response for all reconstruction approaches as a function of indicator concentration. The second row depicts the median of the position error, the third row the median of the PSF. The forth row shows the results for the shape deformation parameter and the last row depicts the median amount of ringing present for each reconstruction algorithm.

the inverse sensitivity became more homogeneous for increasing indicator concentrations.

The IQR of all other parameters did not show a clear dependency on the indicator concentration.

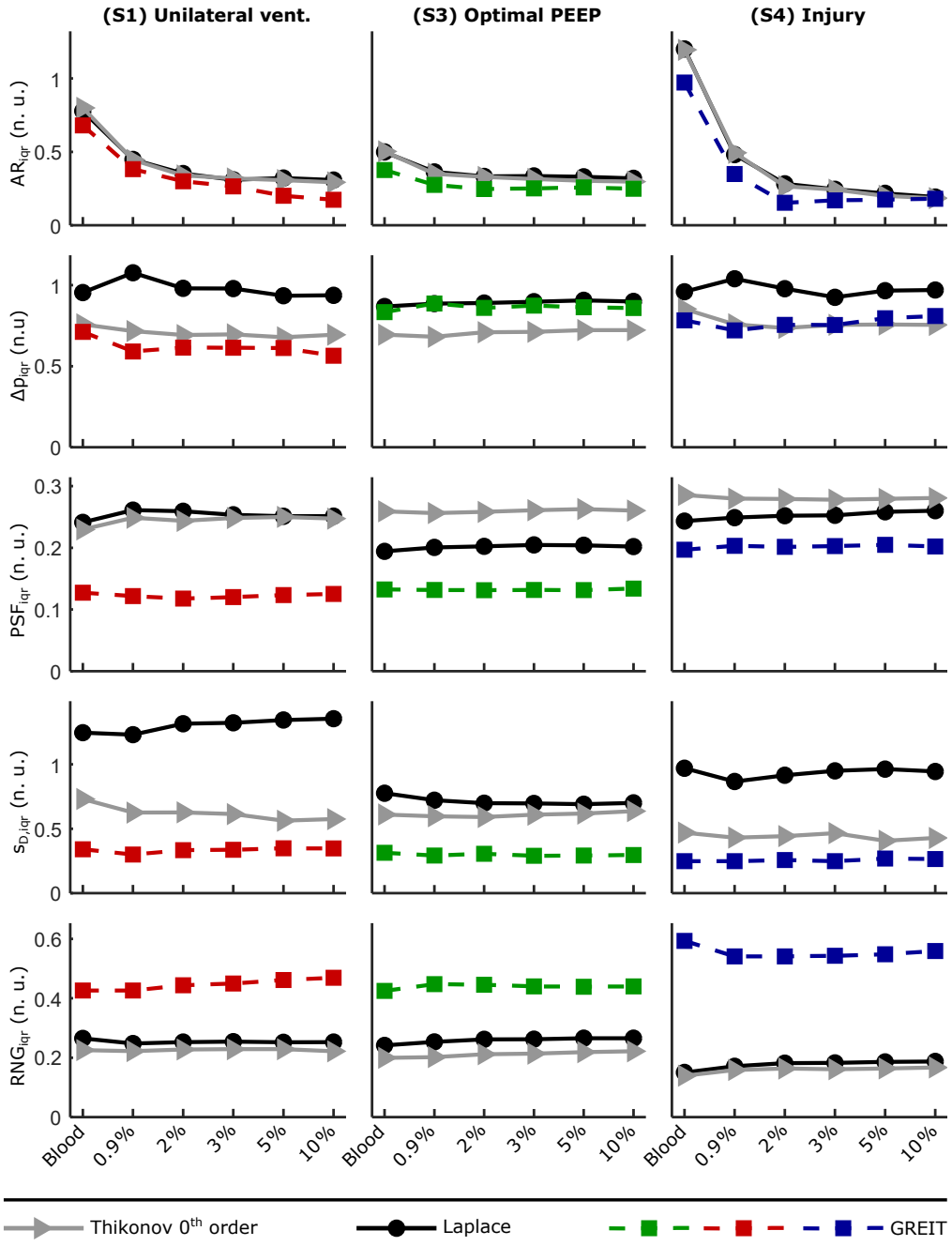

Figure 7.14: IQRs of the figures of merit to assess reconstruction quality within a region around the electrode plane. The top row shows the IQR of the amplitude response for all reconstruction approaches as a function of indicator concentration. The second row depicts the IQR of the position error, the third row the IQR of the PSF. The forth row shows the results for the shape deformation parameter and the last row depicts the IQR amount of ringing present for each reconstruction algorithm.

7.4 Discussion

In this chapter, the forward and inverse sensitivity were investigated. The similarity of spatial distributions of forward and inverse sensitivity was assessed between different experimental states with substantially different and realistic pulmonary conductivity backgrounds.
Forward and inverse sensitivity exponentially decreased with distance from the electrode plane in caudal-cranial direction. At a distance of approximately 10 cm, forward and inverse sensitivity were reduced by almost 90 %. If a sufficient indicator concentration was considered, such that the background influence was reduced, forward sensitivity and amplitude response decreased faster in cranial direction. This might be explained by the very conductive heart region above the electrode plane. The current density is most likely higher around the heart region, which might decrease the sensitivity to a conductivity change in this region. Similar explanation approaches have been also made in [19, 109].
The ventral regions of the lungs were found to be more sensitive (inverse and forward) for all states, indicator concentrations and reconstruction approaches. The distance to the surface electrodes is much smaller in ventral regions of the lungs, compared to dorsal regions of the lungs. This might be a possible explanation for the substantial sensitivity difference between ventral and dorsal lung areas. This finding might also represent an explanation for the repeatedly reported overestimation of lung perfusion in ventral regions compared to an underestimation of perfusion in dorsal regions [19, 109, 121]. This effect might be considerably smaller in clinical measurements, since the human anatomy does not show large muscular and fatty areas dorsal of the lungs. The distance to the electrodes in ventral and dorsal regions are in this case much more similar.
The similarity of the spatial profiles between experimental states increased with increasing indicator concentrations. The conductivity contrast to the pulmonary background increases with increasing concentration, thus the inhomogeneous distribution of background conductivity loses influence. Overall, considering forward and backward sensitivity, a 2 % NaCl indicator seemed to be sufficient to achieve a strong similarity between different experimental states. This does not mean, that a 2 % NaCl indicator achieves sufficiently high SNR to allow robust perfusion estimation in noisy measurements. This analysis will be performed in chapter 12.
The evaluated figures of merit, assessing the reconstruction quality, did not show a dependency on the indicator concentration besides the amplitude response. Overall, the GREIT algorithm seemed to perform best with respect to position error, shape deformation and ringing. Nevertheless, the training data (conductive spheres) were very similar to the spheres of the simulation study. Thus, an overfitting of the algorithm to the problem might have an influence as well.

Limitations The described sensitivity simulation study has only been performed for a single porcine anatomy. Though the findings are very comprehensive and were consistent with our expectations, the meaningfulness might be further increased if a larger cohort

of animals would be considered for simulation. Additionally, during the experimental states, which were compared within the sensitivity study, PEEP levels were different. The different levels of PEEP not only lead to a change of background conductivity, but also to a repositioning of the heart and an enlargement or reduction of lung volume. The altered anatomy also influences the spatial sensitivity distribution and can not be compensated by higher indicator concentrations.

The simulated conductive spheres had a volume matching the 10 ml of the injected indicator during the Dresden study. Nevertheless, the whole amount of indicator will never be in the same spatial region at the same time, since it will most likely (partially) dilute fast within the blood stream.

Chapter 8

Dynamic simulation of indicator-enhanced EIT

María Hernández Mesa contributed to the research for her Master thesis to the following dynamic simulation study [134].

8.1 Motivation

The method of estimating spatial pulmonary perfusion with EIT bases on the tracking of a conductive indicator bolus during its passage through the pulmonary circulation within multiple cardiac cycles. After central venous injection of the indicator bolus, it first passes the right heart with the right cardiac atrium (RA) and ventricle RV and enters into the lungs through the pulmonary artery (PA). After its passage through the larger blood vessels of the left and right lungs, it passes the pulmonary capillary bed (PCB) around the alveoli and flows through the pulmonary veins (PVs) into the left cardiac atrium (LA) and ventricle LV. If EIT electrodes are attached around the thorax, all of these larger blood circulation compartments participating in pulmonary blood flow contribute to the reconstructed EIT image. Due to its low spatial resolution, EIT will not be able to differentiate larger blood vessels from the capillary bed. While the conductivity change caused by the passage of the indicator through the right heart and the pulmonary arteries is presumably large, the capillary bed represents a widespread volume of lower regional conductivity changes. One could argue, that for this reason the main contribution to the measured voltage change at the EIT electrodes results from the blood flow in the larger arteries and the heart. Yet, a larger volume of smaller conductivity changes might nevertheless lead to a similar voltage change at the surface electrodes compared to a large conductivity change in a relatively small volume. With the clinical goal of investigating spatial distributions of the ventilation-perfusion ratio ($\dot{V}/\dot{Q}$) to assess gas exchange quality, the physician is interested in the spatial distribution of perfusion of the PCB, since this contains the blood flow participating in gas exchange. For this reason, it is necessary to understand, which spatio-temporal compartments (PA, PCB,...)

contribute to the measurable EIT voltage changes and to the resulting reconstructed EIT image amplitudes. It is important to understand, if EIT images mainly represent blood flow in larger blood vessels or perfusion from areas with many smaller vessels within the PCB, which would be clinically more relevant.
To investigate the origins of the indicator-enhanced EIT perfusion image amplitudes, a dynamic indicator-enhanced EIT imaging has been simulated. To simulate the indicator passage, the indicator signals have been extracted from 4D indicator-enhanced multidetector Computed Tomography (MDCT) perfusion measurements. All important participating spatio-temporal compartments of pulmonary circulation have been segmented from the same MDCT volumes to form the basis of EIT simulations.

Objectives
The aims of this chapter all refer to the second main objective as stated in the introduction in section 1.2. Under this main objective the following aims are defined:

- Extract spatial compartments of the pulmonary circulation and the dynamic indicator signals from 4D MDCT measurements.
- Create the dynamic 3D EIT bio-impedance model and solve the EIT forward problem.
- Reconstruct 2D EIT images with standard reconstruction algorithms.
- Analyze contributions of different spatio-temporal participants in pulmonary circulation.

8.2 Methods

The following section describes the process of creating a dynamic simulation of an indicator-enhanced EIT measurement based on dynamic 3D indicator-enhanced MDCT perfusion recordings. The simulation setup and the EIT forward and inverse calculations are described. Finally, the methods to analyze, which spatio-temporal compartments of the pulmonary circulation contribute, are described.

8.2.1 Simulation setup

To create a dynamic simulation of the indicator passage trough the pulmonary circulation, the 4D-MDCT images from the experimental state *Healthy-Normoxia* (E1) of the Iowa study (see section 6) were used. The animal was in supine position throughout the experiment and was normally ventilated with a PEEP $= 5\,\text{mbar}$. The pulmonary perfusion was expected to be higher in dorsal than in ventral regions due to gravity.

MDCT Segmentation As described in chapter 6, indicator-enhanced MDCT perfusion was acquired in a volume around the transversal plane of the attached EIT surface electrodes.

The measurement volume extended 2 cm above and below the EIT electrode plane. The reconstructed MDCT scans had a resolution of $0.5 \times 0.5\,\mathrm{mm}^2$ and a slice thickness of 1.2 mm. A temporal ECG gated series of these scans was recorded with a mean temporal sampling of about 0.8 s. The resulting dynamic 4D-MDCT tissue density volume (in Hounsfield units of tissue density, HU) was initially downsampled to a spatial resolution of 2 mm in all spatial directions. The downsampled matrix $\boldsymbol{\rho}_{CT}(n) \in \mathbb{R}^{K_x \times K_y \times K_z}$ had a size of $[K_x \times K_y \times K_z] = [105 \times 105 \times 12]$ and was dynamically sampled at 25 temporal acquisition points. Since the temporal acquisition was ECG-gated, the dynamic sampling was not equidistant. The temporal domain was therefore interpolated at $n = [1, N]$ sampling points with a sampling rate of $f_s = 25\,\mathrm{Hz}$ resulting in $\mathrm{N} = 1000$ sampling points of the MDCT volume. The sampling rate was set to the frame rate of the EIT measurements recorded simultaneously during the Iowa study.

At first, the static tissue background was segmented from the MDCT volume of the first temporal sampling point $\rho_{CT}(n = 1)$, right before the indicator injection and propagation started. The heart, the lungs, the torso and the electrodes were segmented semi-automatically with *ITKsnap* [152]. The resulting tissue segmentation masks were further processed in *MATLAB R2019a*. The masks were smoothed using morphological operators and combined to gain a tissue material label map of the same size as a single static MDCT volume. The segmented and smoothed tissue labels are depicted in Figure 8.1.

In order to enable the evaluation of different contributors to the spatial amplitudes of an EIT perfusion image, all larger blood volumes participating in the pulmonary circulation were additionally segmented. Since iodine was injected as contrast agent for MDCT perfusion estimation, the contrast of larger blood volumes was increased during the progression of the indicator bolus through the pulmonary circulation in comparison to non-perfused regions. For this reason, the larger blood volumes were segmented from a temporal maximum intensity projection (MIP) of the dynamic MDCT tissue density measurement $\boldsymbol{\rho}_{max} \in \mathbb{R}^{K_x \times K_y \times K_z}$:

$$\boldsymbol{\rho}_{max} = \max_{1 \leq n \leq N} \boldsymbol{\rho}_{CT}(n) \tag{8.1}$$

From the tissue density matrix containing the temporal indicator maxima $\boldsymbol{\rho}_{max}$ the larger blood volumes were segmented with a region growing algorithm implemented in *MATLAB R2019a*. The interval of tissue densities considered for region growing was limited to densities larger than 450 HU. The seed points for region growing for the individual blood volumes were set manually. After segmentation, the segmented blood volumes were smoothed by morphological operators. The segmented blood volumes are depicted in Figure 8.1.

Mesh generation The same process, as explained for the background simulation study in the previous chapter 7, was conducted to create suitable meshes for the EIT simulations. To give a short summary, the torso surface was initially triangulated in *MATLAB R2019a* and exported to *MeshLab* [153, 154]. Further smoothing of the torso surface was followed by the final surface meshing in *Instant Meshes* [156], which optimizes the quality of the surface triangles. The thorax volume was finally meshed with *gmsh* [157]. The mesh consisted of

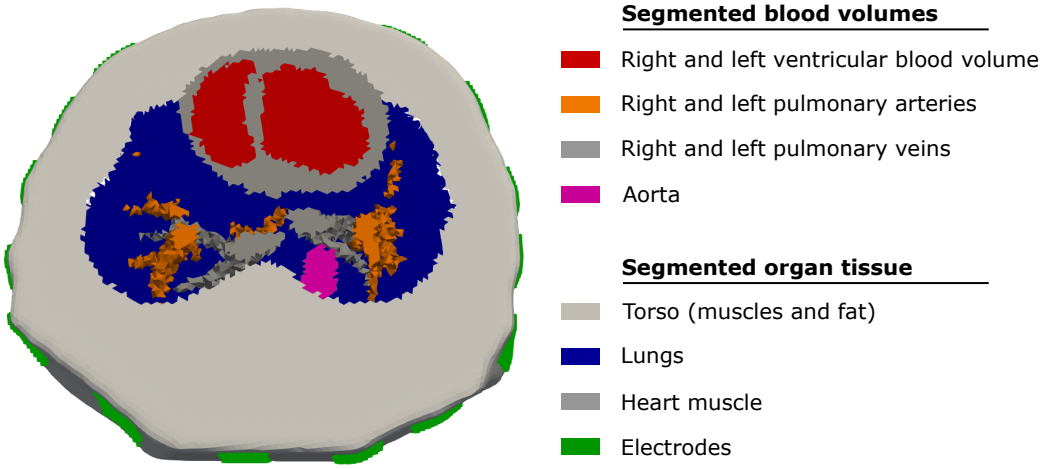

Figure 8.1: Depiction of the simulation mesh with the mapped segmented tissue and electrode labels and blood volumes.

281 172 tetrahedral elements with a mean edge length of 3.19 ± 0.59 mm and a mesh quality (ratio of the shortest to the longest edge length of a tetrahedron) of $\eta = 0.66 \pm 0.07$.

Extraction of indicator signals In order to simulate a dynamic EIT measurement of the indicator bolus propagation through the pulmonary circulation, the temporal indicator signals had to be extracted from the measured MDCT tissue density matrices. For voxels of $\boldsymbol{\rho}_{CT}(n)$ within the segmented blood volume regions or within the lung, the temporal indicator signals were extracted. The static background tissue density was removed in order to separate the MDCT density changes caused by the presence of the indicator. Afterwards, temporal low pass filtering was applied (IIR-Butterworth filter, $f_{3dB} = 0.5\,\text{Hz}$) to remove noise. The cutoff frequency was chosen well below potential heart rates. The heart rate defined the initial non-equidistant sampling due to the ECG-gating. Frequencies of the indicator signals can be expected to be within $f \approx [0, 0.2]\,\text{Hz}$ (compare chapter 9. Within a spatial voxel k, the filtered indicator signal $\Delta\rho_k(n)$ describes the change in density caused by the presence of indicator fluid.

The filtered MDCT indicator signals were approximated by a gamma variate model to suppress additional noise and to analyze and compare the model parameter values of each pulmonary circulation compartment. The gamma variate model consists of four parameters, two shape parameters α and β, a scaling factor g and the arrival time (in samples) of the indicator signal n_A:

$$\gamma(n) = g \cdot (n - n_A)^{\alpha} \cdot exp\left(-\beta(n - n_A)\right) \tag{8.2}$$

The model parameters α, β and g can be expressed by detectable signal features of the indicator signal $\Delta\rho_k(n)$. The dependency is derived in appendix A. For this purpose, five signal features were detected from each indicator signal k within the lung or one of the

important segmented blood volumes:

- indicator maximum $\Delta\rho_{max,k} = \max_n \Delta\rho_k$
- temporal sample of indicator maximum $n_{max,k} = \operatorname{argmax}_n \Delta\rho_k$
- maximal positive slope of indicator signal $\Delta\dot{\rho}_{max,k} = \max_n \frac{d\Delta\rho_k}{dn}$
- temporal sample of maximal positive slope $n_{s+,k} = \operatorname{argmax}_n \frac{d\Delta\rho_k}{dn}$
- temporal sample of indicator arrival $0 \stackrel{!}{=} T(n_{A,k})$

The function $T(n)$ describes the tangent to the point of the maximal slope of the indicator signal. The sample of the indicator arrival was estimated by a method described in [170]. The model parameters for each spatial voxel, besides $n_{A,k}$, were estimated using the identified features. The parameter α_k was estimated by:

$$\alpha_k = \frac{(n_{max,k} - n_{A,k})^2}{(n_{max,k} - n_{s+,k})^2} \tag{8.3}$$

The parameter β_k was set to:

$$\beta_k = \frac{n_{max,k} - n_{A,k}}{(n_{max,k} - n_{s+,k})^2} \tag{8.4}$$

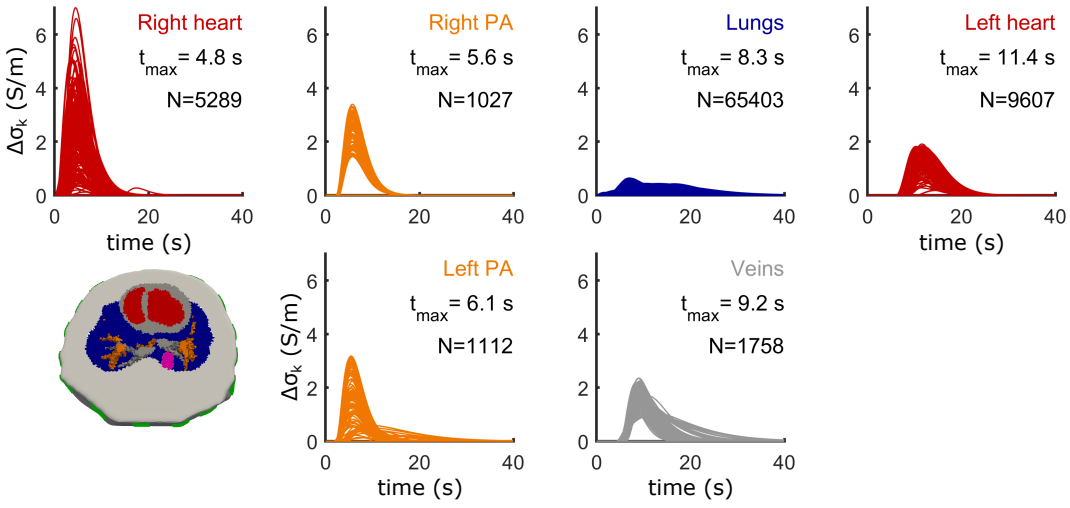

Figure 8.2: Overview of extracted and simulated indicator conductivity changes $\Delta\boldsymbol{\sigma}$ in S/m. The indicator signals are depicted for each individual pulmonary circulation compartment together with its mean TTP t_{max} and the number of participating elements. In the lower left image the segmented tissue and blood volumes are depicted.

Finally, the scaling factor g_k was calculated as a function of $\Delta\rho_{max,k}$ and the previously identified parameters α_k and β_k:

$$g_k = \left(\frac{\beta_k}{\alpha_k}\right)^{\alpha_k} e^{\alpha_k} \cdot \Delta\rho_{max,k} \tag{8.5}$$

The resulting extracted indicator signal for each voxel k within the segmented blood volumes or the lungs was described by its gamma variate model $\gamma_k(n)$. Up to this point, the model function was still a function of tissue density and had to be transformed to electrical conductivity. The indicator signal describes the amount of indicator bolus within a spatial element. It was assumed, that the spatial element k_{max} contains the indicator signal with an overall maximal amplitude, which corresponds to an element completely filled with indicator fluid. The electrically conductive indicators $\Delta\sigma_k(n)$ were created with the following approach:

$$\Delta\sigma_k(n) = \sigma_{indicator} \cdot \frac{\gamma_k(n)}{\gamma_{k_{max}}(n_{max,k_{max}})} \tag{8.6}$$

The electrical conductivity of the injected indicator bolus was set to $\sigma_{indciator} = 7.01\,\mathrm{S/m}$, which corresponds to saline solution with a concentration of 5 % NaCl [168]. The resulting EIT indicator signals are depicted for each compartment of the pulmonary circulation separately in Figure 8.2. For all k outside of the segmented blood volumes or the lungs, the dynamic indicator conductivity was set to $\Delta\sigma_k(n) = 0$.

Conductivity and electrode mapping Based on the voxel based static background label map containing the tissue labels of the organs or blood volumes and the corresponding tissue conductivities in Table 8.1, the background conductivity matrix $\boldsymbol{\sigma}_B$ was created. This matrix had the same size as the tissue label matrix. To simulate the dynamic scenario, the final conductivity matrix was defined by:

$$\boldsymbol{\sigma}(n) = \boldsymbol{\sigma}_B + (\Delta\boldsymbol{\sigma}(n) - \sigma_{B,k_{max}}) \tag{8.7}$$

The maximal conductivity over time was therefore 7.01 S/m.
The voxel based conductivites were mapped onto the tetrahedral mesh for all temporal sampling points n. For each tetrahedral mesh element, the mode of all tissue labels belonging to voxels fully enclosed by the tetrahedron was assigned as tissue label to the element. For simplicity, the spatial element index k will refer to the tetrahedral mesh element index in the following.
Besides the conductivity, the tissue label map indices were also mapped onto the tetrahedral mesh with the same approach. The resulting tetrahedral tissue label matrix is described by

Tissue	Blood	Myocardium	Lung (inflated)	Torso/Muscle tissue
σ_B in S/m	$7.03 \cdot 10^{-1}$	$2.15 \cdot 10^{-1}$	$1.07 \cdot 10^{-1}$	$3.62 \cdot 10^{-1}$

Table 8.1: Overview of the chosen tissue conductivities (S m^{-1}) at a stimulation frequency of $f_I = 100\,\mathrm{kHz}$ [158, 159]. For all segmented blood volumes, the conductivity of blood was chosen.

Blood volume	Right Heart	Right PA	Left PA	Right PA	Lung/PCB	Veins	Left Heart
Tissue label	1	2	3	4	5	6	7

Table 8.2: Overview of the tissue labels of matrix $\mathbf{L}_\mathrm{T}$

$\boldsymbol{L}_T \in \mathbb{N}^{K\times 1}$. Each element of the matrix contained a number representing a blood volume compartment participating in pulmonary circulation (as depicted in Table 8.2).
The segmented electrodes had to be mapped onto the surface of the simulation mesh as well. Instead of point electrodes, a more sophisticated electrode model was used, which introduces additional but realistic boundary conditions for the forward and inverse problem. The *complete electrode model* (CEM) was simulated for this purpose [78–80]. A mixed boundary condition (Dirichlet and Neumann) had to be solved at each electrode to consider the current density and potential distribution on the electrode surface [171]. To map the electrode surface of the segmented electrode voxels to the tetrahedral mesh, the inner normal surface of the segmented electrode was computed with *Matlab R2019a*. All surface nodes of the tetrahedral mesh within the normal projection of the inner electrode surface onto the torso surface were considered as electrode node.

Forward calculation The dynamic 3D EIT simulation was performed in adjacent stimulation and measurement mode, as it has been conducted with the CareFusion *Goe MF II* system. The injected current amplitude was set to $A_I = 4.43\,\mathrm{mA}$ and the stimulation frequency to $f_I = 100\,\mathrm{kHz}$. As described above, a CEM was used and the contact resistance was set to $R_{skin-electrode} = 100\,\Omega$. The forward simulation was performed for each temporal sampling point n with EIDORS [169]. The result of the forward simulation were the dynamic adjacent voltage measurements $\boldsymbol{V} = [\boldsymbol{v}(1),...,\boldsymbol{v}(n)] \in \mathbb{R}^{M\times N}$. Since 16 electrodes were used, the number of voltage measurements results in $M = 208$.
For small conductivity changes, the FEM forward calculation for each temporal sample n can be approximated by a matrix multiplication:

$$\boldsymbol{v}(n) = \mathbf{J}_{3D}(n)\cdot\boldsymbol{\sigma}(n) \tag{8.8}$$

The matrix $\mathbf{J}_{3D}(n) \in \mathbb{R}^{M\times K}$ describes the first-order forward simulation matrix for the temporal sample n.

EIT Reconstruction Normalized linear 2D EIT reconstructions were performed to compute a time series of 2D images of the conductivity changes as it is currently clinically performed. To reconstruct the 2D EIT images, a triangular mesh was created with *Matlab R2019a*. The mesh consisted of $H = 1598$ elements and 849 nodes. The mesh is depicted in Figure 8.3 alongside the 3D simulation mesh. The estimated spatio-temporal normalized conductivity changes are described by the matrix $\Delta\hat{\boldsymbol{\Sigma}} = [\Delta\hat{\boldsymbol{\sigma}}(1),...,\Delta\hat{\boldsymbol{\sigma}}(N)] \in \mathbb{R}^{H\times N}$. To reconstruct three different reconstruction approaches were chosen:

- **Tikhonov 0^{th} order** with reconstruction matrix $\boldsymbol{\Theta}_{T0} \in \mathbb{R}^{H\times M}$

- **Tikhonov 2nd order / Laplace** with reconstruction matrix $\mathbf{\Theta}_L \in \mathbb{R}^{H\times M}$
- **GREIT** with reconstruction matrix $\mathbf{\Theta}_{GREIT} \in \mathbb{R}^{H\times M}$

In general, the time variant conductivity changes in $\Delta\hat{\mathbf{\Sigma}}$ were computed by the multiplication of any of the above reconstruction matrices $\mathbf{\Theta} \in \mathbb{R}^{H\times M}$ and the linearized and normalized simulated voltage changes $\Delta\boldsymbol{V} = diag(\boldsymbol{v}(1))^{-1} \cdot [\boldsymbol{v}(1) - \boldsymbol{v}(1), ..., \boldsymbol{v}(N) - \boldsymbol{v}(1)] \in \mathbb{R}^{M\times N}$

$$\Delta\hat{\mathbf{\Sigma}} = \mathbf{\Theta} \cdot \Delta\boldsymbol{V} \tag{8.9}$$

The reference voltages for the linearization and normalization were defined by the first set of simulated voltage measurements $\boldsymbol{v}(n = 1)$ just before the injection of the indicator.

8.2.2 Analysis of contributions

The goal of the described dynamic EIT simulation was to investigate the contribution of each spatio-temporal contributing compartment of the pulmonary circulation, such as the heart chambers, the pulmonary arteries and veins, and the PCB. For each reconstructed element h, the relative amount of each compartment contributing to the reconstructed conductivity change $\Delta\sigma_h$ was analyzed.
We herefore define a multidimensional function $\mathscr{G}(n) : \Delta\boldsymbol{\sigma}(n) \in \mathbb{R}^{K\times 1} \rightarrow \Delta\hat{\boldsymbol{\sigma}}(n) \in \mathbb{R}^{H\times 1}$. This function projects the simulated 3D indicator related conductivity change $\Delta\boldsymbol{\sigma}(n)$ onto the 2D reconstructed conductivity change image $\Delta\hat{\boldsymbol{\sigma}}(n)$. The function $\mathscr{G}$ is derived in the following.

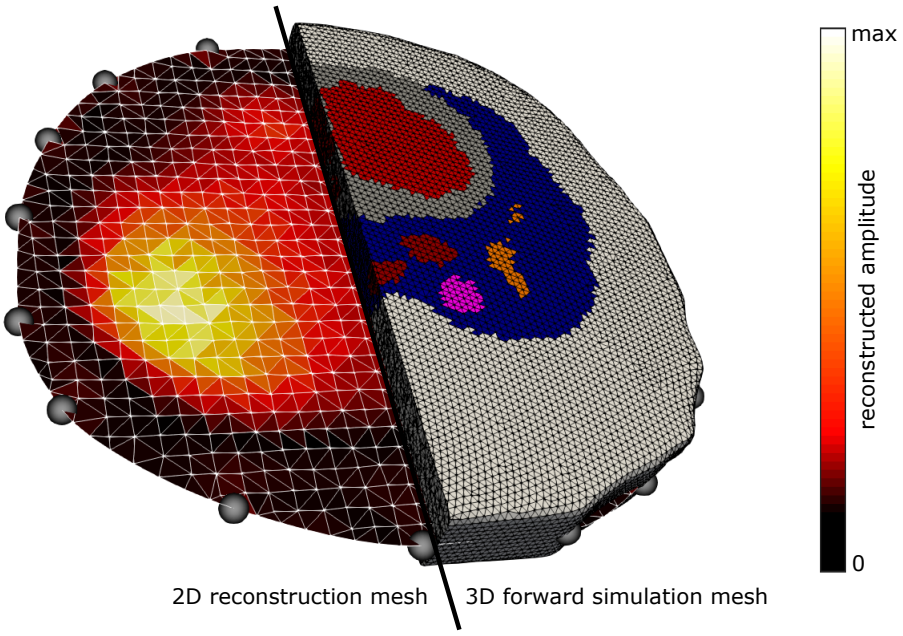

Figure 8.3: Joint depiction of reconstruction and forward simulation meshes. The coloring of the different segmented organ and blood volumes of the simulation mesh are the same as in Figure 8.1

The reconstructed EIT image $\Delta\hat{\boldsymbol{\sigma}}(n)$ of the n^{th} sampling point is related to the normalized voltage change $\Delta\mathbf{v}(n)$ by the general reconstruction matrix $\boldsymbol{\Theta}$:

$$\Delta\hat{\boldsymbol{\sigma}}(n) = \boldsymbol{\Theta} \cdot \Delta\boldsymbol{v}(n) \tag{8.10}$$

We can rewrite the normalized voltage difference and gain:

$$\Delta\hat{\boldsymbol{\sigma}}(n) = \boldsymbol{\Theta} \cdot diag\big[\boldsymbol{v}(1)\big]^{-1} \cdot \big[\boldsymbol{v}(n) - \boldsymbol{v}(1)\big] \tag{8.11}$$

The voltages were simulated and can thus be represented by the ground truth conductivity signal $\Delta\boldsymbol{\sigma}(n)$ and the linear approximation of the FEM EIT forward simulation $\mathbf{J}_{3D}(n)$:

$$\Delta\hat{\boldsymbol{\sigma}}(n) = \boldsymbol{\Theta} \cdot diag\big[\mathbf{J}_{3D}(1)\boldsymbol{\sigma}(1)\big]^{-1} \cdot \big[\mathbf{J}_{3D}(n)\boldsymbol{\sigma}(n) - \mathbf{J}_{3D}(1)\boldsymbol{\sigma}(1)\big] \tag{8.12}$$

If we consider the forward simulation matrix to be time invariant $\mathbf{J}_{3D}(n) = \mathbf{J}_{3D}(1) = \mathbf{J}_{3D}$, we can simplify the equation further to:

$$\begin{aligned} \Delta\hat{\boldsymbol{\sigma}}(n) &= \boldsymbol{\Theta} \cdot diag\big[\mathbf{J}_{3D}\boldsymbol{\sigma}(1)\big]^{-1} \cdot \big[\mathbf{J}_{3D}\boldsymbol{\sigma}(n) - \mathbf{J}_{3D}\boldsymbol{\sigma}(1)\big] && (8.13)\\ &= \boldsymbol{\Theta} \cdot \mathbf{F}_{\mathbf{norm}} \cdot \mathbf{J}_{3D} \cdot \Delta\boldsymbol{\sigma}(n) && (8.14) \end{aligned}$$

We chose the linear time invariant forward simulation matrix $\mathbf{J}_{3D}$ to the mean of all temporal Jacobians during the passage of the indicator:

$$\mathbf{J}_{3D} = \frac{1}{N}\sum_{n} \mathbf{J}_{3D}(n) \tag{8.15}$$

To simplify the equation, the voltage normalization was renamed to $\mathbf{F}_{\mathbf{norm}} = diag\big[\mathbf{J}_{3D}\boldsymbol{\sigma}(1)\big]^{-1}$. The usage of a time invariant approximation of the simulation matrix will introduce an error and a spatial smearing to the reconstructed image, since the indicator will appear in different compartments of the torso at different times and thus the spatial distribution of conductivity within the thorax will not be time variant. Nevertheless, we assume the error to be sufficiently small and make the assumption for simplification of the analysis.
From the final equation (8.14), we arrive at the function

$$\mathscr{G}(n) = \mathbf{G} = \boldsymbol{\Theta} \cdot \mathbf{F}_{\mathbf{norm}} \cdot \mathbf{J}_{3D} \in \mathbb{R}^{H \times K} \tag{8.16}$$

In order to investigate the contribution of different blood volumes to the reconstructed EIT image, binary masks $\mathbf{B} \in \mathbb{R}^{K \times 1}$ for the different blood volumes were defined based on the tissue label map $\mathbf{L}_T$. The definition of the mask is exemplary described for the right PA:

$$B_{rPA,k} = \begin{cases} 1 & \text{if } L_{T,k} = 2 \\ 0 & \text{otherwise} \end{cases} \tag{8.17}$$

With the binary mask, an EIT image was reconstructed, which does only result from the conductivity change within the right PA:

$$\Delta\hat{\boldsymbol{\sigma}}_{rPA}(n) = \mathbf{G} \cdot diag\,(\mathbf{B}_{\mathbf{rPA}}) \cdot \Delta\boldsymbol{\sigma}(n) \tag{8.18}$$

The relative contribution $\mathbf{rC}_{rPA,h}(n)$ of the right PA to element h of the reconstructed image was calculated by:

$$\mathbf{rC}_{rPA,h}(n) = \frac{\Delta\hat{\sigma}_{rPA,h}(n)}{\Delta\hat{\sigma}_{h}(n)} \tag{8.19}$$

In a variety of indicator based perfusion modalities, different features of the indicator dilution curve are analyzed. The maximal slope $\Delta\dot{\hat{\boldsymbol{\sigma}}}_{max}$, the area under the curve (AUC) $\Delta\hat{\boldsymbol{\sigma}}_{AUC}$ and the maximal amplitude $\Delta\hat{\boldsymbol{\sigma}}_{max}$ within a spatial element h are commonly exploited. While the maximal slope of an indicator curve can be related to the blood flow, the AUC is linked to the blood volume of a spatial element. For this reason, the relative contribution to the reconstructed feature images were analyzed in the following. Since $\mathbf{G}$ was approximated to be time invariant, we can calculate the features as follows:

$$\Delta\hat{\sigma}_{max,h} = G_{hk} \cdot \max_{n} \Delta\sigma_k \tag{8.20}$$

$$\Delta\dot{\hat{\sigma}}_{max,h} = G_{hk} \cdot \frac{d\Delta\sigma_k}{dn} \tag{8.21}$$

$$\Delta\hat{\sigma}_{AUC,h} = G_{hk} \cdot \sum_{n} \Delta\sigma_k \tag{8.22}$$

8.3 Results

At first, the different reconstructed indicator-enhanced EIT images are qualitatively compared to the indicator-MDCT ground truth. Afterwards, the relative contributions to the reconstructed EIT image of the different blood volumes participating in pulmonary circulation are investigated and compared between reconstruction approaches.

8.3.1 Comparison of EIT reconstruction approaches

In Figure 8.4 the different EIT reconstruction approaches are compared to MDCT. The rows depict the different indicator features, which were reconstructed. Based on the visual impression, the similarity between actual the simulated EIT reconstructions are high.

In the first row, the reconstructed AUC images for EIT and MDCT reconstructions are

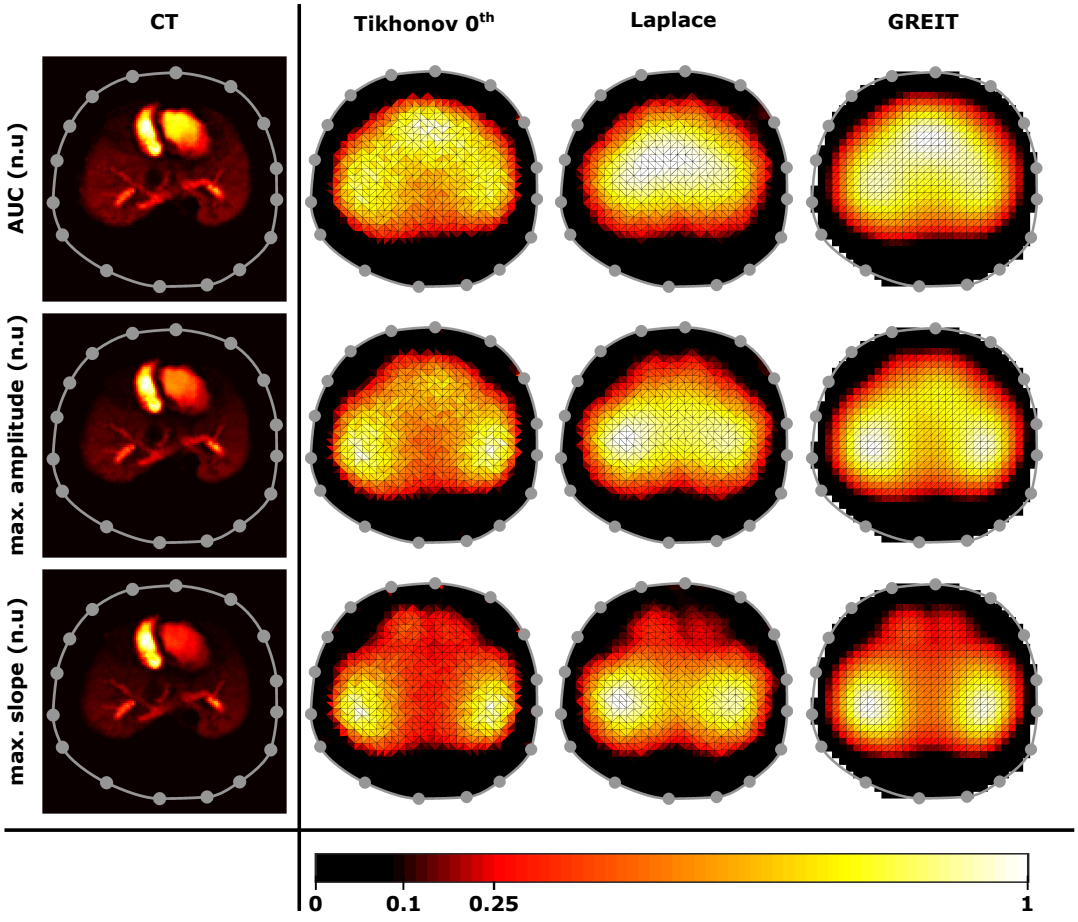

Figure 8.4: Comparison of the different EIT reconstruction approaches to MDCT. Important reconstructed indicator features, such as the maximal slope $\Delta\hat{\boldsymbol{\sigma}}_{max}$, the AUC $\Delta\hat{\boldsymbol{\sigma}}_{AUC}$ and the maximal amplitude $\Delta\hat{\boldsymbol{\sigma}}_{max}$ are compared to indicator MDCT features.

depicted. As defined in section 8.2.2, the AUC represents the area under curve of the indicator dilution curve and therefore enhances areas of larger blood volumes. The left heart within the AUC images was consistently more intense for both modalities compared to the maximal slope and the maximal amplitude images.
The Laplace regularization was not able to distinguish between heart and lung regions and smeared image components into the center of the image. EIT reconstruction with a Tikhonov regularization of 0^{th} order was able to reconstruct lung and heart regions nicely, yet showed patchy or noisy spatial behavior. The GREIT reconstruction results seem to represent a kind of compromise between the results from Thikonov and Laplace regularization. The heart and lung region were still distinguishable, yet amplitudes seemed to be slightly spatially smoothed with a stronger tendency towards the image center.
The middle row of reconstructed images depicts the maximum amplitude $\Delta\hat{\boldsymbol{\sigma}}_{max}$. The relative amplitudes within the heart region were smaller compared to the AUC images. The Laplace regularization lead to a shift of reconstructed amplitudes to the center again. The left heart, with a larger blood volume, seems to contribute more to the EIT images compared to the right heart volume.
The bottom row of images presents the maximal slope of reconstructed conductivity change. The right heart region was enhanced for all EIT reconstructions. Spatial smoothing of the images was again strongest for Laplace regularization, in accordance with the initial expectations. The GREIT reconstruction seemed to be a balanced solution between spatial smoothness and reconstructed detail.

8.3.2 Analysis of relative contributions to the reconstructed EIT image

Figures 8.5, 8.6 and 8.7 depict the relative contribution **rC** of the different participating blood volumes in pulmonary circulation on the reconstructed maximal slope image for the three different reconstruction algorithms. We present only the results for the analysis of the maximal slope reconstruction, since this feature is often and will be later used to estimate pulmonary blood flow. The top left image depicts the reconstructed feature image. The top right image shows the vertical projection of the segmented lung and heart region on the EIT reconstruction mesh. Between the heart and the lung region, an overlap region was considered. In very caudal regions, the overlap region defines lung regions, in very cranial area, heart region. The six lower plots depict the relative contributions **rC** to the EIT feature image of the individual blood volumes. Indicator within the lungs are responsible for the

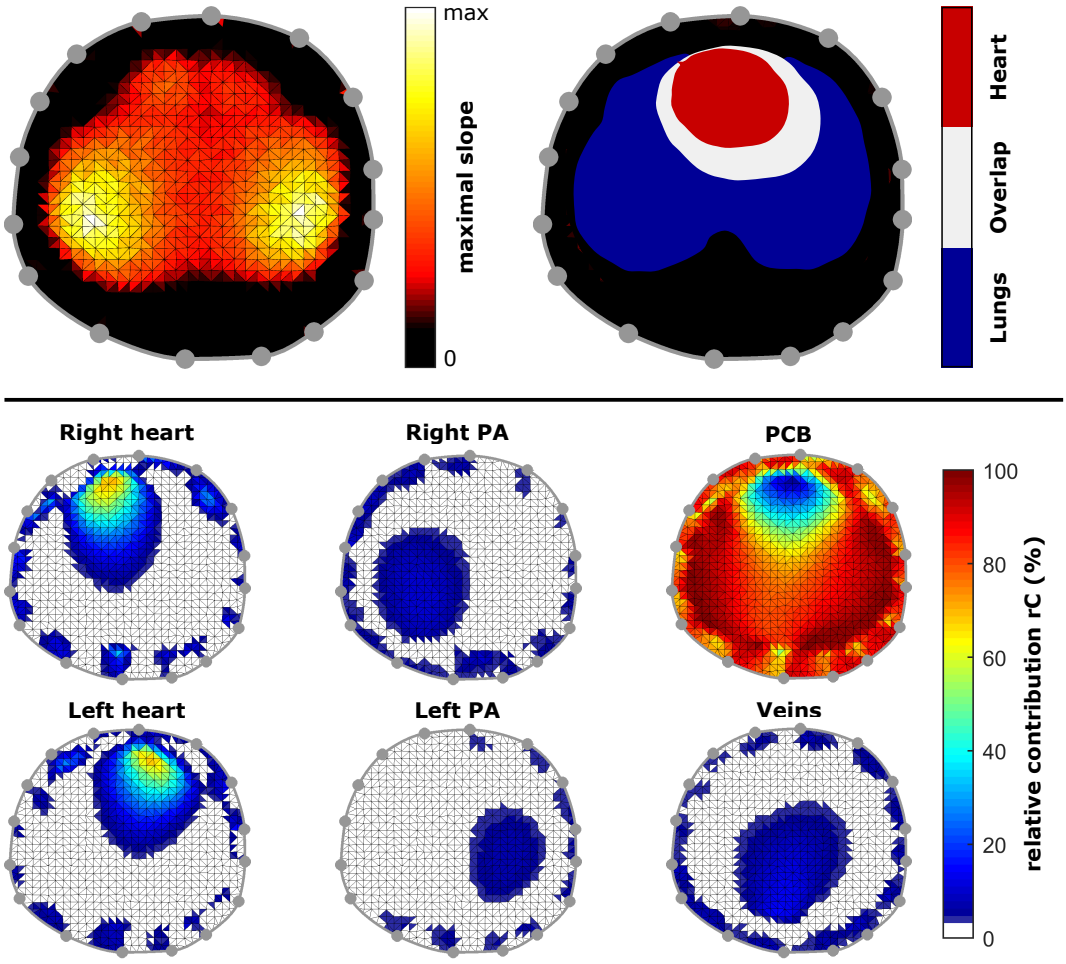

Figure 8.5: Relative contributions of participating blood volumes in pulmonary circulation on EIT maximal slope images for a Tikhonov regularization

largest amount of EIT maximal slope amplitude. The pulmonary arteries only contribute regionally with approximately around 10 % for all reconstruction algorithms. The blood volumes of the heart reach contribution values of approximately 60-70 %. Between the different reconstruction approaches, the relative contribution varied only very slightly. The deviating influence on the shape of the cardiac blood volumes seem to be the only major distinction between the three regarded reconstruction algorithms.

Table 8.3 depicts the contributions to the overall lung and heart region for the reconstructed maximal slope image. The lung region was defined by the vertical projection of the segmented lung volume on the reconstruction mesh. The heart region was equally projected. An overlap region was defined. The defined regions are depicted in the top right image of Figures 8.5, 8.6 and 8.7. In Table 8.3 we can observe the most important result from the described simulation study. Conductivity changes in three dimensional PCB compartments caused by simulated indicator passage had the largest influence on the lung regions of the reconstructed 2D EIT image. For 0^{th} Tikhonov and Laplace regularization we found a relative contribution

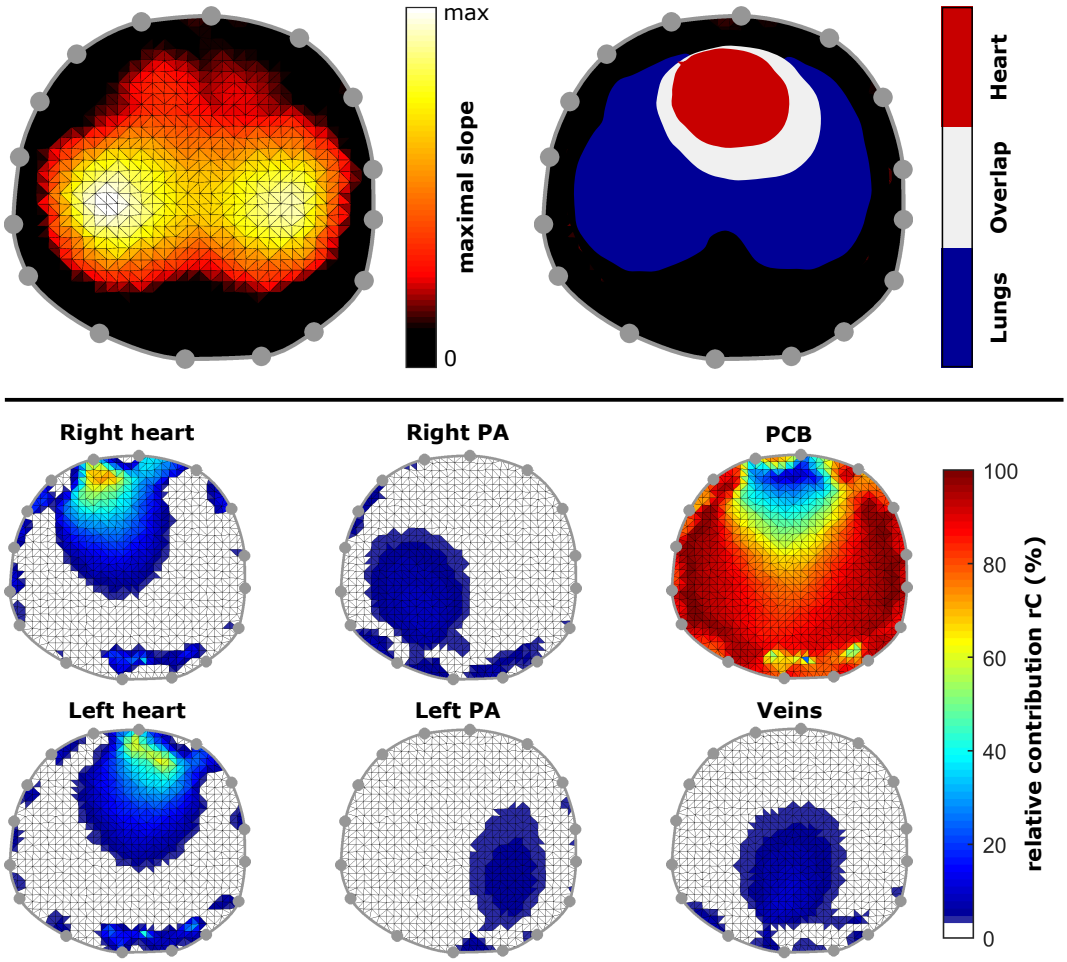

Figure 8.6: Relative contributions of participating blood volumes in pulmonary circulation on EIT maximal slope images for a Laplace regularization

$rC_{PCB} > 80\,\%$ of PCB compartments to the lung regions of the reconstructed EIT image. For the GREIT reconstruction the relative contribution was slightly less. The relative contribution of the pulmonary arteries to the lung regions of the reconstructed EIT image was $rC_{rPA+lPA} \leq 10\,\%$ for all reconstruction algorithms.

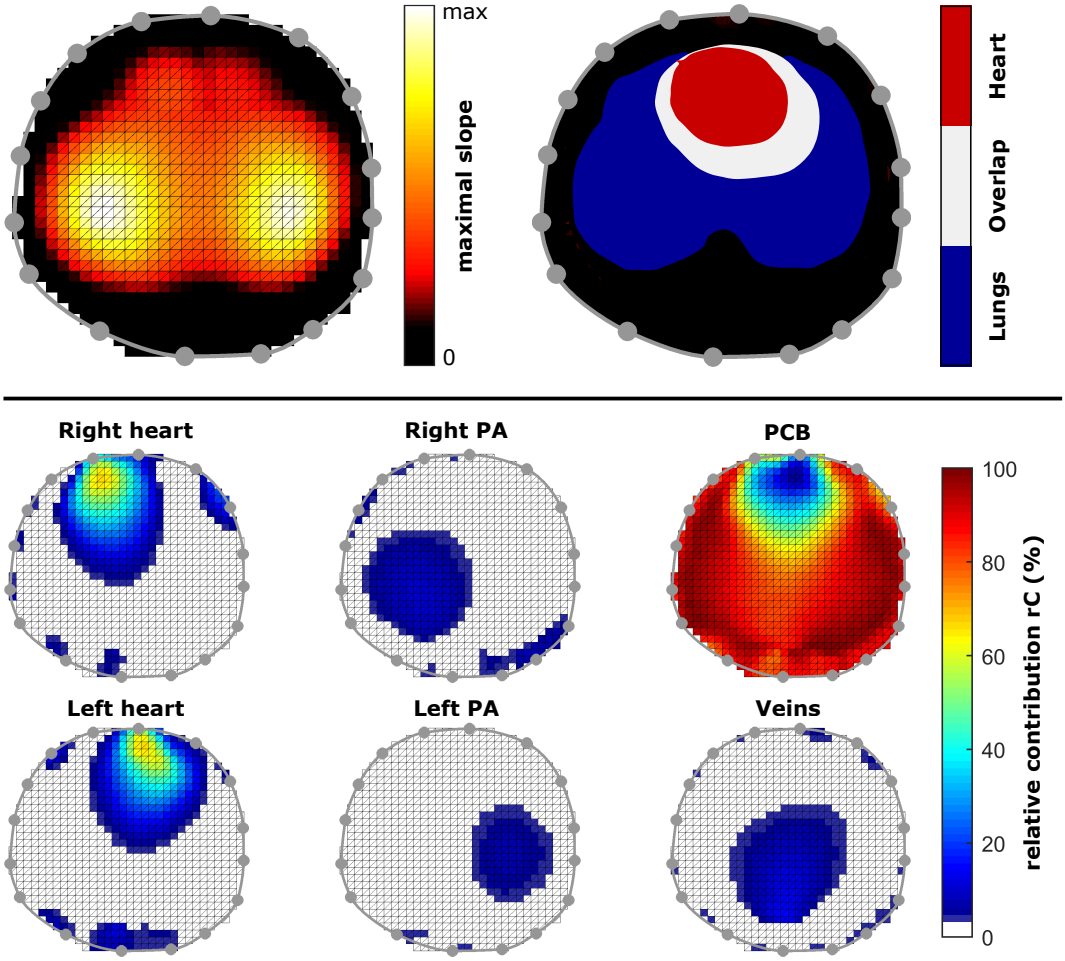

Figure 8.7: Relative contributions of participating blood volumes in pulmonary circulation on EIT maximal slope images for a GREIT reconstruction

8.4 Discussion

A comprehensive dynamic EIT indicator simulation study has been developed and conducted. To our knowledge, this is a novel analysis, since the relative amounts of contribution of the different 3D spatio-temporal compartments of the pulmonary circulation to the 2D EIT image have not yet been investigated. The approach to analyze the different contributors

Origin:	PCB	Left heart	Right heart	Right PA	Left PA	Veins
Tikhonov 0^{th} order						
Lung region	84.9	3.3	5.2	1.5	2.8	2.2
Heart region	40.0	26.6	30.3	0.6	1.1	1.4
Overlap region	60.7	18.1	16.8	1.4	1.1	1.9
Tikhonov 2^{nd} order (Laplace)						
Lung region	81.3	4.0	5.9	1.8	3.5	3.5
Heart region	48.9	22.2	24.0	1.1	1.5	2.3
Overlap region	64.1	15.9	13.5	1.9	1.7	3.0
GREIT						
Lung region	75.1	7.7	8.2	2.0	3.2	3.9
Heart region	73.9	8.2	12.7	0.4	3.0	1.8
Overlap region	64.2	15.1	14.3	1.3	2.0	3.1

Table 8.3: Contributions of different participants of the pulmonary circulation to the reconstructed maximal slope image.

to an reconstructed EIT image or image series has been also conducted by Proenca et al. [172]. They have investigated the different contributors to the pulsatility image by means of dynamic bio-impedance simulations. They have shown, that a strong contributor to the pulsatility images is the heart motion.

In a similar manner, we have simulated the dynamic propagation of an indicator through the pulmonary circulation system. The main finding of the study is, that larger blood vessels only contribute with very small amounts to the EIT image and to different feature images. This finding emphasizes, that indicator-enhanced EIT might be really valuable to assess PCB perfusion to investigate perfusion-ventilation relationships and regional gas exchange. Nevertheless, the larger blood vessels were only segmented down to approximately the third bifurcation. There exist multiple more vessels branching downstream, which do not contribute to gas exchange. These vessels could not be segmented and are therefore assigned to the PCB compartment. Yet, the information, that the main large blood vessels do not contribute substantially to the EIT perfusion image is of high clinical importance.

The MDCT imagse representing the basis of the dynamic EIT indicator simulation, were recorded during a PEEP of 5 mbar. At higher PEEP levels, the contribution of larger blood vessels might increase, since the PVR is increased and the capillary blood volume decreases.

When comparing the different considered EIT reconstruction algorithms, the Laplace regularization always showed a lower spatial resolution and was not able to distinguish between lungs and heart regions robustly. The Tikhonov 0^{th} order regularization qualitatively showed very good results, while GREIT seemed to be a very good trade off and might improve robustness in actual clinical measurements compared to Tikhonov regularization. We have not seen major differences between the considered reconstruction algorithms with respect to the contributions of different spatio-temporal compartments to the lung region. In the heart region, GREIT images contained substantially less contributions from the left and right

cardiac blood volume compared to the other reconstructions. We can not explain this finding so far and further research is needed.

Limitations The simulated conductivity indicator curves are based on the identified and extracted MDCT indicator signals. A major difference between the MDCT and the EIT indicator curve is caused by the viscosity of the indicator. Saline solution has a viscosity very similar to blood, while iodine has a higher viscosity. The pulmonary transit time as estimated with MDCT is expected to be higher than the one detected with EIT. In [173], a comparison between iodine and saline solution was conducted, which underlines this hypothesis. This finding also implies, that the indicator propagation through the pulmonary circulation presumably exhibits higher dispersion for MDCT than for EIT. This might also have a small influence on the assessment of relative contributions.
The study was only performed in a bio-impedance model created from a data set of only one porcine anatomy. To increase the statistical value, more simulations could be performed.

PART IV

METHODS TO OPTIMIZE PULMONARY BLOOD FLOW RECONSTRUCTIONS

Chapter 9

Indicator time series reconstruction

Parts of the developed algorithms in this chapter have been published [124, 142]. I was supported for the development of the described algorithms by multiple students, who published their work in Bachelor and Master theses [131, 134, 174].

9.1 Introduction

As described in chapter 3, the main challenge of EIT is to robustly reconstruct spatial conductivity changes from voltage measurements at n_E electrodes attached around the body surface. One major advantage of EIT is its potential to allow very high temporal sampling such that frame rates of $f_S = 50\,\text{Hz}$ can be achieved, which enables the analysis of fast physiological processes.

For the purpose of estimating spatial distributions of pulmonary blood flow, the image reconstruction describes the first main processing step after preprocessing of the measured voltages. The reconstruction approaches analyzed within this thesis and the necessary pre-

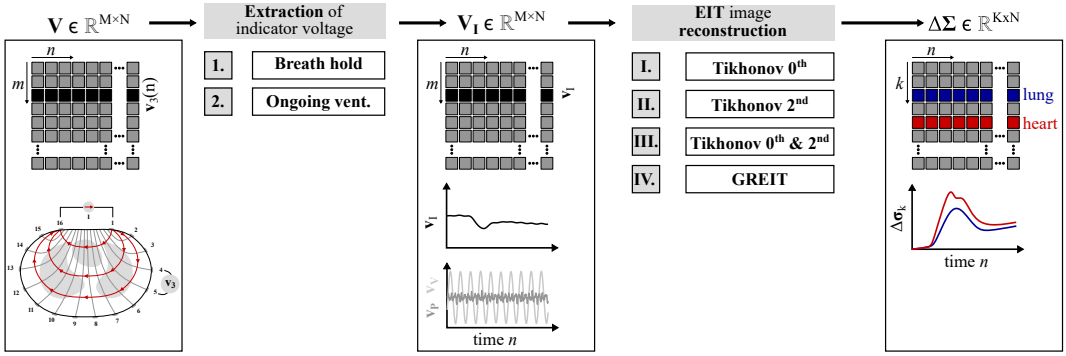

Figure 9.1: Schematic overview of the sequence of methods to reconstruct spatio-temporal conductivity changes.

processing will be introduced in this chapter. The conductivity signal analysis and perfusion parameter estimation forms the second necessary algorithmic step. This step is introduced in the next chapter. From dynamic $M = n_E \cdot (n_E - 3)$ voltage measurements $\mathbf{v}(n) \in \mathbb{R}^{M\times 1}$ between adjacent electrodes at $n = [1,N]$ temporal sampling points, the responsible spatial conductivity distributions $\boldsymbol{\sigma}(n) \in \mathbb{R}^{K\times 1}$ within discrete elements k of the body have to be reconstructed. As described within the fundamentals in chapter 3, for indicator-enhanced pulmonary blood flow reconstructions, it is sufficient to estimate regional conductivity change $\Delta\boldsymbol{\sigma}(n) \in \mathbb{R}^{K\times 1}$ originating from the passage of a proportion of the indicator bolus in front of an approximately static conductivity background $\boldsymbol{\sigma}_B \in \mathbb{R}^{K\times 1}$.
The sequential voltage measurement frames can be combined to form a single spatio-temporal voltage measurement matrix $\mathbf{V} \in \mathbb{R}^{M\times N} = [\mathbf{v}(1),...,\mathbf{v}(N)]$. This spatio-temporal matrix was the starting point of the described algorithm. The processing steps, with all considered alternatives, for the reconstruction of the conductivity changes $\Delta\boldsymbol{\Sigma} \in \mathbb{R}^{K\times N} = [\Delta\boldsymbol{\sigma}(1),...,\Delta\boldsymbol{\sigma}(N)]$ are schematically described in Figure 9.1.

The following chapter is meant to introduce the optimized EIT reconstruction approaches. A comprehensive comparison of all reconstruction approaches will be performed in chapter 12 using the data of the preclinical study in Dresden.

9.2 Separation of the different components comprised in EIT measurements

During the propagation of the indicator bolus through the pulmonary circulation, other dynamic physiological processes, change the regional conductivity within the torso and influence the voltage measurement as well. For EIT reconstruction, we need to solve a severely ill-conditioned problem. To improve the ill-conditioned problem, unnecessary signal components were removed, which might additionally complicate reconstruction. Thus, voltage changes, which exclusively originate from the propagation of the indicator bolus through the heart and lungs, were extracted prior to the EIT reconstruction (see first processing step in Figure 9.1). For the analysis in this thesis, we considered the following voltage signal model for the voltage measurement $\mathbf{v}(n)$ at time point n:

$$\mathbf{v}(n) = \mathbf{v}_I(n) + \mathbf{v}_V(n) + \mathbf{v}_P(n) + \mathbf{v}_B + \mathbf{e}(n) \tag{9.1}$$

The propagation of a hypertonic indicator bolus through the pulmonary circulation causes regional conductivity changes, which result in a measurable voltage $\mathbf{v}_I(n) \in \mathbb{R}^{M\times 1}$ between adjacent surface electrodes during an EIT recording. To estimate regional lung perfusion distributions with EIT, we reconstructed this voltage signal component with respect to the temporally static voltage $\mathbf{v}_B \in \mathbb{R}^{M\times 1}$ originating from the static conductivity background during the indicator-enhanced EIT measurement. Therefore we must identify and separate these signal components from all other additive signal parts.

The largest dynamic component $\mathbf{v}_V(n) \in \mathbb{R}^{M\times 1}$ of the overall signal $\mathbf{v}(n)$, which superimposes the indicator voltage component, originates from ventilation related conductivity changes. The periodic signal component is composed of frequencies within a narrow band width around the respiratory rate (RR) and its harmonics. Most of the performed EIT perfusion measurements, as described in chapter 5 and 6, have been conducted during breath hold phases. For these measurements, no lung aeration related voltage component existed ($\mathbf{v}_V(n) = 0 \; \forall \; n \in [1,N]$). Yet, during the preclinical study in Dresden, we investigated as well if respiratory hold phases could be avoided, which represents a stressful intervention for severely ill patients. Thus, the indicator bolus was additionally applied during ongoing mechanical ventilation for all included states. For these measurements, it was necessary to remove the voltage component $\mathbf{v}_V(n)$.
Besides the ventilation signal part, a pulsatile voltage $\mathbf{v}_P(n) \in \mathbb{R}^{M\times 1}$ caused by circulation related conductivity change (CRIC) can be observed. The origins of these pulsatile conductivity changes are manifold and a matter of research. The main contributors to the pulsatile signal are thought to be blood volume changes in distensible pulmonary vessels, heart and vessel movement and the reorientation of blood cells within the blood stream during a cardiac cycle [18]. Frequencies of the CRIC are located in a narrow bandwidth around the heart rate and its harmonics.
The final signal component $\mathbf{e}(n)$ describes the measurement noise, which we assumed to be sufficiently small, such that no explicit removal has been performed.
In Figure 9.2, the different voltage signal components are depicted for exemplary indicator injections during breath hold in plot (A) and during ongoing ventilation in plot (B). The approaches to extract the indicator component $\mathbf{v}_I(n)$ during breath hold and during ongoing ventilation are described in the following paragraphs.

Extraction of $\mathbf{v}_I(n)$ for measurements during breath hold phases For measurements during breath hold, only the pulsatile CRIC component needed to be removed. For this

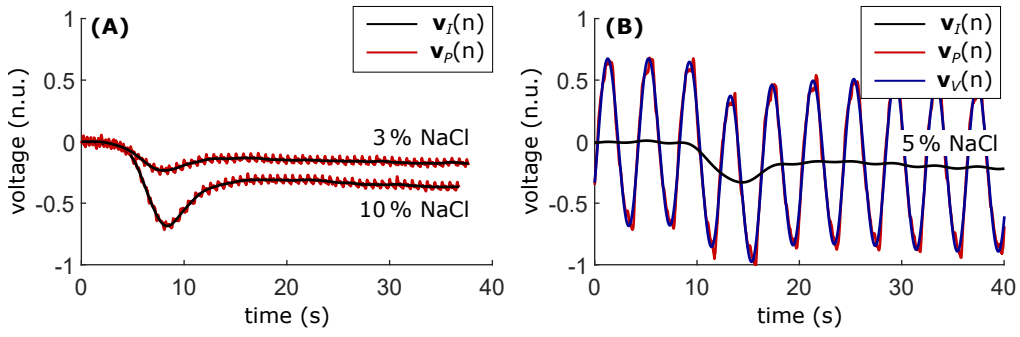

Figure 9.2: Signal components of an EIT voltage measurement during breath hold and during ongoing ventilation. Graph (A) shows the average voltage signal (mean over all voltages of a measurement frame) for measurements with different indicator concentrations during breath hold. Plot (B) depicts the averaged voltage for the injection of the indicator bolus during ongoing mechanical ventilation. The signal components have been separated from each other. The static background $\mathbf{v}_B(n)$ voltage has been removed.

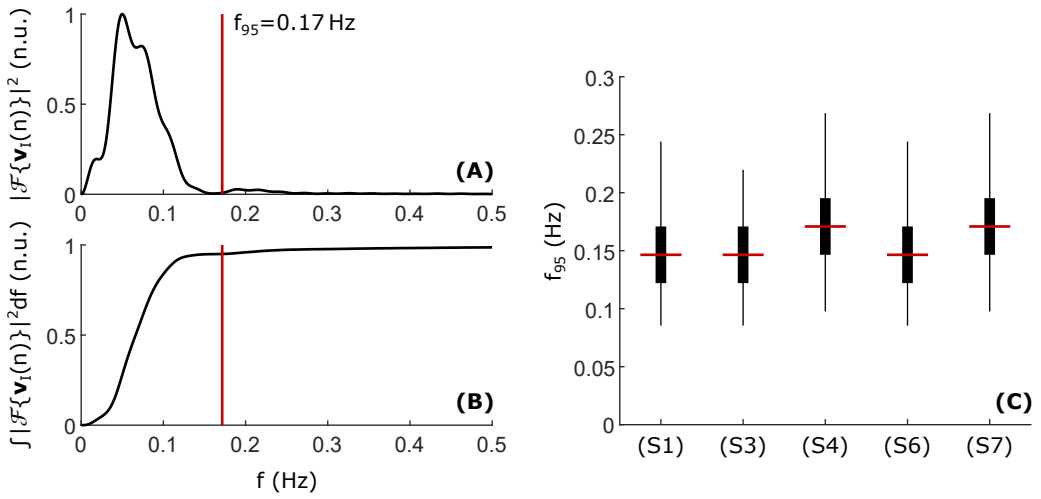

Figure 9.3: Analysis of the frequency bandwidth of the indicator component $\mathbf{v}_I(n)$. The graph in (A) shows the power spectral density (PSD) of an exemplary signal $v_m(n)$. The cumulative sum of the PSD is depicted in graph (B). The statistic of f_{95} in plot (C) was calculated for an indicator concentration of 5 % NaCl and was created by including all elements k and all animals of the preclinical study in Dresden (see chapter 5). The statistic was computed for each experimental state separately: (S1) uni-lateral ventilation; (S3) bi-lateral ventilation at an optimal PEEP; (S4) atelectatic/injured lung; (S6) bi-lateral ventilation at maximal PEEP; (S7) uni-lateral PA block. The graphs were created based on an analysis conducted during the research for a supervised Bachelor thesis [131].

purpose, we applied zero phase digital low pass filtering (forward-backward filtering) [175]. The cut off frequency of the filter was chosen to $f_{3dB} = 0.5\,\text{Hz}$, since we expected heart rates to be well above $0.5\,\frac{1}{s} \cdot \frac{60}{60} = 30\,\text{bpm}$ for humans as well as for pigs [176]. At the same time, the frequencies of the indicator signal component were found to be well below the cut off frequency. In graph (C) of Figure 9.3, boxplots of the f_{95} for measurements during breath hold phases and for the different experimental states of the Dresden study (see chapter 5) are depicted. The frequency f_{95} describes the spectral border below which 95 % of the total spectral power of $\mathbf{v}_I$ is located. The measure is also known as spectral edge frequency [177]. It was calculated by computing the power spectral density (PSD) $|\mathscr{F}\{\mathbf{v}_I(n)\}|^2$ and creating the cumulative sum of the PSD normalized to the total spectral power. The PSD of $\mathbf{v}_I(n)$ is depicted in graph (A) of Figure 9.3, the cumulative sum in plot (B). The statistic in plot (C) shows, that for all states of the Dresden study, the f_{95} was well below the cut off frequency of the low pass filter.

The filter was implemented by cascading second order infinite impulse response (IIR) filters with an overall order of 10. To minimize transient effects at the borders of the relatively short breath hold phase, the signal was symmetrically extended at extrema of the pulsatile signal component before filtering (as we have published in [125, 131]).

Extraction of $\mathbf{v}_I(n)$ for measurements during ongoing ventilation In case the indicator measurement was conducted during ongoing ventilation, the ventilation component $\mathbf{v}_V(n)$ had to be additionally removed. The difficulty in separating the indicator component from

the voltage originating from the cyclic aeration of the lungs during mechanical ventilation is, that typical RRs of mechanical ventilation can be as low as approximately 12 breaths per minute, since this is the lower limit of natural respiration rates of spoantaneous breathing in humans [31]. This minimal rate corresponds to a frequency of 0.2 Hz, thus, the spectrum of the ventilation component $\mathbf{v}_V(n)$ might overlap with the spectrum of the indicator component $\mathbf{v}_I(n)$. In ARDS patients however, respiratory rates are often increased (up to 35 breaths per minute) in order to prevent derecruitment during expiration by minimizing the time of the expiration and increasing intrinsic positive end-expiratory pressure (iPEEP) [178]. At the same time, tidal volume (V_T) can be decreased if respiratory rates are increased, reducing the risk of volutrauma [179]. If the spectra of the two voltage measurement components overlap, a frequency filtering will not be able to extract the indicator signal without deterioration. In these cases other more adaptive filtering techniques must be applied such as introduced in [180]. For this technique, a volume curve, which is perfectly synchronized to the EIT measurement must be known, which for the current ventilator and EIT devices is not always available. At the same time, the method relies on the solution of an additional ill-conditioned problem which might again introduce errors and instabilities.
For the described analyses within this thesis, we made the assumption, that for a future application of the indicator-enhanced EIT measurement during ongoing ventilation, the device might as well remind the physician to set the $RR \geq 15$ breaths per minute ($f_{Resp} = 0.25\,\text{Hz}$) during the indicator application. With this assumption, standard frequency filtering can be applied without altering the indicator component, since the spectral overlap of the signal components is substantially reduced. During the porcine study in Dresden, only $RR \geq 15$ breaths per minute were used for indicator applications during ongoing ventilation.
In order to remove the ventilation component by frequency filtering, the RR was detected from the averaged (global) voltage measurement $\bar{v}(n) \in \mathbb{R}$:

$$\bar{v}(n) = \frac{1}{M} \cdot \sum_{i=1}^{m} v_i(n) \tag{9.2}$$

Since the ventilation component contained the largest periodic signal amplitude, the RR could be detected by finding the frequency $f_{Resp} \in \mathbb{R}$ at the spectral maximum of $|\mathscr{F}\{\bar{v}(n)\}|$. The goal of the filtering was to remove the ventilation component sufficiently, while leaving the indicator component unchanged. For this reason the cutoff frequency f_{3dB} of the filter was adaptively set to:

$$f_{3dB} = \begin{cases} 0.75 \cdot f_{Resp} & \text{if } 0.75 \cdot f_{Resp} \geq 0.2\,\text{Hz} \\ 0.2\,\text{Hz} & \text{otherwise} \end{cases} \tag{9.3}$$

The minimal cutoff frequency was therefore defined by $f_{3dB} = 0.2\,\text{Hz}$, which allows a sufficient removal of the ventilation component, while maintaining the indicator component morphology. The filtering step was again performed by a 10^{th} order IIR-filter. Forward-backward filtering was applied, in order to avoid influencing the instantaneous phase of the indicator signal. The pulsatile signal $\mathbf{v}_P(n)$ was automatically removed as well, since the frequencies of this component are substantially larger and were suppressed by the low pass filter.

In both cases, the static background voltage $\mathbf{v}_B$ was defined as the mean over all temporal samples prior to the indicator injection.

9.3 Indicator reconstruction approaches

The separated voltage component $\mathbf{v}_I(n)$, resulting from the indicator passage through the pulmonary circulation, was subsequently reconstructed to obtain estimations of the dynamic conductivity changes for each spatial element k. For a potential clinical application of EIT perfusion, it is most likely, that linearized and normalized time difference (LNTD) reconstruction will be used. The difference reconstruction as well as the normalization improves robustness, if the exact torso shape and electrode positions are unknown exactly and a standard reconstruction model is used. For this reason, LNTD reconstruction was applied for all reconstructions in this thesis. We therefore normalized the spatio-temporal voltage measurement matrix $\mathbf{V}_I = [\mathbf{v}_I(1), ..., \mathbf{v}_I(N)]$ containing all measurement frames:

$$\Delta\mathbf{V} = diag(\mathbf{v}_B) \cdot \mathbf{V}_I \tag{9.4}$$

$\Delta\mathbf{V} \in \mathbb{R}^{M\times N}$ contained the M normalized voltage differences for all N temporal measurement frames. We reconstructed the normalized dynamic conductivity changes $\Delta\mathbf{\Sigma} \in \mathbb{R}^{K\times N}$ with on single matrix multiplication step:

$$\Delta\mathbf{\Sigma} = \mathbf{\Theta} \cdot \Delta\mathbf{V} \tag{9.5}$$

$\mathbf{\Theta} \in \mathbb{R}^{K\times N}$ describes the inverse reconstruction matrix. For the reconstruction of dynamic indicator dilution related conductivity changes, the choice of the reconstruction matrix $\mathbf{\Theta}$ has not yet been evaluated in any publication. In most of the publications referring to indicator-enhanced EIT spatial pulmonary perfusion estimation, the reconstruction algorithm has not even been described [19, 121]. Therefore, there is a lack of general understanding, which reconstruction approach works best and robust for pulmonary perfusion reconstruction. Four different LNTD reconstruction algorithms were therefore considered and compared in the following. The comparison was conducted using the data of the preclinical porcine study in Dresden and will be described in section 12.3.1. Since there is a vast amount of publications suggesting different regularization strategies and inversion approaches for EIT ventilation reconstruction (e.g. [78, 80, 84, 94, 181–184]), which might be suitable for perfusion reconstruction as well, the considerations leading to the choice of inversion strategies will be summarized in the following.

Considerations for the choice of reconstruction algorithms If we consider EIT as an imaging technique[1] with sufficient spatial resolution to distinguish between different sublobar regions of the lungs, we have to impose additional constraints to the solution of the

[1] We might also consider EIT as a monitor of e.g. eight larger volumes of interest. In [185], such an approach has been described. Their spatial resolution was limited to lobes of the lungs.

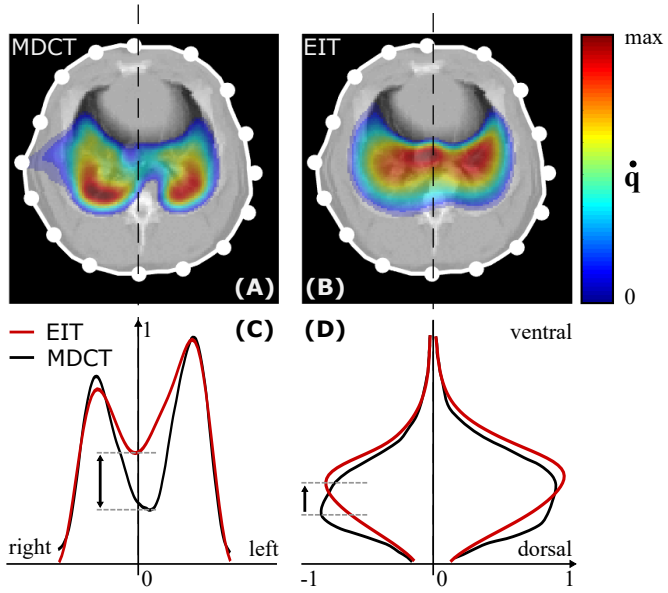

Figure 9.4: Exemplary spatial profiles of EIT and MDCT perfusion reconstructions. Image (A) displays the estimated perfusion distribution by MDCT $\dot{\mathbf{q}}_{CT}$. Image (B) depicts the estimation by EIT $\dot{\mathbf{q}}_{EIT}$. For both perfusion estimations, the maximal slope method has been used as introduced in chapter 10. For the EIT reconstruction, a Laplace regularization has been applied. Graph (C) shows the right-to-left profiles of the MDCT and EIT estimations and graph (D) presents the dorsoventral profiles. The arrows in graph (C) and (D) indicate the largest difference between both modalities.

reconstruction problem to stabilize the inverse solution. Ideally, we can find a regularization to constrain the solution, which does not further decrease spatial resolution and incorporates available *a-priori* information of the underlying spatio-temporal physiological process, in our case the indicator propagation through the pulmonary circulation. The temporal frequency band width of an indicator dilution curve is limited to low frequencies (see graph (C) of Figure 9.3). Spatially, the passage of the indicator dilution, as it can be monitored by EIT, can also be assumed to be smooth and rather a low frequency process, since the perfusion of the capillary bed is often described as continuous sheet of blood flow [26] and neighboring regions experience similar blood flow. In addition, EIT is limited to a rather low spatial resolution, which will most likely not allow to differentiate between element wise differences of blood flow. For these reasons, it seemed reasonable to impose spatial smoothness by incorporating the discrete Laplacian as regularization into the reconstuction. In Figure 9.4, an exemplary reconstruction of the Iowa study using the Laplace regularization is visualized (image (B)). In comparison to the MDCT perfusion reconstruction (image (A)), the EIT reconstruction resulted in slightly shifted spatial distributions towards the image center and towards more ventral parts of the lungs (compare results of chapter 7). This shift can be also observed in the profiles of the images in graphs (C) and (D). The cause for the shift might be manifold and will be discussed in chapter 11.

One possible explanation might be the applied spatial smoothing over larger regions and especially over organ and vessel boundaries. While in MDCT the highest perfusion in

the most dorsal regions of the lungs was detected, an EIT reconstruction comprising a Laplacian regularization might not be able to reconstruct this sharp transition in perfusion amplitude at the dorsal lung boundary due to the imposed spatial smoothness. Additionally, the differentiation between lung and pre-and post-lung phases might become more difficult, since the smoothing is not limited to the organ boundaries and often shifts reconstructed amplitudes into the center of the image [183]. This effect can be minimized, if *a-priori* knowledge about the underlying anatomy is available [183, 186]. Since this information is often not available or directly accessible in an ICU, we will only consider homogeneous backgrounds in the following.

To overcome the disadvantages of spatial smoothing, we also additionally applied a standard 0^{th} order Tikhonov regularization, which only limits large reconstructed image amplitudes. The standard Tikhonov regularization is known to shift reconstructed noise towards the torso boundary, since spatial EIT sensitivity is increasing with decreasing distance to the electrodes for adjacent current stimulation [93]. This often leads to noisy or patchy images and we have observed decreased robustness with this approach. Yet, image amplitudes are not smeared to the center of the image and we expect to be able to better visualize pulmonary perfusion close to the lung boundaries.

In previous publications, the Noser prior has also been recommended to improve image quality and robustness compared to 0^{th} order Tikhonov regularization [94]. The solution is regularized by incorporating the sensitivity distribution. Nevertheless, this regularization also tends to shift image amplitudes towards central regions. We introduce a similar approach, which uses the sensitivity distribution of EIT as weighting for a combined Thikhonov-Laplacian regularization to avoid noise sensitivity towards the torso boundary and prevent spatial smoothing in central regions.

In order to benchmark the reconstructions with a very commonly used reconstruction method, we also applied the GREIT reconstruction. All described approaches, including the new method are introduced in the following.

Tikhonov regularization For the two classes of Tikhonov type EIT reconstruction approaches, we estimated the spatio-temporal conductivity changes $\Delta\boldsymbol{\Sigma}$ by minimizing the following functional as introduced in chapter 3:

$$\Delta\boldsymbol{\Sigma} = \underset{\Delta\boldsymbol{\Sigma}}{\operatorname{argmin}} \left(\|\Delta\mathbf{V} - \mathbf{J}\Delta\boldsymbol{\Sigma}\|_{\mathbf{W}}^2 + \lambda \|\mathbf{R}\Delta\boldsymbol{\Sigma}\|^2 \right) \tag{9.6}$$

The nonlinear EIT forward operator $\mathscr{F}(\boldsymbol{\sigma})$ was always approximated by its Jacobian. The normalized Jacobian $\mathbf{J}$ was calculated using EIDORS [169]:

$$\mathbf{J} = \operatorname{diag}(\mathbf{v}_0)^{-1} \cdot \frac{d\mathscr{F}(\boldsymbol{\sigma})}{d\boldsymbol{\sigma}}\bigg|_{\boldsymbol{\sigma}=\boldsymbol{\sigma}_0} \tag{9.7}$$

For the reconstruction, a homogeneous background $\boldsymbol{\sigma}_0 = \sigma_0$[2] was assumed and the Jacobian was normalized to the corresponding forward calculated voltages $\mathbf{v}_0 \in \mathbb{R}^{M\times 1}$.

[2]It shall be hypothesized, that $\boldsymbol{\sigma}_0 \neq \boldsymbol{\sigma}_B$. Since in an ICU the actual conductivity background $\boldsymbol{\sigma}_B$ is usually not known, the conductivity background is assumed to be homogeneous with an arbitrary conductivity σ_0 for image reconstruction.

Additionally, we weighted the first norm with a diagonal matrix $\mathbf{W} \in \mathbb{R}^{M \times M}$. The matrix can be regarded as a measurement noise compensation. If all measurements M have an identical and uncorrelated measurement noise, the matrix can be chosen to the unit matrix $\mathbf{W} = \mathbf{I}$. For our reconstructions, we assumed uncorrelated measurement noise, but approximated the measurement noise by:

$$\mathbf{W} = \operatorname{diag}\left(\frac{\mathbf{v}_0}{\max \mathbf{v}_0}\right) \tag{9.8}$$

This weighting has been proposed used in other publications before (e.g. [95, 182].

For the reconstruction with a 0^{th} order Tikhonov regularization, the regularization matrix was chosen to the unit matrix $\mathbf{R} = \mathbf{I}$. The final reconstruction was performed by the Pseudoinverse or reconstruction matrix $\mathbf{\Theta}_{\text{T0}} \in \mathbb{R}^{K \times M}$:

$$\Delta\mathbf{\Sigma} = \left[\left(\mathbf{J}^\top \mathbf{W}\mathbf{J} + \lambda_{\text{T0}} \cdot \mathbf{I}\right)^{-1} \mathbf{J}^\top \mathbf{W}\right] \cdot \Delta\mathbf{V} \tag{9.9}$$

$$= \mathbf{\Theta}_{\text{T0}} \cdot \Delta\mathbf{V} \tag{9.10}$$

For the reconstruction with a 2^{nd} order Tikhonov or Laplacian regularization, the regularization matrix was chosen to unit matrix $\mathbf{R} = \mathbf{L}$. The discrete Laplacian $\mathbf{L} \in \mathbb{R}^{K \times K}$ was calculated by EIDORS [169]. The reconstruction matrix $\mathbf{\Theta}_{\text{L}} \in \mathbb{R}^{K \times M}$ was finally defined as:

$$\Delta\mathbf{\Sigma} = \left[\left(\mathbf{J}^\top \mathbf{W}\mathbf{J} + \lambda_{\text{L}} \cdot \mathbf{L}^\top \mathbf{L}\right)^{-1} \mathbf{J}^\top \mathbf{W}\right] \cdot \Delta\mathbf{V} \tag{9.11}$$

$$= \mathbf{\Theta}_{\text{L}} \cdot \Delta\mathbf{V} \tag{9.12}$$

For all studies and reconstructions, the parameters λ_{T0} and λ_{L} controlled the amount of regularization and were always chosen by maximizing the curvature of the L-curve, as proposed by Hansen et al. [90].

Novel sensitivity weighted combination of Tikhonov 0^{th} and 2^{nd} order As we have discussed above, the Laplace regularization stabilizes the EIT reconstruction and increases robustness substantially. Nevertheless, the imposed smoothing, especially over organ boundaries, reduces the image quality and resolution, by pushing image amplitude to central regions of the lungs and towards the center of the thorax. This might especially complicate the removal of pre- and post-lung phases, in order to extract pulmonary perfusion (introduced in the next chapter). A 0^{th} order Tikhonov regularization however pushes noise to the boundary and we generally hypothesize, that equal robustness can not be achieved. Cheney et al. [94] proposed to improve 0^{th} order Tikhonov regularization by considering the sensitivity distribution $\mathbf{J}$ and minimizing the functional:

$$\Delta\mathbf{\Sigma} = \left[\left(\mathbf{J}^\top \mathbf{W}\mathbf{J} + \lambda \cdot \mathbf{P}\right)^{-1} \mathbf{J}^\top \mathbf{W}\right] \cdot \Delta\mathbf{V} \tag{9.13}$$

with $\mathbf{P} \in \mathbb{R}^{M \times 1}$ being a diagonal matrix with the entries $P_{k,k} = \left[\mathbf{J}^\top \mathbf{J}\right]_{k,k}$. This regularization improves the noise sensitivity at the boundary compared to 0^{th} order Tikhonov regularization.

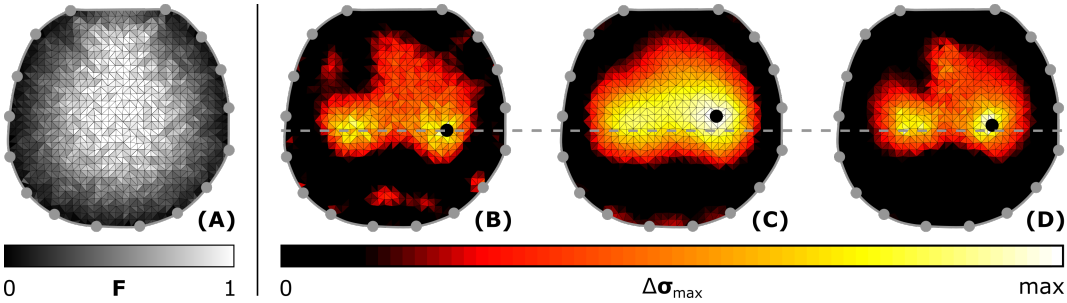

Figure 9.5: Graphical motivation for novel sensitivity weighted combination of different regularization approaches. The weighting matrix $\mathbf{F}$ is depicted in image (A). Image (B) depicts the temporal maximum conductivity change $\Delta\boldsymbol{\sigma}_{max} = \max_n \Delta\boldsymbol{\sigma}(n)$ for a 0^{th} order Tikhonov regularization. Image (C) depicts the maximum reconstructed image amplitude for a Laplace regularization and image (D) the reconstruction for the combined regularization approach. The • dots represent the center of perfusion for the left lung. The – – line indicates the dorsoventral position of the reconstructed perfusion center of the 0^{th} order Tikhonov regularization.

Yet, since we did not include anatomical background information, we could not improve reconstruction quality, since the reconstructed image was again compressed towards the center.

Yet, the idea of incorporating the sensitivity into regularization seemed valuable, since especially in a porcine geometry, the lungs and the heart are located very centrally in the thorax. In swine, a substantial distance between the lung volume and the (especially dorsal) electrodes exists, and we experience a large sensitivity gradient from the boundaries to central regions. We opted for an approach, which incorporated the sensitivity as spatial weighting of the regularization. In a way, we implemented a spatially variant regularization parameter λ. In very sensitive regions towards the boundaries, we wanted to allow spatial smoothing, in order to stabilize the solution and overcome the noise sensitivity of a pure 0^{th} order Tikhonov regularization. Towards the center of the image, the influence of spatial smoothing should be prevented. Thus, we combined 0^{th} order Tikhonov and Laplace regularization by a weighting matrix based on the local absolute sensitivity. The weighting matrix was a diagonal matrix $\mathbf{F} \in \mathbb{R}^{K\times K}$, with diagonal entries [184]:

$$f_k = \left(\sum_{m=1}^{M} J_{mk}^2 \right)^{-\frac{1}{2}} = \left[\mathbf{J}^\top \mathbf{J} \right]_{k,k}^{-\frac{1}{2}} \tag{9.14}$$

The diagonal matrix was created from all diagonal entries $\mathbf{f} = [f_1, ..., f_K] \in \mathbb{R}^{K\times 1}$, which were normalized to achieve entries of the weighting matrix within the interval $[0, 1]$:

$$\mathbf{F} = \operatorname{diag}\left(\frac{\mathbf{f} - \min_k(\mathbf{f})}{\max_k(\mathbf{f}) - \min_k(\mathbf{f})} \right) \tag{9.15}$$

The sensitivity based weighting matrix $\mathbf{F}$ is shown in image (A) of Figure 9.5.

To solve the inverse problem with the introduced combined regularization approach, the

following objective function was minimized:

$$\Delta\boldsymbol{\Sigma} = \underset{\Delta\boldsymbol{\Sigma}}{\operatorname{argmin}} \left(\|\Delta\mathbf{V} - \mathbf{J}\Delta\boldsymbol{\Sigma}\|^2_{\mathbf{W}} + \mathbf{F} \cdot \lambda_{\mathrm{T0}} \|\Delta\boldsymbol{\Sigma}\|^2 + (\mathbf{I} - \mathbf{F}) \cdot \lambda_{\mathrm{L}} \|\mathbf{L} \cdot \Delta\boldsymbol{\Sigma}\|^2 \right) \tag{9.16}$$

The matrix $\mathbf{F}$ weights the first 0^{th} order Tikhonov regularization term, while the Laplace component is weighted by $\mathbf{I} - \mathbf{F}$. Since all regularization matrices are symmetric, we can also interpret the spatial weighting as weighted norm:

$$\Delta\boldsymbol{\Sigma} = \underset{\Delta\boldsymbol{\Sigma}}{\operatorname{argmin}} \left(\|\Delta\mathbf{V} - \mathbf{J}\Delta\boldsymbol{\Sigma}\|^2_{\mathbf{W}} + \lambda_{\mathrm{T0}} \|\Delta\boldsymbol{\Sigma}\|^2_{\mathbf{F}} + \lambda_{\mathrm{L}} \|\mathbf{L} \cdot \Delta\boldsymbol{\Sigma}\|^2_{(\mathbf{I}-\mathbf{F})} \right) \tag{9.17}$$

The objective function is minimized by the reconstruction matrix $\boldsymbol{\Theta}_{\mathrm{T0-L}} \in \mathbb{R}^{K \times M}$, describing the mapping as:

$$\Delta\boldsymbol{\Sigma} = \left[\left(\mathbf{J}^\top \mathbf{W} \mathbf{J} + \lambda_{\mathrm{T0}} \cdot \mathbf{F} + \lambda_{\mathrm{L}} \cdot \mathbf{L}^\top (\mathbf{I} - \mathbf{F}) \mathbf{L} \right)^{-1} \mathbf{J}^\top \mathbf{W} \right] \cdot \Delta\mathbf{V} \tag{9.18}$$

$$= \boldsymbol{\Theta}_{\mathrm{T0-L}} \cdot \Delta\mathbf{V} \tag{9.19}$$

To finding optimal regularization parameters λ_{L} and λ_{T0}, the intuitive and most likely optimal approach would be to maximize the curvature of a 2D L-curve as e.g. proposed in [187]. Nevertheless, we opted for a simpler approach to test the feasibility. The regularization parameters were individually optimized by two L-curves, waiving one of the regularization terms. More robust λ choices could be generated with this approach, though there might be an even more ideal choice for regularization parameters. We have to mention, that the separation of the Laplace and 0^{th} order Tikhonov regularization parameter was only possible, since the norms of both regularization terms were similar $\lambda_{\mathrm{L}} \cdot \|\mathbf{L} \cdot \Delta\boldsymbol{\Sigma}\|_{\mathrm{fro}} \approx \lambda_{\mathrm{T0}} \cdot \|\Delta\boldsymbol{\Sigma}\|_{\mathrm{fro}}$. The operator $\|\cdot\|_{\mathrm{fro}}$ describes the Frobenius norm [188]. Otherwise, the regularization terms would need to be additionally weighted by their respective norms or optimal regularization parameters could be optimized by a 2D L-curve.
An comparison of reconstructions using 0^{th} order Tikhonov (image (B)), Laplace (image (C)) and the novel combined regularization (image (D)) are depicted in Figure 9.5. The combined approach stabilized the reconstruction, but also prevented the shift of reconstructed amplitudes to more ventral and more central regions.

GREIT The final reconstruction approach was the GREIT reconstruction algorithm. The description and motivation of the algorithm can be found in section 3.1.3. The algorithm can be regarded as a trained normalized and linearized reconstruction as the ones described above. Prior to the actual reconstruction, the reconstruction matrix $\boldsymbol{\Theta}_G$ was optimized to a set of small training targets (≈ 0.05 of torso diameter) for each reconstruction mesh. The desired reconstruction of these targets was set with desired reconstruction properties. The properties were set as recommended in [93]:

- reconstructed target radius: 20 % of the torso radius (for all targets at any position). Within this radius the amplitude was set to 1.

- amplitude outside of this radius were set to 0 to suppress ringing.
- noise figure (NF) was set to 0.5

Based on these desired image properties, the reconstruction matrix $\mathbf{\Theta}_G$ was explicitly defined, as described in section 3.1.3.

Chapter 10

Estimating spatial distributions of indicator based blood flow

The algorithms described in this chapter have been partly published in journal articles and conference contributions [125–127, 142]. The development of the described algorithms was partly supported by students, researching for their Bachelor theses [129, 130, 133].

10.1 Introduction

Spatial perfusion parameters were estimated from the reconstructed temporal indicator time curves of matrix $\Delta\mathbf{\Sigma}$ (as explained in the previous chapter). Multiple processing steps have been performed to estimate a spatial perfusion surrogate from the initial indicator time curves. An overview of the applied processing steps is depicted in Figure 10.1. Initially, a superimposed slow temporal drift needed to be removed to recover the pure first-pass indicator signal. After the drift component had been removed, surrogates of regional pulmonary perfusion were estimated by two different approaches and the indicator passage phases, which do not correspond to pulmonary perfusion, were removed.

10.2 Methods

10.2.1 Extraction of first-pass indicator signals

The pulmonary blood circulation related parameters such as pulmonary blood flow (PBF) were estimated from the reconstructed temporal indicator signal matrix with normalized conductivity differences $\Delta\mathbf{\Sigma} \in \mathbb{R}^{K\times N}$. The k^{th} row of this matrix contains the temporal signal $\Delta\sigma_k(n)$ of the discrete spatial element k representing the local dynamic normalized conductivity change after a central venous injection of a conductive saline indicator (see Figure 10.2). This signal can be described by the following model:

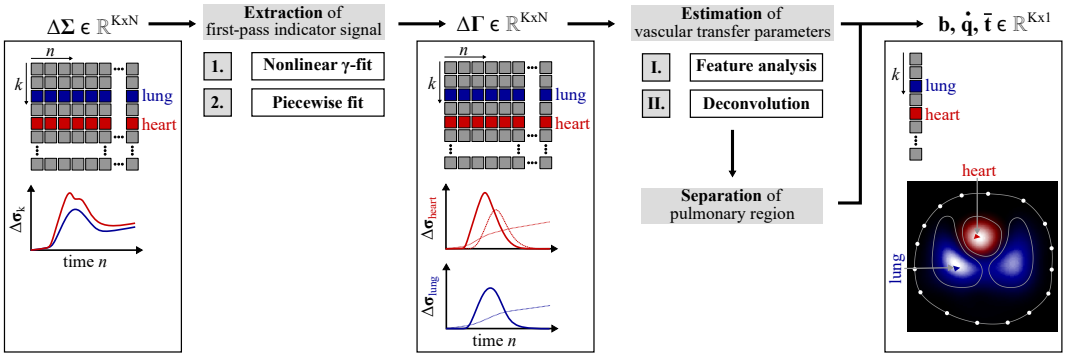

Figure 10.1: Schematic overview of the sequence of methods to estimate spatial distributions of vascular transfer parameters.

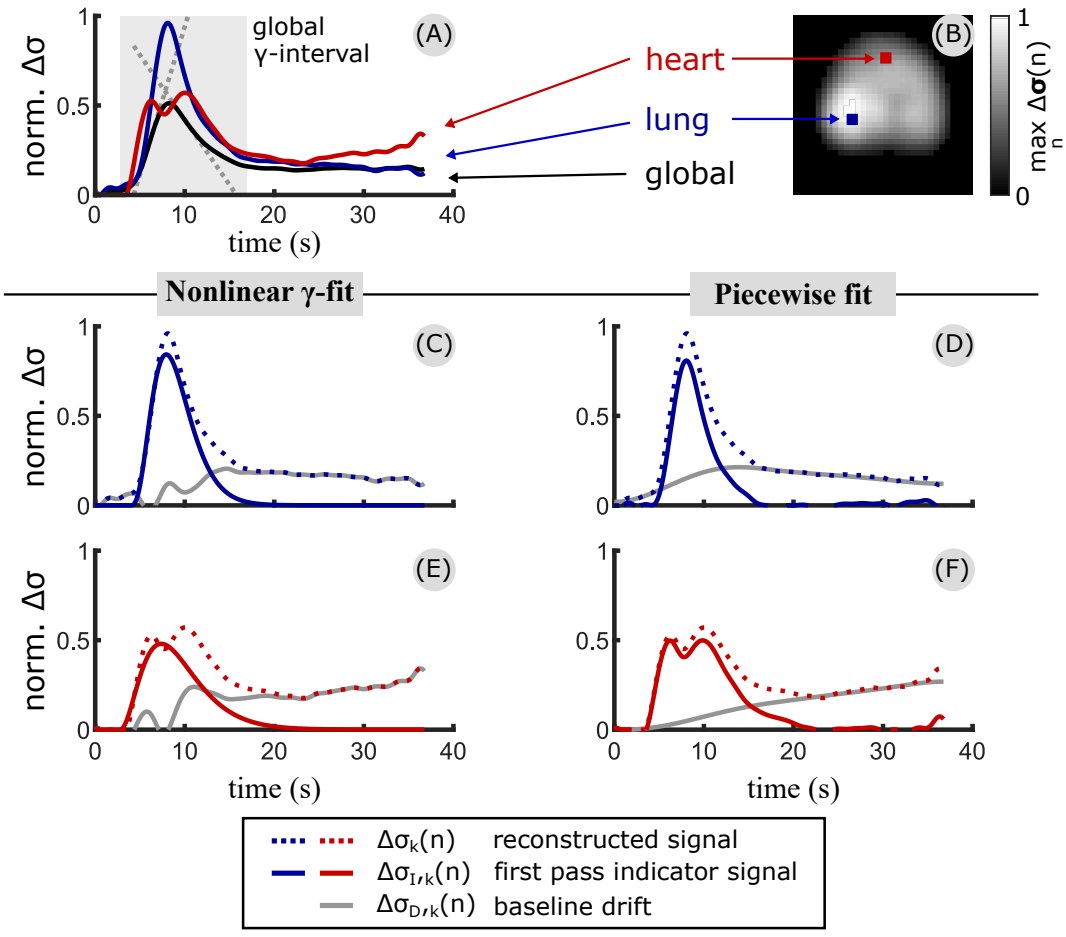

Figure 10.2: Exemplary normalized conductivity difference signal of the k-th spatial element $\Delta\sigma_k(n)$. The signal was taken from the preclinical animal study in Dresden and depicts the conductivity change after the injection of a 10 ml bolus containing a 5% NaCl solution.

$$\Delta\sigma_k(n) = \gamma_k(n) + d_k(n) + e_k(n) \tag{10.1}$$

The first signal component $\gamma_k(n)$ models the first passage of the indicator though the pulmonary circulation, which needs to be extracted for parameter estimation. The second component $d_k(n)$ represents a superimposed baseline drift. This drift has been described before by three different physiological processes: Over a long time sequence of EIT measurements, the baseline of recorded voltage signals commonly slowly decreases, which leads to a slow increase in global conductivity. This effect is most likely because of decreasing contact resistances between the skin and the measuring electrodes due to perspiration and transpiration [189]. Nevertheless, during a single first-pass indicator dilution measurement of approximately $30-40\,\mathrm{s}$ duration, this very slow conductivity increase might not have a strong impact on the measurement. Nevertheless, a linear increase of conductivity during the indicator measurement is often observed, if the measurement is performed during a respiratory hold phase or apnoe phase (see Figure 10.2). It has been proposed, that this increase in conductivity might be linked to pulmonary oxygen uptake [190]. A third and strongest contribution to the observed baseline drift could originate from leakage or diffusion of the conductive saline indicator into the surrounding tissue of the vasculature within the respective spatial compartment. This explanation has been previously used in literature for dynamic contrast agent enhanced magnetic resonance imaging (MRI) measurements [191, 192]. We therefore assume that a proportion of the indicator passing through a measurement compartment remains within this area after the injected indicator bolus continued on downstream.
The baseline drift has to be removed in order to extract the first-pass indicator signal. In previous publications the drift was either not accounted for or only a straight line was used as a drift model. In this thesis, two different more sophisticated approaches were developed making different assumptions, the nonlinear γ-fit and the piecewise fit.

Identification of the *global γ-interval* To simplify the extraction of the first pass signal, the *global γ-interval* $[n_A^\circ, n_E^\circ]$ with $n_A^\circ, n_E^\circ \in [1, N]$ containing the first passage of the indicator in the spatially averaged or global signal $\Delta\bar{\sigma}(n) = \frac{1}{K}\sum_{k=1}^{K}\Delta\sigma_k(n)$ was identified. The left border of the interval n_A° approximates the arrival time of the indicator globally, the right interval limit n_E° the time when the averaged indicator has completely left the measurement compartment. The interval borders were estimated based on the intersecting tangent method which has been described for the detection of arrival times of pulse waves [170]. Briefly, to estimate the arrival time n_A°, a tangent through the point with the maximal positive derivative is calculated. The temporal sample of the intersection point n_{xl} of the tangent with the x-axis was calculated. For the right border n_E° of the *global γ-interval*, the procedure is repeated with a tangent trough the point with the maximal negative derivative resulting in the temporal sample n_{xr} of the intersection point of the tangent with the x-axis. The right border limit of the interval was finally set to $n_E^\circ = n_{xr} + 0.1\cdot(n_{xr} - n_{xl})$ and the left border to $n_A^\circ = n_{xl} - 0.1\cdot(n_{xr} - n_{xl})$. It was assumed that the indicator signals in each spatial element appear within the global γ-interval. For this reason the right border of the interval was increased to account for regional compartments with strong dispersion. The left border was

equally decreased to ensure that indicator signals of regional compartments with an early indicator appearance such as the right heart are fully comprised by the defined interval. The increase (decrease) was hereby chosen empirically to 0.1. An exemplary global signal is shown together with the tangents and the identified global γ-interval in Figure 10.2 (A).

Nonlinear γ-fit In many previous MRT, CT, echocardiographic or optical indicator dilution studies, a model was fitted to recorded indicator dilution curves in order to remove the disturbing recirculation or drift signal and measurement noise. The most common and widely used signal model in indicator dilution imaging modalities is the gamma variate $\gamma(t)$ [117, 118, 193]. The model is motivated stochastically and physically in [116]. The first passage indicator component of the k-th spatial element $\gamma_k(n)$ in equation 10.1 was modeled with such a gamma variate function:

$$\gamma_k(n) = g_k \cdot (n - n_{A,k})^{\alpha_k} e^{-\beta_k (n - n_{A,k})} \tag{10.2}$$

The model is described by two shape parameters $\alpha_k, \beta_k \in \{\mathbb{R} | \alpha_k, \beta_k > 0\}$, an amplitude $g_k \in \{\mathbb{R} | g_k > 0\}$ and the arrival time sample of the indicator entering the k-th spatial element $n_{A,k} \in \{\mathbb{R} | n_A^\circ \leq n_{A,k} \leq n_E^\circ\}$.
In a previous indicator-enhanced EIT study [19] the gamma variate $\gamma_k(n)$ was fitted to the reconstructed conductivity signal $\Delta\sigma_k(n)$ within a small time window from the start of the indicator dilution curve until its maximum. This restriction prevented misfits due to the drift component. Afterwards features of the first pass curve were extracted to estimate pulmonary blood circulation related parameters. Since the recirculation drift was not considered during the fitting process, the resulting features are altered due to the influence of the superimposed drift. We therefore propose to extend the model to integrate the drift into the fitting process. In order to account for the simultaneously occurring superimposed drift, the model is extended by two additional components including two additional parameters. The final estimation of the overall signal was performed with the following model:

$$\Delta\tilde{\sigma}_k(n) = \gamma_k(n) + \kappa_k \sum_{\tau=1}^{n} \gamma_k(\tau) + m_k \cdot n \tag{10.3}$$

The first additional component models the remaining proportion of the indicator within the measurement compartment k by the cumulative sum of the first pass indicator signal. The integral component introduces one additional weighting parameter $\kappa_k \in \mathbb{R}$. The steady conductivity increase during a measurement for example due to oxygen uptake during a respiratory hold phase was considered by a straight line with a slope of $m_k \in \mathbb{R}$.

The final model is a highly nonlinear function with six parameters. The fitting has to be performed in each spatial element k. To increase the fitting success, suitable initial guesses for the six parameters have to be made. All parameters could be expressed by important signal features, while n_A is already an identifiable signal feature. The parameter α_k could be expressed as a function of the arrival time sample $n_{A,k}$, the sample of the maximal positive

slope $n_{s+,k} \in (n_{A,k}, n_E^\circ)$ and of the sample point of the maximum $n_{max,k} \in (n_{s+,k}, n_E^\circ)$ of $\gamma_k(n)$:

$$\alpha_k = \frac{(n_{max,k} - n_{A,k})^2}{(n_{max,k} - n_{s+,k})^2} \tag{10.4}$$

The parameter β_k is described by the same parameters:

$$\beta_k = \frac{n_{max,k} - n_{A,k}}{(n_{max,k} - n_{s+,k})^2} \tag{10.5}$$

Finally, the amplitude g of $\gamma_k(n)$ can be expressed in terms of its maximum $\gamma_{max,k}$ and the previously identified parameters α_k and β_k:

$$g_k = \left(\frac{\beta_k}{\alpha_k}\right)^{\alpha_k} e^{\alpha_k} \cdot \gamma_{max,k} \tag{10.6}$$

The derivation of the model parameters as functions of important signal features is described in appendix A.

In order to identify a suitable initialization of the model parameters in each spatial element k, the features of the gamma variate were approximated by the same features of the reconstructed conductivity signal $\Delta\sigma_k(n)$. Thus, an estimate of the gamma variate maximum $\tilde{\gamma}_{max,k}$ and its sample point $\tilde{n}_{max,k}$ was calculated by searching for the maximum of $\Delta\sigma_k(n)$ within the global γ-interval:

$$\tilde{\gamma}_{max,k} = \max_{n_A^\circ < n < n_E^\circ} \Delta\sigma_k(n) \tag{10.7}$$

$$\tilde{n}_{max,k} = \operatorname*{argmax}_{n_A^\circ < n < n_E^\circ} \Delta\sigma_k(n) \tag{10.8}$$

An estimate of the value and position of the maximal positive slope was equally calculated:

$$\tilde{\dot{\gamma}}_{max,k} = \max_{n_A^\circ < n < \tilde{n}_{max,k}} \frac{d}{dn}\Delta\sigma_k(n) \tag{10.9}$$

$$\tilde{n}_{s+,k} = \operatorname*{argmax}_{n_A^\circ < n < \tilde{n}_{max,k}} \frac{d}{dn}\Delta\sigma_k(n) \tag{10.10}$$

An initial guess of the arrival time sample $\tilde{n}_{A,k}$ was again computed with the intersecting tangent method [170] using the calculated feature estimates $\tilde{\dot{\gamma}}_{max,k}$ and $\tilde{n}_{s+,k}$. From these features, the initial values of g_k, α_k and β_k were calculated. The weighting factor of the integral part was initially set to $\tilde{\kappa}_k = 0.1 \cdot \sum_{n=n_A^\circ}^{n_E^\circ} \Delta\sigma_k(n)$ for all spatial elements k. The slope of the straight line was initially set to $\tilde{m}_k = 0$ also for each spatial element.

With the described initial estimates the nonlinear model $\Delta\tilde{\sigma}_k(n)$ was fitted to $\Delta\sigma_k(n)$ element-wise using a trust region reflective algorithm implemented in MATLAB R2019a [194]. To calculate the resulting estimation of the first-pass indicator signal $\gamma_k(n)$, the estimated parameters were inserted into equation (10.2). The final result of this processing step was the spatio-temporal matrix with the fitted drift-free indicator signals $\mathbf{\Gamma} \in \mathbb{R}^{K \times N}$. Each row of $\mathbf{\Gamma}$ represents the temporal indicator signal of a single spatial element over all time steps $n = [1, N]$. As a side product, the spatio temporal matrix $\mathbf{D} \in \mathbb{R}^{K \times N}$ of all drift signals was estimated as $\mathbf{D} = \Delta\mathbf{\Sigma} - \mathbf{\Gamma}$. Exemplary fits are shown in Figure 10.2 (C) and (E) for a lung and heart compartment.

Piecewise linear fit The nonlinear γ-fit simultaneously adapts to the slow drift and the gamma variate as model of the first passage of the indicator to the reconstructed conductivity signal $\Delta\sigma_k$ with a nonlinear optimization procedure. With the piecewise fit a simplified and potentially more robust and more flexible method was developed. The idea behind this method was to approximate the slow drift component with piecewise linear functions. To retrieve the first pass indicator component, the estimation of the slow drift has to be subtracted from the original reconstructed conductivity signal $\Delta\sigma_k$. This approach reduced the model fitting to a linear problem. Additionally, it was assumed, that the first passage indicator signal does not have to be fitted to reduce noise, since the signal-to-noise ratio (SNR) of the reconstructed conductivity signal was sufficiently high. The method divides the signal into three temporal intervals individually for each spatial element k: time interval before the indicator signal arrives with $n \leq n_{A,k}$; an interval during the passage of the indicator through the compartment with $n_{A,k} < n \leq n_{E,k}$ and a temporal interval after the indicator has left the compartment with $n > n_{E,k}$. For the first and last segment straight lines $l_{A,k}(n)$ and $l_{E,k}(n)$ were fitted by means of linear least squares.

$$l_k(n) = \begin{cases} l_{A,k}(n) = m_{A,k} \cdot n & n \leq n_{A,k} \\ l_{E,k}(n) = m_{E,k} \cdot n + \Delta\sigma_k(n_{E,k}) & n > n_{E,k} \\ \frac{n-n_{A,k}}{n_{E,k}-n_{A,k}} \cdot l_{E,k}(n_{E,k}) - \frac{n-n_{E,k}}{n_{E,k}-n_{A,k}} \cdot l_{A,k}(n_{A,k}) & otherwise \end{cases} \tag{10.11}$$

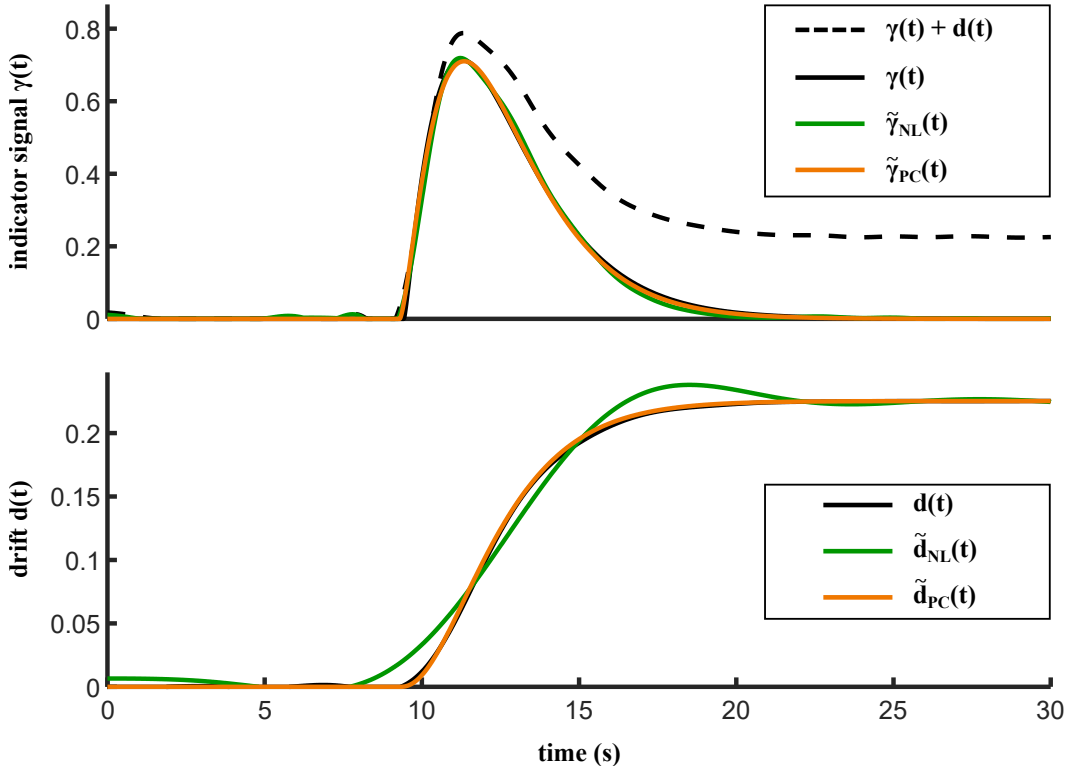

Figure 10.3: Graphs of an exemplary indicator dilution curve with the superimposed drift signal $d(t)$ and the pure indicator dilution curves after estimation by the nonlinear and piecewise fit.

The slope of the straight line before the arrival of the indicator $l_{A,k}$ is $m_{A,k}(n)$, the slope of the straight line after the indicator has left the compartment $l_{E,k}(n)$ is described by $m_{E,k}$. To remove the sharp edges of the estimated piecewise drift signal $l_k(n)$, the signal is low-pass filtered with a zero-phase filter [175] and a cutoff frequency of 0.1 Hz. The final drift signal $d_k(n)$ is subtracted from the reconstructed conductivity signal $\Delta\sigma_k(n)$ to retrieve an estimation of the first-pass indicator signal:

$$\tilde{\gamma}_k(n) = \Delta\sigma_k(n) - d_k(n) \tag{10.12}$$

The tilde in $\tilde{\boldsymbol{\gamma}}$ which indicates, that the true first-passage indicator signal is only estimated, we will waive the operator in the following for simplicity. All first-pass indicator curves form a spatio-temporal matrix $\boldsymbol{\Gamma} = [\boldsymbol{\gamma}(1), ..., \boldsymbol{\gamma}(N)] \in \mathbb{R}^{K\times N}$.
Both fitting methods have been compared using a simulation study and were presented at a conference [125]. The comparison of both methods is summarized in appendix B.

10.2.2 Detection and removal of the pre- and post lung phases

To estimate the regional distribution of pulmonary perfusion, pre- and post-lung phases had to be removed from the spatial first-pass indicator signals $\boldsymbol{\gamma}(n)$. Thus, we need to detect all triangular elements k, which describe regions of the larger pulmonary arteries and veins or the right and left cardiac blood volume, which participate in the pulmonary circulation, but do not contribute to pulmonary capillary perfusion. Since the spatial resolution of 2D-EIT reconstructions does not allow to differentiate between pulmonary arteries, veins or the heart chambers and we can not expect to have CT or MRT images for patients in an ICU, we only considered three compartments S_1 with $i \in [1,3]$: pre-lungs, lungs and post-lungs.
In order to identify and remove pre- and post-lung phases, we assumed that the mean transit time $\bar{\mathbf{t}}_\gamma$ and the maximal indicator amplitude $\boldsymbol{\gamma}_{max,k}(n)$ differ between the compartments. The mean transit time $\bar{t}_{\gamma,k}$ of a spatial element k was described by:

$$\bar{t}_{\gamma,k} = \frac{1}{f_s} \cdot \frac{\sum_{n=1}^{N} n \cdot \gamma_k(n)}{\sum_{n=1}^{N} \gamma_k(n)} \tag{10.13}$$

To distinguish the three compartments, a K-means clustering algorithm was applied [195]. Prior to the clustering, a subset of spatial elements $j = [1,J] \in \{k \mid \gamma_{max,k} \geq 0.1 \cdot \max(\gamma_{max,k})\}$ was created, containing elements with indicator amplitudes exceeding a relative threshold of 10 % of the maximal global indicator amplitude. From each element of the subset, a feature vector $\boldsymbol{x} \in \mathbb{R}^{J\times 2}$ containing the normalized mean transit time and the normalized maximum indicator amplitude. The normalization was necessary to ensure equal influence of both parameters. Thus, the values of the feature vector $\boldsymbol{x}$ were limited to the interval $[0,1]$. Finally, we minimized the sum of all feature distances to the centroid $\boldsymbol{\mu}_j$ of cluster or compartment S_i:

$$\min \sum_{i=1}^{3} \sum_{\boldsymbol{x}_j \in S_i} \left\| \boldsymbol{x}_j - \boldsymbol{\mu}_i \right\|^2 \tag{10.14}$$

10.2.3 Estimation of vascular transfer parameters

Two different approaches have been investigated to estimate regional distributions of perfusion with EIT. The maximal slope method estimates a perfusion surrogate based on an element wise signal feature analysis. The second approach reconstructs a temporal vascular transfer function (TF) to element-wise compartments of the lungs. The first approach can be considered as computationally simple, yet might be sensitive to high frequency noise. The latter one is more computationally expensive and includes solving an inverse problem, which might influence its robustness. The second approach can nevertheless be considered as less sensitive to high frequency noise.

10.2.3.1 Maximal slope method

The first method describes a simple feature analysis based approach of calculating a perfusion surrogate. Pulmonary blood flow $\dot{\mathbf{q}} \in \mathbb{R}^{K\times 1}$ in each discrete element k was estimated by the maximal discrete derivative of the first-pass indicator signal $\gamma_k(n)$

$$\dot{q}_k = \max_n \{(\gamma_k(n) - \gamma_k(n-1))\} \cdot f_s \tag{10.15}$$

in each spatial element k was calculated as proposed in [19, 196–198]. The mean transit time of the indicator to the compartment k was approximated by the first temporal statistical moment of the first-pass signal component:

$$\bar{t}_{\gamma,k} = \frac{1}{f_s} \cdot \left(\frac{\sum_{n=1}^{N} n \cdot \gamma_k(n)}{\sum_{n=1}^{N} \gamma_k(n)} - n_A^{\circ} \right) \tag{10.16}$$

In order to allow a fair comparison of the mean transit times between different states and animals, the transit time was always calculated with respect to the global arrival time n_A°. The perfusion parameters $\dot{\mathbf{q}}$ and $\bar{\mathbf{t}}_{\gamma}$ were set to zero outside of the detected lung compartment S_2.

10.2.3.2 System theoretical or deconvolution based approach

Besides the intuitive approach of estimating the blood flow to a spatial compartment by the maximal slope of the indicator dilution curve and therefore by analyzing its indicator inflow rate, we considered a second approach, which is inspired by a system theory perspective of the given problem. Similar approaches have been proposed for other perfusion imaging modalities, such as for high resolution cerebral blood flow estimations based on CT measurements [115] or for myocardial blood flow estimations from MRI [199]. The proposed methods were adapted to be applicable for spatial EIT perfusion estimation, and optimized to improve robustness.
We consider the pulmonary circulation to be a system with one single input and multiple

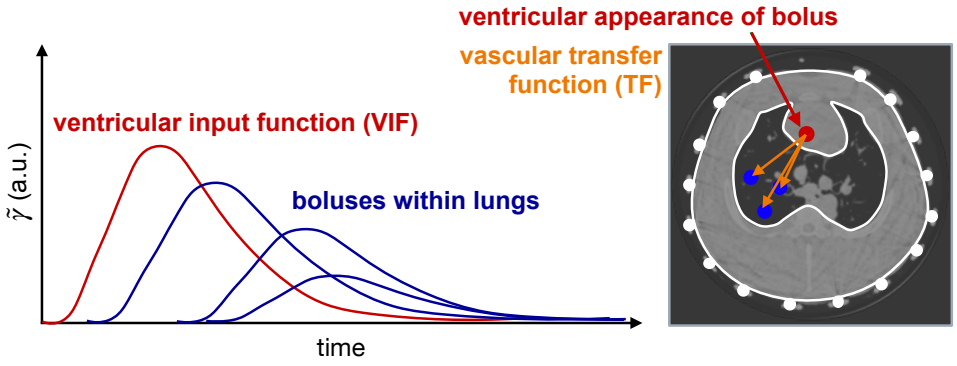

Figure 10.4: Graphical description of the deconvolution based perfusion estimation approach. A ventricular input function (VIF) was estimated from the reconstructed first pass indicator time curves $\boldsymbol{\gamma}$ within the detected pre-lung compartment S_1. This signal was interpreted as input function to the lungs. The element wise indicator time curves $\boldsymbol{\gamma}$ within all other compartments were considered as multidimensional output of the system. Between each output and the VIF a transfer function $\mathbf{h}(n)$ was estimated.

outputs. Between the input and each output k, the system is described by its impulse response $\mathbf{h}(n) \in \mathbb{R}^{K\times 1}$. The Laplace transform of the impulse response describes the TF between this input and the outputs.

The inflow of the pulmonary circulation system is defined by the blood flow in the pulmonary artery and was called arterial input function (AIF), according to the definition for the application to cerebral blood flow estimation [115]. Nevertheless, the resolution of an EIT reconstruction did not allow to robustly define an AIF within the main pulmonary artery (PA) or in the main left and right PA. Additionally, in chapter 8 we have concluded, that the contributions of the left and right PAs to perfusion image amplitudes were rather small, such that we do not assume to be able to find the actual AIF to the left and right lungs. For these reasons, we opted for a slightly different definition of the input function. Before the indicator bolus within the blood reaches the PA, the indicator bolus passes through the right heart and can be acknowledged initially in reconstructed EIT signals. The input to the considered system was therefore detected within the pre-lung region and will be called ventricular input function (VIF) in the following, since the input will be found most likely within the right ventricular region. The underlying idea of the system theoretical approach of estimating spatial pulmonary blood flow is visualized in Figure 10.4.

Definition of the VIF To define a VIF, all K_{pre} extracted first-pass indicator signals within the previously detected pre-lung phase $\boldsymbol{\gamma}_{pre}(n) \in \mathbb{R}^{K_{pre}\times 1}$ were considered. The extracted signals of the pre-lung compartment are depicted in graph (B) of Figure 10.5. Due to the low spatial resolution, the extracted signals $\boldsymbol{\gamma}_{pre}(n)$ were often superimposed by a signal component of the post-lung phase. In order to have a good approximation of the actual input function to the lung circulation, we fitted a gamma variate model to the first passage of the $\boldsymbol{\gamma}_{pre}$ signals (as in [19, 130]). The gamma fits of the extracted first pass signals $\boldsymbol{\gamma}_{pre,1}(n) \in \mathbb{R}^{K_{pre}\times 1}$ are depicted in graph (B1) of Figure 10.5. The VIF $\gamma_{VIF}(n) \in \mathbb{R}$ was

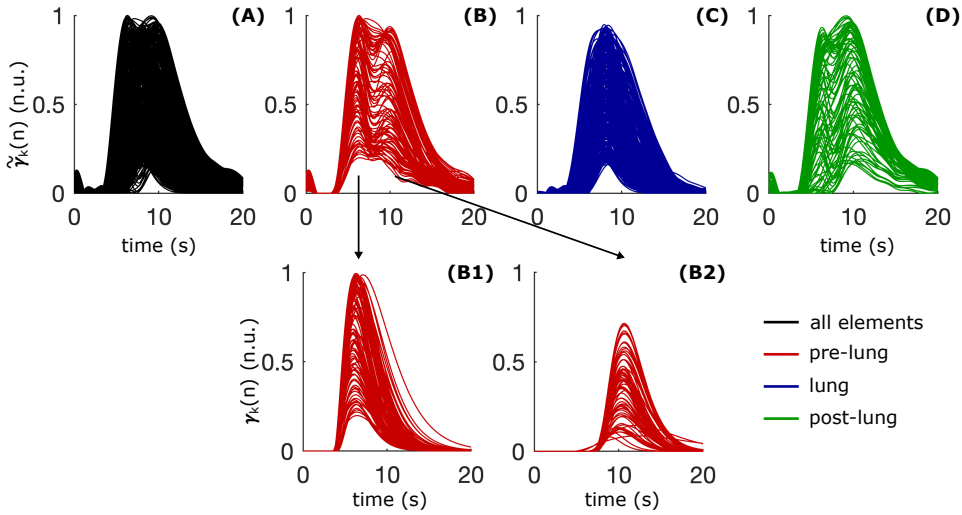

Figure 10.5: First-pass indicator signals within the different detected compartments: pre-lung, lung, post-lung. Graph (A) shows the first-pass indicator conductivity change signals of all elements. Graph (B) depicts the signals of the pre-lung compartment. The signals within the pre-lung compartment have been further separated into a first (B2) and second passage signal (B2). The signals in (B1) have been considered for the VIF definition. Graph (C) presents the indicator signals of the lung and graph (D) the signals of the post-lung compartment.

defined by the mean over the largest 10 % of all fitted first pass signals $\boldsymbol{\gamma}_{pre,1}(n)$ of the pre-lung phase.

Estimation of the system impulse response $\mathbf{h}(n)$ We described the lung as a system with k outputs $\boldsymbol{\gamma}(n)$ and a single input $\gamma_{VIF}(n)$. The multidimensional transfer function of the system was described by $\mathbf{h}(n)$. The following system description was considered for the k^{th} output:

$$\gamma_k(n) = \gamma_{VIF}(n) * h_k(n) \tag{10.17}$$

$$= \frac{1}{f_s} \cdot \sum_{\tau=1}^{n} \gamma_{VIF}(\tau) \cdot h_k(n-\tau)\, d\tau \tag{10.18}$$

Thus, the indicator dilution curve in lung compartment k was calculated by the convolution of the input $\gamma_{VIF}(n)$ and the impulse response $h_k(n)$. Equation (10.18) can be rewritten in matrix form as:

$$\begin{bmatrix} \gamma_k(1) \\ \gamma_k(2) \\ \vdots \\ \gamma_k(N) \end{bmatrix} = \frac{1}{f_s} \cdot \begin{bmatrix} \gamma_{VIF}(1) & 0 & \cdots & 0 \\ \gamma_{VIF}(2) & \gamma_{VIF}(1) & \cdots & 0 \\ \vdots & \vdots & \ddots & \vdots \\ \gamma_{VIF}(N) & \gamma_{VIF}(N-1) & \cdots & \gamma_{VIF}(1) \end{bmatrix} \cdot \begin{bmatrix} h_k(1) \\ h_k(2) \\ \vdots \\ h_k(N) \end{bmatrix} \tag{10.19}$$

We defined $\mathbf{A} \in \mathbb{R}^{N\times N}$ to be

$$\mathbf{A} = \frac{1}{f_s} \cdot \begin{bmatrix} \gamma_{VIF}(1) & 0 & \cdots & 0 \\ \gamma_{VIF}(2) & \gamma_{VIF}(1) & \cdots & 0 \\ \vdots & \vdots & \ddots & \vdots \\ \gamma_{VIF}(N) & \gamma_{VIF}(N-1) & \cdots & \gamma_{VIF}(1) \end{bmatrix} \tag{10.20}$$

Since there exists only a single input to the pulmonary system with all compartments, the equation was extended to include all k outputs by using the spatio-temporal first pass indicator signal matrix $\mathbf{\Gamma}$ and defining a multidimensional impulse response $\mathbf{H} = [\mathbf{h}(1), ..., \mathbf{h}(N)] \in \mathbb{R}^{K\times N}$:

$$\mathbf{\Gamma}^\top = \mathbf{A} \cdot \mathbf{H}^\top \tag{10.21}$$

The goal was to retrieve $\mathbf{H}$ for assessing the vascular transfer from the input to all outputs. Therefore, the matrix $\mathbf{A}$ needs to be inverted. Since the condition of $\mathbf{A}$ is not suitable for a direct inversion, we again need to solve this inverse problem applying some kind of regularization. Tikhonov regularization could be used, as it has previously been done for the EIT reconstruction problem. Since matrix $\mathbf{A}$ was created from the shifted VIF $\gamma_{VIF}(n)$, we assumed, that the largest singular values and their corresponding eigenvectors of the matrix $\mathbf{A}$ contain most of the information. Thus, we chose to invert matrix $\mathbf{A}$ after a truncated singular value decomposition to improve the condition of the matrix.
As introduced in section 3.1.3, we improved the condition of the matrix $\mathbf{A}$ by removing the r smallest eigenvalues and their corresponding eigenvectors. Herefore the matrix $\mathbf{A}$ was decomposed into its singular values $\not{\mathbf{D}} \in \mathbb{R}^{N\times N}$ and the left an right eigenvectors $\mathbf{U}, \mathbf{O} \in \mathbb{R}^{N\times N}$:

$$\mathbf{A} = \mathbf{U}\not{\mathbf{D}}\mathbf{O}^\top \tag{10.22}$$

After removing the eigenvectors corresponding to the r smallest singular values, an approximation $\mathbf{A}_r$ of matrix $\mathbf{A}$ was estimated as:

$$\mathbf{A}_r = \mathbf{U}_r\not{\mathbf{D}}\mathbf{O}_r^\top \text{ with } \mathbf{A_r} \in \mathbb{R}^{N\times N}, \mathbf{U}_r, \mathbf{O}_r \in \mathbb{R}^{N\times N-r} \tag{10.23}$$

The number of removed singular values r was defined by maximizing the curvature of the L-curve as defined by [90]. We performed a comprehensive study to find an optimal value for r published in the Bachelor thesis [133].

Finally, we were able to retrieve the multidimensional impulse response:

$$\mathbf{H}^\top = \mathbf{A}_r^{-1} \cdot \mathbf{\Gamma}^\top \tag{10.24}$$

The pulmonary blood flow was estimated by the temporal maximum of the impulse response:

$$\dot{q}_k = \max_n h_k(n) \tag{10.25}$$

The mean transit time was estimated by the sample of the temporal maximum of the impulse response:

$$\bar{t}_k = \frac{1}{f_s} \cdot \left[\operatorname{argmax}_n h_k(n))\right] \tag{10.26}$$

PART V

EXPERIMENTAL DATA ANALYSIS

Chapter 11

Analysis of the experimental study in Iowa

A preliminary method comparison between EIT and MDCT perfusion estimations was published as a conference contribution [141]. A main part of the comparative study, which will be described in the following chapter, was also published as journal article in the IEEE Transactions of Medical Imaging journal [142].

11.1 Motivation

In order to validate the spatial pulmonary blood flow estimation based on indicator-enhanced EIT, a first comprehensive evaluation of the presented EIT perfusion estimation framework was conducted using the data of the preclinical study performed in Iowa, which has been introduced in chapter 6. EIT perfusion was compared to indicator-enhanced multidetector Computed Tomography (MDCT) in healthy lungs and experimental models of regional, sublobar lung injury at two distinct levels of fraction of inspired oxygen (F_IO_2) (compare Figure 6.1 in chapter 6). The analysis was performed in eight animals in supine position. For both imaging modalities, spatial perfusion distributions were estimated using the dynamic indicator dilution technique. So far, EIT has not been validated against CT perfusion measurements and the potential of EIT to detect regional, sublobar lung injury has not been tested. In previous studies on EIT perfusion measurements, only global lung injury has been investigated and validated against Electron Beam Computed Tomography (EBCT) [197] and Single Photon Emission Computed Tomography (SPECT) [19, 109]. A validation study comparing EIT perfusion against PET will be discussed in chapter 12 and was partly published in [121].
Additionally, since the origin of the EIT perfusion image amplitudes is not fully understood, the following investigation allows to contribute to this question from an experimental point of view, besides the findings of the simulation study in chapter 8. Herefore, pulmonary perfusion as estimated by EIT was compared to MDCT estimation results with and

without excluding major blood vessels from the analysis. If EIT reconstructions represent mainly perfusion of the pulmonary capillary bed (PCB), similarity between EIT and MDCT should increase, in case major blood vessels are excluded from the MDCT perfusion analysis.

Three main objectives have been investigated:

- Analyze similarity between EIT and MDCT relative spatial pulmonary blood flow estimations using correlation and Bland-Altman analyses.
- Investigate, whether similarity between EIT and MDCT perfusion increases, if major pulmonary blood vessels are excluded for MDCT perfusion analysis.
- Analyze, whether EIT can track temporal changes of relative spatial EIT perfusion in accordance with changes of MDCT perfusion.

11.2 Methods

To compute the EIT and MDCT regional perfusion maps and compare their similarity, multiple processing steps had to be performed. A schematic overview of the computational work flow is depicted in Figure 11.1. All necessary processing steps will be introduced in the following.

11.2.1 Image segmentation and EIT reconstruction model creation

Image segmentation The process of segmenting the main organ tissues and blood volumes has been already described in section 8.2. The segmentation process has been conducted for each individual experimental step of each animal. In short, from the spatially downsampled and temporally interpolated tissue density matrix $\boldsymbol{\rho}_{CT}(n)$ with a spatial resolution of 2 mm in all dimensions and at a temporal sampling of $N = 1000$ sampling points with a sampling rate of $f_s = 25$ Hz, a static tissue density matrix $\boldsymbol{\rho}_{CT}(n = 1)$ and a temporal MIP volume $\boldsymbol{\rho}_{max} = \max_{1<n<N} \boldsymbol{\rho}_{CT}(n)$ has been extracted. The electrodes, the torso surface, the heart (heart muscle) and the lungs were segmented from the static matrix and the right and left ventricular blood volumes, the right and left PA, the PV and the aorta were segmented from the maximum intensity projection (MIP) volume. All segmented tissue labels formed a tissue label matrix $\mathbf{L}_{\mathrm{T}} \in \mathbb{R}^{K_x \times K_y \times K_z}$ which is depicted for an exemplary animal in graph (A) of Figure 11.1 and in Figure 8.1 of section 8.2. The tissue label map contained the labels depicted in Table 11.1

Creation of an animal specific reconstruction model Since repositioning of the animal was avoided throughout all experimental steps and the animal was constantly ventilated with a

Blood volume	Right heart	Right PA	Left PA	Right PA
Tissue label	1	2	3	4

Blood volume	Lung/PCB	Veins	Left heart	Heart muscle
Tissue label	5	6	7	8

Table 11.1: Overview of the tissue labels of matrix $\mathbf{L}_T$

PEEP of 5 mbar, an animal specific reconstruction model was created and jointly used for EIT perfusion reconstruction of all experimental steps. Herefore, the segmented torso surface and the electrodes of each experimental step were registered to the initial healthy normoxia state by a singular value decomposition (SVD) based point cloud registration (PCR) algorithm [200]. The center coordinates of all 16 electrodes were used to achieve optimal registration. By averaging over all registered center electrode coordinates, joint electrode positions were computed with minimal position errors for each experimental state. The registered 2D torso boundaries within the electrode plane were extracted and averaged in the polar coordinate space (angular resolution of 1°). The final joint electrode positions and the 2D torso surface were triangulated with a *Delaunay* triangulation algorithm implemented in *MATLAB R2019a*.

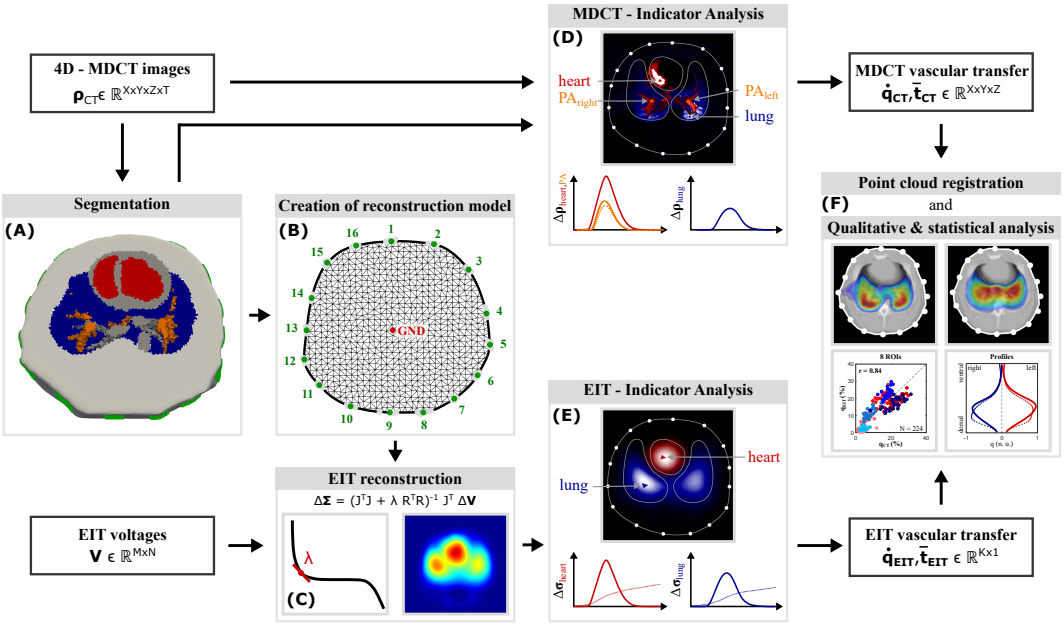

Figure 11.1: Schematic illustration of the computational work flow. First, the torso (), the electrodes (), the heart muslce(), the left and right ventricular blood volume (), the lungs () and the major thoracic blood vessels () are segmented from the MDCT volume (A). From the torso segmentation animal specific EIT reconstruction meshes were constructed (B). EIT image reconstruction was performed (C) and perfusion related parameters were estimated from the dynamic indicator signals for both MDCT (D) and EIT (E). Finally, the similarity of MDCT and EIT perfusion was evaluated (F). The illustration has been adapted from our publication with permission [142].

Over all eight reconstruction meshes corresponding to the investigated animals, the meshes had a mean edge length of 3.8 mm $\pm$ 0.3 mm and consisted of $K = 1612.8 \pm 40.7$ elements.

11.2.2 Estimating spatial pulmonary blood flow with EIT

As described in chapter 9, the $M = (n_E \cdot (n_E - 3)) = 208$ measured voltages $\mathbf{v}(n) \in \mathbb{R}^{M\times 1}$ of the $n_E = 16$ electrodes were preprocessed to extract the indicator signal component $\mathbf{v}_I(n)$. Since the indicator measurement was performed during breath hold, only the pulsatile CRIC component had to be removed from the overall voltages. The voltages were normalized by the static background voltage $\mathbf{v}_B$ resulting in the overall normalized dynamic voltage measurement set $\Delta\mathbf{V} \in \mathbb{R}^{M\times N}$:

$$\Delta\mathbf{V} = diag(\mathbf{v}_B)^{-1} \cdot \mathbf{V}_I \tag{11.1}$$

For the described study, a Tikhonov type reconstruction with a spatial Laplace regularization was performed to receive robust results. With the reconstruction matrix $\mathbf{\Phi}_{T2}$, as derived in chapter 9, the spatio-temporal conductivity changes $\Delta\hat{\mathbf{\Sigma}} = [\Delta\hat{\boldsymbol{\sigma}}(1), ..., \Delta\hat{\boldsymbol{\sigma}}(N)] \in \mathbb{R}^{K\times N}$ were reconstructed by matrix multiplication:

$$\Delta\hat{\mathbf{\Sigma}} = \mathbf{\Phi}_{T2} \cdot \Delta\mathbf{V} \tag{11.2}$$

The regularization parameter λ, controlling the amount of spatial smoothing was optimized using the L-curve for each individual reconstruction.
After EIT reconstruction, the recirculation or drift component was removed within each spatial element applying the *piecewise linear fit* as introduced in chapter 10. The pure indicator passage related signal $\boldsymbol{\gamma}(n) \in \mathbb{R}^{K\times 1}$ was hereby extracted. From the extracted temporal indicator passage signals, the spatial pulmonary blood flow was estimated applying the maximal slope method as described in chapter 10. The pulmonary blood flow surrogate $\dot{\mathbf{q}}_{EIT} \in \mathbb{R}^{K\times 1}$ and the mean transit time $\bar{\mathbf{t}}_{EIT} \in \mathbb{R}^{K\times 1}$ were calculated and later compared to the corresponding MDCT measures.
Finally, the pre- and post lung phases were detected and removed with the method introduced in section 10.2.2. Since the animals were not repositioned throughout the experimental workflow and PEEP and tidal volume (V_T) remained constant throughout all experimental steps, animal specific joint pre-and post-lung regions were computed from all experimental steps. The joint heart mask ensured conservative filtering of pre- and post-lung phases. The joint heart regions are depicted in Figure 11.2.

11.2.3 Estimating spatial pulmonary blood flow with MDCT

In order to have a fair comparison between spatial EIT and MDCT perfusion estimations, the same indicator dilution parameter estimation approach was applied to the MDCT data. The maximal temporal slope $\dot{\mathbf{Q}}_{CT} \in \mathbb{R}^{K_x\times K_y\times K_z}$ within each spatial element served as pulmonary

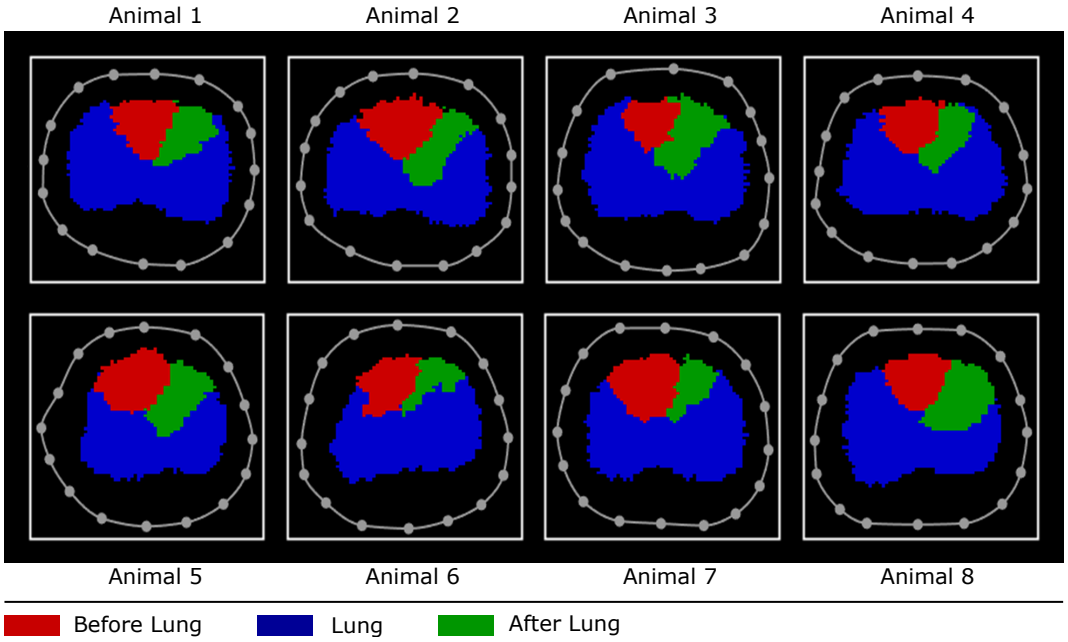

Figure 11.2: Detected indicator passage phases: before, within and after lungs. To extract pulmonary blood flow within the lungs, the pulmonary region was removed. The images depict the computed pre- and post- lung phases in red and green, which were removed to gain pulmonary perfusion estimations.

blood flow surrogate and was calculated as follows:

$$\dot{\mathbf{Q}}_{CT} = \max_{2<n<N} \{\boldsymbol{\rho}_{CT}(n) - \boldsymbol{\rho}_{CT}(n-1)\} \cdot f_s \tag{11.3}$$

The mean transit time (MTT) $\bar{\mathbf{T}}_{CT} \in \mathbb{R}^{K_x \times K_y \times K_z}$ of the indicator bolus to a spatial compartment $[k_x, k_y, k_z]$ was approximated by calculating the first temporal moment of each spatial dilution curve:

$$\bar{T}_{CT,xyz} = \frac{1}{f_s} \frac{\sum_{n=1}^{N} n \cdot \rho_{CT,xyz}}{\sum_{n=1}^{N} \rho_{CT,xyz}} \tag{11.4}$$

From the computed MDCT perfusion parameters, two sets of 2D parameter images were created to be compared with 2D EIT perfusion distributions. For the first set of images $\dot{\mathbf{q}}_{CT} \in \mathbb{R}^{K_x \times K_y}$ and $\bar{\mathbf{t}}_{CT} \in \mathbb{R}^{K_x \times K_y}$, the cardiac phase was removed by extracting regions of the heart muscle and the left and right cardiac blood volume from the pulmonary blood flow parameters. The three-dimensional MDCT volume was projected onto the electrode plane by averaging equally weighted in cranial-caudal dimension. The maximal slope image was additionally normalized to its overall absolute image pixel sum.
For the second set of parameter images $\dot{\mathbf{q}}_{CT,PCB} \in \mathbb{R}^{K_x \times K_y}$ and $\bar{\mathbf{t}}_{CT,PCB} \in \mathbb{R}^{K_x \times K_y}$ the major pulmonary blood vessels - left and right PA, pulmonary veins - were additionally removed from the computed parameter sets representing only PCB perfusion. The 3D parameter volume was again projected onto the electrode plane by averaging in vertical or cranial-caudal direction and the maximal slope image was normalized.

11.2.4 Comparison of spatial MDCT and EIT pulmonary blood flow

First, the EIT perfusion parameters within the triangular reconstruction mesh elements were registered and mapped to the MDCT pixel map for each individual experimental step. The same SVD based PCR method was used to register the animal specific electrode positions of the EIT reconstruction mesh to the mean center electrode positions within the CT domain of each individual experimental step [200].

The similarity of the spatial lung perfusion estimations were evaluated by correlation and Bland-Altman analyses. A bounding box around the segmented lung within the image planes was therefore cut out, in order to suppress the misleading effect, that regions with no expected perfusion (outside of the heart and the lungs) potentially increase the detected similarity of the images. To also reduce the influence of different mesh and image resolutions as well as the influence of different fields of view of the MDCT scanner, the lung region cutout was resampled to a pixel map of $[64 \times 64]$ pixels for both imaging modalities. For simplicity, we will continue do describe the cut out lung images of EIT and MDCT parameters by $\dot{\mathbf{q}}_{CT}$ and $\dot{\mathbf{q}}_{EIT}$, though the pixel map had been altered.

To quantify the spatial similarity of the reconstructed relative perfusion distributions $\dot{\mathbf{q}}_{CT}$ and $\dot{\mathbf{q}}_{EIT}$, ROI based and pixelwise similarity measures were considered.

For the ROI based similarity measures, the lung region cutout was further divided into eight ROIs based on the centroid of the segmented lung volume. The defined ROIs are depicted in Figure 11.3. The relative amount of perfusion within each ROI was compared between EIT and MDCT via correlation and Bland-Altman analysis. The same analysis was also repeated for only four ROIs. Mid-ventral and ventral as well as mid-dorsal and dorsal ROIs were combined.

Since experimental lung injury was established in sublobar segments of the right lung, pixelwise similarity was assessed additionally, in order to consider a higher spatial resolution

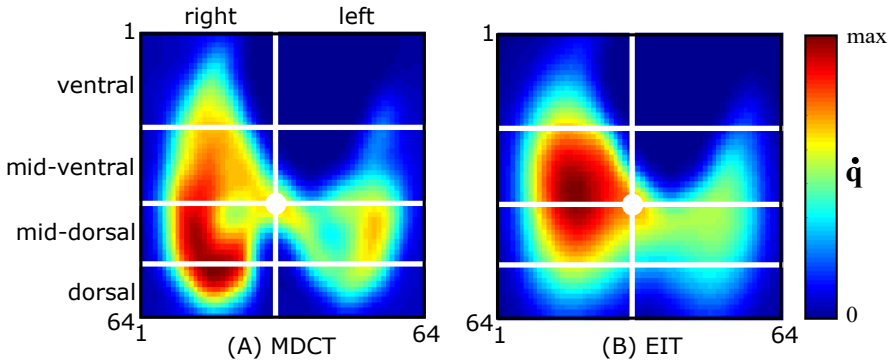

Figure 11.3: Definition of the ROIs to analyze similarity. A region containing the lungs (as defined by CT segmentation) of MDCT and EIT perfusion images was extracted and spatially sampled to [64×64] pixel. The resulting image was divided into eight ROIs around the centroid of the segmented lung. The illustration has been taken from our publication, which is currently under review.

for the comparison. Herefore, the Pearson correlation coefficient r_{Pixel} of the lung image cutouts between MDCT and EIT was computed. Additionally, the ventro-dorsal and right-left profiles of the cutout lung perfusion images were computed by summarizing image rows and image columns. The Pearson correlation coefficient of these profiles between MDCT and EIT was computed to quantify the ventro-dorsal r_{VD} and right-to-left r_{RL} similarity of both perfusion imaging modalities. Exemplary profiles are depicted in graphs (C) and (F) of Figure 11.5.

11.3 Results

During all experiments, monitoring parameters were recorded. The mean and STD values of the main parameters for all animals are assembled for each individual experimental step in Table 11.2. The V_T and the PEEP were kept constant throughout the experimental protocol, while the F_IO_2 was adapted to the normoxia or hyperoxia condition. After lung injury, the partial pressure of end-tidal carbon dioxide ($p_{et}CO_2$) increased and could be decreased by applying a higher F_IO_2. Blood pressures, the heart rate and the cardiac output (CO) increased after lung injury to maintain a sufficient blood oxygenation. An increase of F_IO_2 lead to a decrease of blood pressures and CO. The gas exchange parameters showed corresponding trends. partial pressure of arterial oxygen (paO_2) decreased after lung injury, while partial pressure of arterial carbon dioxide ($paCO_2$) increased. The increase of F_IO_2 compensated the effect of the decrease of paO_2 and the increase of $paCO_2$. The oxygen saturation measured by the peripheral capillary oxygen saturation (SpO_2) and the mixed venous oxygen saturation (SvO_2) also decreased after lung injury and could be increased during hyperoxia.

		Healthy lung		Regional ARDS	
Parameter	**Pre/post indicator**	$\mathbf{F_IO_2 = 0.21}$	$\mathbf{F_IO_2 = 1.0}$	$\mathbf{F_IO_2 = 0.21}$	$\mathbf{F_IO_2 = 1.0}$
Ventilatory parameters					
V_T (ml kg^{-1})	pre & post	12.3(15)	12.1(15)	12.1(14)	12.3(15)
PEEP (mbar)	pre & post	5.0(00)	5.0(00)	5.0(05)	5.0(05)
F_IO_2 (%)	pre & post	20.9(04)	94.6(70)	21.0(06)	86.8(269)
$etCO_2$ (mmHg)	pre	39.1(34)	38.8(34)	48.4(43)	44.8(33)
	post	42.6(43)	43.1(36)	51.3(41)	47.4(46)
Hemodynamic and gas exchange parameters					
HR (min^{-1})	pre	101.0(161)	94.4(159)	109.5(211)	109.1(298)
	post	102.6(169)	102.0(177)	119.9(263)	108.4(286)
MAP (mmHg)	pre	87.0(273)	91.9(256)	72.6(285)	65.8(207)
	post	96.3(288)	85.0(249)	71.3(157)	60.0(111)
CVP (mmHg)	pre	6.6(21)	8.0(40)	8.0(17)	8.0(21)
	post	7.9(25)	7.6(35)	8.8(29)	8.6(19)
MPAP (mmHg)	pre	21.1(50)	18.1(26)	28.1(76)	21.1(68)
	post	25.0(64)	19.9(36)	30.6(66)	22.4(56)
CO (l min^{-1})	pre	3.8(13)	3.5(08)	4.1(15)	3.8(09)
SpO_2 (%)	pre	98.6(20)	99.8(07)	85.4(169)	99.8(05)
	post	98.3(19)	100.0(00)	79.4(184)	99.6(07)
p_aO_2 (mmHg)	pre	90.6(127)	548.3(896)	59.7(123)	449.8(873)
p_aCO_2 (mmHg)	pre	42.0(28)	43.2(44)	49.6(50)	50.4(55)
SvO_2 (%)	pre	64.1(76)	74.3(50)	55.1(143)	75.2(72)

Table 11.2: Overview of the ventilatory, hemodynamic and gas exchange parameters. Mean values and standard deviations over all included animals are presented for each individual experimental step. The table has been adapted from our publication with permission [142].

The comparison of spatial lung perfusion distributions between MDCT and EIT will be presented in the following chapter. Afterwards, the resulting similarity measures between MDCT and EIT of temporal perfusion changes between experimental states will be presented.

11.3.1 Comparison of spatial distributions of lung perfusion based on MDCT and EIT

Qualitative comparison The estimated spatial pulmonary perfusion distributions by MDCT and EIT were visualized in Figure 11.4. The left column (A) depicts the static CT tissue density. During lung injury, a diffuse infiltrate in the middle region of the right lung was visible in the static CT image (left column, second image from the top). The second column (B) depicts the same static CT tissue densities overlayed by the MDCT perfusion estimate $\dot{\mathbf{q}}_{CT,PCB}$. The larger blood vessel and the cardiac phase of the indicator bolus passage through the pulmonary circulation have been removed. The right column (C) depicts the estimated EIT perfusion $\dot{\mathbf{q}}_{EIT}$. Within the bottom row, the spatial differences in relative perfusion between normoxia states before and after lung injury are depicted for MDCT $\Delta\dot{\mathbf{q}}_{CT,PCB}$ and EIT $\Delta\dot{\mathbf{q}}_{EIT}$. Especially the difference images presented a strong decrease of perfusion within the injured lung region for both MDCT and EIT estimates. A strong

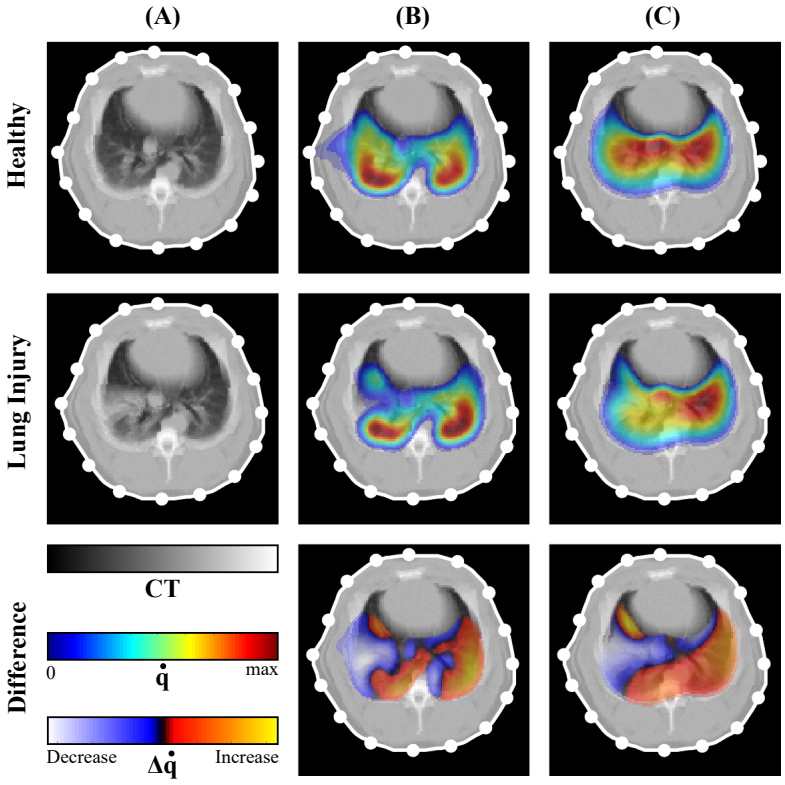

Figure 11.4: Estimated pulmonary perfusion distributions before and after sublobar lung injury. Static CT images (A) are shown alongside of the computed MDCT blood flow $\dot{\mathbf{q}}_{CT,PCB}$ (B), the calculated EIT blood flow $\dot{\mathbf{q}}_{EIT}$ (C) for the healthy (upper row), and the injured lung (middle row). The spatial perfusion increase or decrease ($\Delta\dot{\mathbf{q}}_{CT,PCB}$ and $\Delta\dot{\mathbf{q}}_{EIT}$) after establishing regional lung injury is depicted in the last row. The images have been taken from our publication, which is currently under review.

qualitative similarity was observed between imaging modalities. EIT perfusion distributions showed a slight ventral shift of perfusion.

Quantitative comparison The statistical analyses are visualized in Figure 11.5. The graphs depict the analyses between EIT $\dot{\mathbf{q}}_{EIT}$ and MDCT perfusion $\dot{\mathbf{q}}_{CT,PCB}$, with all larger pulmonary blood vessels excluded. Graph (A) presents the correlation analysis for a spatial division into four ROIs. An overall spatial correlation was $r = 0.97$ over all animals and all experiments could be achieved. There was a strong gradient present between the dorsal/dependent and the ventral/independent lung. For a division of the reconstructed images into eight ROIs, as depicted in graph (B), the overall correlation decreased to $r = 0.84$. A clear gradient of the relative amount of perfusion was observed between dorsal and ventral regions. The averaged (over all states and experiments) dorso-ventral profiles in graph (C) also indicated a higher perfusion in dorsal/dependent areas of the lungs. EIT perfusion estimations tended to be shifted to ventral regions of the lungs compared to MDCT reconstructions. In graph (F), the averaged right-to-left profiles were depicted. For both EIT and MDCT perfusion, less perfusion was directed to the right lung in average compared to the left lung. Sublobar lung injury was also established within the right lung. EIT and MDCT perfusion right-to-left profiles showed a clear visual similarity, while EIT seemed to overestimate

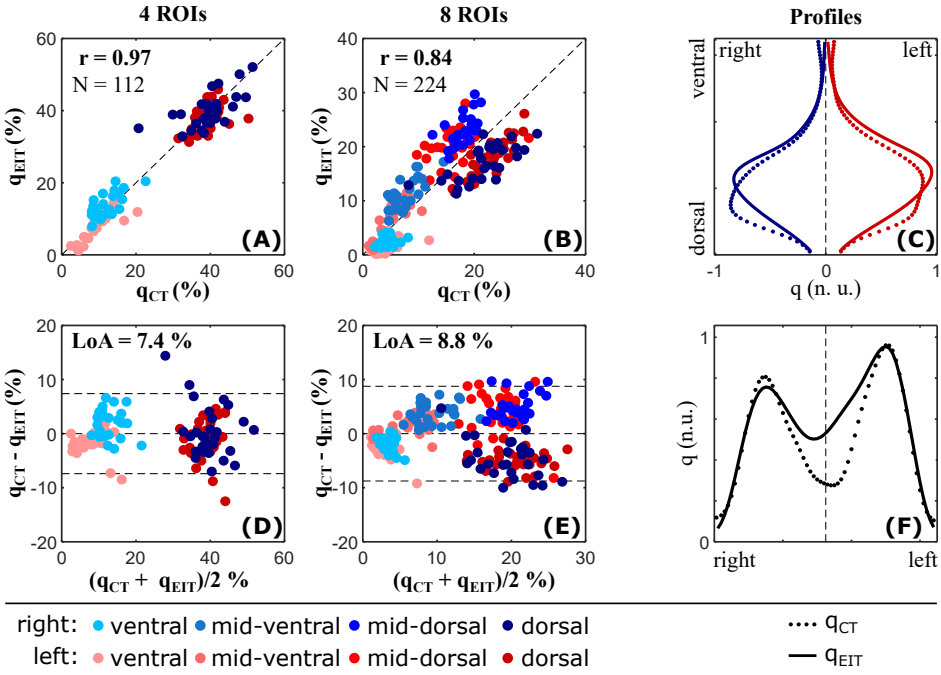

Figure 11.5: Statistical comparison of MDCT $\dot{\mathbf{q}}_{CT,PCB}$ and EIT $\dot{\mathbf{q}}_{EIT}$ pulmonary blood flow distribution. The correlation analysis in four ROIs between MDCT and EIT perfusion is depicted in graph (A). Graph (D) shows the corresponding Bland-Altman plot. The same analysis in eight ROIs is shown in graphs (B) and (E). Mean Dorsal-ventral and right-to-left profiles for both MDCT and EIT are shown in graps (C) and (F). LoA: limit of agreement. The illustration has been adapted from our publication with permission [142].

perfusion within medial regions of the lungs, presumably within the mediastinum. Finally, graphs (D) and (E) include the Bland-Altman analysis results based on four and eight ROIs. The limits of agreement (LoA) were found to be LoA $= 7.4\,\%$ for an analysis in four ROIs and LoA $= 8.8\,\%$ for eight ROIs.

All resulting similarity measures are assembled in Table 11.3. The similarity between EIT and MDCT perfusion has been analyzed with and without excluding large pulmonary arteries from the MDCT estimations. The left half of the table describes the computed similarity measures of the comparison, if larger pulmonary vessels have previously been excluded from the MDCT analysis $\dot{\mathbf{q}}_{CT,PCB}$. The right half of the table describes the same comparative measures without excluding the larger blood vessels from MDCT estimations $\dot{\mathbf{q}}_{CT}$. When larger pulmonary blood vessels were considered for MDCT perfusion estimations, the similarity in four ROIs slightly decreased (e.g. LoA increases from $7.4\,\%$ to $8.59\ \%$). Nevertheless, the similarity slightly increased in eight ROIs, when larger blood vessels were included (e.g. Pearson correlation coefficient increased from $r = 0.85$ to $r = 0.90$). The pixelwise similarity measures did not change significantly.

	Comparison of $\dot{\mathbf{q}}_{CT,PCB}$ and $\dot{\mathbf{q}}_{EIT}$			**Comparison of $\dot{\mathbf{q}}_{CT}$ and $\dot{\mathbf{q}}_{EIT}$**		
	r	**LoA (%)**	**RMSE (%)**	**r**	**LoA (%)**	**RMSE (%)**
4 ROIs	0.97	7.4	3.7	0.97	8.59	3.8
8 ROIs	0.85	8.76	4.33	0.9	7.57	3.64
	r	**r_{RL}**	**r_{VD}**	**r**	**r_{RL}**	**r_{VD}**
Pixel	0.83 ± 0.06	0.85 ± 0.12	0.92 ± 0.05	0.82 ± 0.06	0.82 ± 0.11	0.92 ± 0.05

Table 11.3: Assembled results of the statistical comparison between perfusion estimated from MDCT and EIT measurements. Mean $\pm$ standard deviation over all analyzed animals are depicted. The left half of the table includes the results of the comparison between estimated EIT blood flow $\dot{\mathbf{q}}_{EIT}$ and MDCT estimations without considering larger pulmonary vessels $\dot{\mathbf{q}}_{CT,PCB}$. In the right part of the table the results for the same analysis are shown, but without the removal of larger blood vessels $\dot{\mathbf{q}}_{CT}$. r: Pearson's correlation coefficient; LoA: limits of agreement of a Bland-Altman analysis; RMSE: root mean square error; ROI: region of interest

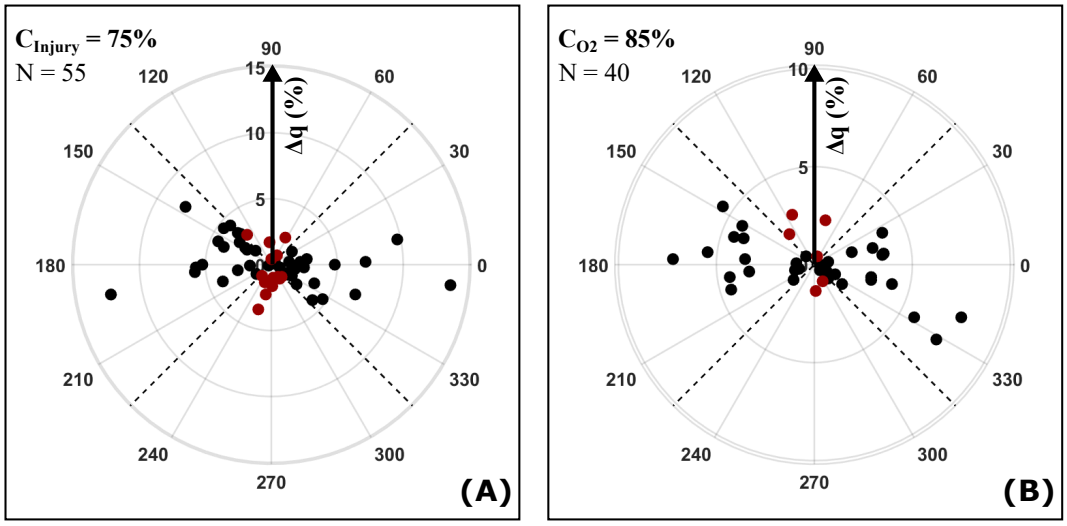

Figure 11.6: Concordance analysis of spatial perfusion changes between MDCT and EIT depicted as polar plot. Spatial increases and decreases in regional blood flow between healthy and injured lung (A) and between normoxia and hyperoxia (B) compared. EIT $\Delta\dot{\mathbf{q}}_{EIT}$ and MDCT differences $\Delta\dot{\mathbf{q}}_{CT}$ showed concordant changes, if the sign of the estimated change was the same (the concordant area is limited by the dashed lines). • points represent concordant differences and • points visualize discordant changes between MDCT and EIT within an ROI. Perfusion changes below 1 % of the maximal detected difference for EIT and MDCT estimations were not considered. The illustration has been adapted from our publication with permission [142].

11.3.2 Tracking temporal changes of relative spatial distribution

During clinical therapy, it might be often more relevant to track changes of spatial perfusion in order to analyze whether the patient responded to the treatment. For example during lung recruitment maneuvers, the anesthetist is interested, whether regions with insufficient pulmonary blood flow (dead space) are reperfused again and matched with ventilation. For this reason, we calculated spatial maps of perfusion changes between injured and healthy lungs with both MDCT and EIT methods $\Delta\dot{\mathbf{q}} = \dot{\mathbf{q}}_{Injury} - \dot{\mathbf{q}}_{Healthy}$. We investigated the concordance between EIT and MDCT changes in eight ROIs (as described in 11.3). Concordance between MDCT and EIT was found, if perfusion within the ROI changed into the same direction for both methods. Changes below 1 % were excluded from the analysis. The corresponding polar concordance plot is depicted in graph (A) of Figure 11.6. We observed concordant blood flow changes by EIT and MDCT in $C_{\text{Injury}} = 75\,\%$ of all ROIs and for all animals.

The concordance analysis was repeated to investigate, whether spatial perfusion changes, as measured with EIT, were in concordance with MDCT estimations after increasing F_IO_2 to 1.0 in healthy or injured lungs. We found a high level of concordance between EIT and MDCT estimations ($C_{O_2} = 85\,\%$). In general we found an increase of perfusion in dorsal regions and a decrease of perfusion in ventral areas of the lungs, after an increase of F_IO_2 to

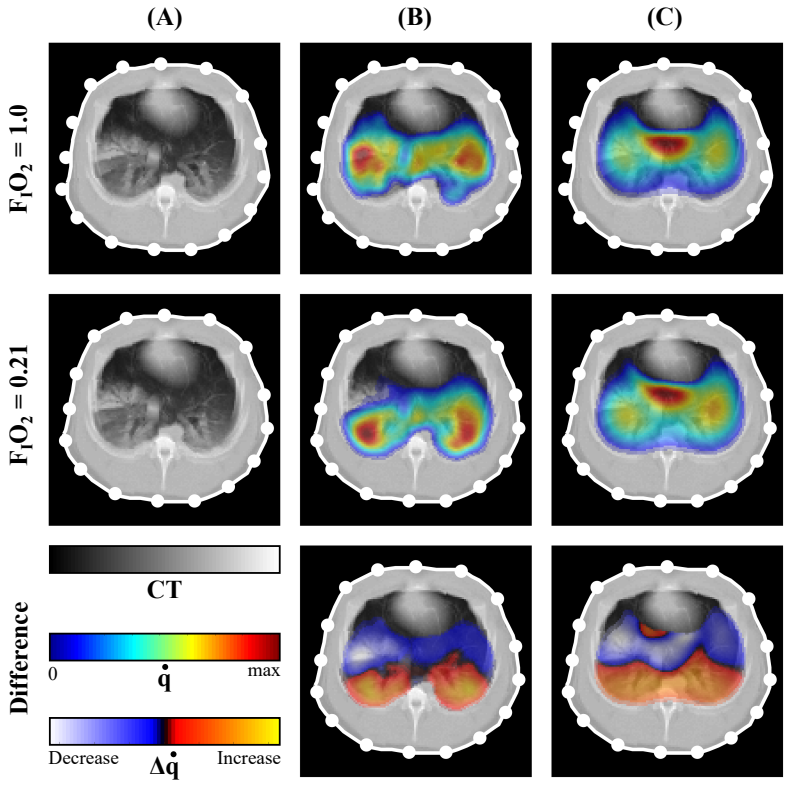

Figure 11.7: Regional blood flow distribution for two different F_IO_2. Grayscale CT images (A) are depicted together with computed CT blood flow $\dot{\mathbf{q}}_{CT,PCB}$ (B) and computed EIT blood flow $\dot{\mathbf{q}}_{EIT}$ (C) for F_IO_2=0.21 in the injured lung (upper row) for F_IO_2=1.0 in the injured lung (middle row). The spatial increases and decreases in perfusion ($\Delta\dot{\mathbf{q}}_{CT,PCB}$ and $\Delta\dot{\mathbf{q}}_{EIT}$) from a F_IO_2=0.21 to a F_IO_2=1.0 are depicted in the last row. The images have been taken from our publication with permission [142].

1.0. A representative image of the redistribution of perfusion due to an increase of F_IO_2 is depicted in Figure 11.7.

11.3.3 Spatial distribution of transit times

The described MDCT and EIT reconstruction methods do not only provide estimations of regional, relative amounts of spatial perfusion, but also enable the analysis of the temporal transit times of an indicator to a specific compartment of the lung. The parameters $\bar{\mathbf{t}}_{CT}$ and $\bar{\mathbf{t}}_{EIT}$ have been exploited as transit time measures. Figure 11.8 depicts an example of mean indicator transit times estimated by MDCT and EIT. For both $\bar{\mathbf{t}}_{CT}$ and $\bar{\mathbf{t}}_{EIT}$, a decrease of mean temporal transit time within the injured right lung was observed. The transit time distributions were found to be very similar between MDCT and EIT. For MDCT estimations, larger blood vessels were excluded from the analysis. A statistical analysis was not conducted.

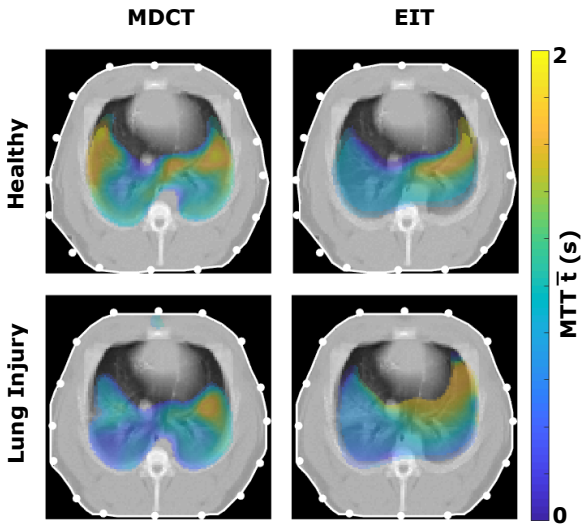

Figure 11.8: Exemplary images of transit time distributions $\bar{\mathbf{t}}$. The left column depicts estimated indicator transit times estimated by MDCT in the healthy and the injured lung. The right column displays the reconstructed mean transit times by EIT for the healthy and the injured lung. MDCT: multidetector computed tomography; EIT: electrical impedance tomography; MTT: mean transit time

11.4 Discussion

In the presented data analysis of an experimental study comprising eight animals, a robust variant of the indicator-enhanced EIT perfusion imaging (as introduced in chapters 9 and 10 was applied to reconstruct spatial pulmonary blood flow in healthy and regionally injured lungs. The estimated spatial distributions were compared against iodine-enhanced MDCT imaging, to our knowledge for the first time. We found strong similarity between MDCT and EIT perfusion images based on ROI based and pixel wise correlation and Bland-Altman analyses. We further evaluated the concordance of MDCT and EIT imaging to track changes in perfusion after establishing regional lung injury of MDCT and EIT. In 75 % of the defined ROIs and over all animals, the direction of change was consistently detected.
The EIT reconstruction algorithm was chosen and optimized to be automatic and robust. A standard normalized and linearized reconstruction algorithm imposing spatial smoothness was used. For reconstruction, we did not consider any *a priori* information about the background conductivity within the thorax. We assumed a homogeneous background distribution, which most likely will also be used in clinical routine, since for ICU patients, CT or MRT scans are usually not available. After reconstruction, the recirculation component was removed by a developed piecewise linear fit in contrast to previous work. In [109], the recirculation component was not explicitly removed, which might result in an overestimation of spatial perfusion. In [19], the recirculation component was removed by a gamma variate fit to the pixel wise fit of a gamma variate model to the measured spatial conductivity changes. The superimposed recirculation was not previously removed, such that regional perfusion might be slightly overestimated. In the presented study, the gamma variate fit was waived to improve robustness, yet the recirculation component was initially and explicitly removed. Furthermore, the regions within the thorax participating in the pulmonary circulation before and after the lungs (left and right heart as well as main PA and PV) were detected with an intuitive, yet robust, method based on K-means clustering. In [109] and [201], the pre- and post lung phases are removed in a very elegant way, based on modeled temporal transfer functions between pre-lung, lung, and post-lung compartments. Yet, the method might lack robustness in clinical practice, since the initialization of the semi-negative-matrix-factorization approach is crucial. In addition, the method suggested by Hentze only considers one single compartment for the whole lung and therefore assumes equal transit times within the whole lung.

Comparison of spatial MDCT and EIT perfusion estimations EIT and MDCT perfusion were found to be very similar, as described by different correlation and Bland-Altman based measures. Ventral regions were observed to be slightly overestimated by EIT in comparison to MDCT. In previously published studies, similar results were found, when comparing EIT to SPECT [19, 109] and to PET [121]. We hypothesize, that the origin of this ventral overestimation is manifold. Though the removal of the non-pulmonary regions have been robustly detected, as depicted in Figure 11.2, contributions of the left heart might be not

removed completely in some cases. This insufficient heart region removal might lead to an overestimation, especially in ventral regions of the left lung, and a potential misinterpretation of pulmonary blood flow. Hentze et al. [109] also came to a similar conclusion. In addition, the anatomical distance of ventral lung regions to the voltage measuring electrodes is substantially smaller compared to distances between electrodes and dorsal lung regions. For adjacent EIT stimulation, the sensitivity to conductivity changes is decreasing with increasing distance to the surface and the measuring electrodes. Thus, a sensitivity gradient between ventral and dorsal regions of the lungs can be expected. This effect might additionally be emphasized by the anatomical position of the heart in anterior position within the thorax. Due to its high electrical conductivity, the current density around the heart is most likely higher than in posterior regions of the body, which hereby further increases sensitivity in ventral regions further.
Additionally, we investigated similarity between EIT and MDCT perfusion with and without the exclusion of the larger PAs and PVs from the MDCT estimations. We did not observe a particular similarity difference after including larger pulmonary vessels. Thus, we did not reach a clear conclusion, whether EIT perfusion represents mainly the perfusion of the PCB, as the simulation study in chapter 8 indicated. Yet, we can state, that EIT perfusion does contain a considerably strong component of capillary perfusion, and consistently follows MDCT perfusion change. In the next chapter, we validated indicator-enhanced EIT perfusion against PET, which purely represents capillary perfusion.
We observed a clear imbalance between perfusion to different ROIs for the similarity analysis in four ROIs. The ROIs were chosen based on MDCT anatomy. Yet, the systematically different amounts of perfusion to the different ROIs leads to an increase in correlation, which is independent of MDCT and EIT perfusion estimation similarity. Thus, the similarity in four ROIs should always be interpreted in conjunction with the eight ROI and pixel wise similarity measures.

Tracking temporal changes of spatial perfusion We found concordant changes of perfusion in 75 % of ROIs between MDCT and EIT perfusion estimations after the induction of regional lung injury. Since a 10 % NaCl indicator was used for the measurement, we do not expect strong differences of spatial sensitivity due to changes of background conductivity in injured regions (compare with results of chapter 7). Two distinctly different experimental lung injury models were used. In three animals, experimental lung injury was induced by repeated saline lavage, which most likely leads to a surfactant washout [202]. We observed a decrease in dorsal perfusion and a shift of perfusion to more ventral regions of the lungs, which is most likely due to hypoxic pulmonary vasoconstriction (HPV) [203, 204]. In the injured region we observed an increase of regional perfusion with both MDCT and EIT measurements. We expected a decrease of perfusion also due to HPV, yet it might be superimposed by the redirection of perfusion from dorsal regions, since the injury was located in the medial lobe of the right lung.
For animals with lung injury induced by Endotoxin, we observed a decrease of perfusion in injured regions. This might be due to the fact, that Endotoxin leads to inflammatory response

and has been associated with the formation of edemas and regional perfusion blocks as well as the reduction of the effect of HPV [205].
When F_IO_2 was increased from 0.21 to 1.0, we found concordant perfusion changes within 85 % of the ROIs across all animals. In almost all cases, a decrease of perfusion in ventral regions of the lungs and an increase of relative perfusion in dorsal regions was observed. This finding is in accordance with the results from Li et al.[206]. They found also found an increase of dorsal perfusion with an increase of F_IO_2 and concluded, that hyperoxic vasodilation might be responsible for this effect.

Investigation of temporal transit times Mean temporal transit times to different regions of the lungs might contain additional clinical information about the PVR in different regions of the lungs. Besides PVR, the transit times are mainly influenced by the pulmonary artery pressure (PAP) and the CO. We visually investigated indicator transit times for EIT and MDCT perfusion estimations. Though we did not statistically investigate similarity between MDCT and EIT transit times, we found MDCT transit times to be generally larger than EIT transit times. This finding might be due to the difference in viscosity of the indicators used for MDCT and EIT. Iodine indicators have a higher viscosity in comparison to saline solutions and presumably need longer propagation times through the pulmonary circulation at the same flow rate, if it is not completely encapsulated by blood. This hypothesis was also investigated in [173]. They found different pulmonary transit times between saline indicators for thermal measurements and indocyanine green for optical measurements [173].

Limitations The study comprised eight animals, which did not allow to test for statistical power. Yet, the study population was still considerably larger compared to previously published EIT perfusion studies [19, 109, 197].
Relatively small pigs were included in this study, which had considerably smaller thorax diameters and circumferences than human thoraxes. Thus, the inverse problem might be slightly less ill posed, since areas within the center of the thorax might be more sensitive to conductivity changes.
Only one EIT indicator perfusion reconstruction algorithm was considered for the described study. A comparison between different reconstruction algorithms has not been performed throughout this study. A very robust algorithm has been chosen, which imposes spatial smoothness on the EIT reconstruction. To improve reconstruction resolution, different reconstruction algorithms such as the Graz consensus reconstruction algorithm for EIT (GREIT) algorithm [93] should be applied and compared, as it has been done for ventilation [183]. A thorough comparison between different reconstruction approaches will be conducted in the next study of chapter 12.
Additionally, a rather large saline indicator concentration of 10 % was used, though it is yet considerably smaller compared to the first published indicator-enhanced EIT perfusion study [19]. The study presented in the next chapter addresses the question on how far we can reduce indicator concentration to maintain sufficient imaging quality.

Chapter 12

Analysis of the preclinical study in Dresden

The study and the EIT-PET method comparison was initially published as journal article [121]. Additionally, we published different aspects of the study analysis in multiple conference contributions [122–124]. The following analysis exceeds the scope of all described publications.

12.1 Motivation

To finally evaluate all variants of the developed EIT perfusion estimation methods, the estimated spatial distributions of pulmonary perfusion have been compared against PET/CT perfusion. In comparison to the comparative perfusion estimation method of the study described in the previous chapter, where EIT perfusion was compared against MDCT perfusion, estimations of perfusion by PET/CT can be regarded as actual ground truth of capillary perfusion. Pulmonary blood flow in larger vessels is not measured with PET, since the injected ^{68}Ga labeled albumin particles of the injected microspheres distribute within the small capillaries during first passage through the lungs [135]. During the following study, we compared the spatial perfusion distributions as estimated by EIT, to PET/CT perfusion estimations for five different experimental states of ventilation and perfusion. The study design and the comprehensive experimental protocol has already been described in chapter 5. Briefly, five different experimental protocol steps have been conducted in 13 animals: uni-lateral ventilation of the lung (S1); bi-lateral ventilation at an optimal PEEP (S3) (as defined by the Costa approach, see section 2.2.3); experimental surfactant washout lung injury model by repeated lung lavage (S4); bi-lateral ventilation at a very high (maximal) PEEP (S6); uni-lateral PA block (S7). To recruit collapsed lung regions after uni-lateral ventilation and experimental lung injury, recruitment maneuvers have been conducted including decremental PEEP trials.
The study was mainly designed to investigate the clinical feasibility of an EIT perfusion

estimation method. Multiple research questions were investigated, in order to assess its clinical potential:

Comparison of EIT perfusion estimation methods For ventilation reconstruction it has been shown, that different EIT reconstruction algorithms produce substantially different images (e.g. [183]). In order to investigate whether different EIT perfusion estimation approaches also produce different reconstructed pulmonary blood flow distributions, we compared the four different reconstruction approaches introduced in chapter 9 against PET perfusion. Additionally, we compared two different types of perfusion parameter estimations.

Necessary saline indicator concentration As described in the state of the art section, there have been a handful of published studies, which validated indicator-enhanced EIT perfusion against other perfusion measurement techniques. Borges et al. [19] have used a saline indicator bolus with a concentration of 20 % sodium chloride (NaCl). The very high sodium concentration and osmolarity of such a solution will lead to substantial changes in pulmonary vascular resistance (PVR) and cause shifts of water. It might even have an influence on cardiac electrophysiology upon indicator arrival in the coronary circulation [108]. In the study published by Hentze et al. [109] and in the study presented in the previous chapter, an indicator bolus with a 10 % NaCl concentrated solution has been injected. While this lower concentration might be a step towards a clinical application, an even lower concentration would most definitely lead to an even larger clinical acceptance. For this purpose, we compared spatial EIT perfusion estimations with PET using different saline indicator concentrations between 2 % and 10 % NaCl.

Tracking temporal perfusion changes Besides the information of the perfusion distribution at a certain time point during therapy or diagnosis, tracking perfusion changes over time might allow the clinical staff to analyze the redistribution of lung perfusion during therapy or lung injury development. Since we have seen in chapter 7, that the comparability of EIT estimates of different perfusion states depend on the background conductivity and the indicator concentration, we also investigated the ability of EIT to track regional perfusion changes for different NaCl concentrations in experimental instead of simulated measurements by comparing them to the changes estimated by PET.

Other secondary research questions Additionally, we have investigated, whether a breath hold phase could be avoided, by injecting the indicator during ongoing ventilation. This would increase clinical acceptance, since a breath hold phase introduces avoidable additional stress for severely ill patients.

12.2 Methods

Besides the main EIT processing methods to estimate spatial perfusion, which have been introduced in chapters 9 and 10, all necessary processing steps needed to compare EIT and PET perfusion are introduced in this section.

12.2.1 Creation of animal specific reconstruction model

In order to reduce EIT reconstruction artifacts due to shape and electrode positioning errors, animal specific reconstruction models have been created. Since the animals were not repositioned during all experiments and the attached electrode belt remained in its initial position, a joint reconstruction model was used for all experimental steps. For each experimental step, the tissue density and hereby the 3D anatomy was recorded by CT measurements. The CT measurements were reconstructed with a slice thickness of 2 mm and matrices of 512×512 pixels ($1.37 \times 1.37\,\mathrm{mm}^2$). The CT volume was downsampled to the resolution of the PET measurements, resulting in a 3D matrix with $168 \times 168 \times 198$ voxels and a resolution of 2 mm in all spatial dimensions. This downsampled matrix was also used for attenuation correction of the PET measurements. The 16 electrodes and the torso surface were automatically segmented from this CT matrix using image thresholding and region-growing in *MATLAB R2017a*. From the segmented electrodes, the central coordinate for each electrode on the torso surface was calculated and defined as electrode position. In order to optimally register the segmented torsos of the individual experiments, point cloud registration (PCR) was performed [200] and all the center electrode positions were hereby aligned to the positions of the reference state (optimal PEEP (S3)). Joint electrode

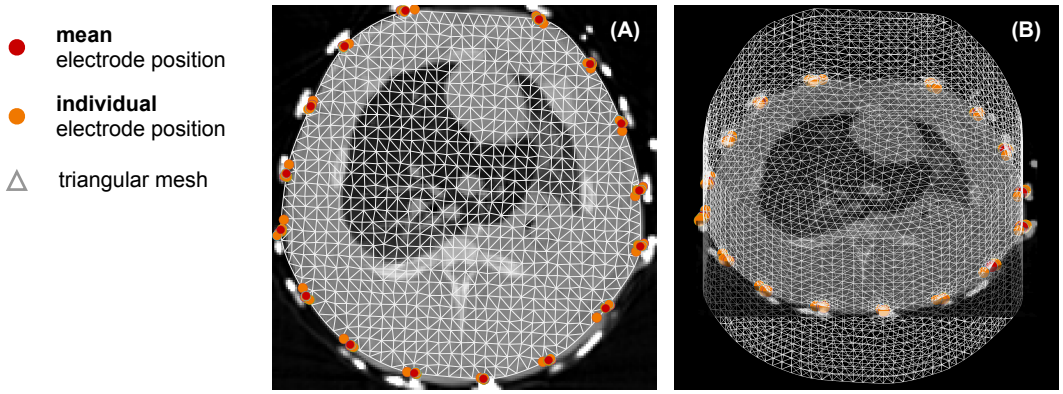

Figure 12.1: Exemplary created reconstruction models used for EIT reconstruction during the analysis of the Dresden study. Image (A) depicts the CT image within the electrode belt level. The individual electrode and joint electrode positions as well as the triangulated 2D reconstruction mesh is shown. The 2D reconstruction model was used for all algorithms. Besides the GREIT reconstruction, the 2D-mesh was also used for the forward calculation. For the GREIT reconstruction, a 2.5D mesh was used for forward calculation as depicted in image (B). The 2D torso surface was herefore extruded.

positions were calculated from the registered electrode positions by averaging. The registered experiment specific electrode positions are depicted together with the mean positions in Figure 12.1. A mean 2D-torso boundary within the electrode plane was computed from all registered boundaries and was additionally smoothed in the polar coordinate space. The 2D torso was triangulated with a *Delaunay* triangulation algorithm implemented in *MATLAB R2019a*. The two-dimensional reconstruction meshes had a mean edge length of 5.2 mm $\pm$ 0.5 mm and comprised $K = 1624.5 \pm 36.8$ elements. For the GREIT reconstruction, the forward calculation was performed in a 2.5D space. The 2D surface was therefore extruded in the vertical (cranial-caudal) direction using functions provided by EIDORS [169] and *NETGEN* [207]. The GREIT forward model consisted of $K = 12345.3 \pm 208.4$ elements and had an average edge length of 4.7 mm $\pm$ 0.81 mm.

12.2.2 EIT reconstruction

One of the main goals of this study was to compare different EIT reconstruction approaches for estimating regional pulmonary perfusion distributions. The four underlying algorithms have been introduced in chapter 9. We compare the standard 0^{th} order Tikhonov and Laplace regularization approaches, the combination of both regularizations and the GREIT algorithm against the ground truth PET perfusion measurement. The performance of the algorithms was evaluated based on the similarity between spatial EIT and PET perfusion. Except for the GREIT approach, the reconstruction algorithms solved the inverse and forward problem for a triangular 2D mesh within the electrode plane, as depicted in graph (A) of Figure 12.1. To simulate the clinical application, in which normally no bedside MRT or CT measurement is available, a homogeneous background conductivity distribution $\boldsymbol{\sigma}_0 \in \mathbb{R}^{K\times 1}$ was assumed for algorithms. For the GREIT approach, the forward problem of EIT was solved in the 2.5D extruded mesh as depicted in image (B) of Figure 12.1.
For all algorithms except the GREIT reconstruction, the regularization weighting parameter λ was calculated using the L-curve method [90]. An optimal λ was found by the L-curve method for each experimental state, animal and indicator concentration individually and was generally robust. Nevertheless we experienced cases were a non-optimal λ was found. To minimize the effect on the reconstruction method comparison of these outliers, the median λ over all animals for each state and indicator concentration was finally used. For the GREIT algorithm however, the regularization weighting was chosen, such that an NF $= 0.5$ was achieved (as recommended in [93], see section 3.1.3).
In addition we compared the two types of perfusion parameter estimation approaches as introduced in chapter 10: maximal slope and deconvolution method. For both methods, we had to remove the pre- and post lung phases to extract pure pulmonary blood flow and neglect right and left heart phases as well as main PA and PV blood flow within the mediastinum. The clustering as introduced in chapter 10 was performed for each individual reconstruction, yet we also computed averaged phases for each experimental state and animal, to neglect the influence of non-optimal detections on the main similarity analysis. Figure 12.2 shows exemplary spatial perfusion estimations by indicator-enhanced EIT with and without the

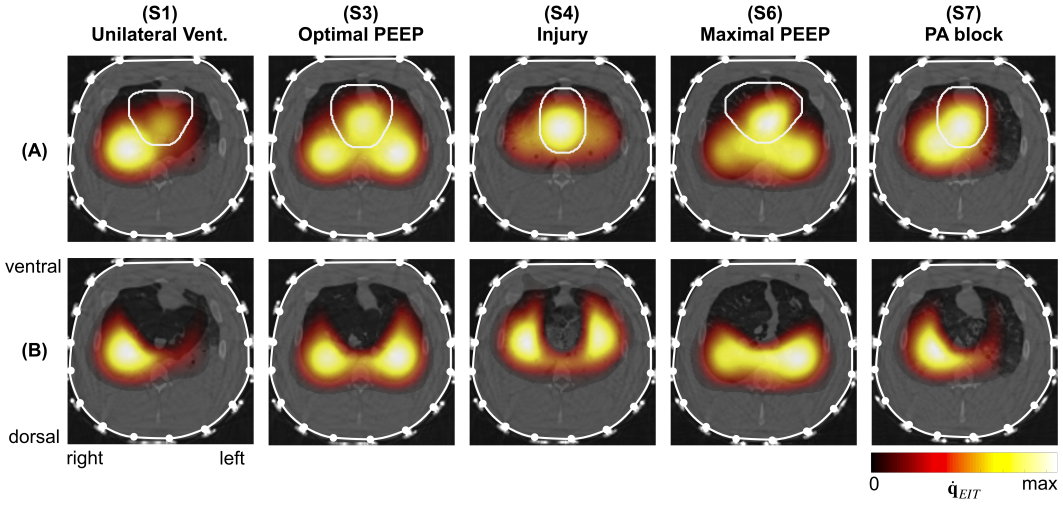

Figure 12.2: Exemplary reconstructed spatial lung perfusion estimations $\dot{\mathbf{q}}_{EIT}$ with and without the removal of pre- and post-lung circulation phases. The images in row (A) shows estimated perfusion without the removal of the heart and major vessels and the images in row (B) depict the lung perfusion estimations after the removal.

removal of the pre- and post-lung phases.
The final lung perfusion estimations $\dot{\mathbf{q}}_{EIT} \in \mathbb{R}^{K\times 1}$ were normalized to the overall image sum in order to achieve relative perfusion estimations:

$$\dot{q}_{EIT,k} = \frac{\dot{q}_{EIT,k}}{\sum_k \dot{q}_{EIT,k}} \tag{12.1}$$

12.2.3 PET/CT imaging

For a detailed description of the PET perfusion measurement and the CT based attenuation correction be referred to our publication [121]. The final three-dimensional PET perfusion distribution $\dot{\mathbf{Q}}_{PET} \in \mathbb{R}^{168\times 168\times 198}$ was calculated by calculating the ^{68}Ga net activity, which was subtracted from the background ^{68}Ga activity from previous PET measurements. To allow a fair comparison between regional EIT and PET perfusion estimates, the three-dimensional PET measurement $\dot{\mathbf{Q}}_{PET}$ was projected on the two-dimensional EIT electrode plane with some vertical (cranial-caudal) weighting $w_{PET}(d)$ depending on the vertical distance d to the EIT electrode plane level z_{E}. We initially considered three different weightings:

- rectangular weighting: $$w_{PET}(d) = \begin{cases} 1 & d \leq 10\,\mathrm{cm} \\ 0 & \text{otherwise} \end{cases}$$
- triangular weighting: $$w_{PET}(d) = \begin{cases} 1 - \frac{1}{10\,\mathrm{cm}} \cdot d & d \leq 10\,\mathrm{cm} \\ 0 & \text{otherwise} \end{cases}$$

- EIT sensitivity based weighting: $w_{PET}(d) = s(d)$

The EIT sensitivity based weighting was proposed in [149]. The weighting was chosen to the proposed profile $s(d) \in [0,1]$, which was similar to the cranial-caudal profiles of the healthy reference state (S3) in chapter 7. The resulting two dimensional PET perfusion images $\dot{\mathbf{q}}_{PET} \in \mathbb{R}^{168\times168}$ were calculated by:

$$\dot{q}_{xy} = \sum_{z} \left(w_{PET}(z - z_{\mathrm{E}}) \cdot \dot{Q}_{xyz} \right) \tag{12.2}$$

Images (B)-(E) of Figure 12.3 show the different two-dimensional weighted PET images. Since the differently weighted PET images were very similar, we only considered the EIT sensitivity weighted PET estimates for the following analyses. The PET perfusion distributions were finally also normalized to the image sum:

$$\dot{q}_{PET,k} = \frac{\dot{q}_{PET,k}}{\sum\limits_{k} \dot{q}_{PET,k}} \tag{12.3}$$

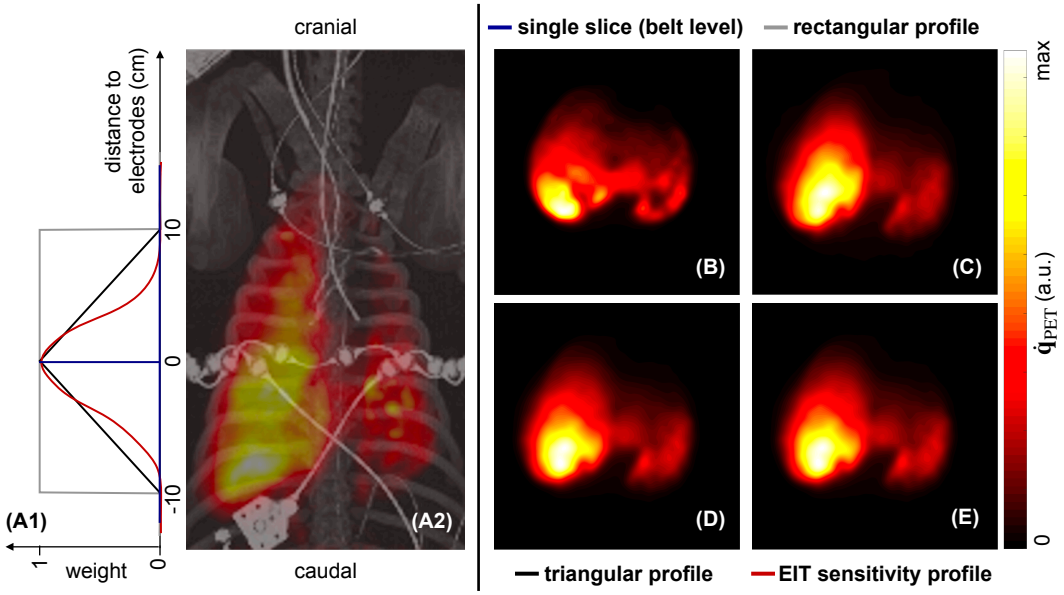

Figure 12.3: Graphical description of the PET image weighting. In order to validate EIT perfusion with PET, the three-dimensional distribution of pulmonary blood flow was projected onto the cross section within the electrode plane. Three different projections have been considered for this reason. The weighting profiles are depicted in graph (A1). The distribution of PET perfusion in cranial-caudal direction is depicted in image (A2). Images (B)-(D) show the different variants of projected 2D PET images.

12.2.4 Comparison of spatial PET and EIT perfusion estimations

The comparison between the two imaging modalities was performed similar to the comparison between EIT and MDCT perfusion estimates in chapter 11. The triangular EIT distributions $\dot{\mathbf{q}}_{EIT}$ were mapped to the $[168 \times 168]$ PET pixel map for each experimental step. The similarity of the perfusion pixel images was evaluated by different ROI and pixel based correlation and Bland-Altman analyses. Additionally, we also calculated the root mean square error (RMSE) within the ROIs or pixels.

ROI based similarity Both PET and EIT images were split into eight ROIs and the relative amount of perfusion to the ROIs were compared between the modalities. We defined the ROIs based on the segmented lung from the CT measurements of the healthy reference state (optimal PEEP (S3)) as depicted in image (A) of Figure 12.4. The lungs were segmented into eight equally large compartments based on the centroid of the segmented lungs and on the bounding box around the lung segmentation. For supine position of the pigs, a strong imbalance between dorsal and ventral lung perfusion will exist for all experimental states. This imbalance will lead to very high correlation values and differences between reconstruction methods will be hard to distinguish. For this reason we opted for a second ROI definition based on the three-dimensional PET distribution of the healthy reference state (optimal PEEP (S3)). The ROIs were therefore not chosen to have equal size but equal relative amount of PET estimated perfusion within the ROI. The ROI definition is depicted in image (C) of Figure 12.4. Image (B) depicts the three dimensional PET distribution of the healthy reference state and its corresponding centroid.

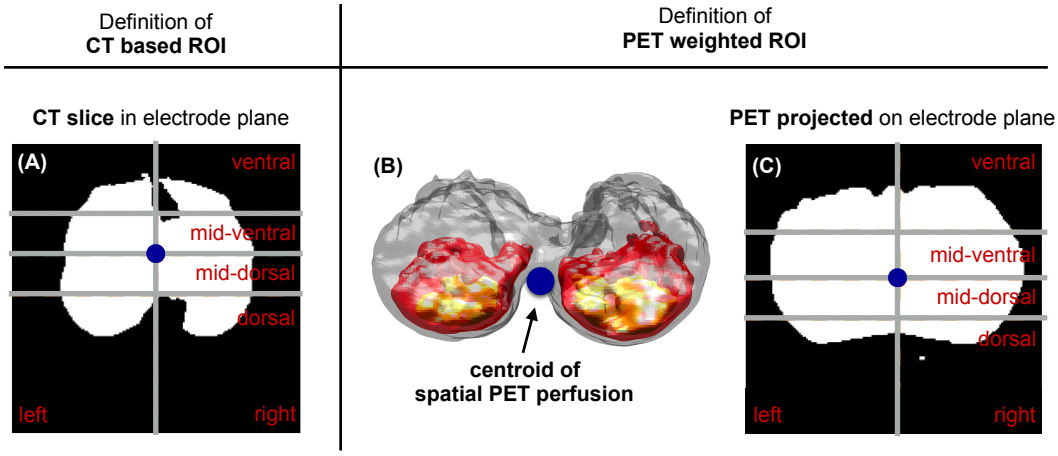

Figure 12.4: Definition of two different types of ROIs for similarity analysis between EIT and PET perfusion. In image (A), the ROI based on the two-dimensional CT segmentation are shown. Image (B) and (C) describe the definition of ROIs based on the three-dimensional PET perfusion distribution.

Pixel based similarity Similar to the pixelwise analysis in chapter 11, we also calculated pixel based similarity measures to especially allow the evaluation of the similarity between perfusion profiles. Herefore, we cut out the lung region from PET and EIT perfusion images as defined by the bounding box around the lung segmentation from the CT matrix. The cutout image was resampled to $[64 \times 64]$ pixel for the same reasons as explained in chapter 11. Based on the cutout PET and EIT images, we calculated a pixelwise Pearson correlation r_{Pixel}, and the correlation between the right-to-left profile r_{RL} as well as for the ventrodorsal profiles for the left r_{DV-L} and right lung r_{DV-R} separately.

12.3 Results

We have considered four different EIT reconstruction approaches, two different perfusion paramater estimation methods and overall four different indicator concentrations. Additionally, we have performed the indicator-enhanced EIT measurement during breath hold and during ongoing mechanical ventilation. To simplify the result interpretation, we did not compare these variants of the EIT based perfusion estimation all at once. At first, we compared the different EIT reconstruction approaches, followed by a comparison of the max-

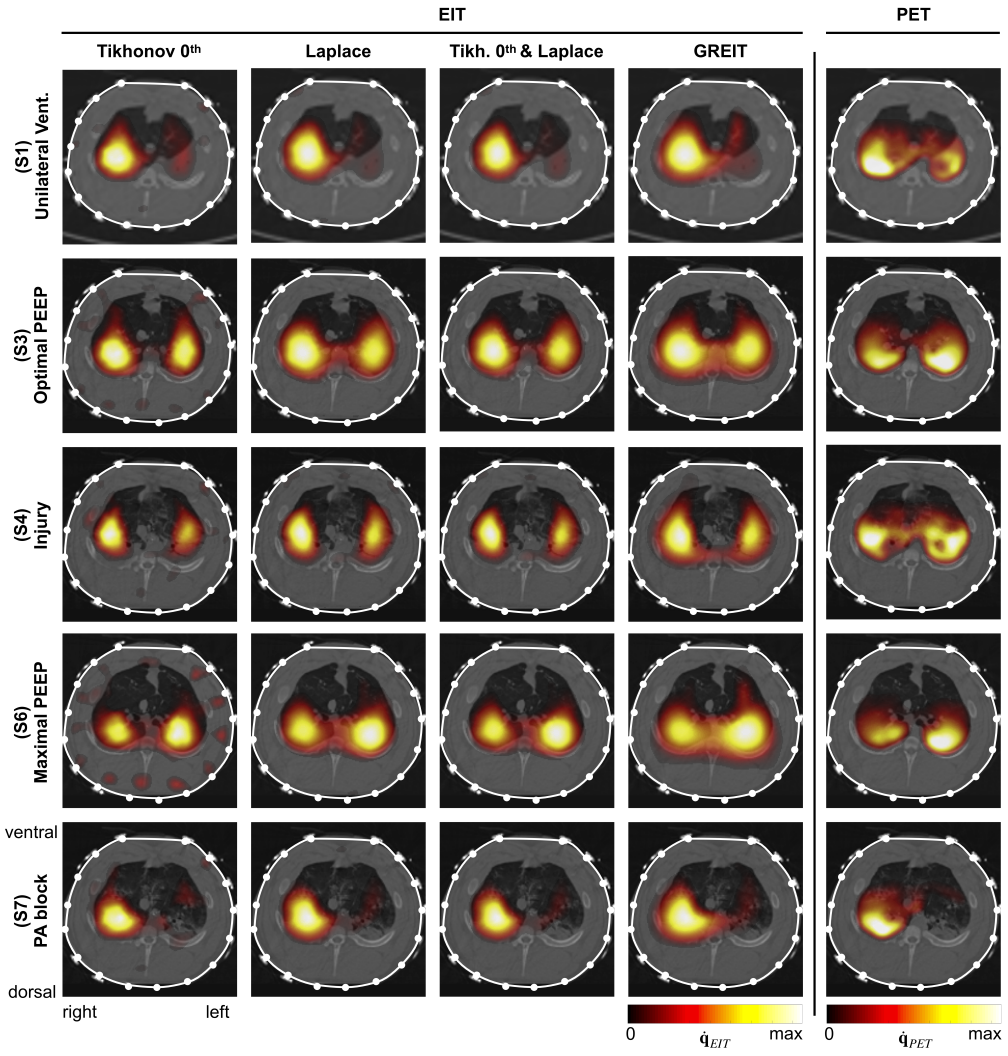

Figure 12.5: Exemplary images of the estimated perfusion distributions by the different EIT approaches (saline concentration: 10 % NaCl) and the PET approach. The first four columns from the left depict the spatial EIT based blood flow distribution for each algorithm separately and after the removal of the non-pulmonary circulation phases. The last column shows the PET based perfusion estimation. The rows represent the different experiments.

imal slope and deconvolution perfusion parameter estimation methods. Finally, we analyzed similarity between PET and EIT perfusion for different concentrations of the conductive saline indicator. All following tables, depicting the similarity measures, show mean (and standard deviation) values over all animals and experiments.

12.3.1 Comparison of reconstruction methods

An overview of exemplary EIT and PET based perfusion distributions for an indicator concentration of 10 % are depicted in Figure 12.5. The four left columns represent the

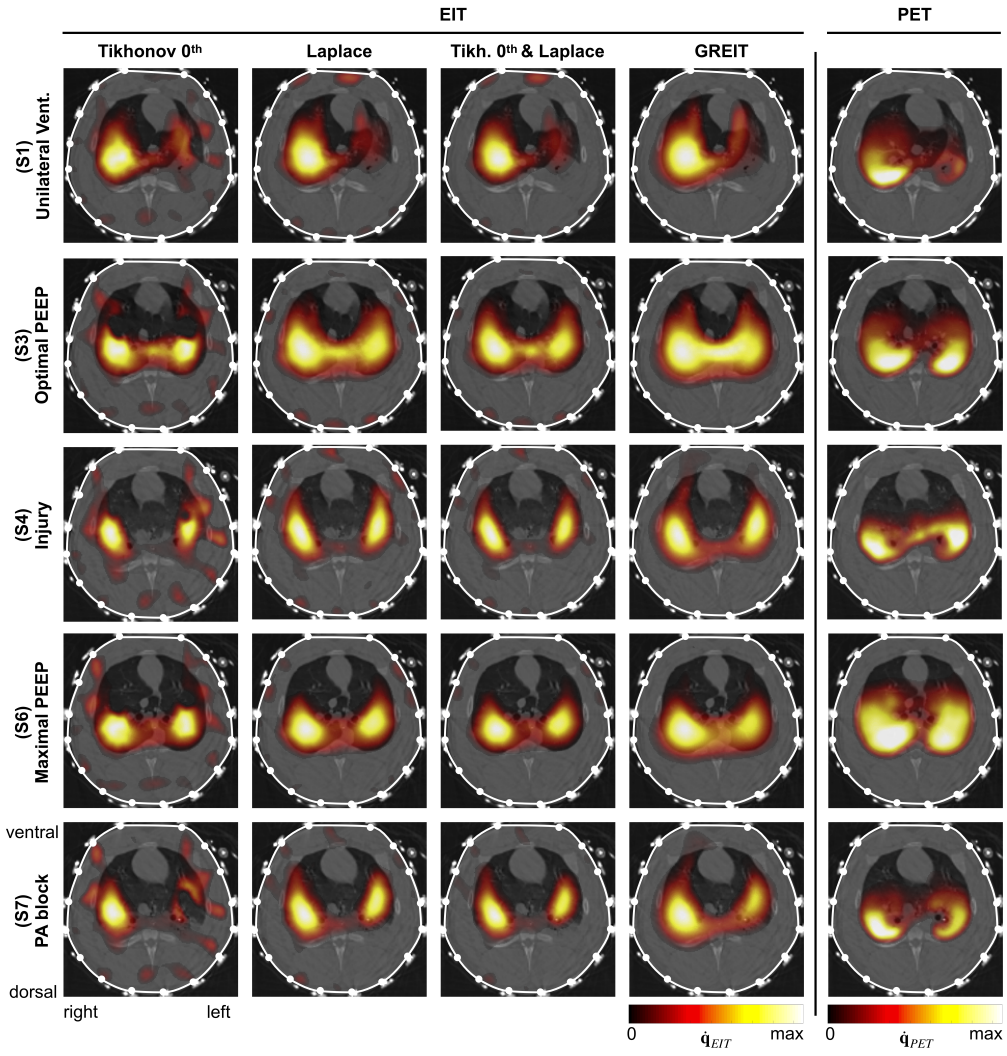

Figure 12.6: Exemplary images of the estimated perfusion distributions by the different EIT approaches (saline concentration: 3 % NaCl) and the PET approach. The first four columns from the left depict the spatial EIT based blood flow distribution for each algorithm separately and after the removal of the non-pulmonary circulation phases. The last column shows the PET based perfusion estimation. The rows represent the different experiments.

estimated spatial perfusion using the different EIT reconstruction approaches, the maximal slope perfusion estimation technique and an indicator concentration of 10 % NaCl. The non-pulmonary circulation phases have been removed and regions with a relative amount of less than 10% of the maximal amount have been made transparent. We observe very similar perfusion distributions for all EIT reconstruction methods. In some cases, the reconstruction applying a 0^{th} order Tikhonov regularization shows non-physiological perfusion amplitudes close to the electrodes. In general, we found strong visual agreement between all EIT reconstruction methods and PET. For EIT reconstructions we observed a slight ventral shift of pulmonary blood flow compared to PET perfusion.

In Figure 12.6, we can see the same perfusion images as depicted in Figure 12.5, but for an indicator concentration of 3 %. We observed stronger artifacts close to the surface especially for the 0^{th} order Tikhonov regularization. Overall the agreement between EIT and PET perfusion estimations was still visually strong.

Table 12.1 summarizes the similarity analysis between EIT and PET perfusion for different EIT reconstruction approaches. The perfusion was always estimated by the maximal slope approach and the saline indicator was 10 % NaCl. In general, for all similarity measures, the spatial perfusion estimations computed with the GREIT algorithm showed the strongest agreement with PET perfusion. We found LoA as low as 7.8 % and a pixelwise correlation of $r_{\text{Pixel}} = 0.78$. For all other regularization techniques, we found slightly decreased similarity for all measures. The ROI based similarity measures showed a slightly stronger similarity for the 0^{th} order Tikhonov and Laplace regularization compared to the combined approach. We observed the second best pixelwise similarities for the Laplace regularization. The

Similarity Measure	Tikh. 0^{th}	Laplace	Tikh. 0^{th} & Laplace	GREIT
Analysis in eight ROIs (CT based)				
r	0.92	0.92	0.91	0.94
LoA (%)	9.25	9.31	9.99	7.78
RMSE (%)	4.41	4.53	4.98	3.74
Analysis in eight ROIs (PET weighted)				
r	0.88	0.89	0.89	0.91
LoA (%)	9.44	9.55	10.45	8.02
RMSE (%)	4.82	4.79	5.12	4.08
Pixelwise analysis				
RMSE (%)	1.46 ± 0.25	1.25 ± 0.27	1.38 ± 0.29	1.16 ± 0.25
r_{Pixel}	0.75 ± 0.09	0.78 ± 0.09	0.77 ± 0.09	0.78 ± 0.09
r_{RL}	0.82 ± 0.18	0.86 ± 0.15	0.86 ± 0.15	0.83 ± 0.18
$r_{\text{DV-L}}$	0.82 ± 0.16	0.86 ± 0.14	0.84 ± 0.13	0.90 ± 0.10
$r_{\text{DV-R}}$	0.87 ± 0.16	0.92 ± 0.08	0.90 ± 0.08	0.94 ± 0.03

Table 12.1: Overview of the similarity analysis between PET and EIT perfusion distributions for different EIT reconstructions, the maximal slope perfusion estimation method and an indicator concentration of 10 % NaCl. For the correlation based measures, a value close to one represents a good correlation, for the limits of agreement (LoA) and root mean square error (RMSE) a smaller value indicates an increasing agreement between EIT and PET.

dorsoventral profiles between EIT and PET perfusion were always more similar in the right lung compared to the left lung for all reconstruction algorithms.

Since the different reconstruction algorithms might respond differently to a decrease of indicator concentration, the similarity measures of the reconstruction method comparison were also summarized for an injection of a 3 % NaCl indicator in Table 12.2. Overall, all similarity measures were slightly decreased compared to a 10 % NaCl indicator. The spatial perfusion reconstructed with the GREIT method still showed stronger similarity to PET perfusion than the other reconstruction algorithms. Interestingly, we found stronger similarity in ROI based similarity measures for 0^{th} order Tikhonov regularization compared to Laplace regularization. For pixelwise similarity measures, Laplace and the combined regularization approach showed stronger agreement with PET perfusion compared to the 0^{th} order Tikhonov regularization.

Similarity Measure	Tikh. 0^{th}	Laplace	Tikh. 0^{th} & Laplace	GREIT
Analysis in eight ROIs (CT based)				
r	0.90	0.90	0.90	0.93
LoA (%)	10.06	10.18	10.31	8.70
RMSE (%)	4.79	4.95	5.09	4.12
Analysis in eight ROIs (PET weighted)				
r	0.85	0.87	0.87	0.88
LoA (%)	9.91	10.16	10.55	8.93
RMSE (%)	5.02	5.16	5.32	4.56
Pixelwise analysis				
RMSE (%)	1.48 ± 0.39	1.33 ± 0.37	1.42 ± 0.40	1.25 ± 0.31
r_{Pixel}	0.72 ± 0.09	0.75 ± 0.09	0.75 ± 0.09	0.75 ± 0.09
r_{RL}	0.77 ± 0.13	0.81 ± 0.11	0.81 ± 0.11	0.79 ± 0.14
$r_{\text{DV-L}}$	0.81 ± 0.16	0.85 ± 0.13	0.85 ± 0.13	0.87 ± 0.09
$r_{\text{DV-R}}$	0.87 ± 0.17	0.90 ± 0.09	0.89 ± 0.09	0.93 ± 0.05

Table 12.2: Overview of the similarity analysis between PET and EIT perfusion distributions for different EIT reconstructions, the maximal slope perfusion estimation method and an indicator concentration of 3 % NaCl. For the correlation based measures, a value close to one represents a good correlation, for the limits of agreement (LoA) and root mean square error (RMSE) a smaller value indicates an increasing agreement between EIT and PET.

12.3.2 Comparison of the blood flow estimation methods

To compare the two perfusion estimation algorithms (maximal slope and deconvolution), we have only regarded the best performing EIT reconstruction approaches, namely the Laplace regularization and the GREIT reconstruction. Also we have compared the methods for an indicator concentration of 3 % NaCl and 10 % NaCl. The similarity measures are shown in Table 12.3. The perfusion estimation based on the deconvolution approach showed a reduced similarity compared to the maximal slope approach for both applied reconstruction algorithms. The differences between the estimation methods were substantial for an indicator concentration of 3 % NaCl and only marginal for 10 % NaCl.

	3 % NaCl		10 % NaCl	
Similarity Measure	**Maximal Slope**	**Deconvolution**	**Maximal Slope**	**Deconvolution**
Laplace regularization				
r	0.87	0.72	0.89	0.86
LoA (%)	10.16	13.80	9.55	9.67
r_{Pixel}	0.75 ± 0.10	0.63 ± 0.17	0.78 ± 0.09	0.73 ± 0.09
GREIT reconstruction				
r	0.88	0.80	0.91	0.88
LoA (%)	8.93	10.99	8.02	8.76
r_{Pixel}	0.75 ± 0.10	0.64 ± 0.13	0.78 ± 0.09	0.74 ± 0.09

Table 12.3: Overview of the similarity between PET and EIT for different perfusion estimation algorithms. We opted for a subset of all similarity measures. The ROI based measures (Pearson correlation r and limits of agreement (LoA) were based on the PET weighted ROIs. The pixelwise similarity was analyzed by the pixelwise Pearson correlation r_{Pixel}.

12.3.3 Analysis for different concentrations of the saline solution

In Table 12.4, the similarity measures are summarized for different indicator concentrations. Between 5 % and 10 % NaCl, no substantial difference in similarity was observed for

Similarity Measure	2 % NaCl	3 % NaCl	5 % NaCl	10 % NaCl
sample size	232	512	512	512
Laplace regularization				
r	0.85	0.87	0.89	0.89
LoA (%)	10.50	10.16	9.50	9.55
r_{Pixel}	0.73 ± 0.14	0.75 ± 0.10	0.77 ± 0.10	0.78 ± 0.09
GREIT reconstruction				
r	0.85	0.88	0.90	0.91
LoA (%)	9.47	8.93	8.37	8.02
r_{Pixel}	0.72 ± 0.13	0.75 ± 0.10	0.76 ± 0.09	0.78 ± 0.09

Table 12.4: Overview of the similarity between PET and EIT for different indicator concentrations. The spatial perfusion was estimated with the maximal slope method. We opted for a subset of all similarity measures. The ROI based measures (Pearson correlation r and limits of agreement (LoA) were based on the PET weighted ROIs. The pixelwise similarity was analyzed by the pixelwise Pearson correlation r_{Pixel}.

all measures. For concentrations below 5 % NaCl we observed a decrease in similarity with decreasing indicator concentration. The decrease of similarity for a decreasing saline concentration was similar for GREIT reconstruction and Laplace regularization. Overall similarity between PET and EIT perfusion was still strong for the lowest concentration of 2 % NaCl (GREIT: LoA = 9.47 %, Laplace: LoA = 10.5 %).

12.3.4 Separation of indicator dilution during controlled mechanical ventilation

In Figure 12.7 exemplary reconstructions for the estimation of spatial perfusion by injecting an indicator during breath hold and ongoing ventilation are shown. A strong visual similarity can be observed between the first and second row. Only for the PA block experiment the estimation during ongoing ventilation showed a substantially different spatial perfusion distribution[1].

In Table 12.5 the similarity measures are summarized. We found only small differences in similarity between EIT and PET perfusion for the injection during breath hold and during

[1] In a few animals, the PA block was not stable throughout all perfusion measurements, which might also have lead to the different estimation.

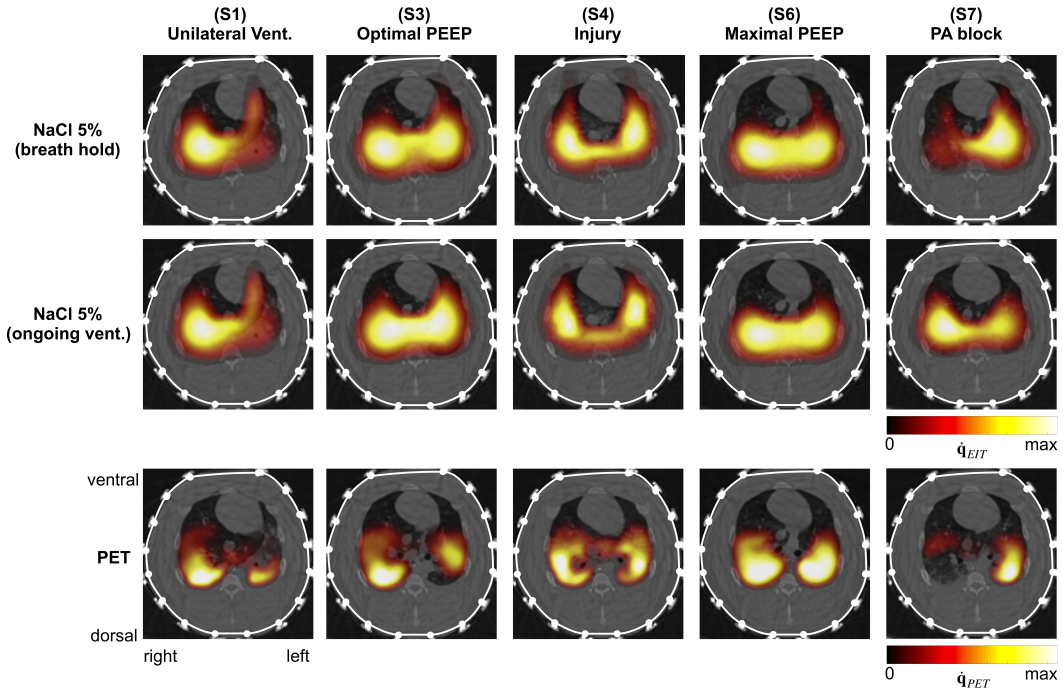

Figure 12.7: Exemplary images of the EIT perfusion estimation during breath hold and ongoing ventilation. In row (A) the reconstructions for the 5 % NaCl indicator injection during a mean airway pressure breath hold are depicted. Row (B) shows the reconstructions for the injection of the same indicator conecntration during ongoing mechanical ventilation. The images in row (C) show the PET reconstructions as a comparison. EIT reconstruction has been performed with the GREIT algorithm.

ongoing ventilation. Above all, the differences were marginal for the GREIT reconstruction approach (breath hold: $r = 0.9$ and ongoing ventilation: $r = 0.87$) .

Similarity Measure	**Breath hold - 5 % NaCl**	**Ongoing ventilation - 5 % NaCl**
sample size	512	224
Laplace regularization		
r	0.89	0.84
LoA (%)	9.50	11.28
r_{Pixel}	0.77 ± 0.10	0.73 ± 0.17
GREIT reconstruction		
r	0.90	0.87
LoA (%)	8.37	9.43
r_{Pixel}	0.76 ± 0.09	0.73 ± 0.14

Table 12.5: Overview of the similarity between PET and EIT for the injection of a 5 % saline indicator during breath hold and ongoing ventilation. The spatial perfusion was estimated with the maximal slope method. We opted for a subset of all similarity measures. The ROI based measures (Pearson correlation r and limits of agreement (LoA) were based on the PET weighted ROIs. The pixelwise similarity was analyzed by the pixelwise Pearson correlation r_{Pixel}.

12.3.5 Tracking blood flow changes

As described in chapter 11, it might be often more relevant to track temporal changes of spatial perfusion in order to analyze whether the patient responded to the treatment. For this reason, we calculated spatial maps of perfusion changes between different experimental states for both PET and EIT methods, e.g. between the unilateral ventilation (S1) and the optimal PEEP experiment (S3): $\Delta\dot{\mathbf{q}} = \dot{\mathbf{q}}_{S1} - \dot{\mathbf{q}}_{S3}$. Changes of relative perfusion can be observed in Figure 12.8. From the healthy reference state (S3) to the unilateral ventilation experiment (S1) we observed a relative increase of perfusion in the ventilated lung and a relative decrease in the blocked lung. The same changes were observed between the PA block (S7) experiment and the healthy reference state (S3). The unblocked lung was less perfused. In the third column of Figure 12.8 we observed a decrease of perfusion in dorsal regions and a increase in ventral areas, when the PEEP was increased to the maximal PEEP (S6). The spatial distribution of perfusion was found to be decreased in dorsal regions, after induction of a lung injury with repeated lung lavage (S4) in comparison to the maximal PEEP experiment (S6).

We investigated the concordance between relative EIT and PET changes in eight ROIs based on the PET distribution. Concordance between PET and EIT was found, if perfusion

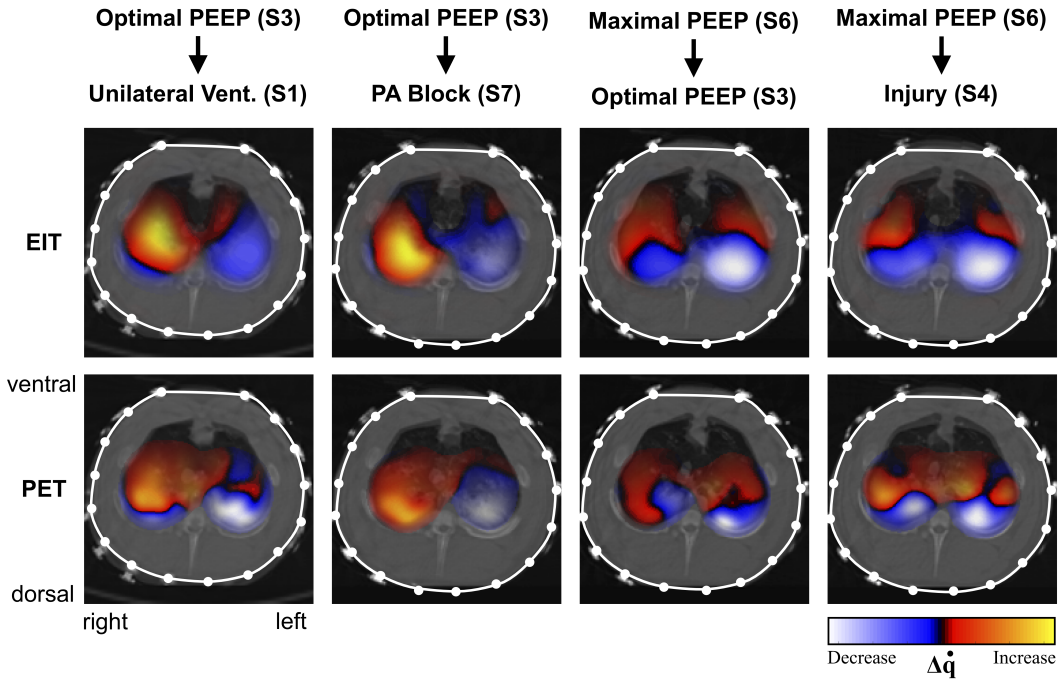

Figure 12.8: Exemplary changes of perfusion between different experimental states for an indicator concentration of 5 %, a EIT reconstruction with the Laplace regularization and the maximal slope perfusion estimation method.

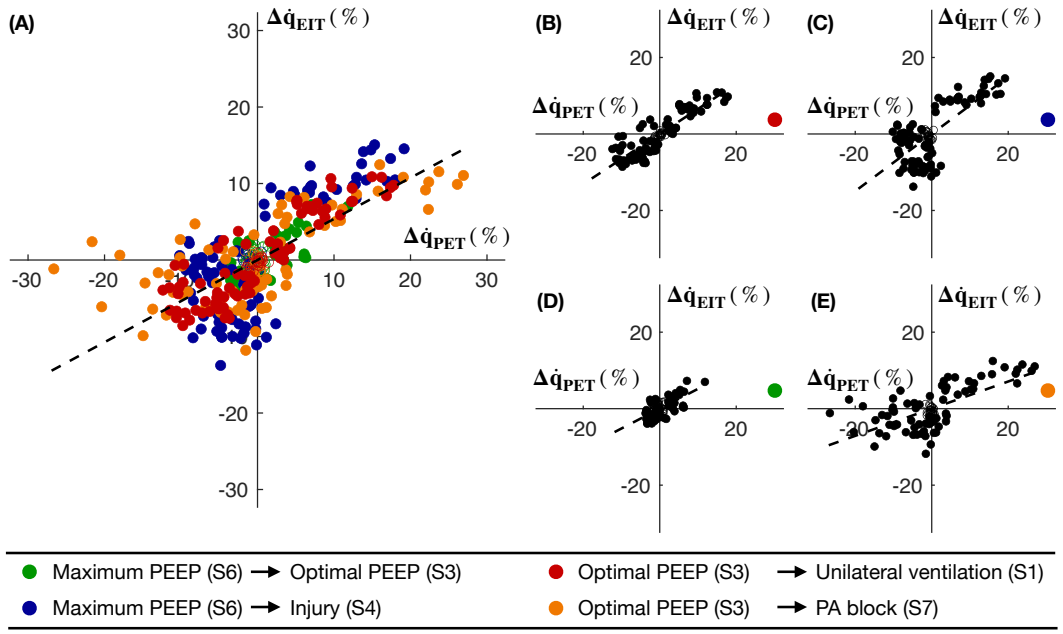

Figure 12.9: Depiction of the concordance analysis for an indicator of 10 % NaCl, the maximal slope perfusion estimation method and a Lapalce regulatization

within the ROI changed into the same direction for both methods. Changes below 2 % were excluded from the analysis. Figure 12.9 shows the the graphs of the concordance analysis for an indicator of 10 % NaCl for each individual considered experiment comparison (graphs (B)-(E)) and for all differences combined (graph (A)). The overall concordances are summarized in Table 12.6 for all indicator concentrations. The strongest overall concordance was found for an indicator concentration of 10 % NaCl. In 84.1 % of all perfusion changes within an ROI, EIT was in accordance with PET. For lower concentrations of the indicator, the concordance decreased slightly. The strongest agreement between perfusion changes as estimated by EIT and PET were found between the unilateral ventilation experiment and the optimal PEEP state.

NaCl concentration:	3 %	5 %	10 %
All changes	82.5	83.0	84.1
Max. PEEP (S6) - Opt. PEEP (S3)	65.9	71.4	68.9
Max. PEEP (S6) - Injury (S4)	82.9	83.3	85.5
Opt. PEEP (S3) - PA block (S7)	77.3	79.1	79.4
Opt. PEEP (S3) - Unilateral vent. (S1)	96.1	93.4	95.9

Table 12.6: Overview of the ventilatory, hemodynamic and gas exchange monitoring parameters. Mean values and standard deviations over all included animals are presented for each individual experimental step.

12.4 Discussion

To assess the feasibility of indicator-enhanced EIT measurements, we evaluated the spatial similarity of EIT perfusion estimates and PET perfusion for different EIT reconstruction algorithms and perfusion estimation approaches, as well as for different concentrations of the saline indicator. In general we found strong similarity between EIT and PET perfusion estimations for all methods and indicator concentrations. For the GREIT reconstruction algorithm, we found the strongest similarity to spatial PET perfusion estimation (LoA = 9.47 % for an indicator concentration of 3 % NaCl and LoA = 8.02 % for 10 % NaCl). We observed a slight ventral shift of EIT perfusion compared to PET perfusion estimations, which resulted in a correlation of the dorsoventral profiles between EIT and PET of $r_{DV-L} = 0.94$ and $r_{DV-L} = 0.90$ (GREIT reconstruction, maximal slope estimation, 10 % NaCl). The dorsoventral correlation was always stronger in the right lung, which might indicate, that the profile of the left lung is slightly compromised by an insufficient removal of especially the post-lung circulation phase. Besides this influence, we expect the sensitivity of EIT to be larger in ventral regions compared to dorsal areas (compare with sensitivity profiles as calculated in chapter 7). The ventral shift of EIT perfusion was also observed for perfusion estimations in the Iowa study in the previous chapter and was reported in multiple publications [19, 109, 121].

We found that the maximal slope perfusion parameter estimation outperformed the deconvolution based approach, especially for low indicator concentrations. A possible explanation for the lower similarity to PET perfusion might be the necessity of finding a suitable input function, which was estimated within the pre-lung phase. If the pre-lung phase is not detected robustly, a non-optimal input function will also be estimated. On top, the defined ventricular input function (VIF) must also be regarded as a rough approximation of the true pulmonary input function. Therefore, based on our results, we recommend the maximal slope approach for clinical application due to its more robust performance.

A major strength of the described study analysis, is the consideration and comparison of many different indicator concentrations. Borges et al. [19] have proposed to use an indicator concentration of 20 % saline. In successive studies, the indicator concentration was reduced to 10 % NaCl [109]. To improve clinical acceptance, the further decrease of indicator concentration would be beneficial. We found no substantial difference in similarity of perfusion estimation compared to PET perfusion between a saline concentration of 5 % NaCl and 10 % NaCl. Perfusion changes were also found with similar concordance to PET perfusion changes. Yet, one could argue, that with lower concentrations we still observed very strong similarity. Since for lower concentrations the detection of non-pulmonary regions is also more complicated (which we have neglected from our analyses by using averaged pre- and post-lung phases), we would recommend the usage of 5 % NaCl solutions based on our findings. Nevertheless, with algorithmic improvements, we feel that a additional decrease of the indicator concentration to 3 % NaCl should also be possible. The usage of different types of indicators besides NaCl might also improve the clinical acceptance.

We could also show, that a spatial perfusion estimation during ongoing ventilation is possible, since the similarity was only slightly decreased compared to the indicator injection during breath hold. The frequency filtering method, as introduced in chapter 9 is nevertheless only applicable if respiratory rates do not fall far below approximately 12 breaths per minute. These respiratory rates might nevertheless be a good choice for some ARDS patients. In this case, the separation method would need to be improved by a more adaptive filtering approach (e.g. presented in [180]) or the physician would need to temporarily change the respiratory rate to a higher value. The perfusion estimation in the current algorithmic implementation is also only possible for controlled mechanical ventilation and not for spontaneous breathing or mechanical ventilation with variations temporal variations in tidal volume (V_T) or respiratory rate (RR).

Limitations We used averaged regularization parameter λ in order to reduced the effect of the regularization weighting on the overall method comparison. A thorough study of the robustness of finding an optimal regularization parameter has not been conducted. Yet, we have observed very similar parameters throughout all experimental states, therefore indicating, that a fixed regularization parameter might be applicable in clinical practice.
The removal of pre- and post-lung phases is a crucial processing step, which is needed to extract pure pulmonary perfusion. The clustering of the pre-and post-lung phases has been averaged over the different reconstruction approaches and indicator concentrations in order to minimize the effect of the heart region on the overall reconstruction method comparison. A thorough study of the detection robustness should be performed and compared to other published techniques such as introduced in e.g. [109, 201].

PART VI

CONCLUSION AND OUTLOOK

Chapter 13

Conclusion

13.1 EIT sensitivity to indicator-enhanced pulmonary blood flow

Two simulation studies have been conducted to investigate the forward and backward sensitivity of indicator-enhanced EIT measurements in front of realistic and inhomogeneous lung conductivity backgrounds and to evaluate the contribution of different spatio-temporal compartments of the pulmonary circulation to the reconstructed EIT perfusion image. The simulation studies address the first and second main thesis objective as defined in the introduction.

1. Understand forward and inverse sensitivity of indicator dilution method in front of substantially inhomogeneous and realistic conductivity backgrounds

We found decreasing forward and inverse sensitivity with increasing distance to the electrode plane (as expected). The sensitivities were reduced by approximately 90 % at a distance of 10 cm to the electrode planes. We generally found a sensitivity imbalance for both forward and inverse sensitivity between dorsal and ventral regions. In ventral regions the sensitivity was higher. This finding might be an effect, which is pronounced for porcine anatomies, due to the large distance of the elctrodes to dorsal regions of the lungs.

The different inhomogeneous distributions of pulmonary background conductivities had a strong influence on the forward and inverse sensitivity if no indicator was used and spheres of blood were integrated as inhomogeneities. We therefore concluded, that CRIC based perfusion measures will tend to underestimate perfusion in collapsed regions and the comparison between different states might not be intuitively possible, if the lung conductivity background also changes substantially. If we integrated spheres with the conductivity of a 2 % saline bolus, the spatial profiles of forward and inverse sensitivity became very similar and even increased for increasing indicator concentration, thus allowing the comparison for measurements with substantially different background conductivities. Within the electrode plane, we found a decreasing inter-quartile range of the amplitude response with increasing

indicator concentration. A small spatial variation of inverse sensitivity is desired [93] and was generally smallest for the GREIT algorithm.

2. Understand the contributions of different spatio-temporal compartments of the pulmonary circulation to the indicator-enhanced EIT blood flow distribution image
We found that the main contributor to EIT perfusion images was the perfusion in smaller blood vessels and the vascular bed and not the larger vessels and cardiac blood volumes. This finding emphasizes that an estimation of the capillary perfusion, which is the type of perfusion participating in gas exchange, is possible with EIT. Yet, we could not incorporate the main stems of the pulmonary artery and pulmonary vein within the medistinum into the analysis.

13.2 Optimization of indicator based pulmonary blood flow parameter estimation

3. Identify the minimal saline indicator concentration necessary to allow a suitable regional estimation of pulmonary perfusion
We have found no substantial differences of similarity between the estimation of regional perfusion based on 5 % NaCl boli or 10 % NaCl boli for all investigated EIT reconstruction methods when comparing them to PET perfusion. Lower concentrations showed slightly decreased similarity, yet we observed still strong agreement with PET perfusion.

4. Develop and optimize algorithms to calculate indicator-enhanced EIT blood flow distributions
We have compared four different reconstruction methods and compared the resulting perfusion estimations against PET perfusion in a comprehensive preclinical study comprising different experimental states. The GREIT reconstruction showed the best performance, since we observed the strongest similarity (r=0.91 in eight ROIs, 10 % NaCl) to PET perfusion for this type of reconstruction. The standard Laplace regularization showed a slightly decreased similarity (r=0.89 in eight ROIs, 10 % NaCl) yet also very robust results. We observed a ventral overestimation of perfusion with EIT, which might be resulting from a relatively increased sensitivity in ventral regions compared to dorsal regions, and possibly due to a insufficient removal of non-pulmonary participants of the pulmonary circulation.
We compared to different perfusion estimation techniques. The first one based on a pure temporal feature analysis (maximal slope method), while the second one computed spatial transfer functions between a pulmonary input function and different compartments within the lungs (deconvolution based method). We observed superior performance of the maximal slope method by analyzing the similarity of EIT and PET perfusion estimations.

5. Compare the indicator-enhanced EIT blood flow estimations during respiratory hold phases to gold standard perfusion imaging

We have compared the relative perfusion estimations based on indicator-enhanced EIT measurements to MDCT and PET perfusion estimations. In both cases, we found strong agreement between the ground truth and the EIT estimation (EIT-MDCT: r=0.90 and EIT-PET: r=0.94 for 10 % NaCl). The analysis was carried out for induced regional ARDS as well as for different PEEP levels and ventilation and perfusion blocks.

6. Develop algorithms to enable indicator dilution during ongoing mechanical ventilation

We compared the estimation of regional pulmonary perfusion by injecting the indicator during a breath hold phase to the injection during ongoing ventilation. We found a slightly decreased similarity to PET perfusion between EIT estimations during breath hold (r=0.90) and ongoing ventilation (r=0.87). Yet, the difference was marginal and we expect the measurement during ongoing ventilation to be possible with our method, if the respiratory rate of the ventilator does not fall below a rate of approximately 12 breaths per minute.

7. Analyze temporal parameters of pulmonary indicator passage.

We have compared distributions of perfusion MTTs between EIT and MDCT perfusion in chapter 11. Qualitatively, we found strong concordance between spatial EIT and MDCT transit time distributions in the lungs. MDCT showed systematically slower transit times compared to EIT, which we hypothesized might be due to the higher viscosity of the MDCT indicator.

The estimation of pulmonary transit times based on indicator-enhanced EIT could potentially allow to uncover information about the CO and the PVR. We have described all necessary methods to perform quantitative analyses, yet a thorough quantitative comparison was not performed during the research for this thesis and should be conducted in the future.

Chapter 14

Outlook

14.1 Spatial sensitivity and information of indicator enhanced EIT perfusion

Both simulation studies have only considered a single porcine anatomy. Though we have observed very similar porcine anatomies among the included study animals, the meaningfulness of the results could be further increased by calculating statistics over multiple animals. The investigations have so far been conducted for porcine anatomies, but should be extended to human anatomies. We have created first human simulations and published the results in [76, 147].

Regarding the simulation study described in chapter 8, which was conducted to analyze the contributions of larger vessels, cardiac blood volumes and the pulmonary capillary bed on the reconstructed spatial perfusion estimation by EIT, the field of view was limited to a 4 cm extent around the electrode belt. The field of view did not allow to segment the main stems of the pulmonary artery and vein, which we believe also contribute to the indicator-enhanced EIT based perfusion reconstruction. Thus, with an indicator based CT blood flow measurement covering a lager volume, these blood vessels could be included into the analysis.

The translation of CT indicator dilution curves to EIT dilution curves is also only a good approximation, since the properties of the indicators are very different (viscosity, diffusibility,...). A dynamic three dimensional blood flow simulation of the pulmonary circulation might be able to allow a more detailed insight into the EIT perfusion image contributors. A similar simulation approach was described by [162] for the aeration of the lungs. A lumped parameter model or transmission line approach could be implemented to have a simplified approach to model the fluid dynamics.

14.2 Optimization of perfusion estimation methods

EIT reconstruction Though we have already compared different EIT reconstruction approaches against gold standard lung perfusion measurements, there is still potential to optimize EIT reconstruction algorithms. Since we are reconstructing dynamic indicator dilution curves, we could consider temporal regularization approaches as e.g. described in [95, 182]. This approach might allow to impose boundary conditions on the reconstructed solution, which lead to less spatial smoothing while stabilizing the solution equally well. Nevertheless, the reconstruction could become much more computationally expensive.
Approximating the pulmonary conductivity background to improve the reconstruction might also bear a large optimization potential. Since CT or MRI measurements are normally not available in an ICU, approximating the background by ventilation reconstructions to find collapsed regions, where sensitivity is decreased, might improve the reconstruction.
Extending the reconstruction to 3D might also be a very interesting step to improve clinical acceptance and the understanding of EIT reconstructions. Yet, the ill-conditioning of the inverse problem is further increased. Also, the applicability in clinical routine in an ICU might be a challenge, since more electrodes over a larger region of the thorax have to be attached. There already has been research on how to combine different sensors into one vest, which might be a first step to a solution of attaching electrodes in multiple planes [208].
In contrast to the previous point, EIT could also be used as rather a monitoring device of larger spatial regions of the lungs than an imaging device. This would allow to reduce the number of spatial compartments to be reconstructed, which would improve the condition of the matrix to be inverted. This could be done for ventilation and perfusion reconstruction and might enable a simpler interpretation of ventilation-perfusion ratio ($\dot{V}/\dot{Q}$) ratios.
So far, we have only investigated relative distributions of perfusion. In a future step, it would be interesting to evaluate quasi absolute perfusion (normalized reconstruction with some kind of absolute weighting) or absolute perfusion (absolute EIT reconstruction). This is much more challenging but might also lead to an improved clinical acceptance.
In order to allow spatial perfusion estimations during ongoing ventilation at low respiratory rates, different more adaptive filtering strategies could be developed. In a conference publication from 2019 [180], a deconvolution based strategy has been introduced. The real time volume curve of the mechanical ventilator has to be known and perfectly synchronized for this approach. Since a non-periodic signal (indicator dilution curve) has to be removed from a periodic signal (ventilation), different blind source separation techniques could be applied such as the periodic component analysis [209].

Perfusion parameter estimation Above all, the detection of the pre-lung and post-lung circulation compartment is a very crucial step during the process of estimating spatial distributions of pulmonary perfusion. If non-lung phases are not removed sufficiently, especially cardiac blood flow might be misinterpreted as lung perfusion. The methods implemented

in this thesis should be compared to the methods described in [109, 201] and different approaches could be combined to further improve redundancy and therefore robustness.
The deconvolution or system theoretic approach of estimating vascular transfer functions could be further improved. We have also implemented methods, which apply Tikhonov regularization to the inverse problem of the parameter estimation. We e.g. imposed a temporal similarity constraint of the reconstructed transfer functions to gamma variate models [133]. The promising preliminary research has been published as conference paper [127].
We have investigated the spatial distribution of indicator transit times and have evaluated its correlation with the CO. An additional evaluation should be conducted, considering the PVR, which has propably the largest influence on the indicator transit times. We have not recorded surrogates for the PVR, such as an estimate based on the pulmonary capillary wedge pressure and the mean pulmonary artery pressure.
CO or stroke volume estimations based on indicator dilution should be investigated comprehensively. We might find a weighting to estimate absolute blood flow from normalized conductivity changes.

14.3 Clinical measurements

Analysis of gas exchange - Global and regional $\dot{V}/\dot{Q}$ measures In this thesis, our main aim was to develop methods to robustly estimate regional pulmonary perfusion with EIT and validate the EIT perfusion distributions against gold standard lung perfusion measurements. Since the estimation of spatial lung aeration was already validated and is already applied clinically, the next step would be to compute regional and global measures to assess ventilation and perfusion ratios. A challenge might be the different reconstruction artifacts and model based shifts and smearing of ventilation and perfusion reconstruction. Hentze et al. have reported, that ventilation tends to be shifted more dorsally and perfusion was found to be often shifted more ventrally [109]. Thus, pixelwise measures of ventilation and perfusion ratios might be misleading. Yet, different measures analyzing the homogeneity and similarity of both distributions might be beneficial. Different measures should be compared against global gas exchange measures e.g. based on blood gas analyses. More research has to be done in this context and will be continued in next steps.

EIT based perfusion estimation in humans In two major experimental studies we have shown feasibility of regional lung perfusion estimation with EIT based on indicator dilution. The necessary next step is to test the perfusion estimation techniques in human measurements to assess the clinical applicability. During the last year, we have contributed to a graphical research tool, which now incorporates the methods developed during the research cooperation with Drägerwerk AG & Co. KGaA. Since we were able to show, that the concentration of the saline indicator can be reduced in order to enable the clinical application without introducing additional risk to the patient, an ethics vote was obtained for a first larger clinical study, enrolling 50 patients. The study has been conducted by the group of Tommaso Mauri

(Department of Anesthesia, Critical Care and Emergency, Fondazione IRCCS Ca'Granda Ospedale Maggiore Policlinico, Milan, Italy). Regional ventilation and perfusion (during breath hold) were assessed and regions of $\dot{V}/\dot{Q}$ match and mismatch were estimated. The study has already been submitted and is currently under review. Exemplary images of a study patient are depicted in Figure 14.1. The study results already indicate, that quasi-

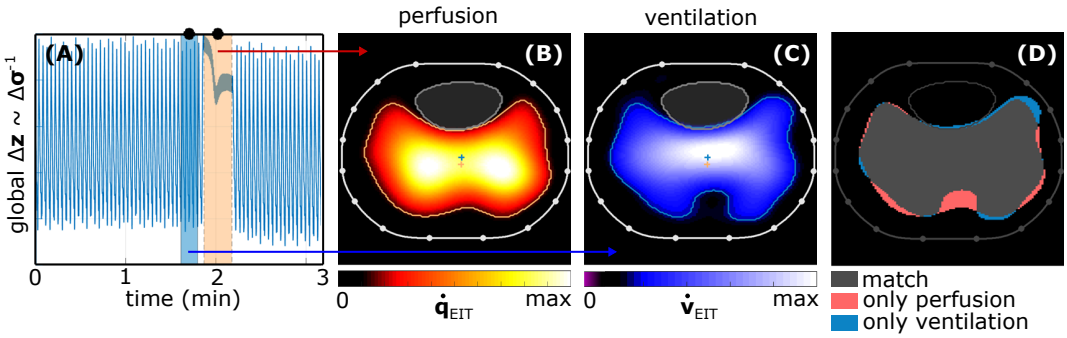

Figure 14.1: Clinical measurement of lung perfusion and ventilation of an ICU patient suffering from ARDS. Graph (A) shows the global EIT impedance change curve with the sections of ventilation and perfusion measurement sections highlighted. Image (B) depicts the estimated EIT perfusion distribution $\dot{\mathbf{q}}_{EIT}$ alongside the estimated ventilation distribution $\dot{\mathbf{v}}_{EIT}$ in image (C). A map of the matched and mismatched regions are depicted in image (D). A region was defined as perfused, if the image amplitude exceeded 10% of the maximal amplitude. The same approach was used for the ventilated regions. The heart region or pre-lung phase was removed.

simultaneous measurement of ventilation and perfusion allows to assess the severity of ARDS by exploiting measures of regional matching of ventilation and perfusion.
In times of the Corona virus pandemic, the demand for a beside lung perfusion measurement is additionally increasing. The same group of Tommaso Mauri has already published early results from ten Covid-19 patients suffering from ARDS [210]. The perfusion measurement should be conducted in many clinical studies in order to assess the potential of improving lung injury diagnosis and lung protective ventilation. The investigation of the medical information of bedside perfusion and ventilation measurements should be accompanied by technical analyses and method improvements to generate trustworthy distributions also for human anatomies in different positions and measurement scenarios. The robust removal of the pre- and post-lung circulation phase from the image is in our opinion the most crucial processing step, which needs to be evaluated in clinical measurements. Otherwise ventral perfusion is overestimated.

Appendix **A**

Derivation of important features of the gamma variate

As described in section 10.2.1, the first passage of an indicator fluid through a spatial compartment is often mathematically described by the gamma variate model $\gamma(t)$ [116, 118] . In this chapter, a description of the model parameters as functions of important signal features shall be derived. These functions were used to calculate suitable initial estimates of the model parameters for nonlinear fitting of the gamma variate to the reconstructed conductivity signals in each spatial element k. The derivation will be described for a continuous time $t \in \mathbb{R}$.

The gamma variate is mathematically described by:

$$\gamma(t) = g \cdot (t - t_A)^{\alpha} \cdot e^{-\beta(t-t_A)} \tag{A.1}$$

The shape of the function is described by its parameters $\alpha, \beta \in \{\mathbb{R} | \alpha, \beta > 0\}$. The model can additionally be scaled by the amplitude $g \in \{\mathbb{R} | g > 0\}$. The initial rise of the function occurs at time $t_A \in \mathbb{R}$, which will be called arrival time in the following. In the end we want to be able describe α, β and a by signal features. In order to derive the most important signal features of the gamma variate besides t_A, the first and second temporal derivative are calculated. Deriving the first derivative of the gamma variate $\frac{\delta\gamma(t)}{\delta t}$ the product rule has to be regarded:

$$\begin{aligned}
\frac{\delta\gamma(t)}{\delta t} &= g \cdot \left(\alpha(t - t_A)^{\alpha-1} \cdot e^{-\beta(t-t_A)} - \beta(t - t_A)^{\alpha} \cdot e^{-\beta(t-t_A)} \right) \\
&= g \cdot (t - t_A)^{\alpha} \cdot e^{-\beta(t-t_A)} \cdot \left(\frac{\alpha}{t - t_A} - \beta \right) \\
&= \gamma(t) \cdot \left(\frac{\alpha}{t - t_A} - \beta \right)
\end{aligned} \tag{A.2}$$

The second derivative is calculated again using the product rule:

$$\frac{\delta^2\gamma(t)}{\delta t^2} = \gamma(t)\cdot\left(\frac{\alpha}{t-t_A}-\beta\right)^2 - \gamma(t)\cdot\left(\frac{\alpha}{(t-t_A)^2}\right) \tag{A.3}$$

$$\frac{\delta^2\gamma(t)}{\delta t^2} = \gamma(t)\cdot\left[\left(\frac{\alpha}{t-t_A}-\beta\right)^2 - \frac{\alpha}{(t-t_A)^2}\right] \tag{A.4}$$

At first the maximum γ_{max} and the time of the maximum $t_{max} \in (t_A,\infty]$ of the gamma variate is calculated as functions of model parameters. At t_{max} $\frac{\delta\gamma(t)}{\delta t}|_{t=t_{max}} \stackrel{!}{=} 0$ applies, resulting in:

$$0 = \gamma(t_{max})\cdot\left(\frac{\alpha}{t_{max}-t_A}-\beta\right) \tag{A.5}$$

Within the possible parameter limits $\gamma(t_{max}) \neq 0 \ \forall t_{max} < \infty$ applies. Therefore it follows:

$$\begin{aligned}\left(\frac{\alpha}{t_{max}-t_A}-\beta\right) &= 0\\ t_{max} &= \frac{\alpha}{\beta}+t_A\end{aligned} \tag{A.6}$$

Based on the second derivative it can be shown, that $\gamma(t_{max})$ is the global maximum, which is trivial. The maximum value of the gamma variate is given by inserting (A.6) in (A.1) and subsequent simplification:

$$\gamma_{max} = a\cdot\left(\frac{\alpha}{\beta}\right)^{\alpha}\cdot e^{-\alpha} \tag{A.7}$$

To be able to describe α and β only in terms of signal features, we need an additional feature besides the maximum. We choose the maximal positive $\dot{\gamma}_{max+}$ and negative slope $\dot{\gamma}_{max-}$ at the time points $t_{s+} \in (t_A,\infty]$ and $t_{s-} \in (t_A,\infty]$, since these parameters will be important features to calculate the pulmonary blood circulation parameters. At t_{s+} and t_{s-} the second derivative vanishes:

$$0 = \gamma(t_{s\pm})\cdot\left[\left(\frac{\alpha}{t_{s\pm}-t_A}-\beta\right)^2 - \frac{\alpha}{(t_{s\pm}-t_A)^2}\right] \tag{A.8}$$

Again $\gamma(t_{s\pm}) \neq 0 \ \forall t_{s\pm} < \infty$ applies. Therefore the following function quadratic in $t_{s\pm}$ applies:

$$\begin{aligned}0 &= \frac{\alpha^2-\alpha}{(t_{s\pm}-t_A)^2} - \frac{2\alpha\beta}{t_{s\pm}-t_A} + \beta^2\\ &= \alpha^2-\alpha-2\alpha\beta(t_{s\pm}-t_A)+\beta(t_{s\pm}-t_A)^2\\ &= \beta^2\cdot t_{s\pm}^2 - \left(2\alpha\beta+2\beta^2 t_A\right)\cdot t_{s\pm} + \left(\alpha^2-\alpha+2\alpha\beta t_A+\beta^2 t_A^2\right)\end{aligned} \tag{A.9}$$

After solving the standard formula for quadratic equations, we end up with:

$$t_{s+} = \frac{\alpha-\sqrt{\alpha}}{\beta}+t_A = t_{max}-\frac{\sqrt{\alpha}}{\beta} \tag{A.10}$$

$$t_{s-} = \frac{\alpha+\sqrt{\alpha}}{\beta}+t_A = t_{max}+\frac{\sqrt{\alpha}}{\beta} \tag{A.11}$$

(A.12)

Subsequently we solve (A.6) for β and insert it in (A.10). Assuming we can identify t_A, t_{max}, t_{s+} and g_{max} by signal analysis, we finally express α, β and a as functions of the identified signal features:

$$a = \left(\frac{\beta}{\alpha}\right)^{\alpha} e^{\alpha} \cdot \gamma_{max} \tag{A.13}$$

$$\alpha = \frac{(t_{max} - t_A)^2}{(t_{max} - t_{s+})^2} \tag{A.14}$$

$$\beta = \frac{(t_{max} - t_A)}{(t_{max} - t_{s+})^2} \tag{A.15}$$

Appendix **B**

Comparison of the nonlinear and piecewise drift fit

In section 10.2.1 of chapter 10, two methods to remove the superimposed recirculation drift component $d_k(n)$ from the temporal indicator dilution signals $\Delta\sigma_k(n)$ in all spatial elements k have been introduced: the nonlinear γ-fit and the piecewise fit. The latter can be interpreted as a simplified and more robust adaption of the nonlinear fit. After fitting process, an estimation of the first-pass indicator dilution signal was recovered by either methods: $\tilde{\gamma}_{NL,k}(n)$ or $\tilde{\gamma}_{PC,k}(n)$. We published a synthetic signal study as a conference contribution [125], in which the accuracy of both fits were compared. A short summary of the results will be presented in the following.

Synthetic signal model: For the method comparison study N=10000 synthetic signals were created using the signal model:

$$\Delta\sigma(n) = \gamma(n) + d(t) + e(t) \quad \text{with}$$
$$\gamma(n) = g \cdot (n - n_A)^{\alpha} \cdot e^{-\beta(n-n_A)}$$

The parameters of the model have been introduced in section 10.2.1. All parameters were varied randomly in realistic intervals. These intervals were identified from the preclinical porcine study (see chapter 5 or [121]) during the research for the Bachelor thesis [131]. Additionally, measurement noise $e(n)$ was modeled as Gaussian white noise with a $SNR = [40dB, 60dB]$.

Comparative results: To compare the accuracy of both fitted/estimated indicator dilution curves, different features $\hat{p}$ of the recovered/estimated first pass indicator curve $\hat{\gamma}(n)$ have been compared to the corresponding features p of the simulated ground truth signal $\gamma(n)$: the maximal amplitude γ_{max}, the maximal slope $\dot{\gamma}_{max}$, the area under the curve $\int \gamma(n)dn$ and the mean transit time MTT. The comparative accuracy parameter was the normalized error: $\varepsilon(p) = (\hat{p} - p)/p$. Additionally, the *Pearson* correlation coefficient r between the ground truth $\gamma(n)$ and the estimated signals was calculated. The results are shown in table B.1:

Table B.1: Synthetic study results: median and interquartile range (IQR) of different feature errors. The table was adapted from our publication [125].

	Nonlinear fit		Piecewise fit	
	Median	IQR	Median	IQR
$\varepsilon(\gamma_{\max})$ in %	-2.12	5.26	-1.39	5.77
$\varepsilon(\dot{\gamma}_{\max})$ in %	-27.32	34.27	-31.79	35.14
$\varepsilon(\int \gamma(\mathrm{n})\mathrm{dn})$ in %	-1.35	1.32	-0.83	4.47
$\varepsilon(\mathrm{MTT})$ in %	-0.63	0.56	2.05	4.96
r	0.998	0.006	0.996	0.01

Application to data from the Dresden study: Both fits, *nonlinear* and the *piecewise* fit, were also compared qualitatively using an exemplary indicator EIT measurement from preclinical porcine study in Dresden (see chapter 5 or [121]). The maximal slope feature $\dot{\gamma}_{max}$ was calculated from both fitted signals. The spatial distributions within the lungs were compared and are visualized in figure B.1. The images or spatial feature distributions were compared by a pixel wise absolute normalized error $\varepsilon(\dot{\gamma}_{max}) = |\dot{\gamma}_{PC,max} - \dot{\gamma}_{NL,max}|/\dot{\gamma}_{max}$. The median of the image error $M(\varepsilon) = 7.4\%$ and the $IQR(\varepsilon) = 9.8\%$.

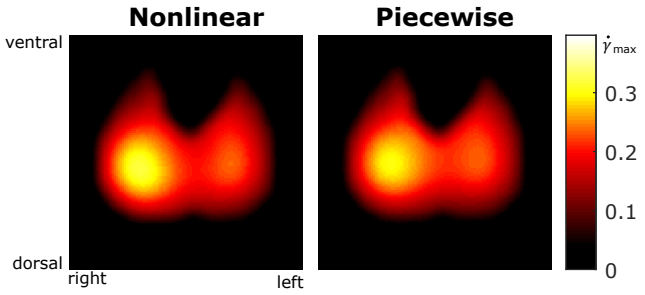

Figure B.1: Distributions of the maximal slope feature in a porcine lung; (left) the *nonlinear fit*; (right) the *piecewise fit*. The image was adapted from our conference contribution [125].

Conclusion: The indicator dilution curve $\gamma(n)$ could be estimated robustly by both fitting methods for the synthetic and preclinical study data. Both fitting methods could recover the pure indicator dilution curve with similar parameter error intervals. Above all, the maximal slope of the ground truth indicator dilution signal was underestimated by around 30% for both fitting approaches. Since both fits showed very comparable fitting results, the simpler piecewise fit, with substantially smaller computational cost, was chosen for all analyses in chapters 11 and 12.

List of Figures

List of Tables

References

[1] V. Fanelli and V. M. Ranieri, "Mechanisms and clinical consequences of acute lung injury." *Annals of the American Thoracic Society*, vol. 12 Suppl 1, pp. 3–8, 3 2015.

[2] E. Fan, D. Brodie, and A. S. Slutsky, "Acute respiratory distress syndrome: Advances in diagnosis and treatment." *Journal of the American Medical Association*, vol. 319, no. 7, pp. 698–710, 2 2018.

[3] Q. Cai, D. Huang, P. Ou, et al., "2019-ncov pneumonia in a normal work infectious diseases hospital besides hubei province, china," *SSRN Electronic Journal*, 1 2020.

[4] D. Wang, B. Hu, C. Hu, et al., "Clinical characteristics of 138 hospitalized patients with 2019 novel coronavirus-infected pneumonia in wuhan, china." *Journal of the American Medical Association*, 2 2020.

[5] T. Pham and G. D. Rubenfeld, "Fifty years of research in ARDS. The epidemiology of acute respiratory distress syndrome. A 50th birthday review." *American Journal of Respiratory and Critical Care Medicine*, vol. 195, no. 7, pp. 860–870, 4 2017.

[6] M. A. Matthay, R. L. Zemans, G. A. Zimmerman, et al., "Acute respiratory distress syndrome." *Nature Reviews. Disease Primers*, vol. 5, no. 1, p. 18, 3 2019.

[7] M. Ferring and J. L. Vincent, "Is outcome from ARDS related to the severity of respiratory failure?" *The European Respiratory Journal*, vol. 10, no. 6, pp. 1297–1300, 6 1997.

[8] B. J. Wright, "Lung-protective ventilation strategies and adjunctive treatments for the emergency medicine patient with acute respiratory failure." *Emergency Medicine Clinics of North America*, vol. 32, no. 4, pp. 871–887, 11 2014.

[9] E. Fan, L. Del Sorbo, E. C. Goligher, et al., "An official american thoracic society/european society of intensive care medicine/society of critical care medicine clinical practice guideline: Mechanical ventilation in adult patients with acute respiratory distress syndrome." *American Journal of Respiratory and Critical Care Medicine*, vol. 195, no. 9, pp. 1253–1263, 5 2017.

[10] A. D. Seagar, D. C. Barber, and B. H. Brown, "Theoretical limits to sensitivity and resolution in impedance imaging." *Clinical Physics and Physiological Measurement*, vol. 8 Suppl A, pp. 13–31, 1 1987.

[11] P. W. Kunst, A. Vonk Noordegraaf, O. S. Hoekstra, et al., "Ventilation and perfusion imaging by electrical impedance tomography: a comparison with radionuclide scanning," *Physiological Measurement*, vol. 19, no. 4, pp. 481–490, 1 1998.

[12] I. Frerichs, J. Hinz, P. Herrmann, et al., "Detection of local lung air content by electrical impedance tomography compared with electron beam CT." *Journal of Applied Physiology*, vol. 93, no. 2, pp. 660–666, 8 2002.

[13] J. Hinz, P. Neumann, T. Dudykevych, et al., "Regional ventilation by electrical impedance tomography: a comparison with ventilation scintigraphy in pigs." *Chest*, vol. 124, no. 1, pp. 314–322, 7 2003.

[14] J. A. Victorino, J. B. Borges, V. N. Okamoto, et al., "Imbalances in regional lung ventilation: a validation study on electrical impedance tomography." *American Journal of Respiratory and Critical Care Medicine*, vol. 169, no. 7, pp. 791–800, 4 2004.

[15] H. Wrigge, J. Zinserling, T. Muders, et al., "Electrical impedance tomography compared with thoracic computed tomography during a slow inflation maneuver in experimental models of lung injury." *Critical Care Medicine*, vol. 36, no. 3, pp. 903–909, 3 2008.

[16] J. C. Richard, C. Pouzot, A. Gros, et al., "Electrical impedance tomography compared to positron emission tomography for the measurement of regional lung ventilation: an experimental study." *Critical Care*, vol. 13, no. 3, p. R82, 1 2009.

[17] T. Muders, H. Luepschen, J. Zinserling, et al., "Tidal recruitment assessed by electrical impedance tomography and computed tomography in a porcine model of lung injury*." *Critical Care Medicine*, vol. 40, no. 3, pp. 903–911, 3 2012.

[18] A. Adler, M. Proenca, F. Braun, et al., "Origins of cardiosynchronous signals in EIT," *EIT Conference, 2017*, p. 73, 6 2017.

[19] J. B. Borges, F. Suarez-Sipmann, S. H. Bohm, et al., "Regional lung perfusion estimated by electrical impedance tomography in a piglet model of lung collapse." *Journal of Applied Physiology*, vol. 112, no. 1, pp. 225–236, 1 2012.

[20] S. Stowe, A. Boyle, M. Sage, et al., "Comparison of bolus- and filtering-based EIT measures of lung perfusion in an animal model." *Physiological Measurement*, vol. 40, no. 5, p. 054002, 6 2019.

[21] P. Meier and K. L. Zierler, "On the theory of the indicator-dilution method for measurement of blood flow and volume." *Journal of Applied Physiology*, vol. 6, no. 12, pp. 731–744, 6 1954.

[22] S. Sisson, "The anatomy of the domestic animals, by septimus sisson ... with 725 illustrations, many in colors." 1 1914.

[23] E. P. Judge, J. M. L. Hughes, J. J. Egan, et al., "Anatomy and bronchoscopy of the porcine lung. A model for translational respiratory medicine." *American Journal of Respiratory Cell and Molecular Biology*, vol. 51, no. 3, pp. 334–343, 9 2014.

[24] G. S. Thompson, *Understanding anatomy & physiology*. F.A. Davis Company, 1 2013.

[25] E. R. Weibel, "Geometry and dimensions of airways of conductive and transitory zones," pp. 110–135, 1 1963.

[26] J. B. West and A. M. Luks, "West's respiratory physiology: The essentials," 2016.

[27] G. Cavagna, "Respiration," in *Fundamentals of Human Physiology*, 1 2019, pp. 125–215.

[28] P. Scheid, *Atmung*, Lehrbuch der Physiologie. Stuttgart: Thieme, 1 2001, no. 2, pp. 217–272.

[29] Y. C. Fung and S. S. Sobin, "Theory of sheet flow in lung alveoli." *Journal of Applied Physiology*, vol. 26, no. 4, pp. 472–488, 4 1969.

[30] S. S. Sobin, H. M. Tremer, and Y. C. Fung, "Morphometric basis of the sheet-flow concept of the pulmonary alveolar microcirculation in the cat." *Circulation Research*, vol. 26, no. 3, pp. 397–414, 3 1970.

[31] S. Silbernagl and A. Despopoulos, "Atmung," in *Taschenatlas der Physiologie*. Stuttgart: Georg Thieme Verlag, 1 2001, pp. 106–137.

[32] U. S. v. EULER and G. LILJESTRAND, "Observations on the pulmonary arterial blood pressure in the cat," *Acta Physiologica Scandinavica*, vol. 12, no. 4, pp. 301–320, 1 1946.

[33] E. K. Weir and S. L. Archer, "The mechanism of acute hypoxic pulmonary vasoconstriction: the tale of two channels." *FASEB Journal*, vol. 9, no. 2, pp. 183–189, 2 1995.

[34] K. J. Dunham-Snary, D. Wu, E. A. Sykes, et al., "Hypoxic pulmonary vasoconstriction: From molecular mechanisms to medicine." *Chest*, vol. 151, no. 1, pp. 181–192, 1 2017.

[35] J. B. West and C. T. Dollery, "Distribution of blood flow and ventilation-perfusion ratio in the lung, measured with radioactive carbon dioxide." *Journal of Applied Physiology*, vol. 15, pp. 405–410, 5 1960.

[36] R. W. Glenny, "Determinants of regional ventilation and blood flow in the lung." *Intensive Care Medicine*, vol. 35, no. 11, pp. 1833–1842, 11 2009.

[37] D. Ashbaugh, D. Boyd Bigelow, T. Petty, et al., "Acute respiratory distress in adults," *The Lancet*, vol. 290, no. 7511, pp. 319–323, 1 1967.

[38] G. D. Rubenfeld, E. Caldwell, E. Peabody, et al., "Incidence and outcomes of acute lung injury." *The New England Journal of Medicine*, vol. 353, no. 16, pp. 1685–1693, 10 2005.

[39] J. Phua, J. R. Badia, N. K. J. Adhikari, et al., "Has mortality from acute respiratory distress syndrome decreased over time?: A systematic review." *American Journal of Respiratory and Critical Care Medicine*, vol. 179, no. 3, pp. 220–227, 2 2009.

[40] G. R. Bernard, A. Artigas, K. L. Brigham, et al., "The american-european consensus conference on ARDS. definitions, mechanisms, relevant outcomes, and clinical trial coordination." *American Journal of Respiratory and Critical Care Medicine*, vol. 149, no. 3 Pt 1, pp. 818–824, 3 1994.

[41] V. M. Ranieri, G. D. Rubenfeld, B. T. Thompson, et al., "Acute respiratory distress syndrome: the berlin definition." *Journal of the American Medical Association*, vol. 307, no. 23, pp. 2526–2533, 6 2012.

[42] E. M. Harman and L. E. Riley, "Acute respiratory distress syndrome: Background, pathophysiology, etiology," 3 2020.

[43] E. R. Johnson and M. A. Matthay, "Acute lung injury: epidemiology, pathogenesis, and treatment." *Journal of Aerosol Medicine and Pulmonary Drug Delivery*, vol. 23, no. 4, pp. 243–252, 8 2010.

[44] D. Ryan, S. Frohlich, and P. McLoughlin, "Pulmonary vascular dysfunction in ARDS." *Annals of Intensive Care*, vol. 4, p. 28, 1 2014.

[45] K. Deden, "Ventilation modes in intensive care," Homepage Drägerwerk AG & Co. KGaA.

[46] F. Rittner and M. Döring, "Kurven und Loops in der Beatmung," Homepage Drägerwerk AG & Co. KGaA.

[47] H. Lüpschen, "Automatisierte protektive Beatmung durch Bestimmung von Ventilation und Perfusion der Lunge mittels Elektrischer Impedanztomographie," PhD thesis, 2012.

[48] M. J. Tobin, "Principles and practice of mechanical ventilation," *Shock*, vol. 26, no. 4, p. 426, 1 2006.

[49] D. Dreyfuss and G. Saumon, "Ventilator-induced lung injury: lessons from experimental studies." *American Journal of Respiratory and Critical Care Medicine*, vol. 157, no. 1, pp. 294–323, 1 1998.

[50] O. Gajic, S. I. Dara, J. L. Mendez, et al., "Ventilator-associated lung injury in patients without acute lung injury at the onset of mechanical ventilation." *Critical Care Medicine*, vol. 32, no. 9, pp. 1817–1824, 9 2004.

[51] L. Pinhu, T. Whitehead, T. Evans, et al., "Ventilator-associated lung injury," *The Lancet*, vol. 361, no. 9354, pp. 332–340, 1 2003.

[52] L. Gattinoni, J. J. Marini, F. Collino, et al., "The future of mechanical ventilation: lessons from the present and the past." *Critical Care*, vol. 21, no. 1, p. 183, 7 2017.

[53] N. Rittayamai, C. M. Katsios, F. Beloncle, et al., "Pressure-controlled vs volume-controlled ventilation in acute respiratory failure: A physiology-based narrative and systematic review." *Chest*, vol. 148, no. 2, pp. 340–355, 8 2015.

[54] E. L. V. Costa, J. B. Borges, A. Melo, et al., "Bedside estimation of recruitable alveolar collapse and hyperdistension by electrical impedance tomography." *Intensive Care Medicine*, vol. 35, no. 6, pp. 1132–1137, 6 2009.

[55] B. Lachmann, "Open up the lung and keep the lung open." *Intensive Care Medicine*, vol. 18, no. 6, pp. 319–321, 1 1992.

[56] J. Mead, T. Takishima, and D. Leith, "Stress distribution in lungs: a model of pulmonary elasticity." *Journal of Applied Physiology*, vol. 28, no. 5, pp. 596–608, 5 1970.

[57] F. Podczeck, C. L. Mitchell, J. M. Newton, et al., "The gastric emptying of food as measured by gamma-scintigraphy and electrical impedance tomography (EIT) and its influence on the gastric emptying of tablets of different dimensions." *The Journal of Pharmacy and Pharmacology*, vol. 59, no. 11, pp. 1527–1536, 11 2007.

[58] D. Leonhäuser, C. Castelar, T. Schlebusch, et al., "Evaluation of electrical impedance tomography for determination of urinary bladder volume: comparison with standard ultrasound methods in healthy volunteers." *Biomedical Engineering Online*, vol. 17, no. 1, p. 95, 7 2018.

[59] K. Y. Aristovich, B. C. Packham, H. Koo, et al., "Imaging fast electrical activity in the brain with electrical impedance tomography." *NeuroImage*, vol. 124, no. Pt A, pp. 204–213, 1 2016.

[60] A. Nissinen, J. P. Kaipio, M. Vauhkonen, et al., "Contrast enhancement in EIT imaging of the brain." *Physiological Measurement*, vol. 37, no. 1, pp. 1–24, 1 2016.

[61] E. Malone, M. Jehl, S. Arridge, et al., "Stroke type differentiation using spectrally constrained multifrequency EIT: evaluation of feasibility in a realistic head model." *Physiological Measurement*, vol. 35, no. 6, pp. 1051–1066, 6 2014.

[62] Y. Zou and Z. Guo, "A review of electrical impedance techniques for breast cancer detection," *Medical Engineering & Physics*, vol. 25, no. 2, pp. 79–90, 1 2003.

[63] R. P. Henderson and J. G. Webster, "An impedance camera for spatially specific measurements of the thorax," *IEEE Transactions on Biomedical Engineering*, vol. 25, no. 3, pp. 250–254, 1978.

[64] D. C. Barber and B. H. Brown, "Applied potential tomography," *Journal of Physics E: Scientific Instruments*, vol. 17, pp. 723–733, 1 1984.

[65] K. S. Cole and R. H. Cole, "Dispersion and absorption in dielectrics I. Alternating current characteristics," *The Journal of Chemical Physics*, vol. 9, pp. 341–351, 1941.

[66] O. Dössel, *Bildgebende Verfahren in der Medizin: Von der Technik zur medizinischen Anwendung*. Springer-Verlag Berlin Heidelberg, 1 2016.

[67] R. Bayford and A. Tizzard, "Bioimpedance imaging: an overview of potential clinical applications." *The Analyst*, vol. 137, no. 20, pp. 4635–4643, 10 2012.

[68] M. Proença, "Non-invasive hemodynamic monitoring by electrical impedance tomography," PhD thesis, École Polytechnique Fédérale de Lausanne, 2017.

[69] D. S. Holder, *Electrical impedance tomography: methods, history, and applications*, Series in medical physics and biomedical engineering, 2005.

[70] "IEC 60601-1:2005," Geneva, Switzerland, 2005.

[71] K. R. Foster and H. C. Lukaski, "Whole-body impedance–what does it measure?" *The American Journal of Clinical Nutrition*, vol. 64, no. 3 Suppl, pp. 388–396, 9 1996.

[72] E. T. McAdams, J. Jossinet, A. Lackermeier, et al., "Factors affecting electrode-gel-skin interface impedance in electrical impedance tomography." *Medical & Biological Engineering & Computing*, vol. 34, no. 6, pp. 397–408, 11 1996.

[73] C. E. Shannon, "Communication in the presence of noise," *Proceedings of the IEEE*, vol. 86, no. 2, pp. 447–457, 1 1998.

[74] D. B. Geselowitz, "An application of electrocardiographic lead theory to impedance plethysmography." *IEEE Transactions on Biomedical Engineering*, vol. 18, no. 1, pp. 38–41, 1 1971.

[75] B. Grychtol, B. Müller, and A. Adler, "3D EIT image reconstruction with GREIT." *Physiological Measurement*, vol. 37, no. 6, pp. 785–800, 6 2016.

[76] M. Kircher, R. Hattiangdi, R. Menges, et al., "Influence of background lung tissue conductivity on the cardiosynchronous EIT signal components: a sensitivity study." vol. 2019. IEEE, 7 2019, pp. 1547–1550.

[77] J. L. Mueller and S. Siltanen, *Linear and nonlinear inverse problems with practical applications*. SIAM, 1 2012.

[78] P. J. Vauhkonen, M. Vauhkonen, T. Savolainen, et al., "Three-dimensional electrical impedance tomography based on the complete electrode model." *IEEE Transactions on Biomedical Engineering*, vol. 46, no. 9, pp. 1150–1160, 9 1999.

[79] M. Soleimani, C. E. Powell, and N. Polydorides, "Improving the forward solver for the complete electrode model in EIT using algebraic multigrid." *IEEE Transactions on Medical Imaging*, vol. 24, no. 5, pp. 577–583, 5 2005.

[80] N. Polydorides, W. R. B. Lionheart, and H. McCann, "Krylov subspace iterative techniques: on the detection of brain activity with electrical impedance tomography." *IEEE Transactions on Medical Imaging*, vol. 21, no. 6, pp. 596–603, 6 2002.

[81] A. Adler, R. Gaburro, and W. Lionheart, "Electrical impedance tomography," pp. 599–654, 1 2011.

[82] D. C. Barber, "Quantification in impedance imaging." *Clinical Physics and Physiological Measurement*, vol. 11 Suppl A, pp. 45–56, 1 1990.

[83] B. Grychtol and A. Adler, "Uniform background assumption produces misleading lung EIT images." *Physiological Measurement*, vol. 34, no. 6, pp. 579–593, 6 2013.

[84] A. Adler and R. Guardo, "Electrical impedance tomography: regularized imaging and contrast detection." *IEEE Transactions on Medical Imaging*, vol. 15, no. 2, pp. 170–179, 1 1996.

[85] C. Gómez-Laberge and A. Adler, "Direct EIT jacobian calculations for conductivity change and electrode movement." *Physiological Measurement*, vol. 29, no. 6, pp. 89–99, 6 2008.

[86] J. C. A. Barata and M. S. Hussein, "The Moore-Penrose pseudoinverse: A tutorial review of the theory," *Brazilian Journal of Physics*, vol. 42, pp. 146–165, 4 2012.

[87] J. S. Hadamard, "Sur les problèmes aux dérivées partielles et leur signification physique," *Princeton University Bulletin*, vol. 13, pp. 49–52, 1 1902.

[88] A. N. Tikhonov and V. Y. Arsenin, *Solutions of ill-posed problems*. Winston&Sons, New York, 1 1977.

[89] C. Hansen, "Analysis of discrete ill-posed problems by means of the L-curve," *SIAM Review*, vol. 34, no. 4, pp. 561–580, 1 1992.

[90] P. C. Hansen and P. C. O'Leary, "The use of the L-curve in the regularization of discrete ill-posed problems," *SIAM Journal of Scientific Computing*, vol. 14, no. 6, pp. 1487–1503, 1 1993.

[91] G. H. Golub, M. Heath, and G. Wahba, "Generalized cross-validation as a method for choosing a good ridge parameter," *Technometrics*, vol. 21, no. 2, p. 215, 1 1979.

[92] F. Braun, M. Proenca, J. Sola, et al., "A versatile noise performance metric for electrical impedance tomography algorithms." *IEEE Transactions on Biomedical Engineering*, vol. 64, no. 10, pp. 2321–2330, 10 2017.

[93] A. Adler, J. H. Arnold, R. Bayford, et al., "GREIT: a unified approach to 2D linear EIT reconstruction of lung images." *Physiological Measurement*, vol. 30, no. 6, pp. 35–55, 6 2009.

[94] M. Cheney, D. Isaacson, J. C. Newell, et al., "NOSER: An algorithm for solving the inverse conductivity problem," *International Journal of Imaging Systems and Technology*, vol. 2, no. 2, pp. 66–75, 1 1990.

[95] T. Dai, "Image reconstruction in EIT using advanced regularization frameworks," PhD thesis, 2008.

[96] G. H. Golub and C. Reinsch, "Singular value decomposition and least squares solutions," *Numerische Mathematik*, vol. 14, no. 5, pp. 403–420, 1 1970.

[97] S. J. Hamilton, W. R. B. Lionheart, and A. Adler, "Comparing D-bar and common regularization-based methods for electrical impedance tomography." *Physiological Measurement*, vol. 40, no. 4, p. 044004, 4 2019.

[98] D. T. Nguyen, C. Jin, A. Thiagalingam, et al., "A review on electrical impedance tomography for pulmonary perfusion imaging." *Physiological Measurement*, vol. 33, no. 5, pp. 695–706, 5 2012.

[99] B. M. Eyuboglu, B. H. Brown, and D. C. Barber, "In vivo imaging of cardiac related impedance changes." *IEEE engineering in medicine and biology magazine : the quarterly magazine of the Engineering in Medicine & Biology Society*, vol. 8, no. 1, pp. 39–45, 1 1989.

[100] J. M. Deibele, H. Luepschen, and S. Leonhardt, "Dynamic separation of pulmonary and cardiac changes in electrical impedance tomography." *Physiological Measurement*, vol. 29, no. 6, pp. 1–14, 6 2008.

[101] R. Pikkemaat, S. Lundin, O. Stenqvist, et al., "Recent advances in and limitations of cardiac output monitoring by means of electrical impedance tomography," *Anesthesia and Analgesia*, vol. 119, no. 1, pp. 76–83, 1 2014.

[102] R. Pikkemaat, "Kardiopulmonales Monitoring mit Hilfe der elektrischen Impedanztomographie," PhD thesis, 8 2015.

[103] A. Fagerberg, O. Stenqvist, and A. Aneman, "Monitoring pulmonary perfusion by electrical impedance tomography: an evaluation in a pig model." *Acta Anaesthesiologica Scandinavica*, vol. 53, no. 2, pp. 152–8, 2 2009.

[104] A. Vonk Noordegraaf, P. W. A. Kunst, A. Janse, et al., "Pulmonary perfusion measured by means of electrical impedance tomography," *Physiological Measurement*, vol. 19, no. 2, pp. 263–273, 1 1998.

[105] H. J. Smit, A. Vonk Noordegraaf, J. T. Marcus, et al., "Determinants of pulmonary perfusion measured by electrical impedance tomography." *European Journal of Applied Physiology*, vol. 92, no. 1-2, pp. 45–49, 6 2004.

[106] B. H. Brown, A. Learthard, A. Sinton, et al., "Blood flow imaging using electrical impedance tomography," *Clinical Physical and Physiological Measurements*, vol. 13, no. Suppl A, pp. 175–179, 1 1992.

[107] I. Frerichs, M. B. P. Amato, A. H. van Kaam, et al., "Chest electrical impedance tomography examination, data analysis, terminology, clinical use and recommendations: consensus state-

ment of the TRanslational EIT developmeNt stuDy group," *Thorax*, vol. 72, no. 1, pp. 83–93, 2016.

[108] N. C. Hellige, G. Hahn, and G. Hellige, "Comment on borges et al. "regional lung perfusion estimated by electrical impedance tomography in a piglet model of lung collapse"." *Journal of Applied Physiology*, vol. 112, no. 12, p. 2127; author reply 2128, 6 2012.

[109] B. Hentze, T. Muders, H. Luepschen, et al., "Regional lung ventilation and perfusion by electrical impedance tomography compared to single-photon emission computed tomography." *Physiological Measurement*, vol. 39, no. 6, p. 065004, 6 2018.

[110] H. Reinius, J. B. Borges, F. Fredén, et al., "Real-time ventilation and perfusion distributions by electrical impedance tomography during one-lung ventilation with capnothorax." *Acta Anaesthesiologica Scandinavica*, vol. 59, no. 3, pp. 354–368, 3 2015.

[111] J. B. Borges, J. N. Cronin, D. C. Crockett, et al., "Real-time effects of PEEP and tidal volume on regional ventilation and perfusion in experimental lung injury." *Intensive Care Medicine Experimental*, vol. 8, no. 1, p. 10, 2 2020.

[112] C. Putensen, B. Hentze, S. Muenster, et al., "Electrical impedance tomography for cardiopulmonary monitoring." *Journal of Clinical Medicine*, vol. 8, no. 8, 8 2019.

[113] E. Hering, "Versuche, die Schnelligkeit des Blutlaufs und der Absonderung zu Bestimmen," *Zeitschrift für Physiologie*, vol. 3, pp. 85–126, 1829.

[114] K. L. Zierler, "Theoretical basis of indicator-dilution methods for measuring flow and volume," *Circulation Research*, vol. 10, no. 3, pp. 393–407, 1 1962.

[115] L. Ostergaard, R. M. Weisskoff, D. A. Chesler, et al., "High resolution measurement of cerebral blood flow using intravascular tracer bolus passages. Part I: Mathematical approach and statistical analysis," *Magnetic Resonance in Medicine*, vol. 36, no. 5, pp. 715–725, 11 1996.

[116] M. Mischi, J. A. den Boer, and H. H. M. Korsten, "On the physical and stochastic representation of an indicator dilution curve as a gamma variate." *Physiological Measurement*, vol. 29, no. 3, pp. 281–294, 3 2008.

[117] R. A. Linton, N. W. Linton, and D. M. Band, "A new method of analysing indicator dilution curves." *Cardiovascular Research*, vol. 30, no. 6, pp. 930–938, 12 1995.

[118] H. K. J. Thompson, C. F. Starmer, R. E. Whalen, et al., "Indicator transit time considered as a gamma variate," *Circulation Research*, vol. 14, no. 6, pp. 502–515, 6 1964.

[119] M. D. Harpen and M. L. Lecklitner, "Derivation of gamma variate indicator dilution function from simple convective dispersion model of blood flow." *Medical Physics*, vol. 11, no. 5, pp. 690–692, 1 1984.

[120] M. T. Madsen, "A simplified formulation of the gamma variate function," *Physics in Medicine & Biology*, vol. 37, pp. 1597–2000, 1992.

[121] T. Bluth, T. Kiss, M. Kircher, et al., "Measurement of relative lung perfusion with electrical impedance and positron emission tomography: an experimental comparative study in pigs." *British Journal of Anaesthesia*, vol. 123, no. 2, pp. 246–254, 8 2019.

[122] T. Bluth, T. Kiss, M. Kircher, et al., "Tierexperimentelle Evaluation der elektrischen Impedanztomographie zur Messung der relativen Lungenperfusion," *Anästhesiologie & Intensivmedizin*, p. 370, 2018.

[123] T. Bluth, T. Kiss, M. Kircher, et al., "Comparison of indicator-based electrical impedance tomography with positron emission tomography for measurements of relative lung perfusion

in pigs," *American Journal of Respiratory and Critical Care Medicine*, vol. 197, pp. A7209–
–A7209, 2018.

[124] M. Kircher, A. Braune, T. Bluth, et al., "Method for comparing pulmonary perfusion measured by PET/CT and indicator based EIT measurements in a porcine model," in *19th International Conference on Biomedical Applications of Electrical Impedance Tomography*, 2018.

[125] M. Kircher, F. Schuderer, B. Stender, et al., "Nonlinear and piecewise fitting of indicator-enhanced EIT signals: Comparison of methods," in *Innovative Verarbeitung bioelektrischer und -magnetischer Signale. Proceedings BBS 2020*, 2020.

[126] F. Schuderer, M. Kircher, O. Dössel, et al., "Introducing a linear gamma variate fit to measure pulmonary perfusion with electrical impedance tomography," *Current Directions in Biomedical Engineering*, vol. 6, no. 3, pp. 345–348, 09 2020.

[127] X. Augustin, M. Kircher, O. Dössel, et al., "Estimating regional pulmonary blood flow in EIT with regularized deconvolution with a Tikhonov regularization," *Current Directions in Biomedical Engineering*, vol. 6, no. 3, pp. 60–63, 09 2020.

[128] M. Schmal, J. Haueisen, G. Männel, et al., "Robust predictive control for respiratory CO2 gas removal in closed-loop mechanical ventilation: An in-silico study," *Current Directions in Biomedical Engineering*, vol. 6, no. 3, pp. 311–314, 09 2020.

[129] K. Jenne, "Automatic detection and classification of respiratory and hemodynamic pulmonary states for cardiac related EIT signal analysis," Bachelor Thesis, Institute of Biomedical Engineering (IBT), Karlsruhe Institute of Technology (KIT), 2017.

[130] F. Schuderer, "Optimized modeling of nonlinear indicator dilution curves in Electrical Impedance Tomography to measure regional lung perfusion," Bachelor Thesis, Institute of Biomedical Engineering (IBT), Karlsruhe Institute of Technology (KIT), 2018.

[131] I. Tabet, "Development and Quantitative Analysis of Automatic Electrical Impedance Tomography Signal Component Detection and Separation Algorithms," Bachelor Thesis, Institute of Biomedical Engineering (IBT), Karlsruhe Institute of Technology (KIT), 2019.

[132] J. Osypka, "EIT sensitivity analysis of local pulmonary blood flow in front of realistic background tissue distributions in a porcine model," Bachelor Thesis, Institute of Biomedical Engineering (IBT), Karlsruhe Institute of Technology (KIT), 2019.

[133] X. Augustin, "Optimierung der Separation des Indikatorsignals in EIT-Messspannungen und der anschließenden regularisierten Entfaltung für die pulmonale Perfusionsschätzung," Bachelor Thesis, Institute of Biomedical Engineering (IBT), Karlsruhe Institute of Technology (KIT), 2019.

[134] M. Hernández Mesa, "Comparison of approaches for solving the inverse problem of regional indicator based EIT pulmonary blood flow exploiting a priori information," Master Thesis, Institute of Biomedical Engineering (IBT), Karlsruhe Institute of Technology (KIT), 2020.

[135] S. R. Hopkins, M. O. Wielpütz, and H.-U. Kauczor, "Imaging lung perfusion." *Journal of Applied Physiology*, vol. 113, no. 2, pp. 328–339, 7 2012.

[136] G. R. Manecke, "Edwards FloTrac sensor and Vigileo monitor: easy, accurate, reliable cardiac output assessment using the arterial pulse wave." *Expert Review of Medical Devices*, vol. 2, no. 5, pp. 523–527, 9 2005.

[137] O. Wendt, "Mini-Handbuch Elektro-Impedanz-Tomografie (EIT)," 11 2018.

[138] M. Russ, S. Kronfeldt, W. Boemke, et al., "Lavage-induced surfactant depletion in pigs as a model of the acute respiratory distress syndrome (ARDS)." *Journal of Visualized Experiments*, no. 115, 9 2016.

[139] B. Lachmann, B. Robertson, and J. Vogel, "In vivo lung lavage as an experimental model of the respiratory distress syndrome." *Acta Anaesthesiologica Scandinavica*, vol. 24, no. 3, pp. 231–236, 6 1980.

[140] G. Elke, M. K. Fuld, A. F. Halaweish, et al., "Quantification of ventilation distribution in regional lung injury by electrical impedance tomography and xenon computed tomography." *Physiological Measurement*, vol. 34, no. 10, pp. 1303–1318, 10 2013.

[141] G. Elke, M. Kircher, O. Dössel, et al., "Regional pulmonary perfusion in experimental regional ARDS - a comparison of EIT and CT," vol. 5 (Suppl 2):0243, no. Meeting abstract, Vienna, Austria; September 23-27, 2017.

[142] M. Kircher, G. Elke, B. Stender, et al., "Regional lung perfusion analysis in experimental ards by electrical impedance and computed tomography," *IEEE Transactions on Medical Imaging*, pp. 1–1, 2020.

[143] A. Noshadi, "Rekonstruktion von 3D Gewebeläsionen aus MRT Aufnahmen," Bachelor Thesis, Institute of Biomedical Engineering (IBT), Karlsruhe Institute of Technology (KIT), 2017.

[144] A. Noshadi, M. Kircher, S. Pollnow, et al., "Automatic lung segmentation in the presence of alveolar collapse," in *Current Directions in Biomedical Engineering*, vol. 3, no. 2. de Gruyter, 1 2017, pp. 807–810.

[145] Y. Li, E. Tesselaar, J. B. Borges, et al., "Hyperoxia affects the regional pulmonary ventilation/perfusion ratio: an electrical impedance tomography study." *Acta Anaesthesiologica Scandinavica*, vol. 58, no. 6, pp. 716–725, 7 2014.

[146] R. Menges, "Separation, analysis and classification of the cardiac dependent EIT signal component using an MRI based reconstruction model," Master Thesis, Institute of Biomedical Engineering (IBT), Karlsruhe Institute of Technology (KIT), 2017.

[147] R. Hattiangdi, "3D sensitivity analysis of human EIT measurements based on EIT forward simulation in the context of pulmonary perfusion monitoring," Master Thesis, Hochschule Karlsruhe - Technik und Wirtschaft; Institute of Biomedical Engineering (IBT), Karlsruhe Institute of Technology (KIT), 2019.

[148] J. Brenneisen, "Analyse und Vergleich verschiedener EIT Rekonstruktionsansätze anhand simulierter und gemessener Daten hinsichtlich herzsynchroner Pulsatilität," Master Thesis, Institute of Biomedical Engineering (IBT), Karlsruhe Institute of Technology (KIT), 2019.

[149] B. Stender and J. Maier, "Weighting functions for image-based validation of EIT," *17th Int. Conf. on Biomedical Applications of EIT*, p. 162, 6 2016.

[150] K. S. Rabbani and A. M. Kabir, "Studies on the effect of the third dimension on a two-dimensional electrical impedance tomography system." *Clinical Physics and Physiological Measurement*, vol. 12, no. 4, pp. 393–402, 11 1991.

[151] B. Grychtol, J. P. Schramel, F. Braun, et al., "Thoracic EIT in 3D: experiences and recommendations." *Physiological Measurement*, vol. 40, no. 7, p. 074006, 8 2019.

[152] P. A. Yushkevich, J. Piven, H. C. Hazlett, et al., "User-guided 3D active contour segmentation of anatomical structures: significantly improved efficiency and reliability." *NeuroImage*, vol. 31, no. 3, pp. 1116–1128, 7 2006.

[153] P. Cignoni, M. Callieri, M. Corsini, et al., "MeshLab: an open-source mesh processing tool," in *Eurographics Italian Chapter Conference*, V. Scarano, R. De Chiara, and U. Erra, Eds. The Eurographics Association, 2008, pp. 129–136.

[154] N. Pietroni, M. Tarini, and P. Cignoni, "Almost isometric mesh parameterization through abstract domains," *IEEE Transactions on Visualization and Computer Graphics*, vol. 16, no. 4, pp. 621–635, 1 2010.

[155] G. Taubin, "Curve and surface smoothing without shrinkage," in *Proceedings of 5th International Conference on Computer Vision (ICCV)*. IEEE Computer Society Press, 1 1995, pp. 852–857.

[156] W. Jakob, M. Tarini, D. Panozzo, et al., "Instant field-aligned meshes," *ACM Transactions on Graphics*, vol. 34, no. 6, pp. 1–15, 1 2015.

[157] C. Geuzaine and J.-F. Remacle, "Gmsh: A 3-D finite element mesh generator with built-in pre- and post-processing facilities," *International Journal for Numerical Methods in Engineering*, vol. 79, no. 11, pp. 1309–1331, 1 2009.

[158] C. Gabriel, "Compilation of the dielectric properties of body tissues at RF and microwave frequencies." 1 1996.

[159] P. Hasgall, E. Neufeld, M.-C. Gosselin, et al., "ITIS database for thermal and electromagnetic parameters of biological tissues, version 2.2," 5 2018.

[160] P. Nopp, E. Rapp, H. Pfützner, et al., "Dielectric properties of lung tissue as a function of air content." *Physics in Medicine and Biology*, vol. 38, no. 6, pp. 699–716, 6 1993.

[161] P. Nopp, N. D. Harris, T. X. Zhao, et al., "Model for the dielectric properties of human lung tissue against frequency and air content." *Medical & Biological Engineering & Computing*, vol. 35, no. 6, pp. 695–702, 11 1997.

[162] C. J. Roth, "Multi-dimensional coupled computational modeling in respiratory biomechanics," PhD thesis, Technische Universität München, 2017.

[163] D. A. Witsoe and E. Kinnen, "Electrical resistivity of lung at 100 khz," *Medical & Biological Engineering*, vol. 5, no. 3, pp. 239–248, 1 1967.

[164] S. Nebuya, G. H. Mills, P. Milnes, et al., "Indirect measurement of lung density and air volume from electrical impedance tomography (EIT) data." *Physiological Measurement*, vol. 32, no. 12, pp. 1953–1967, 12 2011.

[165] C. J. Roth, A. Ehrl, T. Becher, et al., "Correlation between alveolar ventilation and electrical properties of lung parenchyma." *Physiological Measurement*, vol. 36, no. 6, pp. 1211–1226, 6 2015.

[166] N. Epstein, "On tortuosity and the tortuosity factor in flow and diffusion through porous media," *Chemical Engineering Science*, vol. 44, no. 3, pp. 777–779, 1 1989.

[167] K. Markstaller, H.-U. Kauczor, N. Weiler, et al., "Lung density distribution in dynamic CT correlates with oxygenation in ventilated pigs with lavage ARDS." *British Journal of Anaesthesia*, vol. 91, no. 5, pp. 699–708, 11 2003.

[168] R. Weast and D. Lide, "CRC handbook of chemistry and physics," vol. 70, pp. D–221, 1 1989.

[169] A. Adler and W. R. B. Lionheart, "Uses and abuses of EIDORS: an extensible software base for EIT." *Physiological Measurement*, vol. 27, no. 5, pp. 25–42, 5 2006.

[170] Y. C. Chiu, P. W. Arand, S. G. Shroff, et al., "Determination of pulse wave velocities with computerized algorithms." *American Heart Journal*, vol. 121, no. 5, pp. 1460–1470, 5 1991.

[171] N. Saeedizadeh, S. Kermani, and H. Rabbani, "A comparison between the hp-version of finite element method with EIDORS for electrical impedance tomography." *Journal of Medical Signals and Sensors*, vol. 1, no. 3, pp. 200–205, 7 2011.

[172] M. Proenca, F. Braun, M. Rapin, et al., "Influence of heart motion on cardiac output estimation by means of electrical impedance tomography: a case study," *Physiological Measurement*, vol. 36, no. 6, pp. 1075–1091, 1 2015.

[173] M. Arakawa, K. Kambara, T. Segawa, et al., "Usefulness of sodium chloride as a nondiffusible indicator in the measurement of extravascular lung thermal volume in dogs." *Medical & Biological Engineering & Computing*, vol. 31 Suppl, pp. 67–72, 7 1993.

[174] S. Süß, "Determination of the information gain by estimating the instantaneous phase of biosignals," Master Thesis, Institute of Biomedical Engineering (IBT), Karlsruhe Institute of Technology (KIT), 2018.

[175] F. Gustafsson, "Determining the initial states in forward-backward filtering," *IEEE Transactions on Signal Processing*, vol. 44, pp. 988–992, 4 1996.

[176] J. P. Hannon, C. A. Bossone, and C. E. Wade, "Normal physiological values for conscious pigs used in biomedical research." *Laboratory Animal Science*, vol. 40, no. 3, pp. 293–298, 5 1990.

[177] J. C. Drummond, C. A. Brann, D. E. Perkins, et al., "A comparison of median frequency, spectral edge frequency, a frequency band power ratio, total power, and dominance shift in the determination of depth of anesthesia." *Acta Anaesthesiologica Scandinavica*, vol. 35, no. 8, pp. 693–699, 11 1991.

[178] T. Bein, S. Grasso, O. Moerer, et al., "The standard of care of patients with ARDS: ventilatory settings and rescue therapies for refractory hypoxemia." *Intensive Care Medicine*, vol. 42, no. 5, pp. 699–711, 5 2016.

[179] L. Papazian, C. Aubron, L. Brochard, et al., "Formal guidelines: management of acute respiratory distress syndrome." *Annals of Intensive Care*, vol. 9, no. 1, p. 69, 6 2019.

[180] B. Hentze, T. Muders, M. Walter, et al., "A deconvolution method for perfusion imaging under ongoing ventilation using electrical impedance tomography," in *41st Annual International Conference of the IEEE Engineering in Medicine and Biology Society (EMBC)*, 2019.

[181] R. Casanova, A. Silva, and A. R. Borges, "MIT image reconstruction based on edge-preserving regularization." *Physiological Measurement*, vol. 25, no. 1, pp. 195–207, 2 2004.

[182] A. Adler, T. Dai, and W. R. B. Lionheart, "Temporal image reconstruction in electrical impedance tomography." *Physiological Measurement*, vol. 28, no. 7, pp. 1–11, 7 2007.

[183] F. Thürk, S. Boehme, D. Mudrak, et al., "Effects of individualized electrical impedance tomography and image reconstruction settings upon the assessment of regional ventilation distribution: Comparison to 4-dimensional computed tomography in a porcine model." *PloS one*, vol. 12, no. 8, p. e0182215, 1 2017.

[184] W. Fan and H. Wang, "Maximum entropy regularization method for electrical impedance tomography combined with a normalized sensitivity map," *Flow Measurement and Instrumentation*, vol. 21, no. 3, pp. 277–283, 1 2010.

[185] B. Schullcke, B. Gong, S. Krueger-Ziolek, et al., "Reconstruction of conductivity change in lung lobes utilizing electrical impedance tomography," *Current Directions in Biomedical Engineering*, vol. 3, no. 2, 1 2017.

[186] B. Schullcke, B. Gong, S. Krueger-Ziolek, et al., "Structural-functional lung imaging using a combined CT-EIT and a discrete cosine transformation reconstruction method." *Scientific Reports*, vol. 6, p. 25951, 5 2016.

[187] S. Schuler, D. Potyagaylo, and O. Dössel, "ECG imaging of simulated atrial fibrillation: Imposing epi-endocardial similarity facilitates the reconstruction of transmembrane voltages," in *Computing in Cardiology*, vol. 44, 2017.

[188] G. H. Golub and C. F. Van Loan, "Matrix computations," vol. 4, 2012.

[189] A. Boyle and A. Adler, "The impact of electrode area, contact impedance and boundary shape on EIT images." *Physiological Measurement*, vol. 32, no. 7, pp. 745–754, 7 2011.

[190] G. Elke, S. Pulletz, D. Schädler, et al., "Measurement of regional pulmonary oxygen uptake–a novel approach using electrical impedance tomography." *Physiological Measurement*, vol. 32, no. 7, pp. 877–886, 7 2011.

[191] G. Johnson, S. G. Wetzel, S. Cha, et al., "Measuring blood volume and vascular transfer constant from dynamic, T(2)*-weighted contrast-enhanced MRI." *Magnetic Resonance in Medicine*, vol. 51, no. 5, pp. 961–968, 5 2004.

[192] V. Patil and G. Johnson, "An improved model for describing the contrast bolus in perfusion MRI." *Medical Physics*, vol. 38, no. 12, pp. 6380–6383, 12 2011.

[193] R. W. Stow and P. S. Hetzel, "An empirical formula for indicator-dilution curves as obtained in human beings." *Journal of Applied Physiology*, vol. 7, no. 2, pp. 161–167, 9 1954.

[194] T. F. Coleman and Y. Li, "An interior trust region approach for nonlinear minimization subject to bounds," *SIAM Journal on Optimization*, vol. 6, no. 2, pp. 418–445, 1 1996.

[195] S. Lloyd, "Least squares quantization in PCM," *IEEE Transactions on Information Theory*, vol. 28, no. 2, pp. 129–137, 1 1982.

[196] A. A. Konstas, G. V. Goldmakher, T.-Y. Lee, et al., "Theoretic basis and technical implementations of CT perfusion in acute ischemic stroke, part 1: Theoretic basis." *American Journal of Neuroradiology*, vol. 30, no. 4, pp. 662–668, 4 2009.

[197] I. Frerichs, J. Hinz, P. Herrmann, et al., "Regional lung perfusion as determined by electrical impedance tomography in comparison with electron beam CT imaging." *IEEE Transactions on Medical Imaging*, vol. 21, no. 6, pp. 646–652, 6 2002.

[198] K. A. Miles, "Measurement of tissue perfusion by dynamic computed tomography." *The British Journal of Radiology*, vol. 64, no. 761, pp. 409–412, 5 1991.

[199] G. Hautvast, A. Chiribiri, N. Zarinabad, et al., "Myocardial blood flow quantification from MRI by deconvolution using an exponential approximation basis." *IEEE Transactions on Biomedical Engineering*, vol. 59, no. 7, pp. 2060–2067, 7 2012.

[200] R. Siegwart, F. Colas, and F. Pomerleau, "A review of point cloud registration algorithms for mobile robotics," *Foundations and Trends in Robotics*, vol. 4, no. 1, pp. 1–104, 1 2015.

[201] B. Hentze, T. Muders, H. Luepschen, et al., "Gamma-variate modeling of indicator dilution curves in electrical impedance tomography." *Conference proceedings : Annual International Conference of the IEEE Engineering in Medicine and Biology Society*, vol. 2017, pp. 3596–3599, 7 2017.

[202] H. M. Wang, M. Bodenstein, and K. Markstaller, "Overview of the pathology of three widely used animal models of acute lung injury." *European Surgical Research*, vol. 40, no. 4, pp. 305–316, 2008.

[203] L. A. Huppert, M. A. Matthay, and L. B. Ware, "Pathogenesis of acute respiratory distress syndrome." *Seminars in Respiratory and Critical Care Medicine*, vol. 40, no. 1, pp. 31–39, 2 2019.

[204] R. Naeije and S. Brimioulle, "Physiology in medicine: importance of hypoxic pulmonary vasoconstriction in maintaining arterial oxygenation during acute respiratory failure." *Critical Care*, vol. 5, no. 2, pp. 67–71, 1 2001.

[205] R. Gust, J. Kozlowski, A. H. Stephenson, et al., "Synergistic hemodynamic effects of low-dose endotoxin and acute lung injury." *American Journal of Respiratory and Critical Care Medicine*, vol. 157, no. 6 Pt 1, pp. 1919–1926, 6 1998.

[206] Y. Li, E. Tesselaar, J. B. Borges, et al., "Hyperoxia affects the regional pulmonary ventilation/perfusion ratio: an electrical impedance tomography study." *Acta Anaesthesiologica Scandinavica*, vol. 58, no. 6, pp. 716–725, 7 2014.

[207] J. Schöberl, "NETGEN an advancing front 2D/3D-mesh generator based on abstract rules," *Computing and Visualization in Science*, vol. 1, no. 1, pp. 41–52, 1 1997.

[208] M. Rapin, F. Braun, A. Adler, et al., "Wearable sensors for frequency-multiplexed EIT and multilead ECG data acquisition." *IEEE Transactions on Biomedical Engineering*, vol. 66, no. 3, pp. 810–820, 3 2019.

[209] R. Sameni, C. Jutten, and M. B. Shamsollahi, "Multichannel electrocardiogram decomposition using periodic component analysis," *IEEE Transactions on Biomedical Engineering*, vol. 55, no. 8, pp. 1935–1940, 1 2008.

[210] T. Mauri, E. Spinelli, E. Scotti, et al., "Potential for lung recruitment and ventilation-perfusion mismatch in patients with the acute respiratory distress syndrome from coronavirus disease 2019." *Critical Care Medicine*, 4 2020.

List of Publications and Supervised Theses

Journal Articles

- G. Lenis*, **M. Kircher***, J. Lazaro, R. Bailon, E. Gil, O. Dössel; *Separating the effect of respiration on the heart rate variability using Granger's causality and linear filtering*; Biomedical Signal Processing and Control; 2017; 31:272–278
- T. Bluth*, T. Kiss*, **M. Kircher***, A. Braune*, C. Bozsak, R. Huhle, M. Scharffenberg, M. Herzog, J. Roegner, P. Herzog, L. Vivona, M. Millone, O. Dössel, M. Andreeff, T. Koch, J. Kotzerke, B. Stender, M. Gama de Abreu; *Measurement of relative lung perfusion with electrical impedance and positron emission tomography: an experimental comparative study in pigs*; British Journal of Anesthesia; 2019; 123(2):246–254
- **Michael Kircher***, Gunnar Elke*, Birgit Stender, María Hernández, Felix Schuderer, Olaf Dössel, Mathhew K. Fuld, Ahmed Halaweish, Eric A. Hoffman, Norbert Weiler, Inéz Frerichs; *Regional lung perfusion analysis in ARDS by electrical impedance- and computed tomography*, IEEE Transactions on Medical Imaging; 2020; Early Access
- Elena Spinelli, **Michael Kircher**, Birgit Stender, Irene Ottaviani, Maria Cristina Basile, Ines Marongiu, Giulia Colussi, Giacomo Grasselli, Antonio Pesenti, Tommaso Mauri; *Unmatched ventilation and perfusion measured by electrical impedance tomography predicts the outcome of ARDS*; Chest; 2020; under review

* authors contributed equally; shared first authorship

Refereed Conference Articles

- **M. Kircher**, G. Lenis, O. Dössel, *Separating the effect of respiration from the Heart Rate Variability for cases of constant harmonic breathing*, Current Directions in Biomedical Engineering, 2015, 1(1):46–49

- A. Noshadi, **M. Kircher**, S. Pollnow, G. Elke, I. Frerichs, O. Dössel, *Automatic lung segmentation in the presence of alveolar collapse*, Current Directions in Biomedical Engineering, 2017, 3(2):807–810
- S. Pollnow, A. Noshadi, **M. Kircher**, G. Guthausen, T. Oether, O. Dössel, *3D reconstruction of ablation lesions from in-vitro preparations using MRI*, Current Directions in Biomedical Engineering, 2017, 3(2):437–440
- **M. Kircher**, A. Braune, T. Bluth, M. Gama de Abreu, O. Dössel, B. Stender *Method for comparing pulmonary perfusion measured by PET/CT and indicator based EIT measurements in a porcine model*, 19th International Conference on Biomedical Applications of Electrical Impedance Tomography, 2018
- **M. Kircher**, R. Hattiangdi, R. Menges, O. Dössel *Influence of background lung tissue conductivity on the cardiosynchronous EIT signal components: a sensitivity study*, 41st Annual International Conference of the IEEE Engineering in Medicine and Biology Society (EMBC), 2019, 1547-1550
- F. Schuderer, **M. Kircher**, B. Stender, T. Bluth, M. Gama de Abreu, O. Dössel *Introducing a Linear Gamma Variate Fit to Measure Pulmonary Perfusion with Electrical Impedance Tomography*, Current Directions in Biomedical Engineering, 2020, 6(3): 345-348
- X. Augustin, **M. Kircher**, B. Stender, T. Bluth, M. Gama de Abreu, O. Dössel *Estimating regional pulmonary blood flow in EIT with regularized deconvolution with a Tikhonov regularization*, Current Directions in Biomedical Engineering, 2020, 6(3): 60-63
- M. Schmal, J. Haueisen, G. Männel, P. Rostalski, **M. Kircher**, T. Bluth,M. Gama de Abreu, B. Stender *Robust predictive control for respiratory CO2 gas removal in closed-loop mechanical ventilation: An in-silico study*, Current Directions in Biomedical Engineering, 2020, 6(3): 311-314

Refereed Conference Abstracts

- **M. Kircher**, R. Menges, G. Lenis, O. Dössel, *Respiratory influence on HRV parameters analyzed during controlled respiration, spontaneous respiration and apnoe*, Current Directions in Biomedical Engineering, 2017, 3(2)
- **M. Kircher**, B. Stender, O. Dössel, *Investigation of regional pulmonary perfusion using Electrical Impedance Tomography*, Dreiländertagung of the Swiss, Austrian and German Societies for Biomedical Engineering, 2016
- G. Elke, **M. Kircher**, O. Dössel, M.K. Fuld, A.E. Halaweish, E.A. Hoffman, N. Weiler, I. Frerichs, *Regional pulmonary perfusion in experimental regional ARDS - a comparison of EIT and CT*, Intensive Care Medicine Experimental, 2017, 5(Suppl 2):0243
- T. Bluth, T. Kiss, **M. Kircher**, A. Braune, C. Bozsak, R. Huhle, M. Scharffenberg, M. Herzog, J. Roegner, P. Herzog, L. Vivona, M. Millone, O. Dössel, M. Andreeff, T. Koch, J. Kotzerke, B. Stender, M. Gama de Abreu, *Tierexperimentelle Evaluation der elektrischen Impedanztomographie zur Messung der relativen Lungenperfusion*, 32.

Wissenschaftlichen Arbeitstage der Deutschen Gesellschaft für Anästhesiologie & Intensivmedizin Würzburg, 2018

- A. Braune, **M. Kircher**, T. Bluth, T. Kiss, C. Bozsak, R. Huhle, M. Scharffenberg, M. Herzog, J. Roegner, L. Vivona, M. Millone, O. Dössel, M. Andreeff, T. Koch, J. Kotzerke, B. Stender, M. Gama de Abreu, *Comparison of Indicator-Based Electrical Impedance Tomography with Positron Emission Tomography for Measurements of Relative Lung Perfusion in Pigs*, American Journal of Respiratory and Critical Care Medicine, 2018, 197:A7209–A7209
- **M. Kircher**, O. Dössel, *Feature based analysis of the cardiosynchronous EIT signal component using an MRI-based reconstruction model*, Abstracts of the 2018 Annual Meeting of the German Society of Biomedical Engineering (26–28 September 2018, Aachen/DE). Biomedical Engineering / Biomedizinische Technik, 2018, 63(s1)
- **M. Kircher**, F. Schuderer, B. Stender, T. Bluth, M. Gama de Abreu, O. Dössel, *Nonlinear and Piecewise Fitting of Indicator-Enhanced EIT signals: Comparison of Methods*, Workshop Biosignalverarbeitung, 2020
- E. Spinelli, T. Mauri, **M. Kircher**, B. Stender, I. Ottaviani, M.C. Basile, E. Scotti, I Marongiu, G. Colussi, G. Graselli, A. Presenti, *Heterogeneous Distribution of Pulmonary Perfusion is Associated with Mortality in ARDS*, American Journal of Respiratory and Critical Care Medicine, 2020, 201:A2884

Other Presentations

- **M. Kircher**, B. Stender *Regional lung perfusion measured with EIT: Results from the validation study in Dresden* Electrical Impedance Tomography User Workshop organized by Drägerwerk & Co. KGaA, Frankfurt am Main, 2017

Reports and Theses

- **M. Kircher**, *Erfassung von Personen im dreidimensionalen Raum mittels eines 2D-Digital Beamforming Radars*, Bachelor Thesis, Institute of Radio Frequency Engineering and Electronics, Karlsruhe Institute of Technology (KIT), 2012
- **M. Kircher**, *Separating the effect of respiration on the heart rate variability and quantifying the medical impact of the new uncoupled parameters*, Master Thesis, Institute of Biomedical Engineering, Karlsruhe Institute of Technology (KIT), 2015

Supervised Student Theses

- Areg Noshadi, *Rekonstruktion von 3D Gewebeläsionen aus MRT Aufnahmen*, Bachelor Thesis, Institute of Biomedical Engineering, Karlsruhe Institute of Technology (KIT), 2017
- Robert Menges, *Separation, analysis and classification of the cardiac dependent EIT signal component using an MRI based reconstruction model*, Master Thesis, Institute of Biomedical Engineering, Karlsruhe Institute of Technology (KIT), 2017
- Kevin Jenne, *Automatic detection and classification of respiratory and hemodynamic pulmonary states for cardiac related EIT signal analysis*, Bachelor Thesis, Institute of Biomedical Engineering, Karlsruhe Institute of Technology (KIT), 2017
- Felix Schuderer, *Optimized modeling of nonlinear indicator dilution curves in Electrical Impedance Tomography to measure regional lung perfusion*, Bachelor Thesis, Institute of Biomedical Engineering, Karlsruhe Institute of Technology (KIT), 2018
- Simon Süß, *Determination of the Information Gain by Estimating the Instantaneous Phase of Biosignals*, Bachelor Thesis, Institute of Biomedical Engineering, Karlsruhe Institute of Technology (KIT), 2018
- Jochen Brenneisen, *Analyse und Vergleich verschiedener EIT Rekonstruktionsansätze anhand simulierter und gemessener Daten hinsichtlich herzsynchroner Pulsatilität*, Master Thesis, Institute of Biomedical Engineering, Karlsruhe Institute of Technology (KIT), 2019
- Ibrahim Tabet, *Development and Quantitative Analysis of Automatic Electrical Impedance Tomography Signal Component Detection and Separation Algorithms*, Bachelor Thesis, Institute of Biomedical Engineering, Karlsruhe Institute of Technology (KIT), 2019
- Rohit Hattiangdi, *3D sensitivity analysis of human EIT measurements based on EIT forward simulation in the context of pulmonary perfusion monitoring*, Master Thesis, Institute of Biomedical Engineering, Karlsruhe Institute of Technology (KIT), 2019
- Johannes Osypka, *An EIT sensitivity analysis of local pulmonary blood flow in front of realistic background tissue distributions in a porcine model*, Bachelor Thesis, Institute of Biomedical Engineering, Karlsruhe Institute of Technology (KIT), 2019
- Xenia Augustin, *Optimierung der Separation des Indikatorsignals in EIT-Messspannungen und der anschließenden regularisierten Entfaltung für die pulmonale Perfusionsschätzung*, Bachelor Thesis, Institute of Biomedical Engineering, Karlsruhe Institute of Technology (KIT), 2019
- María Hernández Mesa *Comparison of approaches for solving the inverse problem of regional indicator based EIT pulmonary blood flow exploiting a priori information*, Master Thesis, Institute of Biomedical Engineering, Karlsruhe Institute of Technology (KIT), 2020

Awards & Grants

- Student fellowship, e-fellows.net, 2009-2016
- 1st place in student competition, DGBMT and DGMP annual conference Dresden, 2017
  A. Noshadi, **M. Kircher**, S. Pollnow, G. Elke, I. Frerichs and O. Dössel
- 1st place best paper and presentation award, 19. International Conference on Biomedical Applications of EIT, Edinburgh, United Kingdom, 2018:
  M. Kircher, A. Braune, T. Bluth, M. Gama de Abreu, O. Dössel, B. Stender
- 1st place best paper and presentation award, Biosignale Workshop der DGBMT, Kiel, 2020:
  M. Kircher, F. Schuderer, B. Stender, T. Bluth, M. Gama de Abreu and O. Dössel
- 1st place in student competition, DGBMT annual conference Leipzig, 2017
  X. Augustin, **M. Kircher**, B. Stender, T. Bluth, M. Gama de Abreu, O. Dössel